Title	Quantum-limited 0.78–0.95-THz Waveguide SIS Mixers for the ALMA Band 10 Receivers
Author(s)	Kojima, Takafumi
Editor(s)	
Citation	大阪府立大学, 2009, 博士論文.
Issue Date	2009
URL	http://hdl.handle.net/10466/10429
Rights	

Quantum-limited 0.78–0.95-THz Waveguide SIS Mixers for the ALMA Band 10 Receivers

Takafumi Kojima

February, 2010

Osaka Prefecture University

Abstract

This thesis describes the demonstration and the application of a low noise Superconductor-Insulator-Superconductor (SIS) mixer for the Atacama Large Millimeter/submillimeter Array (ALMA) band 10 covering the frequency range of 0.787-0.950 THz. The ALMA is one of the largest ground-based astronomy projects for the next decade. The ALMA telescope covers atmospheric windows in the frequency range from 30 GHz to 0.95 THz, which is divided into 10 frequency bands. Band 10 receivers of the ALMA, which is the highest frequency band, are expected as a key frequency band, e.g. for imaging observations with the very high angular resolution to detect the gaps created by planets undergoing formation in the disk. To enable such a challenging observation, band 10 receivers requires ultimate performance with a Double SideBand (DSB) noise temperature below 230 K ($5hf/k_B$) for 80% bandwidth and 344 K ($7.5hf/k_B$) for 100% bandwidth over the 4–12 GHz intermediate frequency (IF) band. The final goal of this study is to develop low noise and wideband SIS mixers so as to meet the specifications and to enable such challenging observation of ALMA band 10 by demonstrating high performances for each component.

SIS junctions should be the most sensitive mixing elements in this frequency. However, there have been no mixers currently available that satisfy the requirements of both low noise and wideband operation for the ALMA band-10 specification. This is because, thus far, well-established all-Nb SIS mixers can not be used due to radio frequency (RF) losses in their microstrip tuning circuits which increase significantly as a result of the onset of pair-breaking above the Nb gap frequency of 0.7 THz. For example, RF signals are attenuated by more than 60 % per the wavelength in this frequency range. Besides, the RF fractional bandwidth of about 20 % is a critical problem for achieving the specifications as well as the quantum limited sensitivity. Since an SIS junction has a large capacitance, RF bandwidth might be limited by ωRC. For this reason, it might have been believed that the SIS junction's current density (J_c) is the most important factor to make the RF bandwidth wider. This implies that high J_c (>20 kA/cm^2) SIS junctions with very thin barrier have to be developed.

For solving these issues, we have performed the investigation in detail by both design and fabrication approach. Chapter 1 offers introduction to show the importance and position of this thesis. In chapters 2 and 3, theoretical verification and feasibility of material combination for the band 10 mixers are discussed. Chapter 4 presents investigation of SIS mixers with Nb/AlO_x/Nb junctions and new microstrip configuration using epitaxial NbTiN films and normal metal. The device based on NbTiN showed a receiver noise temperature of 171 K at 0.83 THz. On the other hand, the detailed analysis of mixers on the basis of numerical simulations was consistent with the experiment results, and it revealed a possibility of further improvement in the mixer performance. Chapter 5, which is

the core of this thesis, describes the demonstration of a wideband and low-noise SIS mixer satisfying for the ALMA band-10 specification. The SIS mixer adopted Nb/AlO_x/Nb junctions with a moderate current density of 8 kA/cm^2 and low loss NbTiN/SiO_2/Al inverted microstrip lines. Optimal impedances of the twin-junction circuit are theoretically investigated so as to achieve both low noise and wideband performances simultaneously. The heterodyne measurement results of this type of device showed quantum limited mixer sensitivity and wide bandwidth. Chapter 6 presents the design and the analysis of low-noise IF systems using state-of-the-art noise amplifiers and low-loss isolators. In addition, the improvement of frequency dependence of IF noise temperature and output power by detailed system consideration including the SIS mixer will be described. Chapter 7 provides the development of a waveguide SIS mixer incorporating LO directional coupler. The insertion loss of the waveguide and coupling factor of the LO coupler were evaluated at both room and cryogenic temperatures. The mixer block was designed on the basis of the characterization. Finally, we present the result of achieving ALMA band 10 specification. Chapter 8 summarizes the achievement described in this thesis. Low-noise waveguide SIS mixers developed in this work will be installed for the ALMA band 10 receivers. In addition, we believe the instrument and the technologies of the design, fabrication, and measurement will be applied for a variety of high frontier terahertz fields.

Contents

Abstract i
Chapter 1
Introduction 1
1.1 Terahertz detectors 1
1.2 Atacama Large Millimeter/submillimeter Array 1
1.3 ALMA band 10 4
1.3.1 A scientific interest at the band 10 frequencies 4
1.3.2 ALMA band 10 cartridge receiver 5
1.3.3 Receiver specification 7
1.3.4 Other heterodyne Instruments at similar frequency to ALMA band 10. 7
1.4 Heterodyne receiver 8
1.4.1 SIS quasi-particle mixers 9
1.4.2 Receiver sensitivity 10
1.5 Key technologies and problems 11
1.5.1 Low noise and wideband SIS mixers 12
1.5.2 Wideband IF chain of 4-12 GHz 13
1.5.3 Low loss waveguide components and efficient usage of LO Power 14
1.6 Overview of this thesis 15
References 16
Chapter 2
Fundamental theory of heterodyne SIS mixer 19
2.1 Overview 19
2.2 SIS junction as a mixing element 19
2.2.1 General mixer theory 19
2.2.2 Quasi-particle tunneling current in SIS junction 26
2.2.3 Three port quantum mixing theory 29
2.3 Superconducting microstrip line 32
2.3.1 Surface impedance of superconductors and normal conductors 33
2.3.2 Analytical calculation method of superconducting microstrip lines 34
2.3.3 Numerical simulation of a superconducting microstrip line using HFSS 36
2.3.4 Power transmission calculation to junctions using transmission matrix 38
2.4 Receiver noise measurement 40
2.4.1 *Y*-factor method and conversion gain measurement 40

2.4.2 Test receiver 41
References 42
Chapter 3
Material selection and feasibility study on SIS mixers for the ALMA band 10 45
3.1 Overview 45
3.2 Practical application limitation of SIS junctions 45
3.3 Material selection for tuning circuit 48
3.4 Suitable tuning circuit for the ALMA band 10 50
3.5 RF bandwidth and optimum Junction current density 51
3.6 SIS mixer fabrication 52
3.6.1 Film properties for superconductor and normal conductor 52
3.6.2 X-ray diffraction patterns 54
3.6.3 Resistance-temperature characteristic and residual resistance ratio 55
3.6.4 Properties of Al films 55
3.6.5 Sequence of process steps 56
3.6.6 Mixer chip fabrication 57
3.7 Current-voltage characteristics and resonance step 58
References 59
Chapter 4
Development of waveguide SIS mixers based on epitaxial NbTiN films on MgO substrates 63
4.1 Overview 63
4.2 Design 63
4.3 Evaluation of the mixer 66
4.4 Improved design 69
4.4.1 Higher mode and choke filter design 69
4.4.2 Probe design 71
4.4.3 Mixer chip and tuning circuit design 71
4.5 Mixer performance and discussion 73
4.6 Conclusion 75
References 75
Chapter 5
Demonstration of a low-noise waveguide NbTiN-based SIS mixer on a quartz substrate 77
5.1 Motivation and Overview 77
5.2 Wideband and low-noise SIS mixer design 79
5.2.1 Mixer chip design 79
5.2.2 Tuning circuit with the inverted NbTiN/SiO_2/Al microstrip line 80

5.2.3 Optimum noise match design based on RF embedding analysis 82
5.3 Mixer performance 85
5.3.1 Source impedance dependence 85
5.3.2 Optimal bias point for the receiver noise and the mixer gain 87
5.4 Fourier transform spectrometer measurement 88
5.4.1 Fourier transform spectrometer 88
5.4.2 FTS measurement 89
5.5 Mixer performance analysis 92
5.5.1 Bandwidth limitation 92
5.5.2 Estimation of noise parameters for the twin-junction circuit at LO 0.88 THz 92
5.6 Performance at an operating temperature of 2 K 95
5.7 Conclusion 96
References 97
Chapter 6
Consideration of 4–12 GHz optimum IF circuits for the band 10 mixers 101
6.1 Motivation and Overview 101
6.2 Characterization of the IF components 101
6.2.1 4-12 GHz IF component used for the band 10 receivers 101
6.2.2 Noise temperature measurement using cryogenic attenuator 103
6.3 IF circuits for band 10 SIS mixers 105
6.3.1 Design of two IF circuits 105
6.3.2 Calculation of the receiver noise temperature 106
6.4 Measurement results and the analysis 107
6.4.1 Shot noise measurement 107
6.4.2 Receiver noise temperature for two circuit designs 108
6.4.3 Receiver noise temperature for different bias conditions of the IF amplifier 109
6.4.4 Analysis 110
6.5 Improvement of IF characteristics 113
6.6 Conclusion 114
References 114
Chapter 7
A low-noise waveguide SIS mixer incorporating 10-dB directional coupler 117
7.1 Motivation and Overview 117
7.2 Design and evaluation of the waveguide components 117
7.2.1 Evaluation of WR-1.2 waveguide losses at cryogenic temperature 117
7.2.2 Mixer block design 119

7.2.4 Evaluation of the 10 dB coupler at room temperature 122
7.3 LO injection scheme for the band 10 cartridge 124
7.3.1 Consideration of waveguide and quasi-optical coupling scheme 124
7.3.2 LO chain for the band 10 cartridges 126
7.3.3 Preliminary test 128
7.4 Performance of the cartridge receiver engineering model 128
7.4.1 Current response of an SIS junction for LO signals 128
7.4.2 Receiver noise temperature 130
7.5 Prototype mixer for the prototype cartridge receiver 131
7.5.1 Prototype mixer block design 132
7.5.2 Horn-to-horn coupling measurement at room temperature 133
7.5.3 Heterodyne measurement sets in test cryostat 134
7.5.4 LO current response 134
7.5.5 Heterodyne measurement 135
7.6 Conclusion 138
References 139
Chapter 8
Summary 141
Appendix A
Transmission loss for polyimide films and Teflon sheets 145
A.1 Overview 145
A.2 Measurement 145
A.3 Estimation of reflectivity for the beam splitter 146
Appendix B
Junction coupling measurement using an LO source 149
B.1 Overview 149
B.2 Investigation using large signal source 149
B.3 Comparison of coupling between two methods 151
Appendix C
Water absorption at the experimental room 153
C.1 Overview 153
C.2 Mixer performance measurement for two conditions 153
C.2.1 Junction current response measurement using an LO source 154
C.2.2 Noise temperature measurement 154
C.3 Conclusion 155

Appendix D
On optimization process of NbTiN films on quartz 157
D.1 Overview 157
D.2 Optimization process 157
Publications and research achievements 159
Acknowledgement 163
論文要旨 167

Chapter 1
Introduction

1.1 Terahertz detectors

Terahertz frequency sandwiched between microwave and lightwave is loosely defined from 0.1 THz to 10 THz. It is a high frontier region where remains one of the least tapped regions of the electromagnetic spectrum. Besides continuum emission, interstellar dust clouds likely emit some 40 000 individual spectral lines in the terahertz band, only a few thousand of which have been resolved and many of these have not been identified [1]. This is because that, so far, sensitivity issue of the detector and high absorption from especially water and oxygen has made it extremely difficult for significant propagation and detection of terahertz energy in almost all Earthly environments.

Progress of astronomical observation has been driven strongly by the development of new technology and instrumentation with high sensitivity. Superconducting detectors has been studied for realizing such high sensitive observation. Kinetic Inductance Detectors (KIDs), Superconducting Transition Edge Sensor (TES) detectors, and Superconducting Tunnel Junction (STJ) as a direct detector, will show great capabilities for photometrical observation with low spectral observation of 3-10 by taking an advantage of high sensitivity due to large bandwidth and not limited by quantum noise. On the other hand, with the aims of spectroscopic or high spatial resolution observation, Superconductor-Insulator-Superconductor (SIS) and Hot Electron Bolometer (HEB) mixers as a heterodyne one are widely used for practical low-noise receivers of radio astronomy and remote sensing up to 0.7 THz.

The main goal of this thesis is to develop low-noise SIS mixer so as to meet very tough specifications for the Atacama Large Millimeter/submillimeter Array (ALMA) Band 10 covering 0.787-0.950 THz. In this thesis, we present new technology development for terahertz circuit design, superconducting device fabrication, low-loss terahertz waveguide transmission technology, and their measurement method. Their technologies will be applicable to not only astronomical field but also biological and biomedical areas, security and so on as spreading effects.

1.2 Atacama Large Millimeter/submillimeter Array

The ALMA is one of the largest ground-based astronomical projects for the next decade [2]–[8]. The ALMA is being built by collaboration among Europe, Japan, and North America and the start of full operations is expected in late 2012. It is being constructed on the Atacama Desert of northern

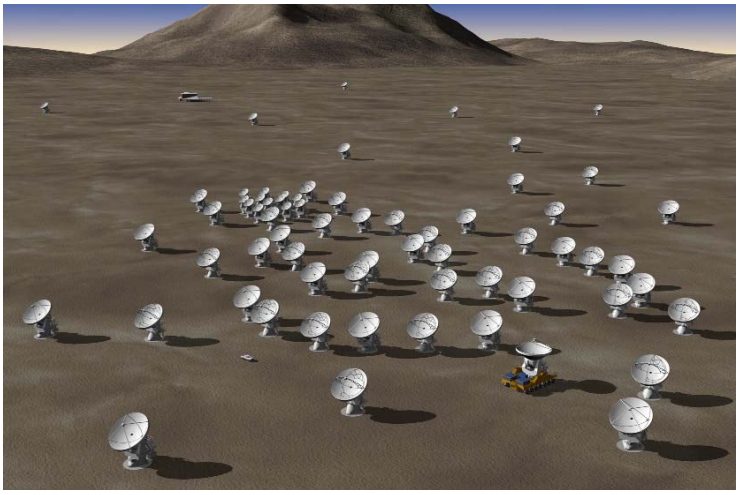

Fig. 1-1 Artist's concept of ALMA © European Southern Observatory (ESO)/ALMA

Chile at an altitude of about 5000 m. ALMA consists of a homogeneous array of about fifty 12-m diameter antennas for the interferometer (12 m Array) and a set of four 12-m and twelve 7-m diameter ones for the Atacama Compact Array (ACA) [9] for realizing fidelity of imaging with mosaicing observation (see Fig. 1-1).

With excellent sensitivity and high resolution at a high dry location (see Fig. 1-2), ALMA will allow sensitive heterodyne observation in the range 31 GHz–0.95 THz (0.3–10 mm) and is expected to have impacts on three important scientific fields, that is, the formation and history of galaxies, the formation of extraterrestrial planetary systems, including the emergence of the life, and the history of the universe for the Big Bang. The highest level science requirements for ALMA are:

1. The ability to detect spectral line emission from CO or C II in a normal galaxy like the Milky Way at a redshift of z = 3, in less than 24 hours of observation.
2. The ability to image the gas kinematics in protostars and protoplanetary disks around young Sun-like stars at a distance of 150 pc (roughly the distance of the star forming clouds in Ophiuchus or Corona Australis), enabling one to study their physical, chemical and magnetic field structures and to detect the tidal gaps created by planets undergoing formation in the disks.
3. The ability to provide precise images at an angular resolution of 0.1. Here the term precise image means representing within the noise level the sky brightness at all points where the brightness is greater than 0.1 % of the peak image brightness. This requirement applies to all sources visible to ALMA that transit at an elevation greater than 20 degrees.

Table 1-I Frequency coverage and sensitivity requirement of the ALMA frequency bands

Band	1	2	3	4	5	6	7	8	9	10
Lowest Freq. (GHz)	30	67	84	125	163	211	252	385	602	787
Center Freq. (GHz)	35	79	100	144	187	243	323	442	660	869
Highest Freq. (GHz)	40	90	116	163	211	275	370	500	720	950
Fractional Bandwidth	0.29	0.29	0.32	0.26	0.26	0.26	0.29	0,26	0.18	0.19
Trx (DSB) over 80% (K)	7.5	14	17	23.5	30	37.5	66.5	90.5	168	230
Institute	TBD	TBD	HIA	NAOJ	CUT	NRAO	IRAM	NAOJ	SRON	NAOJ

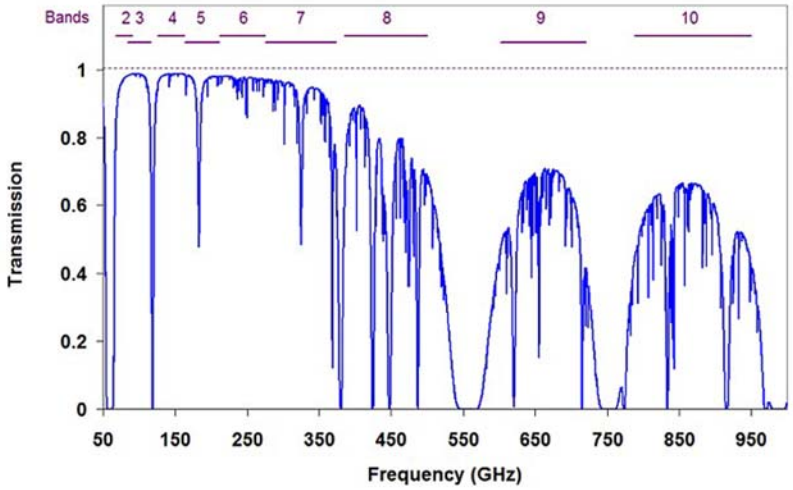

Fig. 1-2 Atmospheric transparency at the Chajnantor site in good condition and frequency coverage of the ALMA frequency bands [6].

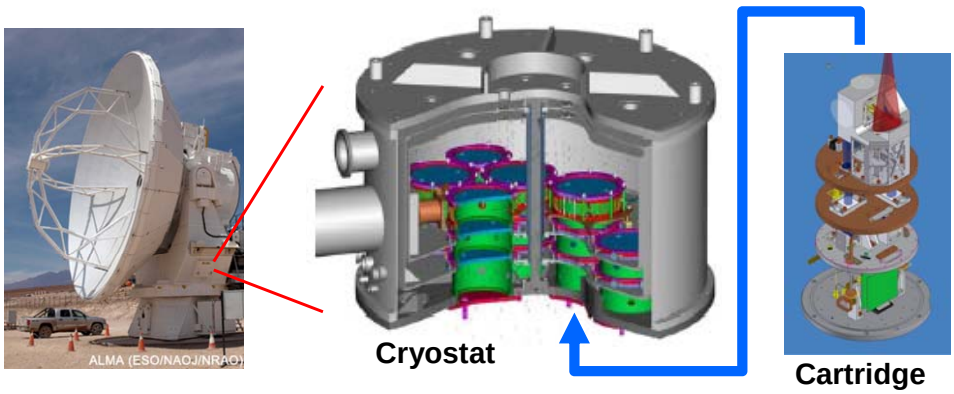

Fig. 1-3 photograph of ALMA antenna, cryostat, and cartridge. Each receiver is packaged in the form of a cylindrical cartridge (right), which are mounted within a 4-K circular cryostat of radius approximately 1 m (center). The cryostat is located on at the cassegrain focus of the antenna (left)

In order to achieve such the challenging observation, very tough specifications is set in terms of sensitivity as listed in Table 1-I. Each of the ALMA antennas will be equipped with a receiving system to cover the range of 31 GHz to 0.95 THz divided into ten bands which are determined by astronomical and atmospheric considerations [8]. Each receiver is packaged in the form of a cylindrical cartridge, which are mounted within a 4-K circular Dewar of radius approximately 1 m. The receivers in lower bands (Bands 1 and 2) use a high electron mobility transistor (HEMT) and the other (Bands 3–10) use superconductor-insulator-superconductor (SIS) mixers to achieve quantum limited sensitivities and wideband intermediate frequencies (IFs)

1.3 ALMA band 10

Band 10 of the ALMA is the highest frequency band covering 0.787-0.950 THz and can be achieved to be the highest angular resolution of 0.01 arc/s. Such the high spatial resolution may clear up a problem whether our solar system is special or general.

1.3.1 A scientific interest at the band 10 frequencies

Planets are expected to form in circumstellar disks, which are considered the natural outcome of the protostellar evolution in the case of low- and intermediate-mass stars. A detailed picture of the evolution of circumstelar/protoplanetary disks, which provide the material and environment from and in which planets are expected to form, has been developed. However, the planet formation process itself is in major parts still under discussion. S. Wolf and G. D'Angelo have investigated the

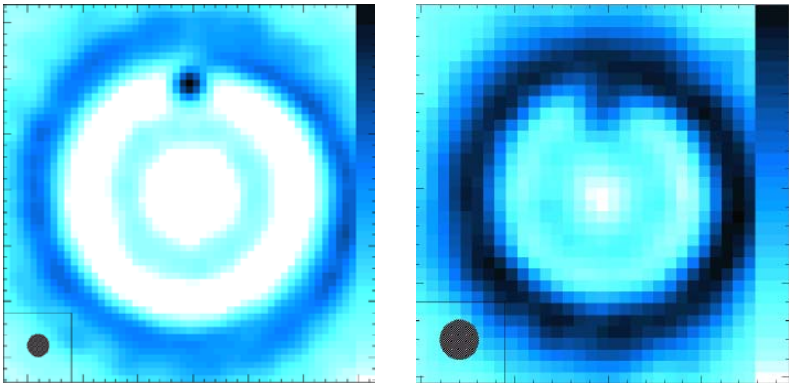

Fig. 1-4 Simulation of ALMA observations of disk at 0.9 THz with an embedded planet of $1M_{jup}$ around a $0.5M_{\odot}$ star (orbital radius: 5AU). The assumed distance is 50 pc (left) / 100 pc (right). The disk mass amounts to $M_{disk} = 1.0 \times 10^{-2}\ M_{\odot}$. The size of the combined beam is symbolized in the lower left edge of each image. Note the reproduced shape of the spiral wave near the planet and the slightly shadowed region behind the planet in the left images. The images are from [11].

possibility of detecting giant planets that are still embedded in young circumstellar disk ([11] Fig. 1-4). They made the point that the hot region in the proximity of a young planet, along with the gap, could be detected and mapped with the ALMA band 10 in the case of nearby circumstellar disks (d < 100 pc) in approximately face-on orientation by showing dust reemission images of the disks. So far, it has been impossible to resolve such the disk spatially due to a limited spatial resolution. Thus ALMA band 10 will play a crucial role by allowing to trace features in disks which are indicative for various stages of the formation and early evolution of planets in circumstellar disks [12].

1.3.2 ALMA band 10 cartridge receiver

Fig. 1-5 and Fig. 1-6 show a view of the cold optics designed by M. Candotti and the entire prototype band 10 cold cartridge and components, respectively. All of the cartridges are included in a single cryogenic cryostat located on at the cassegrain focus. The beam coming from the telescope passes through the vacuum window and infrared filters. Two ellipsoidal mirrors are used to match the incoming beam and the corrugated feed horn. After reflecting the beam by the pair of the mirrors, the two orthogonal polarizations are split by a free-standing wire grid. Then each beam enters the corresponding feed horn. It should be noted that the optical components consisting of the mirrors, wire grid and feed horns are mounted to the 4-K optics support structure made from one Aluminum block in order to reduce alignment errors.

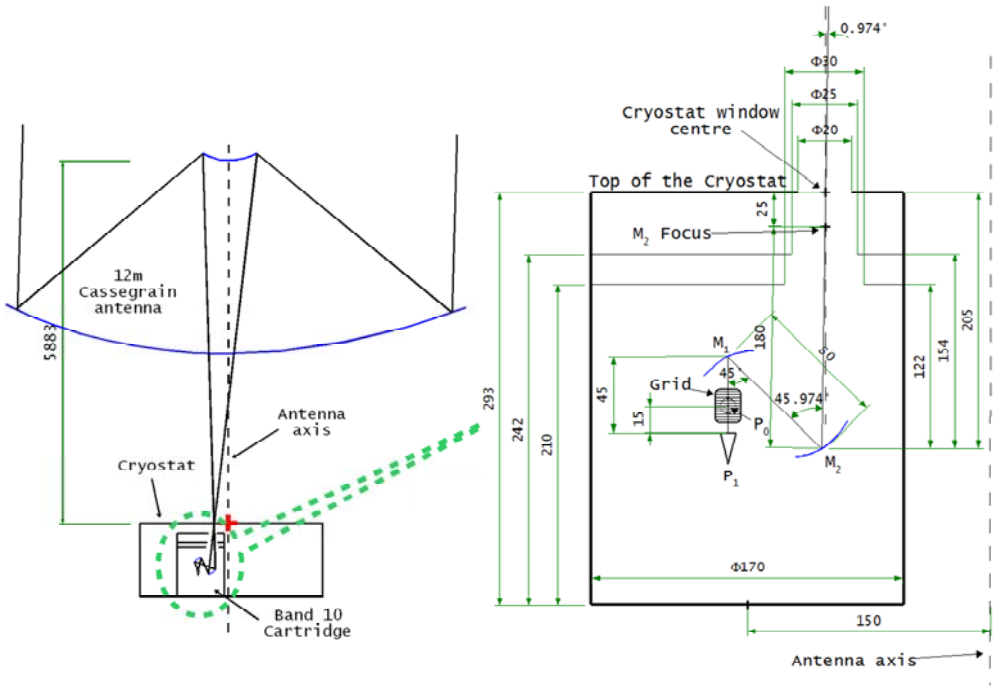

Fig. 1-5 Schematic view of the cold optics for the ALMA band 10 designed by M. Candotti.

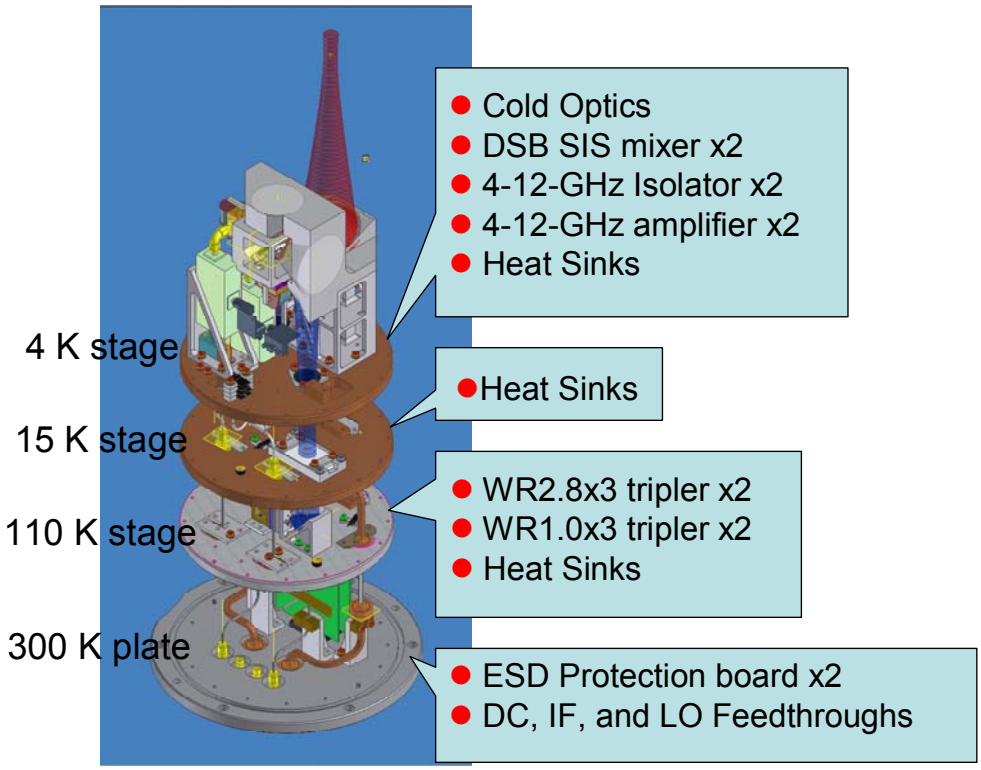

Fig. 1-6 Schematic view of a prototype cartridge for the ALMA band 10. This was drawn by K. Kaneko.

Table 1-II ALMA band 10 major specifications

1. RF frequency	**0.787-0.950 THz**
2. Cartridge IF output	**4-12 GHz for DSB**
3. Cartridge noise performance	**< 230 K ($5hf/k_B$) (over 80%)** **< 344 K ($7.5hf/k_B$) (full band)**
4. IF ripple	**< 4.0 dB/2 GHz, < 6.0 dB/8 GHz**
5. Gain compression	< 5% between 77 and 373 K
6. Amplitude stability	0.05 and 100 sec $< 4.0 \times 10^{-7}$ 300 sec $< 3.0 \times 10^{-6}$
7. Signal path stability	< 3 degree/5 minutes
8. RF beam efficiency	> 90% at the subreflector
9. Beam squint separation	< 10% HPBW on the sky
10. Polarization efficiency	> 99.5% (23 dB)

The cartridge receivers of the ALMA band 10 use two Double Sideband (DSB) mixers with orthogonal linear polarizations. Each polarization provides IF bandwidth of 8 GHz centered at 8 GHz (4-12 GHz), which will be achieved by using a 4-12 GHz IF system. The cartridge consists of three cooled stages with operating temperatures of 4 K, 15 K and 110 K, and a room-temperature base-plate which acts as the vacuum seal. The stages are supported by GFPR 10 tubes which have low thermal conductance. LO triplers for generating 300 GHz band (input frequency is the 100 GHz band), heat sinks for the LO waveguides, coaxial cables and wiring, are on the 80 K stage. The only components on the 15 K stage are the heat sinks for the coaxial cables and wiring. The 4 K stage has the mirrors, wire-grid, horns, mixer blocks, isolators, IF amplifiers, and heat sinks for the LO waveguides.

1.3.3 Receiver specification

Major band 10 specifications are listed in Table 1-II. Especially, band 10 requires receivers with a DSB noise temperature below 230 K ($5hf/k_B$) for 80% bandwidth and 344 K ($7.5hf/k_B$) for 100% bandwidth over the 4–12 GHz intermediate frequency (IF) band at an operating temperature. However, there have been no receivers currently available that satisfy the requirements of both low noise and wideband operation such as the ALMA band 10 specifications as shown in Fig. 1-9.

1.3.4 Other heterodyne Instruments at similar frequency to ALMA band 10.

The Heterodyne Instrument for the Far Infrared (HIFI) of the Herschel Space Observatory provides continuous coverage over the range of 0.480 to 0.125 THz in five bands and 1.41 to 1.91 THz in two additional bands at an operating temperature of 2 K (e.g. [15]). HIFI band 3 instrument covers 0.8–0.96 THz [16] , similar frequency range to the ALMA Band 10. The primary mirror is 3.5-m diameter which is the largest satellite mirror to date. The Herschel spacecraft with HIFI onboard has been launched successfully 14 May 2009.

The Carbon Heterodyne Array of the MPIfR (CHAMP$^+$) is dual channel heterodyne receiver array of 7 pixels operating in the 0.6–0.72 THz and 0.79–0.95 THz atmospheric windows. In early 2007.CHAMP was installed at the Atacama Pathfinder Experiment (APEX) telescope with a antenna diameter of 12 m on the high altitude site of Llano Chajnantor [13][14].

The Caltech Airborne Submillimeter Interstellar Medium Investigations Receiver (CASIMIR) is a far-infrared (FIR) and submillimeter, very high-resolution, heterodyne spectrometer [17] installed on Stratospheric Observatory for Infrared Astronomy (SOFIA). The primary mirror is 2.7 m in diameter. It is anticipated SOFIA will eventually achieve a flight rate of up to 160 flights per year, with a lifetime of 20 years [18]. During the initial flights in 2010, CASIMIR will have two bands available, 1.0 and 1.25 THz. Three additional bands will be added with ongoing instrument development, providing frequency coverage from 0.5 THz up to 1.4 THz.

Millimetron planed for launch after 2015 is a large (12m diameter) space observatory for millimeter, submillimeter and far-infrared observations. High sensitivity and (extremely) high angular resolutions are achieved by using a 12m diameter space antenna, either in single-dish mode or as element of a spaceground VLBI system. The instrumentation for the single-dish observing mode consists of the two heterodyne instruments HET-1 and HET-2 which cover the astrophysically important frequencies 0.55 and 1.1 THz, 1.9, 2.7 and 4.7 THz, but not including 0.9 THz [19].

1.4 Heterodyne receiver

In the region from millimeter to terahertz wave, electric pre-amplification of weak signals is not yet possible and heterodyne process. For this reason, the low-noise heterodyne mixer is used to downconvert weak RF signals f_{RF} to IF ones f_{IF} by modulating a large LO signal f_{LO}. As shown in Fig. 1-7, incoming signal from space is collected by the optics and coupled with the LO signal. The RF signal is down-converted to IF signal by the mixer. After that, the IF signal is amplified the low noise amplifier. In this case, the downconverted IF signal composed of the two frequencies:

$$f_{RF} = f_{LO} \pm f_{IF} \quad . \qquad 1\text{-}1$$

Band 10 cartridges detect both sidebands without sideband separation, so-called, Double Sideband (DSB) receiver.

A feature of heterodyne receiver is to allow coherent detection of incoming signal, because

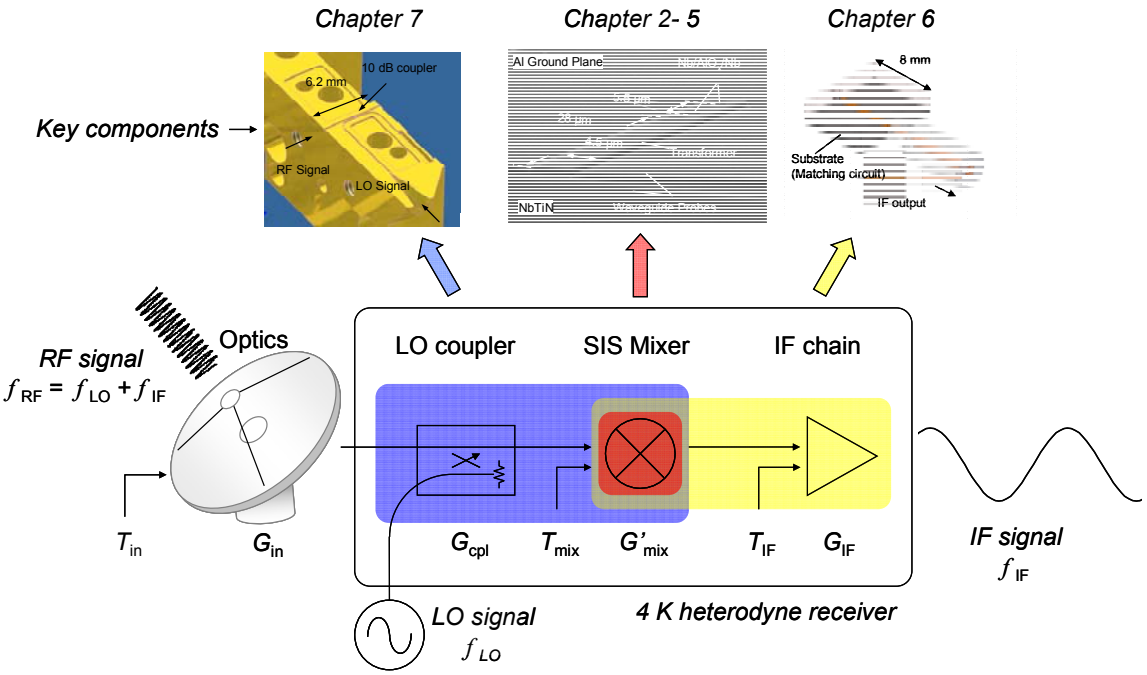

Fig. 1-7 Schematic block diagram of a typical heterodyne receiver and key components described in this thesis.

mixing element preserves phase information. Then telescopes incorporating the heterodyne receiver can be used as elements in interferometers, which achieve high spatial resolution required for ALMA. Another is to obtain very high spectral resolution (up to ~ 10^7 for ALMA receiver, corresponding to Doppler velocities of 0.03 km/s). This is important in that atomic and molecular lines can be observed to study the constituents and dynamics of the gas [3]. Meanwhile, it is well-known that signal-to-noise ratio for a spectrum detected by heterodyne receiver is proportional to a square root of the product of integration time and simultaneous bandwidth, and inverse proportional to the system noise temperature. Since it can not be increased by enlarging the bandwidth for spectral line detections, it is essentially important to reduce the noise temperature. Besides, to measure the chemical properties of the disk, the receiver also needs a wide IF bandwidth, capable of simultaneously measuring emission lines from many different atomic or molecular species. The wide IF bandwidth would be important when continuum spectrum feature from dust is observed as well.

1.4.1 SIS quasi-particle mixers

SIS quasiparticle mixers are widely used for applications of the radio astronomy and planetary atmosphere taking the low noise performance approaching quantum limit. A waveguide SIS mixer consist of input waveguides, an antenna probe doubled with transition to microstrip mode, tuning circuits and SIS junctions (see Fig. 1-8). The SIS junction has a sandwiched structure of two superconductors separated by very thin insulator layer (~ 5 nm) and then has large geometric capacitance which can shunt the RF signal. Thus the tuning circuits are employed for tuning out the junction capacitance and matching the junction impedance to the antenna impedance.

The SIS mixer relies on an extremely nonlinear *I-V* characteristic of the SIS junction. The current flow mechanism in the case injected microwave electromagnetic radiation is based on the photon-assisted tunneling process discovered by Day and Martin in the early 1960s [20]. The first receivers using this effect were developed by groups at Bell Laboratories, and the California Institute of Technology [21], and the University of California at Berkeley [22].

Unlike direct detection, in heterodyne detection mode, the Heisenberg uncertainty principle puts a limit to the mixer noise temperature, the quantum limit being

$$T_{\mathrm{Q}} = \frac{hf}{k_B}. \qquad 1\text{-}2$$

This derives from following things. If one measures the energy E of a system and the precise time t at which the system possesses this energy, the uncertainties in these quantities are related by

$$\Delta E \Delta t \geq \hbar / 2. \qquad 1\text{-}3$$

This leads to the equation

$$\Delta n \Delta \varphi \geq 1/2, \qquad 1\text{-}4$$

relating uncertainties in the simultaneous measurement of the number of quanta n and phase of

signal φ. Thus one can not measure both amplitude and the phase of a sinusoidal signal precisely.

So far, the high sensitivities for the SIS mixers has been demonstrated that fell close to the quantum limit for frequencies up to 0.7 THz at least and within a factor of ten of this limit up to 1 THz. This would be the greatest merit of using SIS mixers compared to other superconducting heterodyne mixers, such as the Hot Electron Bolometer (HEB) and Josephson effect mixer. The detailed noise property of SIS mixers will be described in later chapter as based on the theory by Tucker and Feldman [23][24].

1.4.2 Receiver sensitivity

In general, the heterodyne receiver sensitivity may be represented by the equivalent input receiver noise temperature

$$T_{\mathrm{RX}} = T_0 + \sum_{k=1}^{N-1} \frac{T_k}{\prod_{l=0}^{k-1} G_l}, \qquad 1\text{-}5$$

which is known as *Friis' formula*, where T_k, and G_l are kth equivalent input noise temperature and lth (= k-1) available power gain. A passive component with the gain G of less than 1 generates the noise

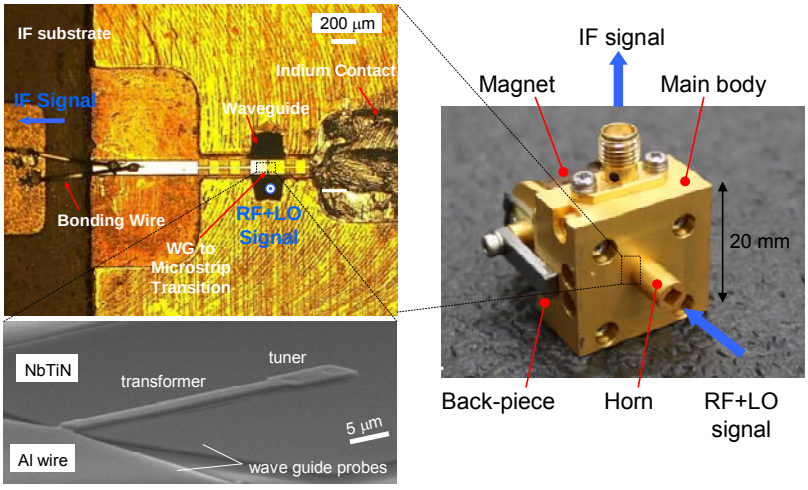

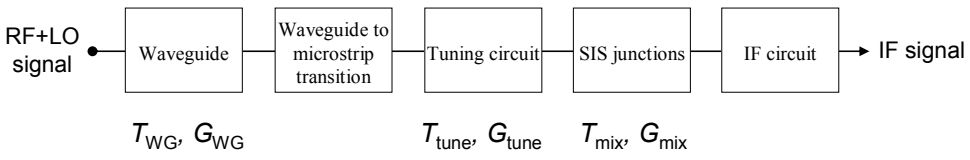

Fig. 1-8 Photograph and block diagram showing composition of an SIS mixer. T_{WG}, G_{WG}, T_{tune}, G_{tune}, T_{mix} and G_{mix}, are the equivalent input noise temperatures and the power available gains of the waveguide, the tuning circuit, and the SIS mixer.

temperature related to ambient temperature T_{amb}:

$$T_{Att} = \left(\frac{1}{G} - 1 \right) T_{amb} . \quad 1\text{-}6$$

Thus the equivalent input receiver noise temperature shown in Fig. 1-7 can be described by

$$T_{RX} = T_{in} + \frac{T_{mix}}{G_{in} G_{cpl}} + \frac{T_{IF}}{G_{in} G_{cpl} G'_{mix}} , \quad 1\text{-}7$$

where T_{IF} (~10 K), T_{mix} (~100 K) and T_{in} (~15 K) are respectively the equivalent input noise temperatures of the IF chain, the SIS mixer, and the optics, and G'_{mix}, G_{cpl} and G_{in} (< 1) are respectively the available power gains of the SIS mixer, the LO coupler, and the optics. G_{tune} and G_{WG} would not be negligible at the band 10 frequencies, although T_{tune} and T_{WG} should be less than 1 K. These G_{tune} (~1.5 dB) and G_{WG} (0.5 dB/10 mm) are one of the parameters making it difficult to achieve high sensitivity receiver performances in this frequency range, compared to ones in lower frequencies, because the lossless all-Nb circuits are not available and waveguide losses are significantly higher. Therefore, the total receiver noise temperature is given by

$$T_{RX} = T_{in} + \frac{T_{mix}}{G_{in} G_{WG} G_{tune} G_{cpl}} + \frac{T_{IF}}{G_{in} G_{WG} G_{tune} G_{cpl} G_{mix}} . \quad 1\text{-}8$$

In conclusion, it is essentially important to reduce T_{mix} and to make all the gains G_{in}, G_{WG}, G_{tune}, G_{cpl}, and G_{mix} as high as possible.

1.5 Key technologies and problems

In this section, key technologies and the problem are overviewed. Thus far, except for the atmospheric absorption, a cause that has made astronomical observation difficult was degradation of the receiver sensitivity. Fig. 1-9 shows state-of-the-art sensitivity results of receivers developed in some laboratories and also shown is sensitivity goals for ALMA receivers at the operating temperature of 4 K. The data are summarized by Kerr et al [25] and are updated based on refs. [26]-[29]. It can be seen that the receiver noise temperature above 0.7 THz increases rapidly. This is caused by degradation of noise performance of the SIS mixers due to Nb gap frequency as described later. In addition, this may imply that technologies to develop high sensitivity receivers have not been established yet in this frequency range. This is because there have been many technical difficulties, such as development of small waveguide component and low-noise and wideband IF chain.

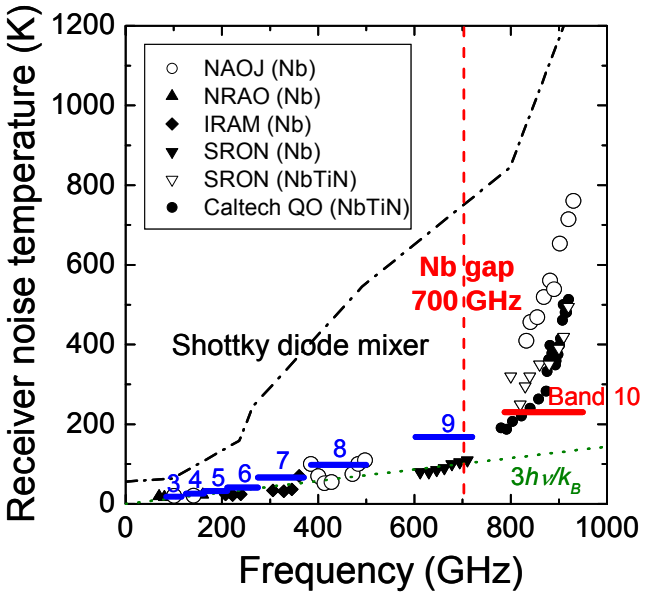

Fig. 1-9 State of the art results and sensitivity goal of receivers developed in some laboratories. The data are summarized by Kerr et al [25] and are updated based on refs. [26]-[29]

1.5.1 Low noise and wideband SIS mixers

Noise performance

In this frequency range, well-established all-Nb SIS mixers can not be used because RF losses in their microstrip tuning circuits increase significantly as a result of the onset of pair-breaking above the Nb gap frequency of 0.7 THz. For example, RF signals are attenuated by more than 60 % per the wavelength in this frequency range as shown in Fig. 1-10 (a). Thus far, a combination of normal metal and a higher gap superconductor, such as NbN or NbTiN, has been successfully used to reduce the circuit losses in the range 0.7–1.3 THz. However, there are no mixers currently available that satisfy the requirements of both low noise and wideband operation such as the ALMA band 10 specifications. In order to improve the mixer performance, it is important not only to establish the low-loss microstrip lines but also to investigate the mixer noise properties of the Nb junctions above its gap frequency where the mixer gain is significantly degraded.

RF bandwidth

The fractional bandwidth of 19 % for the band 10 receivers has to be covered. Since an SIS mixer has a large capacitance, the RF bandwidth might be limited by ωRC. For this reason, it might have been believed that the SIS junction's current density (J_c) is the most important parameter to make the RF bandwidth wider. In this case, we have to develop high J_c (>20 kA/cm^2) SIS junctions

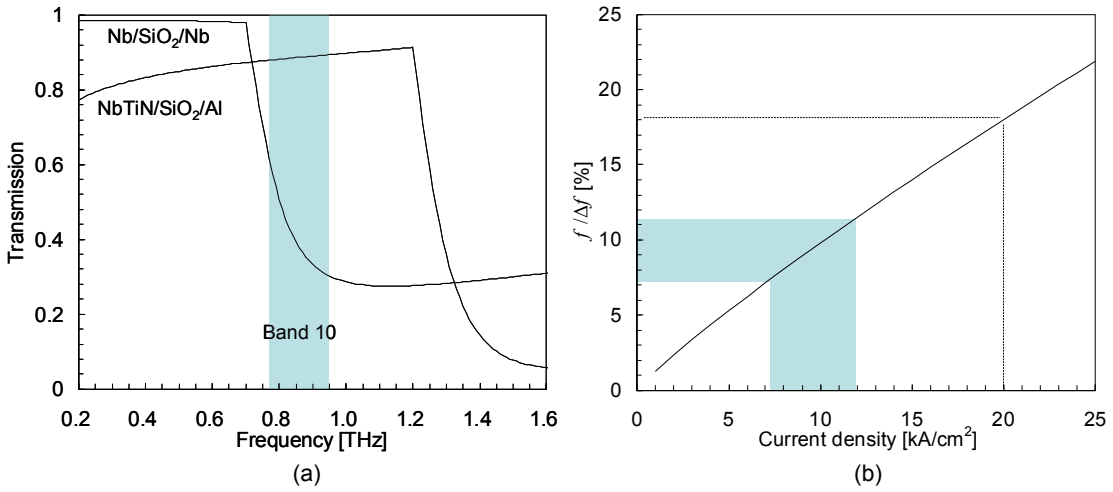

Fig. 1-10 Technological problem of SIS mixers for the ALMA band 10. (a) Transmission characteristics of superconducting microstrip lines per the wavelength as a function of frequency and (b) Fractional bandwidth versus junction's current density. At the band 10 frequencies, well-established all-Nb SIS mixers can not be used because RF losses in their microstrip tuning circuits increase significantly as a result of the onset of pair-breaking above the Nb gap frequency of 0.7 THz.

with very thin barrier as shown in Fig. 1-10 (b). However, it is difficult to obtain such high current density keeping the junction quality. A study of the fabrication using new barrier, such as Aluminum Nitride, would be considered as a candidate to solve the problem.

1.5.2 Wideband IF chain of 4-12 GHz

Another reason which has degraded the receiver sensitivity is IF noise performance, because it is difficult to obtain high mixer conversion efficiency (–5 ~ –10 dB) in the range of this frequency. In our analysis, IF noise temperature accounts for about 20–30 % of the receiver noise temperature. For this reason the IF noise temperature and mixer gain should be kept below 10 K and as high as possible over 4-12 GHz, respectively. However, it is very difficult to achieve the bandwidth beyond 1 octave, keeping such a performance. Although SIS mixers with the high dynamic resistance is allowed to obtain the intrinsic high mixer gain, this has difficulties to match the output impedance of the SIS mixer into 50 Ω network and may result in occurrence of the ripple structure for IF characteristics due to standing wave or oscillation. In addition, this problem makes it hard to achieve the specification that has to be the IF flatness within 4.0 dB per any 2 GHz, and 6.0 dB per any 8 GHz.

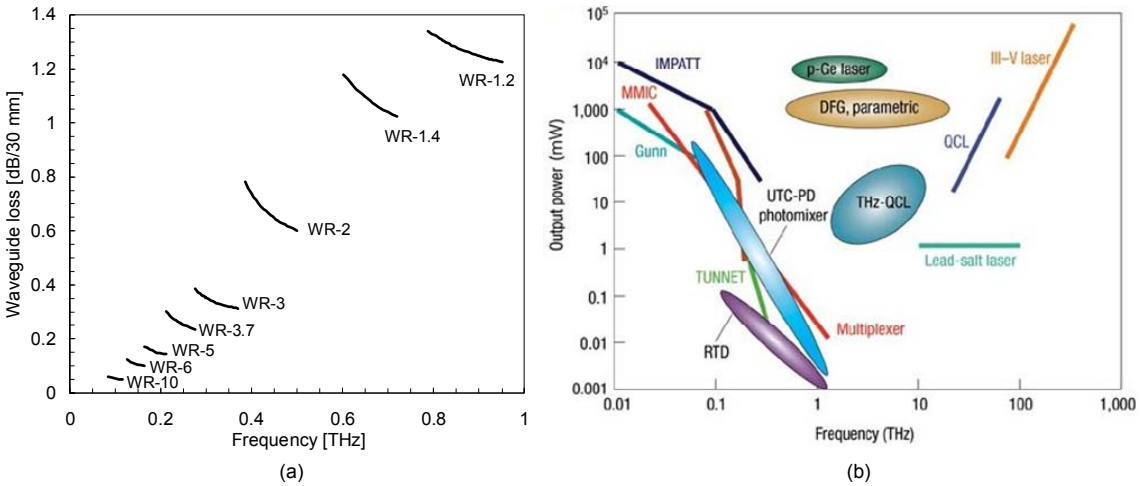

Fig. 1-11 Problems of waveguide losses and LO power in terahertz bands. (a) Comparison of gold-plated rectangular waveguide (TE_{10} mode) losses used in Band 3 to 10 at a temperature of 4 K. The calculation is based on consideration in section 7.2.1 and assumed to be 30 mm for the length of the waveguide, which is typical one for modular type waveguide components. The waveguide size is based on Virginia Diodes Inc. (VDI) waveguide band designations. (b) THz-emission power as a function of frequency. Solid lines are for the conventional THz sources. This figure is from [30].

1.5.3 Low loss waveguide components and efficient usage of LO Power

Fig. 1-11 (b) shows calculated losses of the gold-plated rectangular waveguide with the sizes of WR-10 to WR-1.2. The waveguide length is 30 mm, which is typical one for modular type waveguide components. At the band 10 frequencies, very small waveguide with the size of 152 μm×304 μm (WR-1.2) has to be used. The waveguide has very large losses to be 1.2-1.4 dB, compared to that of low frequency. The losses allow noise temperature to be increased by 30-40 %. Therefore, the modular type of waveguide component is no longer available due to the RF losses. In addition, such small waveguide component needs high accuracy fabrication within 5 μm at a circuit part and 10 μm at a flange part. Thus, we must consider the circuit so as to simplify the fabrication or another scheme.

An advantage of using the SIS mixers is the very modest LO power requirement compared to Shottky diodes. However, in this frequency band close to 1 THz, a lack of local oscillator (LO) power has been a significant issue as shown in Fig. 1-11 (b). The ALMA requires an LO source with no mechanical tuners. Thus, the LO system must consist of electrically-tunable component as based on solid-state devices. Although the high power output devices for terahertz region have been studied, the output power of the sources rapidly diminish at higher frequency (~ 20 μW at 0.9 THz, typically) due to the terahertz gap. For this reason we would have to come up with some kind of method to propagate the limited LO power to the SIS mixer.

Table 1-III Noise budget of the band 10 receiver. The color indicates key components to achieve the specification of 230 K, which are described in this thesis.

	Temp. [K]	Gain [dB]	Input noise [K]	Noise at Rec. Input [K]	
Window	300	-0.1	6	6.3	
IR filter	110	-0.2	5	5.0	
Cold optics	4	-0.2	1	1.1	5% Loss at 4 K
Waveguide	4	-0.5	1	1.1	10 dB coupler
10 dB Coupler	4	-0.5	5	6.3	10 K/μW
Tuning circuit	4	-1.5	1.7	2.3	NbTiN/SiO_2/Al
Mixer	4	-4.0	83	165	2 hf/k_B at 0.87
Isolator	4	-0.6	2.4	12	
1st amplifier	4	34	5	29	
Cable	150	-2.8	136	0.3	Estimated cable
2nd amplifier	300	28.5	120	1	typical gain
Attenuator + Cable	300	-7.1	1239	0.0	Estimated cable
				229	

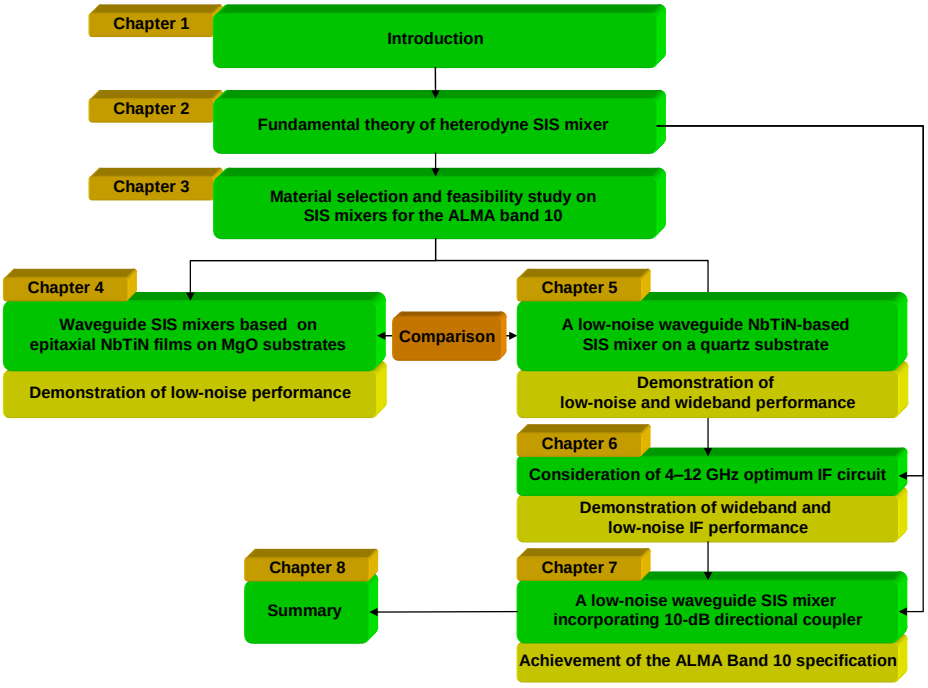

Fig. 1-12 Flow chart of this thesis.

1.6 Overview of this thesis

Table 1-III shows the estimated budget of the band 10 receiver noise temperature. In order to achieve the noise temperature of 230 K, all the components have to accomplishment the state of the art performance. This needs to be verified by measurement of the whole cartridge since the loss and

noise listed in Table 1-III. In this thesis, cryogenic devices which contributes to the receiver noise temperature, that is, the waveguide coupler, SIS mixer, and cryogenic IF chain are focused on.

Construction of this thesis is shown in Fig. 1-12. Chapter 2 describes fundamental theory of SIS mixer for modeling the circuit. As based on the theory, chapter 3 provides theoretical verification and feasibility study of material combination for the band 10 SIS mixers, and two microstrip combinations are narrowed down here: epitaxial NbTiN on MgO and poly-crystal NbTiN on quartz. Chapter 4 presents investigation of SIS mixers with Nb junctions and microstrip configuration using epitaxial NbTiN films on MgO and normal metal. On the other hand, chapter 5 deal with SIS mixers with Nb junctions and inverted microstrip lines incorporating poly-crystal NbTiN films on quartz and normal metal. Finally, an SIS mixer satisfying wideband and low noise performances simultaneously was demonstrated. Chapter 6 describes low-noise IF chains using a state-of-the-art ultra low noise amplifier and a low-loss isolator. In addition, improvements of frequency dependence of IF noise temperature and output power by detailed system consideration including the SIS mixer are described. Chapter 7 presents development of waveguide SIS mixer incorporating LO directional coupler. The insertion loss of the waveguide and coupling factor of the LO coupler were evaluated at both room and cryogenic temperatures. The mixer block was designed on the basis of the characterization. Finally, we present the result of achieving ALMA band 10 specification. Chapter 8 summarizes the work described in this thesis.

References

[1] T.G. Phillips, J. Keene, “Submillimeter astronomy [heterodyne spectroscopy],” Proc. of the IEEE 80 (11), 1992.

[2] A. Wootten and A. R. Thompson, “The Atacama Large Millimeter/submillimeter Array,” Proc. of the IEEE 97 (8), 2009.

[3] R. E. Hills, A. J. Beasley, “The Atacama Large Millimeter/submillimeter Array,” Proc. of the SPIE 7012, 2008.

[4] A. B. Peck and A. J. Beasley, “High resolution sub-millimeter imaging with ALMA,” J. Phys.: Conf. Ser. 131, 2008.

[5] R. L. Brown, W. Wild, C. Cunningham, “ALMA – the Atacama large millimeter array,” Advances in Space Research 34, 2004.

[6] L. Testi, “The Atacama Large Millimeter/Submillimeter Array,” Science with the VLT in the ELT Era, Astrophysics and Space Science Proc., ISBN 978-1-4020-9189-6. Springer Netherlands, 2009.

[7] R.Kurz, S.Guilloteau, P.Shaver, “The Atacama Large Millimetre Array,” The Messenger 107, 2002.

[8] ALMA Construction Project Book, 2002, [Online]. Available: http://www.alma.nrao.edu/projectbk/construction/

[9] S. Iguchi, K. Morita, M. Sugimoto, B. V. VilarÓ, M. Saito, T. Hasegawa, R. Kawabe, K. Tatematsu, S. Sakamoto, H. Kiuchi, S. K. Okumura, G. Kosugi, J. Inatani, S. Takakuwa, D. Iono, T. Kamazaki, R. Ogasawara, and M. Ishiguro, “The Atacama Compact Array (ACA),” Publ. Astron. Soc. Japan 61, 2009.

[10] A. W. Blain, I. Smail, R. J. Ivison, J.-P. Kneib, D. T. Frayer, “Submillimeter Galaxies,” Physics Reports 369 (2), 1992.

[11] S. Wolf and G. D'Angelo, “On the Observability of Giant Protoplanets in Circumstellar Disks,” Astrophys. J. 619, 2005.

[12] S. Wolf, “Detecting protoplanets with ALMA,” Astrophys Space Sci. 313, 2008.

[13] C. Kasemann, S. Heyminck, A. Bell, A. Belloche, C. Castenholz, R.Güsten, H. Hafok, A.Henseler, S. Hochgürtel, B. Klein, T. Klein, I. Krämer, A. Korn, K. Meyer, D. Muders, F. Pacek, F. Schäfer, G. Schneider, G. Wieching, H-J. Wunsch, A. Baryshev, R. Hesper, T. Zijlstra, C.F.J. Lodewijk, T.M. Klapwijk, “CHAMP+: A powerful submm Heterodyne Array,” Proc. 19th Int. Symp. on Space THz Technology, Groningen, 28-30 Apr. 2008.

[14] R. Güsten, A. Baryshev, A. Bell, A. Belloche, U. Graf, H. Hafok, S. Heyminck, S. Hochgürtel, C.E. Honingh, K. Jacobs, C. Kasemann, B. Klein, T. Klein, A. Korn, I. Krämer, C. Leinz, A. Lundgren, K.M. Menten, K. Meyer, D. Muders, F. Pacek, D. Rabanus, F. Schäfer, P. Schilke, G. Schneider, J.Stutzki, G. Wieching, A. Wunsch, F. Wyrowski, “Submillimeter Heterodyne Arrays for APEX,” Proc. SPIE. 7020, 2008.

[15] P. Dieleman, D. Teyssier, T. Klein, J. C. Pearson, W. Jellema, J. W. Kooi, J. Braine, P. W. Morris, A. R.W. de Jonge, R. Haan, W. M. Laauwen, H. P. Smit, N. D. Whyborn, P. R. Roelfsema, F. P. Helmich, and T. W.M de Graauw, on behalf of the HIFI team, “Performance of HIFI in flight conditions,” Proc. 20th Int. Symp. on Space THz Technology, Charlottesville, 20-22 Apr. 2009.

[16] B. D. Jackson, G. de Lange, T. Zijlstra, M. Kroug, J. W. Kooi, J. A. Stern, and T. M. Klapwijk, “Low-Noise 0.8–0.96- and 0.96–1.12-THz Superconductor–Insulator–Superconductor Mixers for the Herschel Space Observatory,” IEEE Trans. Microwave Theory Tech. 54 (2), 2006.

[17] D. Miller, M. L. Edgar, A. Karpov, S. Lin, S. J. E. Radford, F. Rice, J. Zmuidzinas, and A. I. Harris, “CASIMIR – Caltech Airborne Submillimeter Interstellar Medium Investigations Receiver,” proc. 19th Int. Symp. on Space THz Technology, Groningen, 28-30 Apr. 2008.

[18] E. E. Becklin and R. D. Gehrz “Stratospheric Observatory for Infrared Astronomy approaches first light,” SPIE Newsroom 6 Oct. 2009.

[19] W. Wild, A. Baryshev, T. Graauw, N. Kardashev, S. Likhachev, G. Goltsman, V. Koshelets, "Instrumentation for Millimetron - a large space antenna for THz astronomy," Proc. 19th Int. Symp. on Space THz Technology, Groningen, 28-30 Apr. 2008.

[20] A. H. Dayem and R. J. Martin, "Quantum Interaction of Microwave Radiation with Tunneling Between Superconductors," Phys. Rev. Lett. 8 (6), 1962

[21] G. J. Dolan, T. G. Phillips, and D. P. Woody, "Low-noise 115-GHz mixing in superconducting oxide-barrier tunnel junctions," Appl. Phys. Lett. 34, 1979.

[22] P. L. Richards and T. M. Shen, R. E. Harris and F. L. Lloyd, "Quasiparticle heterodyne mixing in SIS tunnel junctions," Appl. Phys. Lett. 34, 1979.

[23] J. R. Tucker, "Quantum limited detection in tunnel junction mixers," IEEE J.Quantum Electron. 15 (11), 1979.

[24] J. R. Tucker and M. J. Feldman, "Quantum detection at millimeter wavelengths," Rev. Mod. Phys. 57, 1985.

[25] A. Kerr, S.-K. Pan, J. Webber, "MMA Receivers: SIS Mixers," MMA project book, April,1999 http://www.tuc.nrao.edu/~demerson/project_book/chap5/chap5.3/chap5.3.html

[26] W. Shan, S. Asayama, M. Kamikura, T. Noguchi, S. Shi and Y. Sekimoto, "A 385-500 GHz Low Noise Superconductor-Insulator-Superconductor Mixer for ALMA Band 8," IEICE Trans. on Electron. E89-C (2), 2006.

[27] A. M. Baryshev, F. P. Mena, R. Hesper, T. Zijlstra, C. F. J. Lodewijk, W. Wild and T. M. Klapwijk, "A waveguide NbTiN SIS mixer for THz Array Applications," Proc. Int. J. Infrared and Millimeter Waves-THz 2006, Shanghai, China, Sep. 2006.

[28] W. Shan, S. Shi, T. Matsunaga, M. Takizawa, A. Endo, T. Noguchi, and Y. Uzawa, "Design and Development of SIS Mixers for ALMA Band 10," IEEE Trans. Appl. Supercond. 17 (2), 2007

[29] C. F. J. Lodewijk, E. van Zeijl, T. Zijlstra, D. N. Loudkov, F. P. Mena, A. M. Baryshev, and T. M. Klapwijk, "Bandwidth of Nb/AlN/Nb SIS Mixers Suitable for Frequencies around 700 GHz," Proc.19th Int. Symp. on Space THz Technology, Groningen, 28-30 Apr. 2008

[30] M. Tonouch, "Cutting-edge terahertz technology," Nature Photonics 1, 2007

Chapter 2
Fundamental theory of heterodyne SIS mixer

2.1 Overview

In this chapter, fundamental principles of mixing with quasi-particle tunneling and superconducting transmission line are summarized. T_{mix} and G_{mix} in eq. 1-7 are determined by the embedding circuits and the SIS junction properties: nonlinearity and leakage current of the *I-V* curve. Tucker and Feldman established the theory of mixing with quasi-particle tunneling by combining the general diode mixing theory with the quantum theory [1]. It is summarized in section 2.2. Besides, it is important to characterize losses G_{tune} in the tuning circuit, because the input loss not only increases the receiver noise temperature entirely but also forces the apparent bandwidth of noise temperature narrower. Fundamental principle of the transmission line using superconducting materials is summarized in section 2.3 on the basis of Mattis-Bardeen theory [2].

2.2 SIS junction as a mixing element

Mixing properties of SIS junction are determined by the nonlinear current-voltage characteristics and the embedding circuits. Since the SIS mixer is nonlinear circuit, we require a formulation of the nonlinear circuit that relates the small-signal voltages and currents at the harmonic sidebands in order to analysis the SIS mixer performance. Then the SIS junction can be treated as a linear transadmittance. The transadmittance relates voltage at each port to current at each port (e.g. voltage at RF port to current at IF port). The vehicle for this transformation is called a conversion matrix. In nonlinear noise analysis, we must calculate the spectra and correlation properties of those cyclostationary noise sources. The spectra are noise sidebands on each of the harmonics of the large-signal waveform. The correlation properties and transconductance determine the noise and conversion properties [3].

2.2.1 General mixer theory

Although some of the early theoretical work was completely analytical, accurate simulation of practical SIS mixers requires a fully numerical approach. For the practical analysis, in general, there are assumptions that the LO voltage serves only to vary the small-signal SIS junction conductance and capacitance, and that frequency conversion occur via time-varying, small-signal elements. A large signal nonlinear analysis is performed first to determine the junction voltage waveforms. The

small-signal time waveforms for the conductance and susceptance are then found from the junction voltage waveforms. The conversion performance is derived from these, and the set of impedances seen by the junction at each significant mixing frequency, without further consideration of the LO excitation.

When a small-signal voltage is applied to the pumped diode at any one of these frequencies, currents and voltages are generated in and across the junction at all other sideband frequencies. These frequencies are called the small-signal mixing frequencies, ω_m (ω_{RF}), and are given by the relation:

$$\omega_m = \omega_0 + m\omega, \qquad 2\text{-}1$$

where

$$m = 0, \pm 1, \pm 2, \pm 3 \ldots.$$

The frequencies are separated from each LO harmonic by an amount equal to the frequency, ω_0, the difference between the LO frequency and the RF frequency, usually the IF.

Large signal analysis

The goal of the large-signal analysis is to determine the amplitude V_J of the LO waveforms, which controls the nonlinear junction current and susceptance, and thereby to determine the small-signal time waveforms for the junction conductance and susceptance. It is assumed that the RF excitation is negligibly small compared to the LO. It is necessary to include the external embedding network. Fig. 2-1 shows a mixer equivalent circuit under LO excitation only. The mixing element is modeled by its large-signal equivalent circuit. The LO is represented by a current generator with

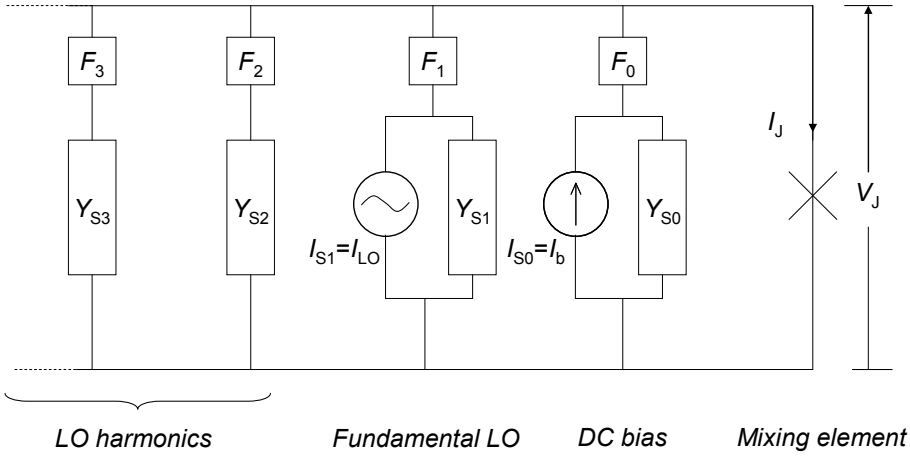

Fig. 2-1 Large-signal equivalent circuit of the mixer under LO excitation only. The external circuit is equivalent to set of impedances, the LO embedding impedances, each in series with an ideal series LO filter F_m. F_m has zero impedance at $m\omega$ and infinite impedance at all other frequencies.

amplitude and effective source admittance. The embedding network is equivalent to a set of individual impedances except the *m*th LO harmonic, $m\omega$. The mixing element is, therefore, terminated in only one impedance at each LO harmonic. The equations for the circuit at each harmonic give

$$I_{sm} - Y_{sn}V_{jm} - I_{jm} = 0\,, \qquad 2\text{-}2$$

where m is the harmonic number. I_{sm}, the source current, is normally zero except for m = 0, 1. I_{jm} and V_{jm} are the frequency-domain current and voltage at the mixing element terminals, respectively. V_{jm} is the embedding admittance at the *m*th harmonic. One practical solution to this problem is to use a type of e.g. harmonic balance [4]. In the case that mixing element is an SIS junction, it is assumed that the higher LO harmonics are short-circuited by the junction capacitance, and then the equation is reduced to the eq. 2-42 in later section.

Small signal analysis

Equation 2-1 defines the mixing frequencies in the time-varying circuit elements, either the conductance or susceptance. At each of these frequencies phasors represent the voltage across the element and the current in it:

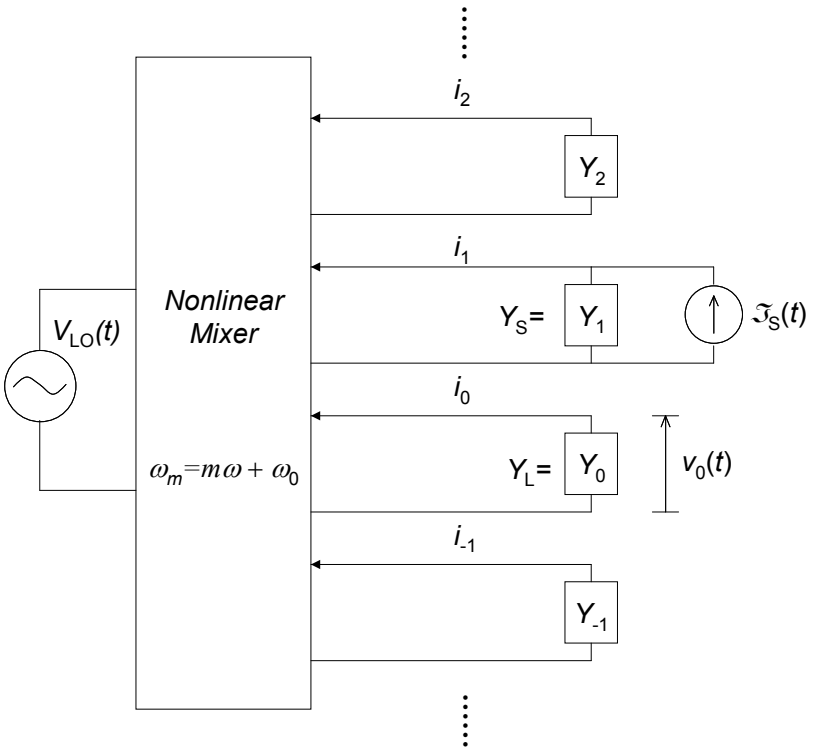

Fig. 2-2 Schematic diagram of a general heterodyne mixer, with applied LO frequency ω, signal frequency $\omega_I=\omega_S$ and IF output at ω_0. The equivalent embedding networks at all of the sideband frequencies $\omega_m=m\omega+\omega_0$, are indicated, with termination admittances Y_m.

$$v'(t) = \mathrm{Re} \sum_{m=-\infty}^{\infty} v_m e^{j\omega_m t} , \qquad 2\text{-}3$$

$$i'(t) = \mathrm{Re} \sum_{m=-\infty}^{\infty} i_m e^{j\omega_m t} . \qquad 2\text{-}4$$

These voltage and current components will be linearly related for small signals by an admittance matrix:

$$i_m = \sum_{m'} Y_{mm'} v_{m'} . \qquad 2\text{-}5$$

This $Y_{mm'}$ indicates conversion matrix, which relates small-signal voltage and current at each port. The ports are different frequencies at a single set of terminals instead of physically separate ports. Consequently, multiport network theory is directly applicable to the conversion matrix, and such operations as determining voltage gain, input impedance, and conversion to another type of matrix, such as an S-parameter matrix, involve the same relations as conventional multiports. Also, the matrix representation implies that Kirchhoff's laws must hold for the voltage and current vectors as well as scalar quantities, because sinusoids at different frequencies are linearly independent.

Once the admittance matrix elements $Y_{mm'}$ relating the small-signal currents and voltages at the various sideband frequencies have been determined, the analysis of mixer performance is straightforward. In general, there may be incoming radiation applied to the mixing element at any of the sideband ports in Fig. 2-2. An arbitrary set of current generators $\{\Im_m\}$ placed at each sideband port ω_m of the mixer will produce small-signal current and voltage components across the junction satisfying

$$\begin{aligned} \Im_m &= i_m + Y_m v_m \\ &= \sum_{m'} (Y_{mm'} + Y_m \delta_{m,m'}) v_{m'} \end{aligned} . \qquad 2\text{-}6$$

Inverting these equations, one obtains the signal voltages produced by this arbitrary set of current generators,

$$v_{m'} = \sum_{m'} Z_{mm'} \Im_{m'} , \qquad 2\text{-}7$$

where, in matrix notation,

$$\left\| Z_{mm'} \right\| = \left\| Y_{mm'} + Y_m \delta_{m,m'} \right\|^{-1} . \qquad 2\text{-}8$$

In the practical situation, the output voltage at ω_0 (=ω_{IF}) may be written in the form

$$v_0 = Z_{00} \sum_{m'} \lambda_{0m} \Im_m , \qquad 2\text{-}9$$

where the quantity

$$\lambda_{0m} = Z_{0m} / Z_{00} , \qquad 2\text{-}10$$

does not depend upon the output load termination $Y_0 = Y_L$. This conclusion is obtained by explicitly performing the matrix inversion in eq. 2-8, and will prove useful in analyzing the noise properties of the mixer. The effect of a current source $\Im_m$ at ω_m is thus equivalent at the output to a fictitious source $\lambda_{0m}\Im_m$ of frequency ω_0, which depends upon the properties of the mixer but not on the value of $Y_0 = Y_L$.

In a fundamental heterodyne mixer, the incoming signal may be represented by $\Im_I = \Im_S$ at frequency $\omega + \omega_0$, as illustrated in Fig. 2-2. The total signal power available at the input is therefore

$$P_{in} = \frac{|\Im_S|^2}{8G_S}. \qquad 2\text{-}11$$

The power that is frequency down-converted and delivered into the output load may be written in the form

$$P_{out} = \frac{1}{2}G_L|v_0|^2 = \frac{1}{2}G_L|Z_{01}|^2|\Im_S|^2. \qquad 2\text{-}12$$

The conversion efficiency of the mixer in single sideband is then given by

$$G_{mix,SSB} = \frac{P_{out}}{P_{in}} = 4G_S G_L |Z_{01}|^2. \qquad 2\text{-}13$$

In these expressions, the conductances G_S and G_L represent the real parts of the source and load admittances Y_S and Y_L, respectively. The conversion efficiency is therefore readily calculated in terms of the small-signal admittance matrix $Y_{mm'}$ and the terminations Y_m of the mixer element at each of the sideband frequencies. The double sideband (DSB) gain of the mixer can be expressed as

$$G_{mix,DSB} = 2G_L(G_S|Z_{01}|^2 + G_I|Z_{0-1}|^2). \qquad 2\text{-}14$$

Noise properties

The electronic noise we treat here is a stationary random process. This is that the noise voltage or current at any point in a circuit varies randomly, but with statistical characteristics that do not change with time. The major noise sources in diodes are thermal noise and shot noise.

Shot noise

Shot noise is generated by a random process that each electron probabilistically passes through the junction which creates potential barrier. The shot noise may be analyzed by placing a noise generator $\delta I(t) = [I(t) - \langle I(t)\rangle]$ in parallel with an idealized noiseless mixer, where $I(t)$ is the induced LO current through the intrinsic device and $\langle I(t)\rangle$ is its expectation.

When the LO voltage is applied, the shot noise is modulated at the LO frequency. Each shot noise component at each missing frequency is converted to the other missing frequencies by the LO fundamental and its harmonics. The noise components at any mixing frequency therefore include up- and down-converted components from each other mixing frequency. Once they are converted to the

IF frequency, those components are correlated.

As with the small-signal analysis, the noise currents in the diode junction at each mixing frequency can be expressed via a vector:

$$[I_s]=\begin{bmatrix} I_{s-N} \\ I_{s-N+1} \\ \cdot \\ I_{s0} \\ \cdot \\ \cdot \\ I_{sN} \end{bmatrix} \qquad 2\text{-}15$$

where I_{sN} are the shot noise currents at each mixing frequency ω_m. The goal is to find the IF output voltage due to these noise sources, each of which may be considered as an input noise source at each mixing frequency. The voltage across the junction at mixing frequency ω_m due to shot noise is

$$[V_{sm}]=[Z_m]\cdot[I_s] \qquad 2\text{-}16$$

where $[Z_m]$ is the row of the conversion matrix. The mean-square value of the junction noise voltage is

$$\langle|V_{sm}|^2\rangle=[Z_m]\cdot\langle[I_s]\cdot[I_s]^{\dagger t}\rangle\cdot[Z_m]^{\dagger t} \qquad 2\text{-}17$$

where †t represents the conjugate transpose of the matrix. The term $\langle[I_s]\cdot[I_s]^{\dagger t}\rangle$ is a matrix representing the correlations between the shot noise components at the various mixing frequencies. It is, therefore, called the correlation matrix $[C_s]$ for the pumped mixer. The term in this matrix have been evaluated and are

$$\langle[I_s]\cdot[I_s]^{\dagger t}\rangle=C_{smn}=2eI_{m-n}B \qquad 2\text{-}18$$

where I_{m-n} is the coefficient for the *m-n* th harmonic in the Fourier series representation of the local oscillator current.

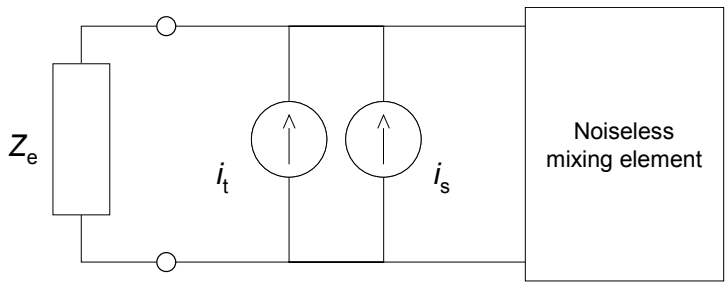

Fig. 2-3 Intrinsic and external noise equivalent circuit of the mixing element The thermal noise source converted to a current source via Thevenin's theorem

Thermal noise

The other noise source of interest is thermal noise which arises from the random agitation of electrons and is related to black-body radiation with a temperature. Although the noise is treated as a voltage source, it can be converted to a current source via Thevenin's theorem (see Fig. 2-3), that is, the magnitude of the thermal noise current source is

$$\langle i_{\mathrm{t}}{}^{2} \rangle = \frac{4\hbar\omega BG}{e^{\hbar\omega/kT}-1}, \qquad 2\text{-}19$$

where T, B, and ω is the physical temperature of the blackbody, the bandwidth, and angular frequency. Also G is the conductance of embedding circuit. Since the thermal noise arises in G, which does not vary with LO excitation, its components at different frequencies have no correlation, and the correlation matrix is simply a diagonal. Therefore, the correlation matrix for the thermal noise is

$$C_{\mathrm{t}mn} = \begin{cases} \dfrac{4\hbar\omega BG_m}{e^{\hbar\omega/kT}-1} & m = n \\ 0 & m \neq n \end{cases}, \qquad 2\text{-}20$$

where G_m is the real part of the embedding impedance.

Total noise

The voltage at an IF frequency of ω_0 is the sum of the shot noise and thermal noise components:

$$\langle |V_0|^2 \rangle = [Z_0] \cdot (C_{\mathrm{s}} + C_{\mathrm{t}}) \cdot [Z_0]^{\dagger \mathrm{t}} \qquad 2\text{-}21$$

Total noise power referred to the input port using this output voltage and eq. 2-16 is given by

$$P_{\mathrm{total}} = \frac{\langle |V_0|^2 \rangle}{|Z_{01}|^2 \,\mathrm{Re}(Y_1)}. \qquad 2\text{-}22$$

Therefore the equivalent input mixer noise temperature can be characterized by defining the noise current source $4kT_{\mathrm{mix}}B\mathrm{Re}(Y_1)$ connected in parallel with an idealized noiseless mixer

$$T_{\mathrm{mix}} = \frac{[Z_0] \cdot (C_{\mathrm{s}} + C_{\mathrm{t}}) \cdot [Z_0]^{\dagger \mathrm{t}}}{4kB \cdot |Z_{01}|^2 \,\mathrm{Re}(Y_1)}. \qquad 2\text{-}23$$

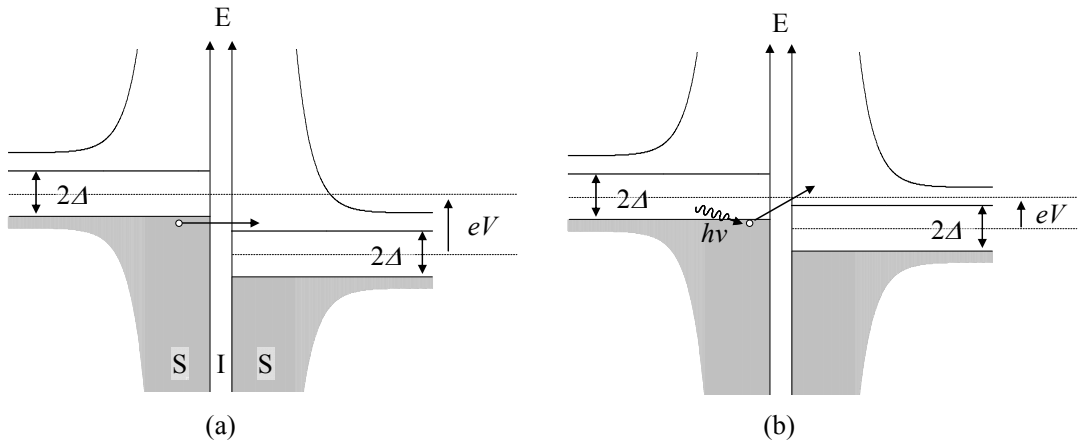

Fig. 2-4 Energy diagram of an SIS junction. Quasi-particle tunneling at the same energy level (a), by photon assisted tunneling (b).

2.2.2 Quasi-particle tunneling current in SIS junction

Theoretical DC *I-V* curve of an SIS junction

An SIS junction has a sandwiched structure of two superconductors separated by very thin insulator layer. The current-voltage characteristics shows an extraordinary nonlinearity which is created by the gap in available energies for single-electron quasiparticles on both sides of SIS tunnel barrier. As illustrated in Fig. 2-4, when both electrodes are an identical superconductor having gap energy Δ, the quasi-particle tunneling current from the left to the right electrode is given by

$$I_{\mathrm{dc}}(V)=\frac{G_{\mathrm{N}}}{e}\int_{-\infty}^{\infty}\frac{|E-eV|}{[(E-eV)^2-\Delta^2(T)]^{1/2}}\frac{|E|}{[E^2-\Delta^2(T)]^{1/2}}[f(E-eV,T)-f(E,T)]dE\,, \qquad 2\text{-}24$$

where e, G_{N} and T is the charge of a single, electron tunnel conductance, and physical temperature. In eq. 2-24, f(E) Fermi-Dirac distribution is given by

$$f(E,T)=\frac{1}{e^{E/k_{\mathrm{B}}T}+1}\,. \qquad 2\text{-}25$$

When a voltage V<2Δ/e is applied there is still no current flowing because the electrons below the gap on the have no access to empty states on the right. At V = 2Δ/e there is a sudden rise in current because electrons on the left suddenly gain access to the states above the gap on the right. The resulting dc tunneling current as a function of bias voltage is shown in Fig. 2-5 (a).

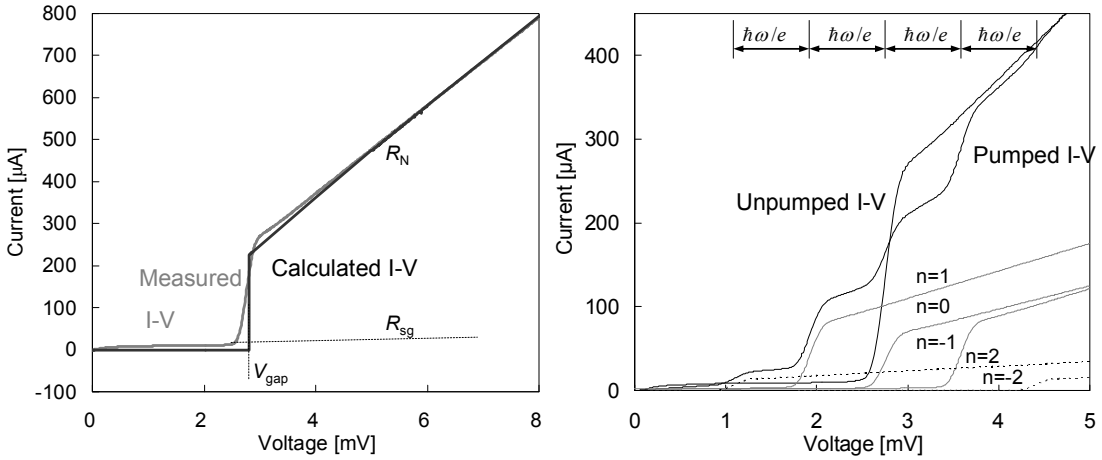

Fig. 2-5 Calculated (ideal) and measured dc *I-V* curve (a). Also shown is theoretical photon assisted tunneling current induced by electro-magnetic field in the SIS junction at 0.2 THz as a function of bias voltage (b). The pumped *I-V* curve is summation of *n* order term component of Bessel function.

Photon assisted tunneling

Unlike classical diode as a mixing element, it is not possible to describe nonlinear *I-V* characteristic of quasiparticle tunneling current with a Taylor series due to quantum mechanics. In the situation that the cooper-pair tunneling current is suppressed by applied magnetic field, Werthamer [5] derived an expression for the quasiparticle tunneling current as a function of time in the presence of both dc and ac bias.

$$I(t) = \mathrm{Im}\iint d\omega' d\omega'' W(\omega') W^*(\omega'')\, e^{-i(\omega'-\omega'')t}\, j(\omega' + eV_0/\hbar)\,, \qquad 2\text{-}26$$

$W(\omega)$ is the Fourier frequency component of the time-varying phase factor caused by the ac bias voltage:

$$\exp\left[-i\frac{e}{\hbar}\int^t dt'[V(t') - V_0]\right] = \int_{-\infty}^{\infty} d\omega W(\omega)\, e^{-i\omega t}\,. \qquad 2\text{-}27$$

Besides, j(V) in eq.2-26 is complex current response function:

$$j(V_0) = iI_{\mathrm{dc}}(V_0) + I_{\mathrm{KK}}(V_0)\,. \qquad 2\text{-}28$$

When the bias voltage V(t) contains only a dc component V_0, then $W(\omega)$ = $\delta(0)$, which is delta function, and from eq. 2-26 we have

$$\mathrm{Im}\left[j(eV_0/\hbar)\right] = I_{\mathrm{dc}}(V_0)\,. \qquad 2\text{-}29$$

This equation implies that the imaginary part of the quasiparticle response function at frequency $\omega_0 = eV_0/\hbar$ is equal to the dc tunneling current at bias voltage V_0. It is clear that the reactive part of the quasiparticle response function has no contribution to the tunneling current when the bias voltage is

time independent. The real part of the complex current function is related to the imaginary part by Kramers-Kronig transform:

$$\begin{aligned}\mathrm{Re}\left[j(eV_0/\hbar)\right] &= I_{\mathrm{KK}}(V_0)\\ &= P\int_{-\infty}^{\infty}\frac{dV'}{\pi}\frac{I_{\mathrm{dc}}(V')-V'/R_{\mathrm{N}}}{V'-V_0}\end{aligned} \qquad 2\text{-}30$$

The dc current $I_{\mathrm{dc}}(\mathrm{V})$ as a function of dc bias voltage gives the imaginary part of the response function as a function of frequency; its voltage Kramers-Kronig transform gives the real part of the response function. Therefore, the dc *I-V* curve, which can be easily measured, contains all the information about the response of the quasiparticles in an SIS junction at high frequencies. These equations suggest a good way of deducing the frequency-dependent response function of quasiparticles. It should be suggested that the reactances calculated in terms of $I_{\mathrm{KK}}(\mathrm{V})$ are nonclassical, and are present in addition to the junction capacitance.

The time dependent voltage across the tunnel barrier will be of the term

$$V(t) = V_0 + V_{\mathrm{LO}}\cos\omega t\,. \qquad 2\text{-}31$$

The additional phase factor multiplying the Schrödinger wave function for each quasiparticle state on the left side of barrier due to the LO is given by

$$\exp\left[-i\frac{e}{\hbar}\int^{t}dt'V_{\mathrm{LO}}\cos\omega' t\right] = \sum_{n=-\infty}^{\infty}J_n(eV_{\mathrm{LO}}/\hbar\omega)\,e^{-in\omega t}\,. \qquad 2\text{-}32$$

The Fourier transform of this phase factor defined by eq.2-27 then becomes

$$W(\omega') = \sum_{n=-\infty}^{\infty}J_n(eV_{\mathrm{LO}}/\hbar\omega)\,\delta(\omega'-n\omega)\,. \qquad 2\text{-}33$$

Substituting this result into eq. 2-26 for the induced tunneling current gives

$$\begin{aligned}I_{\mathrm{LO}}(t) &= \mathrm{Im}\sum_{n,m=-\infty}^{\infty}J_n(\alpha)J_{n+m}(\alpha)\,e^{im\omega t}\,j(V_0+n\hbar\omega/e)\\ &= a_0+\sum_{m=1}^{\infty}(2a_m\cos m\omega t+2b_m\sin m\omega t)\end{aligned} \qquad 2\text{-}34$$

where the amplitude of the local oscillator waveform is contained in the argument of the Bessel functions:

$$\alpha = eV_{\mathrm{LO}}/\hbar\omega\,. \qquad 2\text{-}35$$

The averaged current induced by the local oscillator thus contains components at all the various harmonic frequencies, with magnitudes given by

$$2a_m = \sum_{n,m=-\infty}^{\infty}J_n(\alpha)(J_{n+m}(\alpha)+J_{n-m}(\alpha))\,I_{\mathrm{dc}}(V_0+n\hbar\omega/e)\,, \qquad 2\text{-}36$$

$$2b_m = \sum_{n,m=-\infty}^{\infty}J_n(\alpha)(J_{n+m}(\alpha)-J_{n-m}(\alpha))\,I_{\mathrm{KK}}(V_0+n\hbar\omega/e)\,. \qquad 2\text{-}37$$

Equations 2-34, 2-36 and 2-37 indicate that many harmonics of the drive frequency ω exist in an SIS

junction, and that there exists an out-of-phase reactive component $\sin\omega t$ as well as an in-phase component $\cos\omega t$. Assuming that all harmonics are shorted, a dissipative and reactive currents can be derived by setting m to 1 at a frequency ω:

$$I'_{\mathrm{LO}}(V_0, V_{\mathrm{LO}}) = \sum_{n=-\infty}^{\infty} J_n(\alpha)(J_{n+1}(\alpha) + J_{n-1}(\alpha))\, I_{\mathrm{dc}}(V_0 + n\hbar\omega/e)\,, \qquad 2\text{-}38$$

$$I''_{\mathrm{LO}}(V_0, V_{\mathrm{LO}}) = \sum_{n=-\infty}^{\infty} J_n(\alpha)(J_{n+1}(\alpha) - J_{n-1}(\alpha))\, I_{\mathrm{KK}}(V_0 + n\hbar\omega/e)\,. \qquad 2\text{-}39$$

Thus the dissipative and reactive currents is defined in complex notation by

$$I^{\omega}_{\mathrm{LO}} = I'_{\mathrm{LO}} + iI''_{\mathrm{LO}}\,. \qquad 2\text{-}40$$

In addition, it should be noted that the current component for $m = 0$ corresponds to dc I-V curve of a voltage-pumped SIS junction, which is completely independent of the real part of the quasiparticle response function I_{KK}.

$$I_0(V_0, V_{\mathrm{LO}}) = a_0 = \sum_{n=-\infty}^{\infty} J_n^2(\alpha)\, I_{\mathrm{dc}}(V_0 + n\hbar\omega/e)\,. \qquad 2\text{-}41$$

This equation describes the structure of I-V by photon assisted tunneling shown in Fig. 2-5. Dayem and Martin experimentally observed it for the first time in 1962 [6]. It was later explained theoretically by Tien and Grodon [7].

2.2.3 Three port quantum mixing theory

In previous section, tunneling current in the SIS junction induced by electro-magnetic field was described. In this section, three-port-mixing theory assumed that higher harmonics of the local oscillator are short-circuited is constructed by being combined the theories of the general mixer and tunneling current in SIS junction.

Large-signal analysis

With the assumption that the higher harmonics of the local oscillator are short-circuited in three-port-mixing theory, the only physically relevant component of the large-signal as current through the tunnel junction is $\mathrm{Re}(I_{\mathrm{LO}}e^{i\omega t})$. The equivalent circuit for the mixer at the LO frequency ω is illustrated in Fig. 2-6 by being simplified for Fig. 2-1. The local oscillator is represented by a current generator with complex amplitude $\Im_{\mathrm{LO}}$ and an effective source admittance $Y_\omega = G_\omega + iB_\omega$ determined by the input waveguide and mounting structure. The susceptance B_ω will include a contribution ωC due to the junction's geometrical capacitance. According to Fig. 2-6, the circuit equation may be written in the form

$$\Im_{\mathrm{LO}} = I^{\omega}_{\mathrm{LO}} + Y_\omega V_{\mathrm{LO}}\,. \qquad 2\text{-}42$$

This is exactly same as the eq. 2-2 of the case assumed that all LO harmonics are short-circuited. The total local oscillator power incident on the mixer is equal to the available power from the current source:

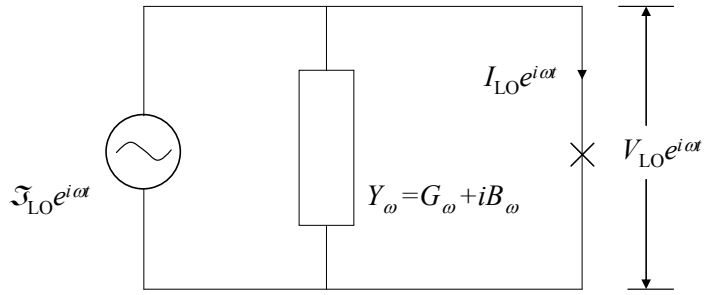

Fig. 2-6 Equivalent circuit for the SIS mixer at the LO frequency ω. All higher harmonics are assumed to be short circuited

$$P_{\mathrm{LO}} = \frac{|\mathfrak{I}_{\mathrm{LO}}|^2}{8G_\omega}\,. \qquad 2\text{-}43$$

Small-signal admittance matrix

The small-signal mixing properties of the tunnel junction may be calculated once the amplitude of the local oscillator waveform has been determined. As shown in Fig. 2-2, strong pumping at the LO frequency ω mixes the output frequency ω_0 all sidebands described in 2-1.

Each of these sidebands is represented in Fig. 2-2 by a mixer port with a termination admittance Y_m. The incoming signal at frequency $\omega_S=\omega_1$ is represented by a current generator $\mathfrak{I}_S$ with a source admittance $Y_S=Y_1$. The function of the mixer is to convert this incoming signal power to the output frequency ω_0, and couple it into the load admittance $Y_L=Y_0$ representing the first stage IF amplifier.

As derived from general mixer theories in section 2.2.1, the voltages and currents at the sideband frequencies may be represented in the form of eqs. 2-3 and 2-4, and also these components will be linearly related for small signals by an admittance matrix in eq. 2-5. The values of the admittance matrix elements are determined by the large-signal solution, and depend on the strength of the local oscillator and the nonlinear dc *I-V* characteristic of the tunnel junction. They are calculated by expanding the total current through the tunnel barrier and identifying those terms that are linear in the small-signal voltages.

The total voltage and current across the tunnel barrier my be written in the form

$$V(t) = V_0 + V_{\mathrm{LO}}(t) + v_{\mathrm{sig}}(t)\,, \qquad 2\text{-}44$$

$$\langle I(t)\rangle = I_{\mathrm{LO}}(t) + i_{\mathrm{sig}}(t)\,. \qquad 2\text{-}45$$

The inclusion of $v_{\mathrm{sig}}(t)$ in the applied voltage in eq. 2-27 requires additional terms in the time-dependent phase factor, which multiply the result of eq. 2-32 for $V_{\mathrm{LO}}(t)$ alone. Retaining only terms to first order in the sideband voltage components $v_{m'}(t)$, we generalize eq. 2-33 to

$$W(\omega') = \sum_{n=-\infty}^{\infty} J_n(eV_{LO}/\hbar\omega)\left[\delta(\omega' - n\omega) + \sum_{n=-\infty}^{\infty} \frac{e}{2\hbar\omega_{m'}}[v_{m'}^{*}\delta(\omega' - n\omega - \omega_{m'}) - v_{n'}\delta(\omega' - n\omega + \omega_{m'})]\right].$$

2-46

Inserting this result into eq. 2-26 for the total current, and again retaining only terms linear in the sideband voltages $v_{m'}(t)$, we find the admittance matrix elements that give the signal currents $i_m(t)$ in eq. 2-5 to be

$$Y_{mm'} = G_{mm'} + iB_{mm'},$$

2-47

where

$$G_{mm'} = \frac{e}{2\hbar\omega_{m'}} \sum_{n',n=-\infty}^{\infty} J_n(\alpha)J_{n'}(\alpha)\delta_{m-m',n-n'}[I_{dc}(V_0 + n'\hbar\omega/e + \hbar\omega_{m'}/e) - I_{dc}(V_0 + n'\hbar\omega/e) + I_{dc}(V_0 + n\hbar\omega/e) - I_{dc}(V_0 + n\hbar\omega/e - \hbar\omega_{m'}/e)],$$

2-48

$$B_{mm'} = \frac{e}{2\hbar\omega_{m'}} \sum_{n',n=-\infty}^{\infty} J_n(\alpha)J_{n'}(\alpha)\delta_{m-m',n-n'}[I_{KK}(V_0 + n'\hbar\omega/e + \hbar\omega_{m'}/e) - I_{dc}(V_0 + n'\hbar\omega/e) - I_{KK}(V_0 + n\hbar\omega/e) + I_{dc}(V_0 + n\hbar\omega/e - \hbar\omega_{m'}/e)]$$

2-49

The elements of the small-signal admittance matrix in this model are seen to separate into real and imaginary parts, which depend only upon the dissipative and the reactive components, respectively, of the junction response.

Noise properties

The SIS mixer noise property is determined by its intrinsic shot noise caused by local oscillator pump and dc bias, and the extrinsic noise sources by the unavoidable quantum fluctuations of the signals presented at signal and image port and thermal noise of the image termination. The combination of dc bias voltage and local oscillator waveform in eq. 2-31 produces large tunneling currents through the junction at frequency multiples $m\omega$ of the LO drive. This current results from the tunneling of individual quasiparticles. However, fluctuations of the tunneling current due to its random process in the SIS junction about the average will produce noise current at other frequencies.

Correlation matrix of shot noise generated by the SIS junction is given by

$$H^{S}_{mm'} = e \sum_{n',n=-\infty}^{\infty} J_n(\alpha)J_{n'}(\alpha)\delta_{m-m',n-n'}\{\coth[\beta(eV_0 + n'\hbar\omega + \hbar\omega_{m'})/2]\, I_{dc}(V_0 + n'\hbar\omega/e + \hbar\omega_{m'}/e) + \coth[\beta(eV_0 + n\hbar\omega - \hbar\omega_{m'})/2] I_{dc}(V_0 + n\hbar\omega/e - \hbar\omega_{m'}/e)\},$$

2-50

where $\beta = 1/k_B T$. A standard measure of the sensitivity of a heterodyne mixer is the minimum detectable power: the incident signal power required in order to produce an output equal to noise output. The signal generator $\mathfrak{I}_S$ at the input port in Fig. 2-2 is equivalent, according to eq. 2-9, to a

current source $\lambda_{01}\Im_S$ at the output frequency whose square may be expressed in terms of the available incident power eq.2-11 in the form

$$\langle[\delta I_0]^2\rangle_{sig} = \frac{1}{2}|\lambda_{01}\|\Im_S|^2 = 4G_L|\lambda_{01}|^2 P_{in} . \quad 2\text{-}51$$

The equivalent noise temperature referring to input port due to shot noise in SIS junction can be found by using the correlation matrix

$$T_{mix}^{LO} = \frac{1}{G_L|\lambda_{01}|^2}\sum_{m,m'}\lambda_{0m}\lambda_{0m}^* H^s_{mm'} . \quad 2\text{-}52$$

The behavior of thermal noise generated in SIS junction is exactly the same as in classical resistive mixer, as derived in eq 2-20. The correlation matrix in terms of the thermal noise is given by

$$H^t_{mm'} = \begin{cases} \dfrac{4\hbar\omega BG_m}{e^{\hbar\omega/kT}-1} & m = n \\ 0 & m \neq n \end{cases} \quad 2\text{-}53$$

From eqs. 2-50 and 2-53, the total correlation matrix by shot noise and thermal noise is as follows:

$$H_{mm'} = H^t_{mm'} + H^s_{mm'} . \quad 2\text{-}54$$

2.3 Superconducting microstrip line

As well as SIS junctions, superconducting microstrip lines for SIS mixers takes an important role in low-loss propagation of the electro-magnetic field for RF and LO signals and in elements of distributed constant circuit to control embedding impedance. In order to work a receiver in low noise temperature, selection and fabrication of appropriate material combinations have been one of the important problems in this frequency range, because well-established all-Nb SIS mixers cannot be employed due to the RF losses in their tuning circuits caused by the onset of pair-breaking above the Nb gap frequency of approximately 0.7 THz. Therefore, it is necessary to establish new technologies adopted superconducting materials with large gap frequencies. Although NbN and NbTiN, which have a large gap frequency above 1 THz, are promising superconductors, modelling of circuit using their materials is necessary for the accurate design. In this section, some fundamental principles of transmission line using superconductors are presented for calculating power transmission or losses from a feed point to junctions. In section 2.3.1, surface impedance concept for superconductors and normal conductors is described for modelling superconducting microstrip lines. In sections 2.3.2 and 2.3.3, two analysis methods for the superconducting microstrip line are presented on the basis of an analytical calculation and numerical simulation using High Frequency Structure Simulator (HFSS) which is the software with 3D-finite element method [10].

2.3.1 Surface impedance of superconductors and normal conductors

It is well-known that surface impedance concept plays an important role in the characterization of the microstrip lines. The surface impedance of thin film conductor with the thickness t is defined by

$$Z_s(\omega) = \frac{E_s(0,\omega)}{\int_0^t dz J_x(z,\omega)} = R_s(\omega) + jX_s(\omega), \qquad 2\text{-}55$$

where $E_s(0,\omega)$ is the electric field parallel to the surface of the conductor and $J_x(z,\omega)$ is the current density in the conductor at depth z. For the magnetic and electric field penetration depths, λ and δ respectively, we then can write the following expressions:

$$\lambda = \frac{\mathrm{Im}[Z_s]}{\mu_0 \omega}, \qquad 2\text{-}56$$

$$\delta = \frac{\mathrm{Re}[Z_s]}{\mu_0 \omega}. \qquad 2\text{-}57$$

The surface impedance Z_s is distinguished by three regions, in local limit, anomalous limit, and extreme anomalous limit. In the local limit, defined by $l_e << \delta_c$ for normal metals or $\xi << \lambda$ for superconductors, the frequency-dependent surface impedance for the thin conductor with thickness t, conductivity σ at the operating temperature is solved from Maxwell's equations and is given by

$$Z_s = \sqrt{\frac{j\omega\mu_0}{\sigma}} \coth(t\sqrt{j\omega\mu_0\sigma}), \qquad 2\text{-}58$$

where δ_c is the classical skin depth, l_e is the mean free path of electrons, $\lambda = \lambda_L(\xi/\xi_0)^{1/2}$ is the effective penetration depth, and $\xi = 1/(\xi_0^{-1} + l_e^{-1})$ is the Pippard coherence length [15].

In the non-local case where $l_e \geq \delta_c$ or $\xi \geq \lambda$, the surface impedance needs to be calculated using the Mattis-Bardeen theory, however very complicated calculation is necessary [2].

In the extreme anomalous limit where $\xi >> \lambda$ for the superconductor, the frequency dependent complex conductivity $\sigma = \sigma_r - j\sigma_i$ can be analytically resolved

$$\frac{\sigma_1}{\sigma_n} = \frac{2}{\hbar\omega}\int_{\Delta}^{\infty}[f(E) - f(E+\hbar\omega)]g(E)dE + \frac{1}{\hbar\omega}\int_{\Delta-\hbar\omega}^{-\Delta}[1 - f(E+\hbar\omega)]g(E)dE, \qquad 2\text{-}59$$

$$\frac{\sigma_2}{\sigma_n} = \frac{1}{\hbar\omega}\int_{\Delta-\hbar\omega,-\Delta}^{\Delta}\frac{[1-2f(E+\hbar\omega)][E^2+\Delta^2+\hbar\omega E]}{[\Delta^2-E^2]^{1/2}[(E+\hbar\omega)^2-\Delta^2]^{1/2}}dE, \qquad 2\text{-}60$$

where $f(\eta)$ is equilibrium Fermi-Dirac distribution function at ambient temperature that is

$$f(\eta) = \frac{1}{1+e^{\eta/k_BT}}, \qquad 2\text{-}61$$

and

$$g(E) = \frac{E^2+\Delta^2+\hbar\omega E}{[E^2-\Delta^2]^{1/2}[(E+\hbar\omega)^2-\Delta^2]^{1/2}}. \qquad 2\text{-}62$$

σ_n is the normal conductivity of a superconductor just above the critical temperature T_c. The first

integral of σ_1 represents conduction of thermally excited normal electrons, while the second integral of σ_1 introduces generation of quasiparticles by the incoming radiation, which is called as pair-breaking. The lower limit on the integral for σ_2 becomes $-\Delta$ when the frequency exceeds the gap frequency. σ_2 results from inertia of cooper pair. The surface impedance of the superconducting film is defined as the complex conductivity in the extreme anomalous limit, and eq. 2-58 in the local limit. For the normal metal at cryogenic temperature and higher frequency, the surface impedance for the extreme anomalous limit $l_e >> \delta_c$ by Reuter-Sodheimer [16]

$$Z_s = \frac{1+j\sqrt{3}}{\sqrt{3}\cdot\sqrt[3]{\pi}}\sqrt[3]{\frac{9\omega^2\mu_0{}^2 l_e}{16\sigma}}\,. \qquad 2\text{-}63$$

Thus, the surface resistance becomes a material constant in the extreme anomalous limit. For frequencies above 1 THz Al can be taken to be in the extreme anomalous limit [17].

2.3.2 Analytical calculation method of superconducting microstrip lines

A piece of line of infinitesimal length Δz for a transmission line can be modeled using a lumped element as shown in Fig. 2-7, where R, L, G, C are series resistance, series inductance, shut conductance, and shunt capacitance per unit length. L represents the total self-inductance of the two conductors, and C is due to the close proximity of the two conductors [8]. R represents the resistance due to the finite conductivity of the conductors, and the shunt conductance G is due to dielectric loss in the material between the conductors. For wave equations of the voltage and current in the sinusoidal steady-state condition, characteristic impedance Z_0 and complex propagation constant γ relating to loss constant α and phase constant β are defined as

$$Z_0 = \sqrt{\frac{Z}{Y}} = \sqrt{\frac{R+j\omega L}{G+j\omega C}}\,, \qquad 2\text{-}64$$

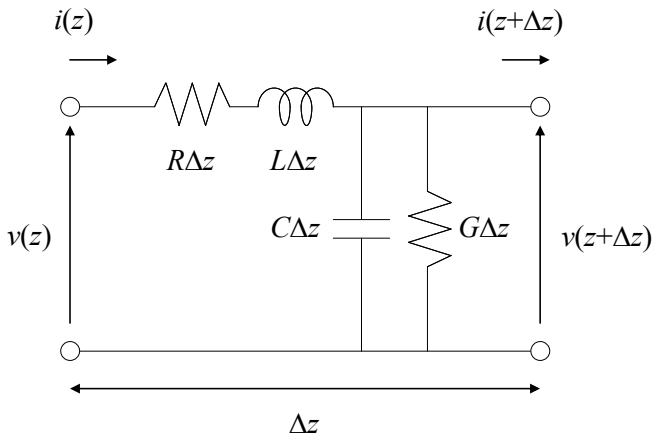

Fig. 2-7 Generalized representation of equivalent circuit for an infinitesimal length of transmission line with lumped elements.

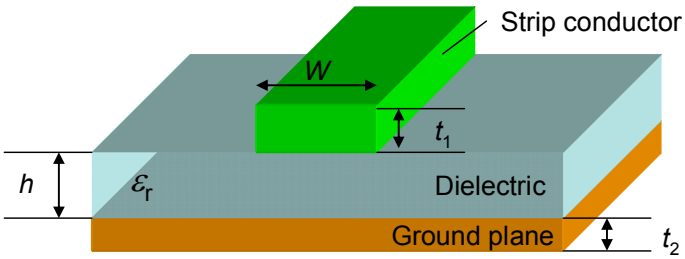

Fig. 2-8 Geometry of a microstrip line

$$\gamma = \alpha + j\beta = \sqrt{(R + j\omega L)(G + j\omega C)}\,. \qquad 2\text{-}65$$

For a microstrip line illustrated in Fig. 2-8, the series impedance and shunt admittance, per unit length, can be written as [11] [12](referring to [13])

$$Z = j\omega\mu_0 g_1 + g_2\left(Z_{s1} + Z_{s2}\right), \qquad 2\text{-}66$$

$$Y = j\omega\varepsilon_0\varepsilon_{re} / g_1\,, \qquad 2\text{-}67$$

where g_1 and g_2 are geometrical factors, ε_{re} is the effective dielectric constant of the corresponding perfectly conducting microstrip line and Z_s is the surface impedance for superconductor or normal conductor. Here we assume that the loss of the dielectric is negligible. The characteristic impedance and propagation constant of this superconducting transmission line are [14]

$$Z_{line} = \sqrt{\frac{Z}{Y}} = \frac{g_1\eta_0}{\sqrt{\varepsilon_0}}\sqrt{1 - j\frac{g_2(Z_{s1} + Z_{s2})}{\omega\varepsilon_0 g_1\eta_0^2}}\,, \qquad 2\text{-}68$$

$$\gamma_{line} = \alpha + j\beta = \sqrt{ZY} = jk_0\sqrt{\varepsilon_{re}}\sqrt{1 - j\frac{g_2(Z_{s1} + Z_{s2})}{\omega\varepsilon_0 g_1\eta_0^2}}\,, \qquad 2\text{-}69$$

where η_0 is the free space impedance. For the corresponding perfectly conducting line, $Z_{s1} = 0$ and $Z_{s2} = 0$. Its characteristic impedance is

$$Z_p = \frac{g_1\eta_0}{\sqrt{\varepsilon_0}}\,. \qquad 2\text{-}70$$

Applying the eq. 2-70 to eqs. 2-68 and 2-69, we obtain

$$Z_{line} = Z_p\sqrt{1 - j\frac{g_2\eta_0(Z_{s1} + Z_{s2})}{\omega\mu_0 Z_p\sqrt{\varepsilon_{re}}}}\,, \qquad 2\text{-}71$$

$$\gamma = jk_0\sqrt{\varepsilon_{re}}\sqrt{1 - j\frac{g_2\eta_0(Z_{s1} + Z_{s2})}{\omega\mu_0 Z_p\sqrt{\varepsilon_{re}}}}\,. \qquad 2\text{-}72$$

Closed form analytical expression for g_2 is given by

$$g_2 = \frac{\left(w' + \frac{w'}{\pi(w'/2+0.94)}\right)\left(1 + \frac{1}{w'} + \frac{\ln(2h/t_1) - t_1/h}{\pi w'}\right)}{h\left\{w' + \frac{2}{\pi}\ln\left[2\pi e\left(\frac{w'}{2} + 0.94\right)\right]\right\}}, \quad 2\text{-}73$$

where

$$w' = \frac{w + \frac{t_1}{\pi}\ln\left(\frac{2h}{t_1} + 1\right)}{h}. \quad 2\text{-}74$$

At frequencies below the gap, the loss of the line can be neglected. Assuming also that both the strip and the ground are thick compared to the penetration depth, we can calculate the surface impedance using the two fluid model. At frequencies near the gap, the loss and the effective penetration depth of the line should be considered. In this case, surface impedance calculated by Mattis-Bardeen theory as described later, is used.

2.3.3 Numerical simulation of a superconducting microstrip line using HFSS

Representing the superconducting film by thin sheets with complex surface impedance [18], we are also able to extend HFSS for simulating superconducting microstrip lines [19][20]. To verify the feasibility of this method, we calculated an NbTiN/SiO_2/Al (300/300/500 nm) superconducting microstrip line with a width of 4.5 μm from 0.7 to 1.3 THz and compared the results with analytical ones described in section 2.3.2. The simulation model is shown in Fig. 2-9. The strip was set as a box structure with conducting sheets having different surface impedances Z_{strip_v} and Z_{strip_h}

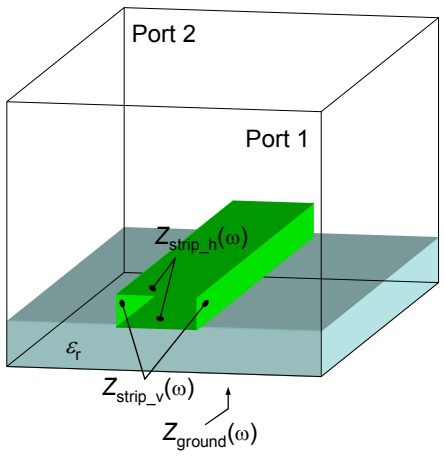

Fig. 2-9 Simulation model of the superconducting microstrip line using HFSS. The strip is set as a box structure with conducting sheets having different surface impedances for vertical and horizontal planes. Note that the dimension of the strip conductor and dielectric are highlighted to understand the model easily.

depending on the actual thickness for vertical and horizontal planes. Likewise, the ground plane is represented as the infinite conducting sheet having Z_{ground}. Since HFSS does not correctly treat a wave port containing highly inductive impedance boundaries, a short section of microstrip line of ideal conductor was added to the front of a short-circuited superconducting section. The reflection at the input of the superconducting section could be easily de-embedded and in turn the superconducting microstrip line characteristic parameters were calculated.

Fig. 2-10 (a) shows calculated real and imaginary parts of the surface impedance used for both analysis of the microstrip characteristic. The complex conductivity for the NbTiN film (T_c = 14.5 K, $2\Delta/e$ = 4.9 mV, ρ = 100 μΩcm) with a thickness of 300 nm is based on the Mattis-Bardeen theory in the extreme anomalous limit, while the surface impedance of the Al (ρ = 0.25 μΩcm) with a thickness of 500 nm is calculated in the local limit. The simulation results of characteristic impedance Z_0, effective dielectric constant ε, and transmission loss are compared with analytical ones in Fig. 2-10 (b). Obviously, both results give consistent dispersion characteristics as well as ref. [19], except for the differences of about 15 % in Z_0, which are caused by slightly different current distribution on the surfaces of the wiring and ground plane layers developed in the two methods.

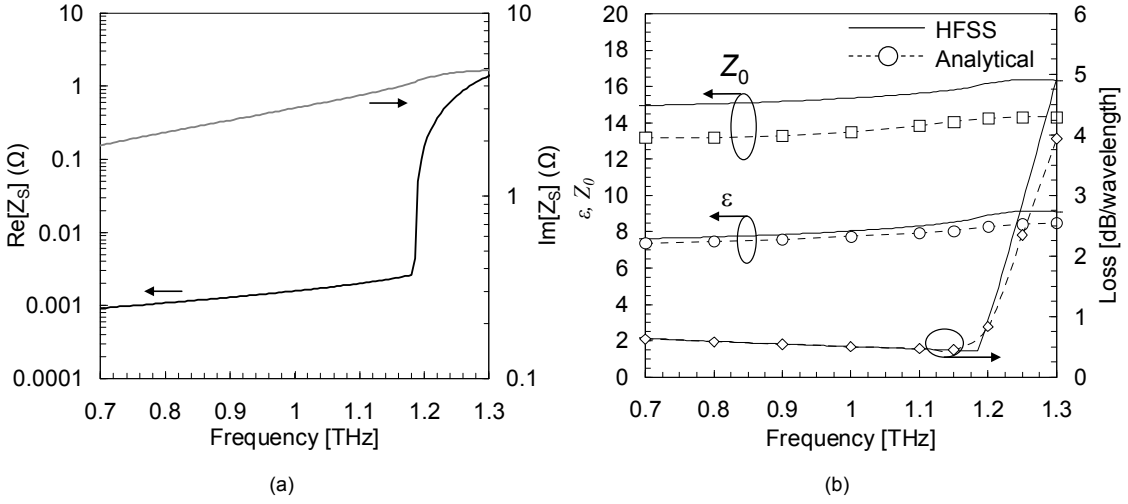

Fig. 2-10 Calculated real and imaginary part of the surface impedance (a) used for the analysis of the microstrip characteristic (b). The solid line and the open symbol indicate the results for analytical calculation and numerical simulation using HFSS, respectively. The complex conductivity for the NbTiN film (T_c = 14.5 K, $2\Delta/e$ = 4.9 mV, ρ = 100 μΩcm) with a thickness of 300 nm is based on the Mattis-Bardeen theory in the extreme anomalous limit, while the surface resistance of the Al (ρ = 0.25 μΩcm) with a thickness of 500 nm is calculated in the local limit.

2.3.4 Power transmission calculation to junctions using transmission matrix

In this section, power transmission method from feed-point to junctions is presented using transmission matrix (***T***-matrix). The calculation is conventional way to estimation the bandwidth and tuning circuit loss, and allows direct comparison with junction coupling measured by Fourier Transform Spectroscopy.

T-matrix is very convenient measure for the calculation of practical microwave networks consisted of a cascade connection of two-port network [8]. The ***T***-matrix is defined for a two-port network in terms of the total voltages and currents as shown in Fig. 2-11 in matrix form:

$$\begin{pmatrix} V_1 \\ I_1 \end{pmatrix} = [T] \cdot \begin{pmatrix} V_2 \\ I_2 \end{pmatrix}, \tag{2-75}$$

where

$$[T] = \begin{bmatrix} A & B \\ C & D \end{bmatrix}. \tag{2-76}$$

For a cascade connection of two-port networks, as a more general case, the ***T***-matrix is given by

$$[T] = [T_1] \cdot [T_2] \cdots [T_N] = \prod_N [T_m]. \tag{2-77}$$

Fig. 2-12 shows the most popular circuit of SIS mixers which is consisted of a quarterwavelength impedance transformer, two junctions, and a tuning line to construct resonance circuit. Let us consider the power transmission coefficient for the circuit from a feed point to each SIS junction. ***T***-matrix $[T_t]$ for a transmission line with characteristic impedance Z_0, length d, and complex propagation constant γ described in previous section is represented by

$$[T_t] = \begin{bmatrix} \cosh(\gamma \cdot d) & Z_0 \sinh(\gamma \cdot d) \\ \dfrac{\sinh(\gamma \cdot d)}{Z_0} & \cosh(\gamma \cdot d) \end{bmatrix}. \tag{2-78}$$

It is well-know that an equivalent circuit of the SIS junction can be represented by a capacitance C_j in parallel with the junction's resistance R_j. In a similar way, since the SIS junction is connected in parallel to the transmission line, then ***T***-matrix $[T_j]$ for the SIS junction is represented by

$$[T_j] = \begin{bmatrix} 1 & 0 \\ 1/Z_j & 1 \end{bmatrix}, \tag{2-79}$$

where $Z_j = (1/R_j + j\omega C_j)^{-1}$.

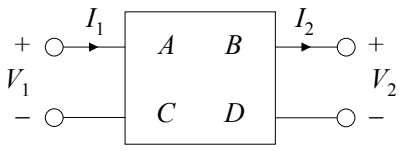

Fig. 2-11 Two-port network related to the current and voltage

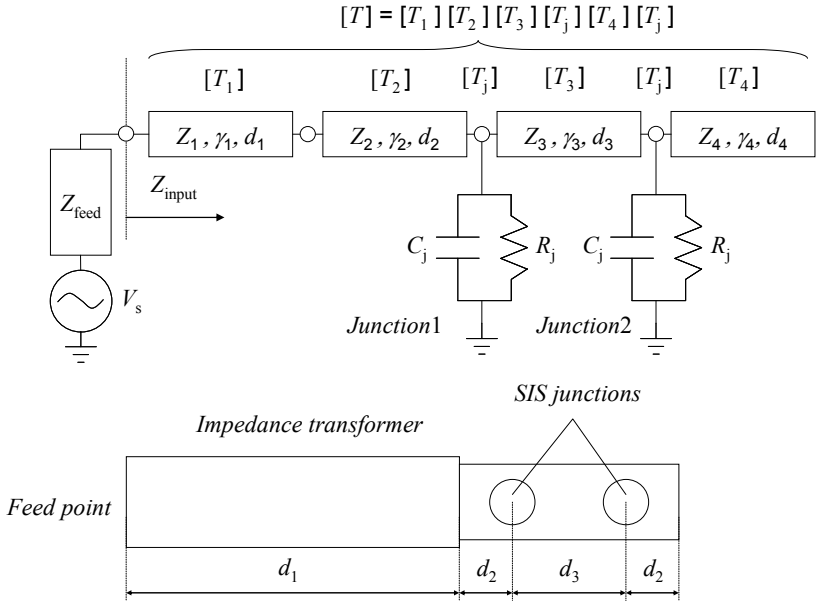

Fig. 2-12 A circuit of an SIS mixer consisted of a quarterwavelength impedance transformer, two junctions, and a tuning line to construct resonance circuit.

For $\alpha << 1$, the junction resistance determined by *I-V* curve is

$$R_{\mathrm{j}} = 1/G_{\mathrm{j}} = \left[\frac{e}{2\hbar\omega}\left(I_{\mathrm{dc}}\left(V_0 + \frac{\hbar\omega}{e}\right) - I_{\mathrm{dc}}\left(V_0 - \frac{\hbar\omega}{e}\right)\right)\right]^{-1}. \qquad 2\text{-}80$$

From eqs.2-78 and 2-79, total ***T***-matrix becomes as follows:

$$[T] = [T_1]\cdot[T_2]\cdot[T_{\mathrm{j}}]\cdot[T_3]\cdot[T_{\mathrm{j}}]\cdot[T_4]. \qquad 2\text{-}81$$

By using components of the matrix, the input impedance on the right side of the circuit seen at the position of the feed point is determined to be

$$Z_{\mathrm{input}} = \frac{[T]_{11}}{[T]_{21}} = \frac{A}{C}, \qquad 2\text{-}82$$

where the subscript indicates the components of the row and column of the total *T*-matrix. If the voltage source at input port is V_{s}, a matrix to define the input current and voltage can be represented by

$$[U] = \frac{1}{Z_{\mathrm{input}} + Z_{\mathrm{feed}}}\begin{pmatrix} V_{\mathrm{s}} Z_{\mathrm{input}} \\ V_{\mathrm{s}} \end{pmatrix}. \qquad 2\text{-}83$$

The voltage across each junction can be calculated to be

$$V_{\mathrm{j1}} = [([T_1]\cdot[T_2])^{-1}[U]]_1, \qquad V_{\mathrm{j2}} = [([T_1]\cdot[T_2]\cdot[T_j]\cdot[T_3])^{-1}[U]]_1. \qquad 2\text{-}84$$

The subscript also indicates the row component of the matrix. Therefore, consumed powers in each junction are

$$P_{\mathrm{j1}} = \frac{\left|V_{\mathrm{j1}}\right|^2}{\mathrm{Re}(Z_{\mathrm{j}})}, \qquad P_{\mathrm{j2}} = \frac{\left|V_{\mathrm{j2}}\right|^2}{\mathrm{Re}(Z_{\mathrm{j}})}. \tag{2-85}$$

The available power of the circuit is

$$P_{\mathrm{avl}} = \frac{V_{\mathrm{s}}^2}{4\,\mathrm{Re}(Z_{\mathrm{feed}})}. \tag{2-86}$$

Thus, dividing eqs.2-85 by eq. 2-86, it can be calculated that the transmission power coefficient is

$$C_{\mathrm{total}} = \frac{P_{\mathrm{j1}} + P_{\mathrm{j2}}}{P_{\mathrm{avg}}}. \tag{2-87}$$

Furthermore the reflection coefficient is given by

$$\Gamma = \frac{Z_{\mathrm{feed}} - Z_{\mathrm{input}}^*}{Z_{\mathrm{feed}} + Z_{\mathrm{input}}}. \tag{2-88}$$

Employing the above calculation method, the loss G_{tune} in the tuning circuit can be included for the mixer gain

$$G'_{\mathrm{mix}} = G_{\mathrm{mix}} \cdot G_{\mathrm{tune}}. \tag{2-89}$$

2.4 Receiver noise measurement

2.4.1 *Y*-factor method and conversion gain measurement

Assuming that the output power of the receiver does not saturate to input signal,

$$P_{\mathrm{out}} = G_{\mathrm{rec}}\left(P_{\mathrm{rec}} + P_{\mathrm{in}}\right), \tag{2-90}$$

where P_{REC}, P_{IN} and G_{REC} are equivalent input noise power for the receiver, input power from a blackbody source and receiver conversion gain. The available power radiated at the surface of the blackbody at a temperature T is given by

$$P = k_{\mathrm{B}} T B, \tag{2-91}$$

where k_{B} is Boltzmann's constant. At high frequencies or low physical temperature, Callen-Welton formula [9] suggested by A.R. Kerr et al [22] is used for the calculation of effective input temperature, which includes Planck's law plus zero-point quantum fluctuations:

$$T_{\mathrm{C\&W}} = \frac{hf}{kT}\frac{1}{e^{\hbar\omega/kT} - 1} + \frac{hf}{2k_{\mathrm{B}}} \tag{2-92}$$

Using the powers from a blackbody source at a temperature of $T_{\mathrm{C\&W,\,hot}}$ and $T_{\mathrm{C\&W,cold}}$ we have

$$P_{\mathrm{out,hot}} = G_{\mathrm{rec}} k_{\mathrm{B}} B (T_{\mathrm{RX}} + T_{\mathrm{C\&W,hot}}) \quad \text{and} \tag{2-93}$$

$$P_{\mathrm{out,cold}} = G_{\mathrm{rec}} k_{\mathrm{B}} B (T_{\mathrm{RX}} + T_{\mathrm{C\&W,cold}}). \tag{2-94}$$

The equivalent input receiver noise temperature is calculated as:

$$T_{\mathrm{RX}} = \frac{T_{\mathrm{C\&W,hot}} - Y T_{\mathrm{C\&W,cold}}}{Y - 1}, \tag{2-95}$$

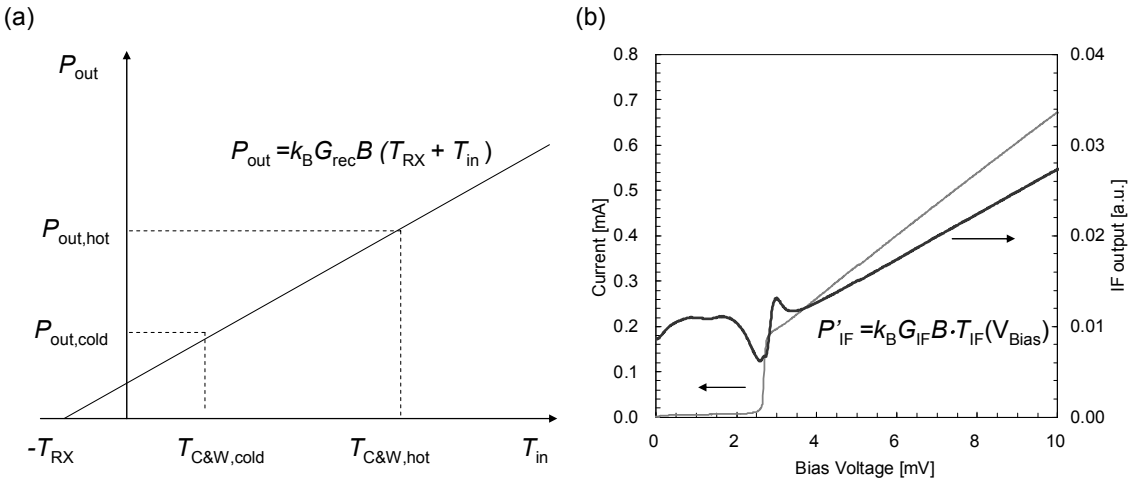

Fig. 2-13 Schematic of (a) *Y*-factor method and (b) shot noise method.

where the Y is defined as the ratio of P_{hot}/P_{cold} and the measurement method is often referred to as the *Y*-factor method. From the measurement, receiver conversion gain can be also found as

$$G_{rec} = \frac{P_{out,hot} - P_{out,cold}}{(T_{C\&W,hot} - T_{C\&W,cold})k_B B} = G_{RF} G_{mix} G_{IF}. \quad 2\text{-}96$$

The receiver conversion gain corresponds to the slope of Fig. 2-13 (a). We can also estimate the mixer conversion gain G'_{mix} containing RF gain G_{RF} (<1, usually) by subtracting the IF gain measured with shot noise method [21][23]. It is calibrated by the linear branch of IF output shown in Fig. 2-13 (b):

$$G_{IF} = \frac{P'_{IF}}{\frac{eB}{2k}\eta}, \quad 2\text{-}97$$

P'_{IF} is the derivative of IF power with respect to dc bias voltage in the linear region beyond the junction's gap voltage, and

$$\eta = \frac{4R_{in}R_{ne}}{(R_{in} + R_{ne})^2}, \quad 2\text{-}98$$

represents the IF coupling efficiency (neglecting the reactive components) with the IF load resistance and the equivalent normal resistance.

2.4.2 Test receiver

Fig. **2-14** shows schematic diagram and photograph of a typical test receiver system. Receiver noise measurements takes blackbody loads at room-temperature (295 K) and liquid-nitrogen-cooled (77 K). The local oscillator (LO) source is an all-solid-state multiplier chain comprising a synthesized microwave signal generator (SG), an active frequency quadrapler (×4) for W-band, an 88–105

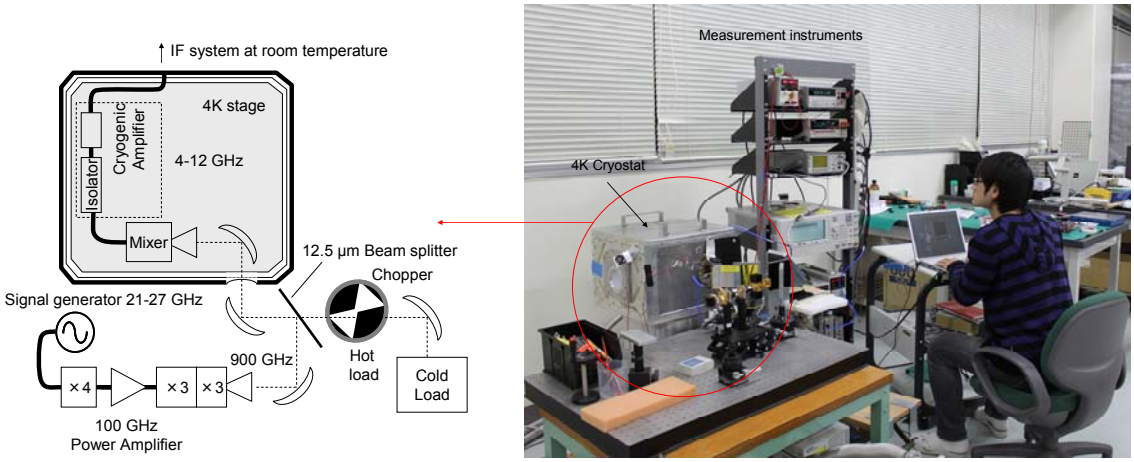

Fig. 2-14 Schematic diagram and photograph of a mixer test receiver.

GHz power amplifier, and a frequency nonupler (×9) for the 0.9-THz band. The LO power and RF signal are quasi-optically combined by a 12.5-μm-thick polyimide beam splitter, radiation then enters the cryostat through a 12.5-μm-thick polyimide vacuum window and a porous Teflon sheet as an infrared filter. The down-converted IF signal is amplified by using a cryogenic HEMT low-noise amplifier having a noise temperature of 5 K over 4–12 GHz.

References

[1] J. R. Tucker and M. J. Feldman, “Quantum detection at millimeter wavelengths,” Rev. Mod. Phys. 57, 1985.

[2] D. C. Mattis and J. Bardeen “Theory of the anomalous skin effect in normal and superconducting metals,” Phys. Rev. 111, 1958.

[3] S. A. Maas, “Microwave Mixers,” Artech House Inc. 1986

[4] K. S. Kundert, and A. S. Vincentelli, “Simulation of Nonlinear Circuits in the Frequency Domain,” IEEE Trans. Comp.-Aided Design of Integrated Circuits and Systems 5 (4), Oct. 1986.

[5] N. R. Werthamer, “Nonlinear Self-Coupling of Josephson Radiation in Superconducting Tunnel Junctions,” Phys. Rev. 147, 1966.

[6] A. H. Dayem and R. J. Martin, “Quantum Interaction of Microwave Radiation with Tunneling Between Superconductors,” Phys. Rev. Lett. 8 1962.

[7] P. K. Tien and J. P. Gordon, "Multiphoton Process Observed in the Interaction of Microwave Fields with the Tunneling between Superconductor Films," Phys. Rev. 129, 1963.

[8] D. M. Pozar, "Microwave Engineering 3rd edition," WILEY, 2003.

[9] H. B. Callen and T. A. Welton, "Irreversibility and Generalized Noise," Phys. Rev. 83 (1),1951

[10] High Frequency Structure simulator, http://www.ansoft.com/

[11] C.-Y.E. Tong, R. Blundell, S. Paine, D.C. Papa, J. Kawamura, Xiaolei Zhang, J.A.Stern, H.G. LeDuc, "Design and characterization of a 250-350-GHz fixed-tuned superconductor-insulator-superconductor receiver," IEEE Trans. Microwave Theory and Tech., 44 (9), Sep. 1996.

[12] Y. Uzawa, "Study on Quasi-Optical SIS Mixers with NbN/AlN/NbN Tunnel Junctions in the Submillimeter-Wave Band, " Phd thesis in Tokyo Institute of Technology. 2000.

[13] K. C. Gupta, R. Garg, and I. J. Bahl, Microstrip Lines and Slotlines, Artech House: Dedham, MA, 1979.

[14] R. L. Kautz, Picosecond pulses on superconducting striplines, J. Appl. Phys. 49 (1), 1978.

[15] A. B. Pippard, "An Experimental and Theoretical Study of the Relation between Magnetic Field and Current in a Superconductor," Proc. Royal Society of London. Series A, Mathematical and Phys. Sciences, 216 (1127), 1953.

[16] G. E. H. Reuter and E. H. Sondheimer, "The Theory of the Anomalous Skin Effect in Metals," Proc. Royal Society of London. Series A, Mathematical and Physical Sciences 195 (1042),1948.

[17] M. Schicke, "Superconducting Mixer Elements for Terahertz Frequencies", PhD thesis in University of Hamburg, 1998.

[18] A. R. Kerr, "Surface Impedance of Superconductors and Normal Conductors in EM Simulators", Electron. Division Internal Report No. 302, NRAO, February 1996. Available also as MMA Memo #245, http://www.alma.nrao.edu/memos/html-memos/abstracts/abs245.html.

[19] W. Shan, S. Shi, T. Matsunaga, M. Takizawa, A. Endo, T. Noguchi, and Y. Uzawa, "Design and Development of SIS Mixers for ALMA Band 10," IEEE Trans. Appl. Supercond. 17 (2), 2007.

[20] V. Belitsky, C. Risacher, M. Pantaleev, V. Vassilev, "Superconducting Microstrip Line Model Studies At Millimetre And Sub-millimetrewaves," Int. J. Infrared and Millimeter Waves 27 (6), 2007.

[21] W. Shan, T. Noguchi, S. Shi, and Y. Sekimoto, "Design and Development of SIS Mixers for ALMA Band 8," IEEE Tran. Appl. Supercond., 15 (2), 2005.

[22] A. R. Kerr, M. J. Feldman and S.-K. Pan, "Receiver Noise Temperature, the Quantum Noise Limit, and the Role of the Zero-Point Fluctuations," 18th Int. Symp. on Space THz Tech., March 25-27, 1997.

[23] D. P. Woody, R. E. Miller, and M. J. Wengler, "85–115-GHz Receivers for Radio Astronomy," IEEE Trans. Microwave Theory Tech., 33 (2), 1985.

Chapter 3
Material selection and feasibility study on SIS mixers for the ALMA band 10

3.1 Overview

This chapter provides a brief overview of material's selection and better combination, circuit selection and its fabrication for the terahertz waveguide SIS mixer. It is well-known that the waveguide SIS mixer is the most important component, which consist of input waveguides, an antenna probe doubled with transition to microstrip mode, tuning circuits, SIS junctions, and IF circuits, because it dominants the performance of the low-noise receiver. In eq. 1-7, the SIS mixer performances are defined by T_{mix}, G_{mix}, and G_{tune}. T_{mix} and G_{mix} are determined by SIS junction properties, such as nonlinearity of the *I-V* curve and leakage current, and the embedding circuits. The Ohmic loss G_{tune} in the tuning circuit which might be included in G_{RF} strongly depends on film properties and combination of the material. In addition, the input loss not only increases the receiver noise temperature but also forces the apparent bandwidth of noise temperature narrower, unlike bandwidth determined by *Q* of resonance circuit in this case.

Unfortunately, the performance of well-established Nb-based SIS mixers is degraded at the frequency of above 0.7 THz due to two factors: (a) Firstly a drop of the mixer performance the T_{mix} and G_{mix}, because n=1 and n=2 photon steps completely overlap above 0.7 THz, while the upper limit for SIS mixers using Nb junction is 1.4 THz in principle, twice the gap frequency [1]. In addition, the mixer can only be operated at a limited bias voltage of $V > \hbar\omega/e - V_g$ because of the overlapping n=1 photon step from the negative branch. (b) Secondly, increase of the RF losses G_{tune} in their tuning circuits significantly due to the onset of pair-breaking above the Nb gap frequency. Hence it is no longer available for well-established *all*-Nb SIS mixer technologies at this frequency. It would be, therefore, needed to verify the performance and limitation for each junction and microstrip line, and to select the best combination of material out at this frequency.

3.2 Practical application limitation of SIS junctions

We investigated mixing properties for three SIS junctions as the candidate of terahertz mixing element as follows:

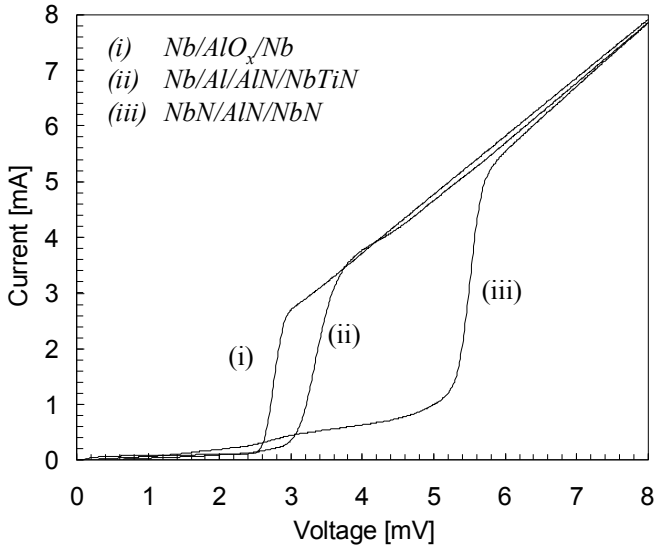

Fig. 3-1 Three current-voltage characteristics of (i) Nb/AlO_x/Nb, (ii) Nb/Al/AlN/NbTiN, and (iii) NbN/AlN/NbN junctions. Those referred to a typical experimentally-result for the Nb-based junction fabricated in our laboratory, to one for the NbN-based junction in NiCT [4], and to the paper of **[5]** for the NbTiN-based junction in JPL. The normal state resistances were set to 10 Ω

(i) Nb/AlO_x/Nb (Nb-based) junction:

The commonly used and well-established junctions having the gap voltage about 2.8 mV allowing building sensitive receivers up to the frequency of about 1.1 THz.

(ii) Nb/Al/AlN/NbTiN (NbTiN-based) junction

Junction having the gap voltages of 3.3-3.6 mV that promising results are reported at the 1.1–1.3 THz [5][9].

(iii) NbN/AlN/NbN (NbN-based) junction

Junction expected as promising device above 1 THz to 2.8 THz because of having the gap voltage of 5.6 mV, and that superior performance are demonstrated at the 0.5 and 0.8 THz [2]-[4].

SSB receiver noise temperature and SSB conversion gain was simulated for the mixers using quasi-five-port model based on Tucker's quantum theory of mixing, at frequencies up to 2.5 THz. As a typical example, the *I-V* curve of the junctions used for the simulation is shown in Fig. 3-1. Those referred to a typical experimentally-result for the Nb-based junction fabricated in our laboratory, to one for the NbN-based junction in NiCT [4], and to the paper of [5] for the NbTiN-based junction in JPL. The normal state resistances were set to 10 Ω. It was assumed that the junction capacitance was tuned out, and the embedding and IF load conductances seen by the intrinsic SIS junction were $1/R_j$ and 1/50 Ω^{-1} at each simulation, respectively. The noise temperature of an IF chain was 10 K at 8

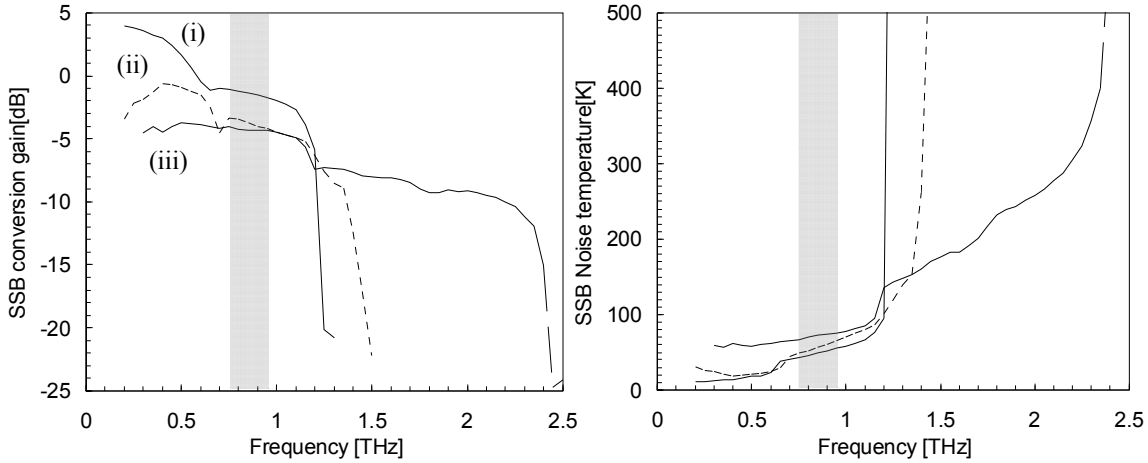

(a) (b)

Fig. 3-2 Simulated (a) receiver noise temperatures and (b) conversion gains for each junction at a physical temperature of 4.2 K. The gray zone indicates the frequency range of ALMA band 10.

GHz. The pumping parameter α was fixed to be 0.8 and bias voltage was optimized at each frequency. The resulting receiver noise temperatures and conversion gains at a physical temperature of 4.2 K are shown in Fig. 3-2. The simulation suggested that the Nb-based junction achieved the highest gain, while the NbTiN- and NbN-based junctions were not so high in the frequency range of the ALMA band 10. The higher gain of the Nb-based junction is attributed to the stronger rising current at gap voltage compared to that of the NbTiN-based junction, while both leakage currents is not so different. Since the NbN-based junction has slope due to the leakage current in the subgap current region, the slope makes it low the dynamic resistance and then difficult to obtain high conversion gain. Regarding their receiver noise temperature, there is slight difference within about 20 K among the junctions, but that of the Nb-junction is still better. Note that the noise is not including input loss, which increases their noise temperature entirely. In addition, as discussed in later section 3.5, SIS junctions having a larger gap voltage are needed to achieve relatively high current density to obtain the wider bandwidth. Thus, the performance of Nb-based junction might be reasonably good for the ALMA Band 10 because of advantages of low noise temperature, established fabrication, and moderate current density.

3.3 Material selection for tuning circuit

For the terahertz transmission line, NbN and NbTiN having the gap frequency above 1 THz is the most promising superconducting material. Their films should be deposited directly on a substrate as ground plane to obtain ideal superconducting properties unlike wiring layer, because their properties on dielectric layer, such as SiO_2, can be degraded [6]. Accordingly, we evaluated the attenuation of several microstrip lines consisted of different materials combination, which are practically expected to achieve low-loss transmission for the terahertz frequencies as follows:

(a) Nb/SiO_2/Nb (M-I): commonly used microstrip up to 0.7 THz, e.g. [1], [6].

(e) NbTiN/MgO/NbN (M-II): a full epitaxial superconducting film [2]–[4].

(b) NbTiN/SiO_2/Al (M-III): taken at the frequencies of 0.8-1.1 THz e.g. [7],[8].

(c) Nb/SiO_2/Au (M-IV): using epitaxial Nb films [5], [9]

(f) Al/SiO_2/Al (M-V): normal metal microstrip [10]–[12].

The calculation was taken into account parameters summarized in Table 3-I and performed as based on Mattis-Bardeen theory described in chapter 2. The characteristic impedance of the microstrip line is 15 Ω. Fig. 3-3 shows the calculated attenuation of five types of microstrip lines as a function of frequency. As predicted by theory, the loss of M1 microstrip increases rapidly above 0.7 THz because of the pair-breaking, so it is no longer available at the terahertz frequency. For the ALMA Band 10 mixer design centered at the frequency of 0.87 THz, NbTiN/SiO_2/Al or NbTiN/MgO/NbN microstrip line should be used because the lower attenuation can be theoretically achieved to be 0.52 dB/wavelength or close to 0 dB/wavelength, respectively.

Table 3-I Resistivity at 4.2 K for the normal conductor and gap frequency and normal state resistivity for the superconductor to estimate the microstrip loss. ρ of Au, Nb-a (typical) and Nb-b(epitaxial) were assumed from [14], [5] and [13].

Material	F_{gap} [THz]	ρ [μΩ cm]
Al	-	0.25
Au	-	0.22
Nb-a	0.7	6.4
Nb-b	0.7	0.3
NbTiN	1.2	100
NbN	1.4	50

Table 3-II Material Parameters used for the calculation of the microstrip attenuation

	Ground plane (270 nm thick)	Dielectric layer (300 nm thick)	Wiring layer (500 nm thick)	Highest application Frequency [THz]
M-I	Nb-a	SiO_2 ($\varepsilon_r = 4.4$)	Nb-a	0.7
M-II	NbN	MgO ($\varepsilon_r = 9.8$)	NbTiN	1.2
M-III	NbTiN	SiO_2	Al	1.2
M-IV	Nb-b	SiO_2	Au	-
M-V	Al	SiO_2	Al	-

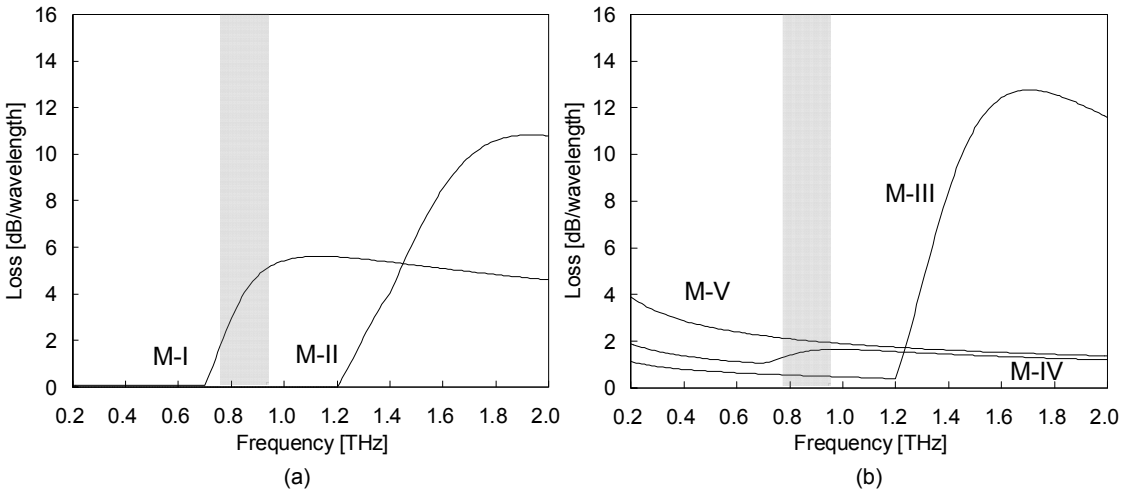

Fig. 3-3 Calculated attenuation of five types [(a) superconductor only and (b) superconductor with normal metal] of microstrip lines as a function of frequency.

If NbTiN/SiO_2/Al microstrips are used for the tuning circuit with Nb-based junction, the loss G_{tune} in the tuning circuit is 1.9 dB and 2.5 dB better compared to those in Nb/SiO_2/Au and Al/SiO_2/Al microstrip from the feed point to the junctions. Meanwhile, it is reported that all-superconducting NbTiN/MgO/NbN configuration can not be applied for Nb-based junction due to the occurrence of junction heating [15] . B. Leone et al described the heating as a trapping of heat in the junction caused by the geometrical arrangement of the different materials constituting the mixer [16]. The heating causes backbending of *I-V* curve and is also believed to degrade the mixer performance. Hence, NbTiN/MgO/NbN configuration is applicable only for NbN-based junction. As mentioned in previous section, receiver noise temperature of NbN-based junction is slightly higher, and higher current density junction is needed. In conclusion, the combination of NbTiN/SiO_2/Al microstrip with the Nb-based junction would be promising for the ALMA Band 10.

3.4 Suitable tuning circuit for the ALMA band 10

An SIS junction has large geometric capacitance which can shunt the RF signal. Thus tuning circuits are necessary to tune out the junction capacitance and to match the junction impedance to the antenna impedance. Unfortunately, since the NbTiN/SiO_2/Al microstrip lines have Ohmic losses, short matching circuit as possible must be designed, e.g. one section impedance transformer. So far, three types of tuning circuits mainly have been suggested and used for SIS mixers as shown in Fig. 3-4: (a) End-loaded, (b) RF-shunted capacitor, and (c) twin-junction. Of them, it is well-known that the twin-junction resonance circuit whose detailed description is given by J. Zmuidzinas et al [23], namely parallel-connected-twin-junction (PCTJ) [24], has advantages in broader bandwidth, easier matching to antenna impedance, and better peak coupling for the case of using lossy material [25]. The PCTJ is composed of two parallel-connected SIS junctions at the two ends of an inductive superconducting microstrip line that compensates for the geometric capacitance of SIS tunnel junctions at a desirable frequency. The quantum mixing theory was applied for the twin-junction by S. C. Shi et al [26]. We adopted the twin junctions tuning circuit for the band 10 mixer, investigated the characteristics theoretically and experimentally in detail. The design method will be described in chapter 5.

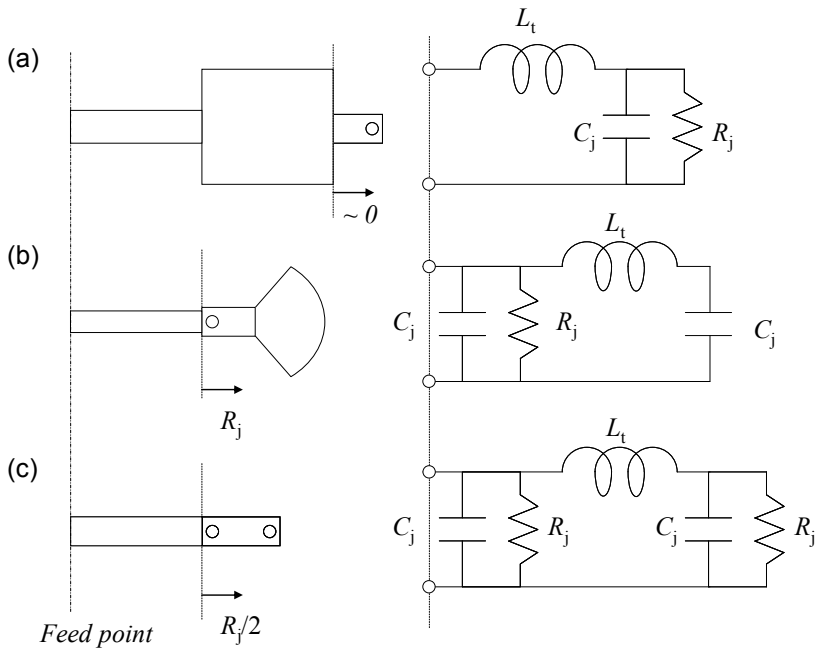

Fig. 3-4 Schematic and equivalent circuit for three types of the tuning circuit (a) End-loaded, (b) RF-shunted capacitor, and (c) twin-junction. Dashed line indicates boundary between the impedance and the resonance circuit.

3.5 RF bandwidth and optimum Junction current density

In general, the bandwidth of resonance circuit is characterized by Q-factor (= $f_0/\Delta f$). When the SIS junction capacitance is tuned out by an external inductance, the Q-factor of the resonance circuit is related to the $\omega R_N C_j$ product, where the ω, R_N, and C_j are angular frequency, normal state resistance and specific capacitance, respectively. As discussed in later chapter 5, the bandwidth of receiver noise temperature is not simply determined only by the $\omega R_N C_j$ product for this frequency at least, but the product is still important indicator to characterize the SIS junction. The $\omega R_N C_j$ product is related to the junction current density, which is evaluated with the gap voltage V_{gap} and tunnel resistivity $R_N A$:

$$J_c = \frac{\pi}{4}\frac{V_{gap}}{R_N A}. \qquad 3\text{-}1$$

Q-factor, i.e. the $\omega R_N C_j$ product can be represented as a function of J_c.

$$\omega R_N C_j = \omega(R_N A)C_s = \omega\left(\frac{\pi}{4}\frac{V_{gap}}{J_c}\right)C_s, \qquad 3\text{-}2$$

where C_s is specific capacitance depending on the J_c and is estimated to be

$$C_s = \frac{1.33 * 10^{-14}}{0.2 - 0.043\log(J_c 10^{-7})}, \qquad 3\text{-}3$$

for Nb/AlO_x /Nb junction with J_c = 0.1 to 18 kA/cm^2,

$$C_s = 71\times 10^{-3}(J_c 10^{-7})^{0.16}, \qquad 3\text{-}4$$

for NbN/AlN/NbN junction with J_c more than 15 kA/cm^2 [19].

The junction dependence of the eq. 3-3 is assumed on the basis of ref. [18], with a scale factor of 1.33 used to yield a specific capacitance of 85 fF/μm^2 for a current-density of 10 kA/cm^2, as well as ref. [17]. From the eq. 3-2 , it is found that the junction coupling bandwidth is approximately proportional to $V_{gap}C_s/J_c$. This implies that higher J_c, that is, thinner junction is needed with frequency. Besides, since the NbN/AlN/NbN junction has about twice larger gap voltage to Nb junction, the J_c should be about two to three times higher than that of the Nb/AlO_x/Nb junction to achieve the same bandwidth from the eqs. 3-2, 3-3, and 3-4. Conversely, the Nb/AlO_x/Nb junction has the advantage regarding J_c as well.

In terms of the optimum $\omega R_N C_j$, Kerr et al proposed a rule $\omega R_N C_j = 400/f$ (GHz) [20], but then a frequency-scaled 500 GHz SIS mixer should have $J_c > 50$ kA/cm^2, much higher than can be conveniently fabricated. In contrast, this rule does not seem to reflect actual experimental results for submillimeter mixers, e.g. [21] and Q. Ke and M. Feldman claims GR_N is only weakly dependent upon frequency for high frequency SIS mixers [22]. Obviously, the low product, i.e. high J_c makes it possible to achieve the wide bandwidth and to reduce the tuning circuit loss. However, too high J_c

junction may result in the saturation, harmonics generation which causes degradation of the conversion efficiency, and increasing noise due to enhanced shot noise. Therefore, optimum J_c should be chosen. Our theoretical and experimental results suggested that the optimum J_c of the Nb/AlO_x/Nb junction at the 0.9 THz band was 10 to 15 kA/cm^2 which yields the $\omega R_N C_j$ of 7 to 10, combined with the consideration of the easier fabrication as discussed in next section.

3.6 SIS mixer fabrication

This section provides a brief overview of fabrication process for the Nb-based SIS junction mixer in combination with higher-gap superconductors and low-resistivity normal metals for the embedding circuit. Such a hybrid structure might make the fabrication process complicate and difficult, compared to all-Nb mixers, cause degradation of the SIS junction quality. For the higher-gap superconductors, nitride compounds such as NbN or NbTiN have been used as bottom layer on a substrate. Unlike NbN, NbTiN has the advantage that films with decent quality can be obtained using conventional types of substrates, such as quartz. Quartz with its low dielectric constant (ε_r = 4) and relatively good mechanical stability is the most widely used substrate for waveguide type SIS mixers. On-chip hybrid structures consisting of Nb/AlO_x/Nb SIS junctions and an NbTiN/SiO_2/Al microstrip line yield state-of-the-art performance and look like the most promising option for the ALMA-Band 10 receiver as described in sections of 3.2 and 3.3. One possibility for further improvement might be to perform either deposition at elevated temperature, employing buffer layers or using single-crystalline MgO as a substrate, with the latter enabling epitaxial growth of these materials. A fabrication process for SIS junctions and films that use epitaxial NbN technology on an MgO substrate has been developed in National Institute of Information and Communications technology (NiCT). The epitaxially-grown NbTiN films on MgO have advantages of higher critical temperature and conductivity, nearly perfectly smooth surface, and weak dependence of electrical parameters on deposition condition. On the other hand, the one possible problem is that MgO has a relatively large dielectric constant of about 10, requiring very thin substrates for the mixer chips. In this section, film quality and fabrication process are summarized as the basis on refs. [26], [28], and [31]

3.6.1 Film properties for superconductor and normal conductor

3.6.1.1 Fabrication of NbTiN films on fused quartz substrate

This section reports investigation and optimization of electrical properties for NbTiN films on fused quartz substrates. It is known that the film properties on fused quartz substrates have significantly dependence on the deposition condition, and influence SIS mixers sensitivity near its gap frequency [30]. One of the possibilities for further improvement of ρ_{20K} and T_c is deposition at

Target: NbTi (Nb:100, Ti:20 in weight)
Size: 8 inch
Base pressure: > 2 x 10^{-5} Pa
Ar: N_2 = 100:36 sccm
Pressure: 2 mTorr
Bias current: 4 A
P.D.: 4.6 W/cm^2

Fig. 3-5 DC magnetron sputtering machine for the deposition of NbTiN films in NiCT and typical deposition condition.

an elevated temperature, e.g. 400 °C [29][30]. However this might cause increase of stress, which makes it difficult to fabricate high quality SIS junction on the film. Our approach optimizes the deposition condition yielding low ρ_{20K} and high T_c at room temperature. The optimization process has been established by M. Takeda (of Sizuoka university at present) et al using facilities of NiCT located in Kobe [27] and is summarized in Appendix D. The NbTiN film is deposited by DC magnetron sputtering (see Fig. 3-5) using 8-inch-NbTi target onto a 3 inch fused quartz substrate. The compounding ratio of the target is 100 in Nb and 20 in Ti in weight.

3.6.1.2 Fabrication of epitaxial NbTiN films on single-crystal MgO substrate

The NbTiN films are deposited on MgO substrates in the same condition (Fig. 3-5) as the one for the fused quartz substrates at ambient temperature, because it has little dependence on deposition conditions. The properties of the epitaxial-grown film are discussed in later section. MgO substrate takes a role as dielectric material to construct circuits of waveguide-microstrip transition and choke filter. In order to design more accurately and to know the loss, the complex dielectric constant of MgO substrate was measured by using THz Time-Domain Spectrometer (THz-TDS) system, which can simultaneously determine the amplitude and phase information of samples from transmission or reflection measurements [32]. The transmission measurements were done in the frequency range of 0.1-4.0 THz at room temperature and at 5 K. The signal to noise ratio of the system is about 10000 and the spectral resolution is 10 GHz. As shown in Fig. 3-6, the refraction index was measured to be 3.1 which corresponds to a relative dielectric constant of 9.8 at the band 10 frequency [33]. The result would suggest that it is available up to 2.5 THz at least because of the low dielectric loss of the MgO substrate which will have insignificant effect on mixing properties.

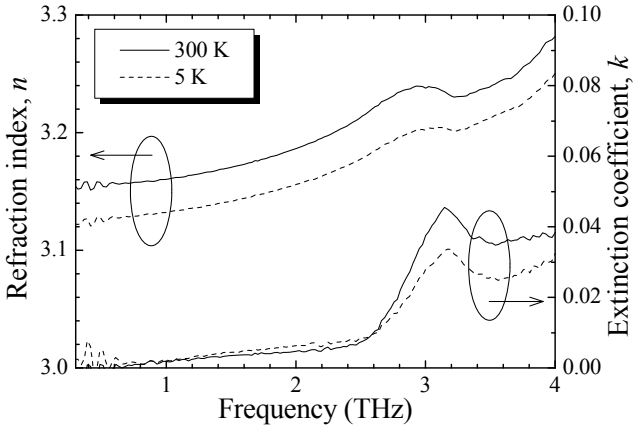

Fig. 3-6 Complex refractive index of MgO substrate at room temperature and 5 K measured by M. Takeda using Terahertz Time-Domain Spectrometer.

3.6.2 X-ray diffraction patterns

In order to confirm the crystal properties of the NbTiN films on the fused quartz and single-crystal MgO, X-ray diffraction (XRD) patterns were measured [28]. Fig. 3-7 presents measured typical XRD patterns reflecting those crystal properties. In the film deposited on the MgO substrate, strong (200) peaks were obtained for the NbTiN film and MgO substrate, indicating that the NbTiN film could be epitaxially grown on the MgO substrate. The lattice constant of the NbTiN films was found

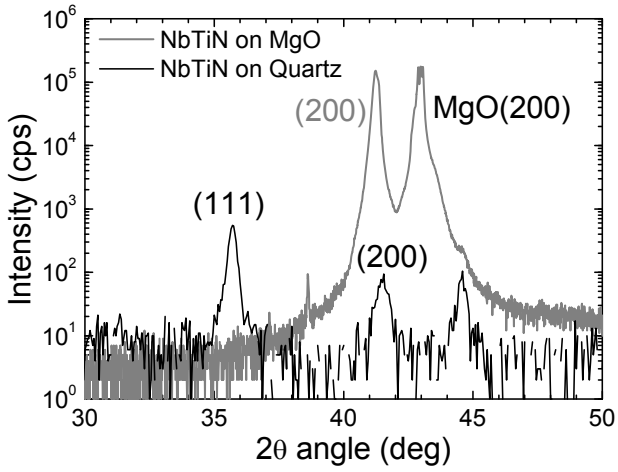

Fig. 3-7 XRD patterns of NbTiN films deposited on MgO and fused quartz substrates. Solid line is for the film deposited on MgO substrate and dashed line is for the film deposited on fused quartz substrate.

to be 0.438 mm and the lattice mismatch between the NbTiN film and the MgO substrate was approximately 4 %. In contract, the film deposited on the fused quartz showed some weak XRD patterns, indicating that the film was polycrystalline.

3.6.3 Resistance-temperature characteristic and residual resistance ratio

According to Mattis-Bardeen theory [34], it is generally accepted that electrical important parameters for superconducting films are transition temperature T_c and normal resistivity ρ_{20K} relating to gap frequency and surface impedance, respectively. Fig. 3-8 presents the best Resistance-Temperature (R–T) characteristics of those NbTiN films. T_c and ρ_{20K} residual resistance ratio RRR (=R_{300K} /R_{20K}) were obtained to be 14.8 K, 52 μΩcm and 1.18 in an epitaxial NbTiN film, and were 14.5 K, 80 μΩcm and 1.10 in an poly-crystal NbTiN film, respectively (Note that an used NbTi target is changed from one in sections 3.6.1). Combined with their measured properties, these results infer their films are very high quality despite of the ambient deposition. Besides, it was found that stress of these films is not strong: this might offer improvement for a yield and quality of Nb junctions.

3.6.4 Properties of Al films

Evaporated Al films which are used as wiring layer are deposited by e-gun evaporation (EIKO EB-5033) in an UHV vacuuming chamber. Typical RRR and conductivity σ_{4K} at 4 K are 10-15 and 4×10^8 $\Omega^{-1}m^{-1}$ for a 500-nm-thick film deposited on sputtered SiO_2 which is chosen to ensure good step coverage and minimize dc resistance [31][30].

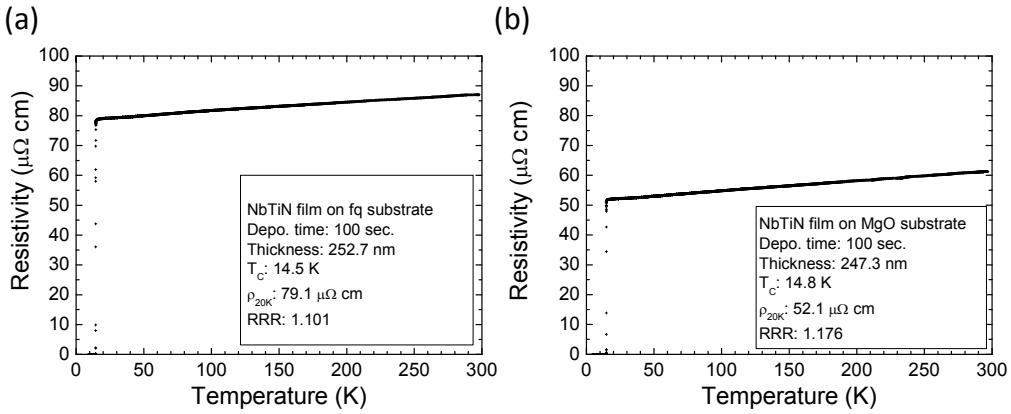

Fig. 3-8 Resistivity of NbTiN films on (a) fused quartz substrate and on (b) MgO substrate as a function of temperature.

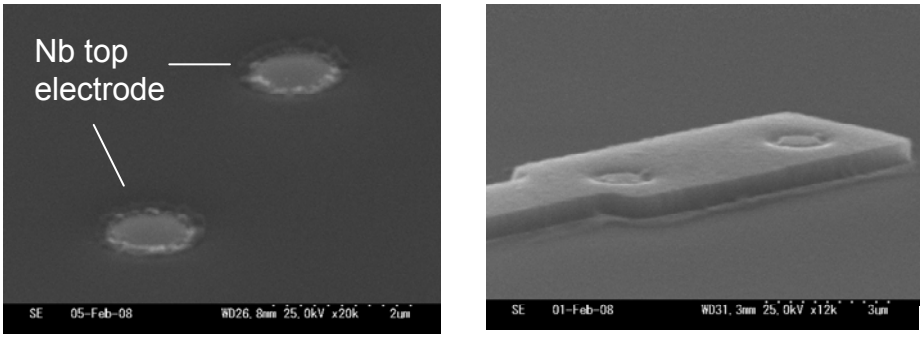

Fig. 3-9 Left: Twin-junctions after SiO_2 lift-off (nominal diameter ϕ =1 μm). Right: The tuning section after Al lift-off.

3.6.5 Sequence of process steps

The sequence of process steps is described by M. Kroug in detail [31]. There are two important differences in the type of equipment that is used: Optical lithography is done with an i-line (365 nm) stepper which offers excellent control over resist pattern sizes down to 0.5 μm and an overlay accuracy of about 40 nm [35]. The short time required for alignment *and* exposure, usually a few minutes, is a great advantage over the use of either a contact mask aligner or e-beam lithography. The second difference is the introduction of an ICP etcher for junction definition to our fabrication.

All devices are fabricated on double-side polished 300-μm-thick quartz wafers having a diameter of 35 mm, or on 400-μm thick single-crystal MgO wafers of square 20 mm on a side. Fabrication starts with deposition of a 270 nm thick NbTiN layer by reactive magnetron sputtering, as described in section 3.6.1. The ground plane pattern is defined by etching NbTiN in a $5\%O_2/SF_6$ plasma. In the next step a standard Nb/Al-AlO_x/Nb trilayer (100 nm/8 nm/100 nm) is deposited covering the whole wafer. Junction definition is based on a self-aligned process: The photoresist pattern first serves as an etching mask and subsequently for lift-off of the dielectric. A *single-step* etching process is used to remove the entire trilayer. NbTiN layer and junctions are doubly passivated, first by anodization up to a voltage of 12 V, then 300 nm SiO_2 are deposited by rf magnetron sputtering and subsequently lifted off. For wiring, a lift-off mask is patterned, 500 nm Al is deposited by e-gun evaporation and then lifted off. Micrographs show results of the last two process steps in Fig. 3-9 and the process is summarized in Fig. 3-10

.

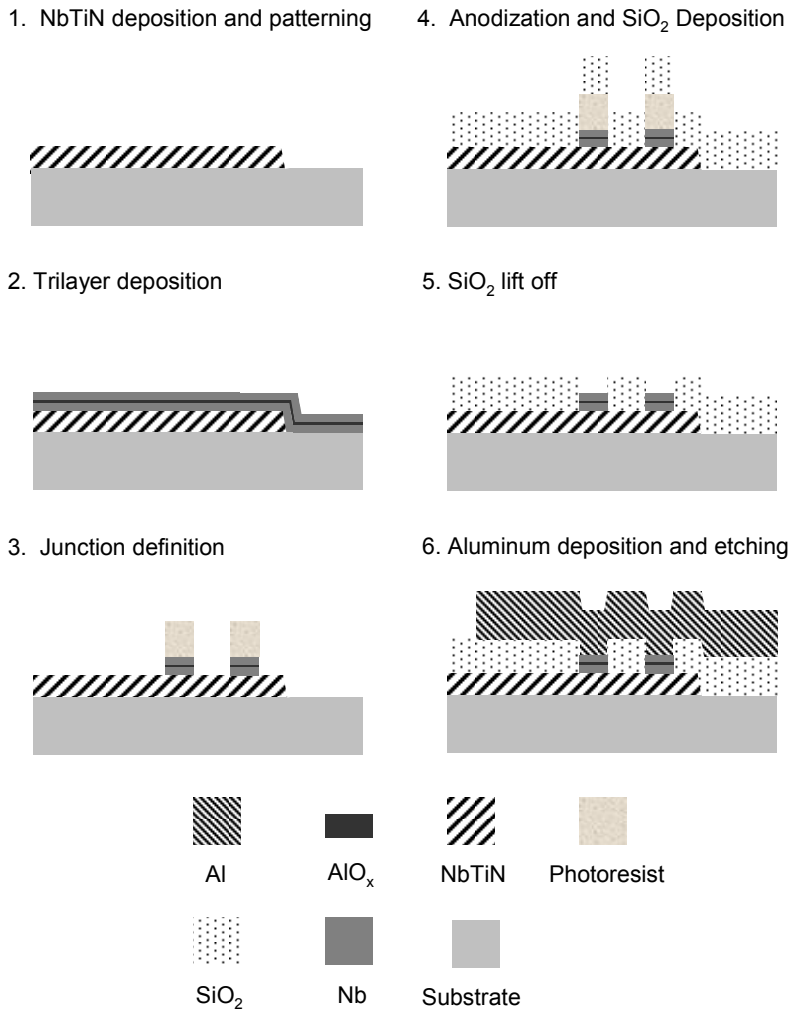

Fig. 3-10 Sequence of process steps

3.6.6 Mixer chip fabrication

The method used to fabricate the mixer chip is shown in Fig. 3-12. After the junction fabrication process, the MgO or quartz wafer are cut from the surface using a DISCO dicing machine. The dicing blade is with a thickness of 25 μm. As the wafer is cut to a depth of 70 μm, the shape of the blade does not appear in the cutting plane. The cut wafer is glued upside down on a lapping holder and its backside is then polished down to a design thickness of 25 μm (MgO) or 40 μm (quartz) using a Multiprep lapping machine. The polishing starts with a diamond lapping film with a rough grain. The polishing rate is then gradually lowered from 3 μm/min., and is finally performed with high accuracy at a rate of 0.4 μm/min. We are now able to fabricate the mixer chip with an accuracy of around 5 μm in the width and thickness.

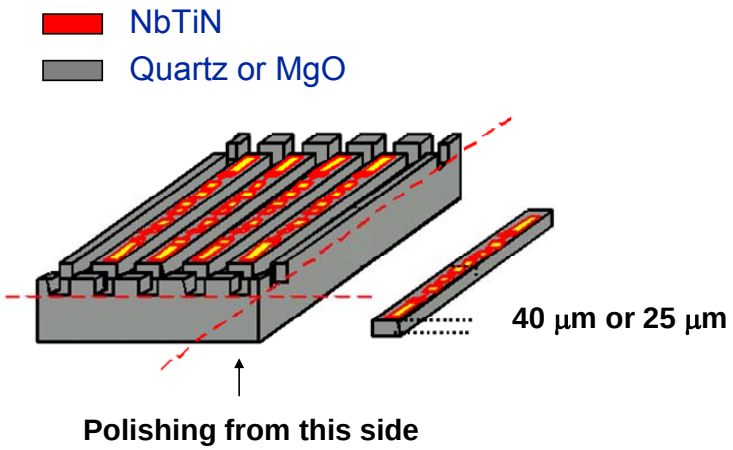

Fig. 3-12 Method used to fabricate mixer chip

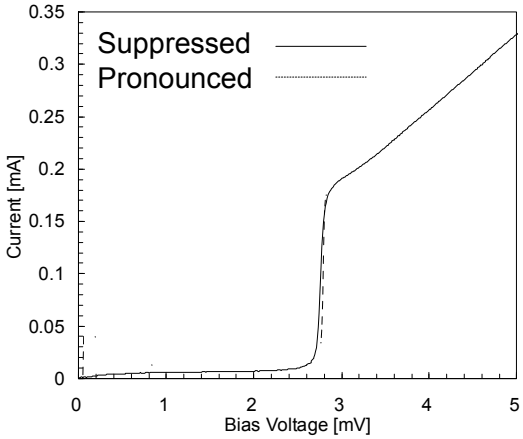

Fig. 3-11 Current-voltage characteristics of a twin junction, nominal junction diameter 1 μm, current density 8 kA/cm^2 (solid line). A self resonance step by a tuning circuit is pronounced by adjusting a magnetic field applied to the junction (dashed line).

3.7 Current-voltage characteristics and resonance step

Fig. 3-11 shows current-voltage characteristics and a self-resonance step by a tuning circuit. Device with good junction quality factor R_{sg}/R_N, which is defined as ratio of normal resistance and subgap resistance at a bias voltage of 2 mV, have been obtained to be around 20 for several batches with current densities between 6.5-10 kA/cm^2. The resonance step was observed in the position of 1.8 mV, which corresponds to 0.87 THz. For higher current density junction, the quality drops quickly and fabrication yield is low.

References

[1] P. Febvre, M. Salez, W. R. McGrath, B. Bumble, and H. G. LeDuc, “Performance limitations of niobium-based submillimeter-wave quasiparticle mixers operating near the gap frequency,” Appl. Phys. Lett. 67 (3), 1995.

[2] J. Li, M. Takeda, Z. Wang, S. Shi, and J. Yang, “Low-noise 0.5 THz all-NbN superconductor-insulator-superconductor mixer for submillimeter wave astronomy,” Appl. Phys. Lett. 92, 2008.

[3] W. Shan, M. Takeda, T. Kojima, Y. Uzawa, S. Shi, and Z. Wang, “Design and Performance of Waveguide Mixers with All NbN tunnel junctions on MgO substrates,” Proc. 19th Int. Symp. on Space THz Technology, Groningen, 28-30 Apr. 2008.

[4] M. Takeda, W. Shan, T. Kojima, S. Saito, M. Kroug, Y. Uzawa and Z. Wang, “Low-noise waveguide SIS mixer with NbN/AlN/NbN tunnel junctions tuned by an NbN/MgO/NbTiN microstrip circuit,” Supercond. Sci. Technol. 22, 2009.

[5] A. Karpov, D. Miller, F. Rice, J. A. Stern, B. Bumble, H. G. LeDuc, and J. Zmuidzinas, ”Low Noise 1 THz–1.4 THz Mixers Using Nb/Al-AlN/NbTiN SIS Junctions,” IEEE Trans. Appl. Supercond., 17 (2) 2007.

[6] C. F. J. Lodewijk, T. Zijlstra, S. Zhu, F. P. Mena, A. M. Baryshev, and T. M. Klapwijk, ”Bandwidth Limitations of Nb/AlN/Nb SIS Mixers Around 700 GHz,” IEEE Trans. Appl. Supercond, 19 (3), 2009.

[7] B. D. Jackson, G. de Lange, W. M. Laauwen J. R. Gao, N. N. Iosad and T. M. Klapwijk, “NbTiN/SiO2/NbTiN and NbTiN/SiO2/Al tuning circuits for 1 THz waveguide SIS mixers,” Proc. 11th Int. Symp. on Space THz Technology, University of Michigan Ann Arbor, Michigan, May 1-3, 2000.

[8] Y. Uzawa, Zhen Wang, and Akira Kawakami, “Terahertz NbN/AlN/NbN with Al/SiO/NbN microstrip,” Appl. Phys. Lett. 73. 680, 1998.

[9] A. Karpov, D. Miller, J. A. Stern, B. Bumble, H. G. LeDuc, and J. Zmuidzinas, “Development of Low Noise THz SIS Mixer Using an Array of Nb/Al-AlN/NbTiN Junctions,” IEEE Trans. Appl. Supercond., 19 (3), 2009.

[10] H. van de Stadt, A. Baryshev, P. Dieleman, Th. de Graauw, T. M. Klapwijk, S. Kovtonyuk, G. de Lange, I. Lapitskaya, J. Mees, R. A. Panhuyzen, G. Prokopenko, and H. Schaeffer, A 1 THz Nb SIS heterodyne mixer with normal metal tuning structure, Proc. 6th Int. Symp. on Space THz Technology, California Institute of Technology, Pasadena, 1995.

[11] M. Bin, M. C. Gaidis, J. Zmuidzinas, T. G. Phillips, and H. G. LeDuc, Low-noise 1 THz niobium superconducting tunnel junction mixer with a normal metal tuning circuit, Appl. Phys. Lett. 68, 1996.

[12]P. Dieleman, T. M. Klapwijk, J. R. Gao, and H. van de Stadt, Analysis of Nb superconducting-insulator-superconducting tunnel junctions with Al striplines for THz radiation detection, IEEE Trans. on Appl. Supercond. 7, 1997.

[13]R. L. Kautz, "Picosecond pulses on superconducting striplines," J. Appl. Phys. 49 (1), 1978.

[14]B. Bumble, H.G. LeDuc, J. A. Stern and K. G. Megerian,, "Fabrication of Nb/Al-Nx/NbTiN junctions for SIS mixer applications," IEEE Trans. Appl. Supercond. 11 (1) 2001.

[15]B. D. Jackson, N. N. Iosad, B. Leone, J. R. Gao, T. M. Klapwijk, W. M. Laauwen, G. de Lange, and H. van de Stadt, DC and terahertz response in Nb SIS mixers with NbTiN striplines, Proc. 10th Int. Symp. on Space THz Technology, U. of Virginia, Charlottesville, Virginia, 144-156, 1999.

[16]B. Leone, B. D. Jackson, J. R. Gao, and T. M. Klapwijk, "Geometric heat trapping in niobium superconductor–insulator–superconductor mixers due to niobium titanium nitride leads," Appl. Phys. Lett. 76, 2000.

[17]B. D. Jackson, "NbTiN-based THz SIS Mixers for the Herschel Space Observatory," PhD Thesis, 2005.

[18]M. Maezawa, M. Aoyagi, H. Nakagawa, I. Kurosawa, and S. Takada "Specific capacitance of Nb/AlOx /Nb Josephson junctions with critical current densities in the range of 0.1–18 kA/cm^2," Appl. Phys. Lett. 66 (16), 1995.

[19]Z. Wang, Y. Uzawa, and A. Kawakami, "High Current Density NbN/AlN/NbN Tunnel Junctions for Submillimeter Wave SIS Mixers," IEEE Trans. Appl. Supercond. 7 (2), 1997

[20]A. R. Kerr and S.-K. Pan, "Some Recent Developments in the Design of SIS Mixers," Int. J. of lnfrared and Millimeter Waves, 11(10), 1990.

[21]W. Shan, S. Asayama, M. Kamikura, T. Noguchi, S. Shi and Y. Sekimoto, "A 385-500 GHz Low Noise Superconductor-Insulator-Superconductor Mixer for ALMA Band 8," IEICE Trans. Electron. E89-C, (2), 2006.

[22]Q. Ke, and M. J. Feldman, "Optimum Source Conductance for High Frequency Superconducting Quasiparticle Receivers," IEEE Trans. on Microwave Theory and Tech. 41 (4), 1993.

[23]J. Zmuidzinas, H. G. LeDuc, J. A. Stern, and S. R. Cypher, "Two-junction Tuning Circuits for Submillimeter SIS Mixers," IEEE Trans. on Micarowave Theory and Tech. 42 (4), 1994.

[24]T.Noguchi, S. Shi, and J. Inatani, "Parallel Connected Twin SIS Junctions for Millimeter and Submillimeter Wave Mixers: Analysis and Experimental Verification," IEICE Trans. Electron. E78-C (5), 1995.

[25]S. C. Shi, T. Noguchi, H. Iwashita, and J. Inatani "A W-band SIS Mixer Employing PCTJ," Technical report of IEICE, MW95-62, 1995.

[26] S. C. Shi, T. Noguchi, H. Iwashita, and J. Inatani, "Analysis of the bandwidth performance of SIS Mixers with distributed junction arrays," Proc. 8th Int. Symp. on Space Terahertz Tech., Harvard University, March 1997.

[27] M. Takeda, M. Kroug, T. Kojima, Y. Uzawa, and Z. Wang, "In-plane distribution of superconducting properties of NbTiN thin films on fused quartz substrates," presented at 70th Japanese Society of Appl. Phys. conf., University of Toyama, 2009.

[28] M. Takeda, S. Nakayama, A. Saito, H. Shimakage, Y. Uzawa, S. Ohshima, and Z. Wang, "Measurements of Microwave Surface Resistances of NbN and NbTiN Thin Films," proc. 12th Int. Supercond. Electron. Conf., Fukuoka, JAPAN, June 16-19, 2009.

[29] A. Shoji, S. Kiryu, and S. Kohjiro, "Superconducting properties and normal-state resistivity of single-crystal NbN films prepared by a reactive rf-magnetron sputtering method," Appl. Phys. Lett. 60, 1992.

[30] B. D. Jackson, G. de Lange, T. Zijlstra, M. Kroug, T. M. Klapwijk, and J. A. Stern, "Niobium titanium nitride-based superconductor-insulator-superconductor mixers for low-noise terahertz receivers," J. Appl. Phys. 97, 2005.

[31] M. Kroug, A. Endo, T. Tamura, T. Noguchi. T. Kojima, Y. Uzawa, M. Takeda, Z. Wang, and W. Shan: IEEE Trans. Appl. Supercond. 19, 2009.

[32] B. Ferguson and X. C. Zhang, "Materials for terahertz science and technology," Nat. Mater. 1, 2002.

[33] M. Takeda, W. Shan, T. Kojima, S. Saito, M. Kroug, Y. Uzawa and Z. Wang, "Low-noise waveguide SIS mixer with NbN/AlN/NbN tunnel junctions tuned by an NbN/MgO/NbTiN microstrip circuit," Supercond. Sci. Technol. 22, 2009.

[34] D. C. Mattis and J. Bardeen "Theory of the anomalous skin effect in normal and superconducting metals," Phys. Rev. 111, 1958.

[35] I-line stepper model "FPA-3000I5+" manufactured by Canon.

Chapter 4
Development of waveguide SIS mixers based on epitaxial NbTiN films on MgO substrates

4.1 Overview

In this section, we present a design, and test of waveguide SIS mixers with Nb/AlO_x/Nb tunnel junctions and NbTiN/SiO_2/Al or NbN/SiO_2/Al microstriplines in the terahertz band. This SIS mixer adopts epitaxial NbTiN or NbN films grown on single crystal MgO substrates [1]; this mixer possesses superior superconducting properties as compared to that with polycrystalline NbTiN films grown on quartz substrates. By adopting these epitaxial films in well-established Nb SIS mixers [2], the low-noise performance of the devices can be optimized at terahertz frequencies. On the other hand, using an MgO substrate increases the difficulty in designing mixer chips for waveguides because of the high dielectric constant of the substrate. This implies that some artifice is required for designing the mixer chips as compared to using quartz substrates.

In first test, we design and test SIS mixers integrated with either NbTiN/SiO_2/Al or NbN/SiO_2/Al microstrip lines. Results obtained from a detailed analysis of mixers on the basis of numerical simulations are consistent with those obtained from the experiment and they reveal the possibility of further improvement in the mixer performance. In second step, we offer a demonstration of low noise mixer performance using NbTiN/SiO_2/Al microstrip lines.

4.2 Design

We designed a waveguide-to-microstrip transition in order to achieve the following goals.

1. Low leakage of RF signal to IF port.
2. Suppression of the higher mode
3. Low-impedance probe using flat backshort cavity.
4. Easier mounting SIS chip
5. Full height waveguide WR1.2 to reduce its loss.

Fig. 4-1 shows a schematic of the design. The RF signal leakage is prevented by using a choke filter, and the IF signal is allowed to pass through the IF port. Fundamental mode propagation to the IF port or non-propagating higher mode causes additional loss. Occurrence of the higher mode depends on the dielectric constant, strip width, and thickness of the substrate. The MgO substrate has a

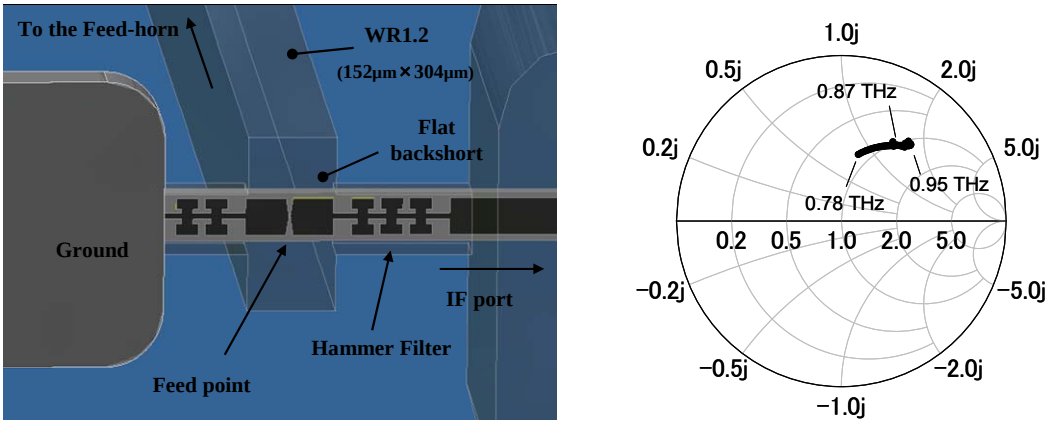

Fig. 4-1 Schematic layout of probe and choke filter on MgO substrate (left). The mixer chip width and thickness are 85 μm and 28 μm respectively. Analyzed feed point impedance of waveguide-to-microstrip transition over 0.78-0.95 THz (right). The Smith chart is normalized to 15 Ω.

relatively higher dielectric constant $\varepsilon_r \sim 9.8$ as compared with the commonly used quartz substrate. Therefore, we need to use a smaller size of the MgO chip than that of quartz. On the other hand, in order to ease in handling, it is better to use the substrate as thick as possible. A resonance choke filter called *hammer filter* help to suppress higher modes and prevent leakage of the fundamental mode to the IF port better than a conventional choke filter, if the substrate thickness is the same [1], [4]. We decided to use an MgO chip with a width of 85 μm and thickness of 28 μm based upon simulations with the high-frequency structure simulator (HFSS).

We selected a WR-1.2 (152 μm × 304 μm) full-height waveguide to reduce additional losses due to resistance and surface roughness. For lower frequencies, a reduced-height waveguide is used to obtain low impedance, and the backshort cavity is milled to achieve wideband operation at a desirable frequency. However in this frequency regime, because some fabrication errors due to machining cause additional loss, the mechanical structure of the waveguide should be simplified. To improve the accuracy in mounting the SIS chip, we design the bow-tie probe with a length of 152 μm, being equal to that of the short side of the rectangular waveguide [1]. We optimized the bow-tie probe to use the flat backshort to minimize the difficulty involved in fabrication, by using HFSS. Bow-tie and choke structures consisting of NbN and Al films are represented by a thin sheet with a complex surface impedance [5], [6]. The structure is set to an open angle of 23° so that the impedance is low. The feed point impedance has 15 Ω for both the real and imaginary parts, depending on the frequency, as shown in Fig. 4-1. According to simulations, this inductive part is helpful in achieving a high mixer gain despite slight degradation in the LO coupling frequency [1].

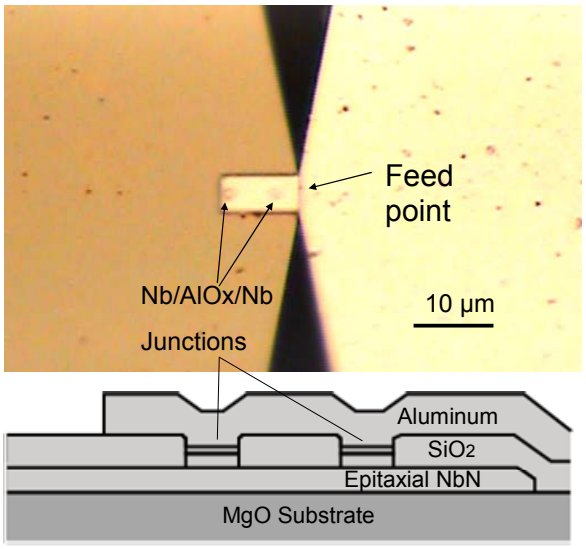

Fig. 4-2 Optical photograph of the mixer and schematic structure of the NbN/SiO_2/Al microstrip-line and SIS junction. The PCTJ is directly located on the feed point without the quarter-wavelength impedance transformer.

We designed a tuning circuit at 0.87 THz, which is the center frequency of ALMA Band 10. We used a two-junction tuning circuit, which has a structure composed of two SIS junctions connected in parallel by an inductive line. The PCTJ has the advantages of larger junction size and reduced RF resistance [7]. The critical current density J_c of an SIS junction is set to 10 kA/cm^2 in order to operate it wideband, and its specific capacitance is assumed to be 85 fF/μm^2. The size of an SIS junction is 1.0 μm in diameter. The microstripline used to tune out the geometric capacitance of the SIS junction consists of NbN/SiO_2/Al. We assumed in the design that the Al conductivities at 4.2 K and NbN normal state are 1.1×10^8 and 0.8×10^6 $\Omega^{-1}m^{-1}$, respectively, and the gap frequency of NbN is 1.4 THz. By using these parameters, the surface impedance of the NbN film was estimated by calculating the penetration depth using the Mattis-Bardeen theory [8]. In addition, by taking into account the spread inductance, which is the effect of curved current around the junction, we determined a tuner length of 6 μm as the standard. In order to characterize the tuning circuit experimentally, the tuner length was varied from 5 to 7 μm, and the junction size was varied by 0.1 μm in diameter. The two-junction circuit, which has an impedance of approximately 13 Ω is directly located on the feed point without the quarter-wavelength impedance transformer, as shown in Fig. 4-2. The mixer fabrication processes are described in chapter 3.

4.3 Evaluation of the mixer

We firstly observed the Josephson resonance step of MA-mixer, which appears on the *I-V* curve as a result of the ac-Josephson effect, as shown in Fig. 4-3 (a). The resonance step was pronounced by applying a magnetic field to the junctions. It can be seen that the voltage position of the resonance step is approximately 2.1 mV, which corresponds to 1 THz. This result predicts that the tuning frequency is slightly higher than the designed frequency of 0.87 THz because of the shorter tuner length. Fig. 4-3 (b) shows a typical *I-V* curve of one of the several measured mixers. Nb junctions with a current density of 6.5 kA/cm^2, which are lower than the designed value, show good *I-V* characteristics yielding a subgap-to-normal-state resistance ratio greater than 20. Receiver noise measurements were conducted using the standard *Y*-factor method with room-temperature (295 K) and liquid-nitrogen-cooled (77 K) loads.

Corrected for losses in the beam splitter and the vacuum window, the receiver noise temperature, which was calculated on the basis of the Callen and Welton formula [9], is shown in Fig. 4-4 as a function of LO frequency. The measured result of the A-mixer shows 440 K (DSB) at 1 THz, which is approximately 10 times that of the quantum limit, despite the low conversion gain of approximately –10 dB. We evaluated MB- and MC-mixers (with J_c = 8 kA/cm^2) in which an epitaxial

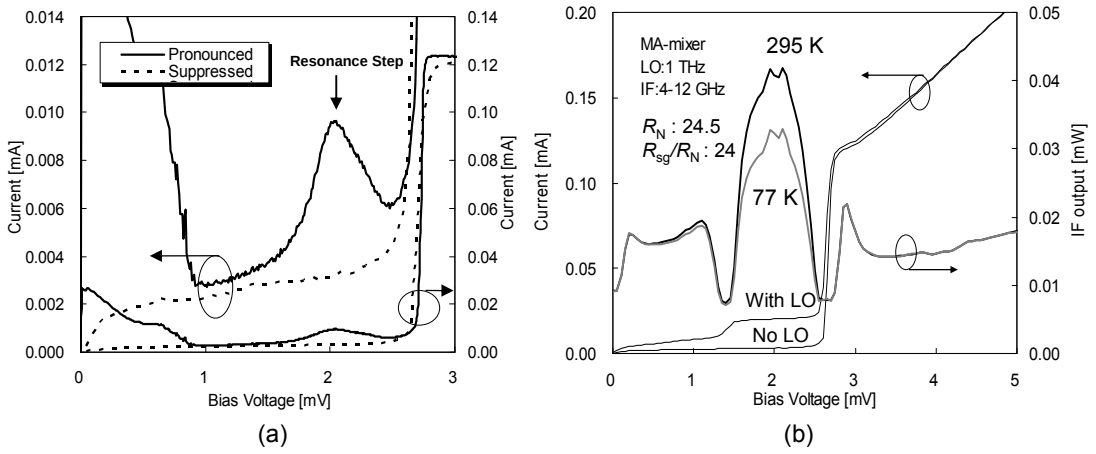

Fig. 4-3 (a) An observed resonance-induced Josephson step in the *I-V* curve. The step was pronounced and suppressed by changing applied magnetic fields. It appears at about 2.1 mV which corresponds to 1 THz. (b) Typical *I-V* characteristic and heterodyne response of the MA-mixer with hot and cold load at LO frequency of 1 THz and over the IF of 4-12 GHz.

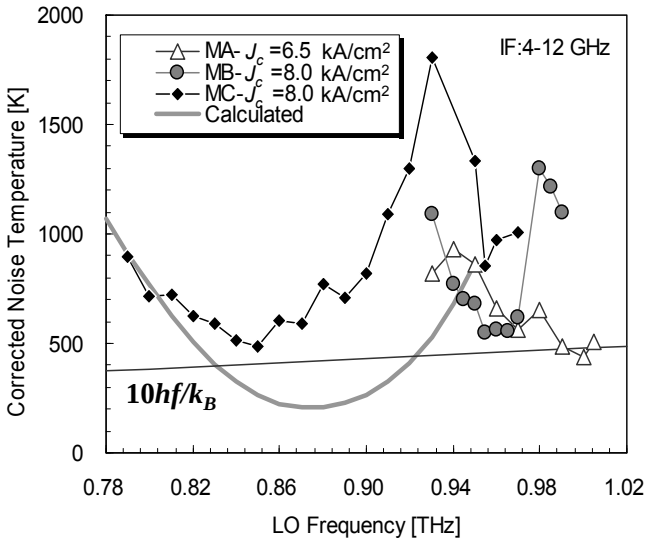

Fig. 4-4 Measured receiver noise temperature of three devices with different tuning lengths as a function of LO frequency. They are corrected for losses in the beam splitter and the vacuum window. Also shown is theoretical calculation based on design parameters with J_c of 8 kA/cm^2.

NbTiN film, instead of NbN, is used as the ground plane. Because the noise performances are similar to that of MA-mixer, the epitaxial NbTiN film may have almost the same properties with the epitaxial NbN film. An interesting feature is that all mixers show sharp noise increase at around 0.94 THz, which is not expected from a theoretical calculation based on our design parameters.

We verified the validity of these results in the following ways. The thickness of the mixer chips, which is important to influence feed impedance, was measured using an optical microscope. The thickness of the MA-mixer was found to be 29 μm close to the designed mixer and two MB- and MC-mixers were observed to be 36 μm, which was much thicker than the designed mixer. Based on their thickness, we analyzed the microstrip-waveguide transition for the feed point impedance and transmission characteristics of fundamental and higher modes to the IF port with the HFSS. The results showed that their modes pass to the IF port over the entire band of more than 0.93 THz in the thickness of 29 μm and more than 0.88 THz in the thickness of 36 μm. As a result, feed point impedance becomes an undesirable value on the Smith chart. In addition, by using the feed point impedance, we calculated the conversion gains for the mixers, as based on Tucker's simplest 3 port mixing theory, to be compared with the measured gains, as shown in Fig. 4-5 [10]. These parameters were calculated at IF of 8 GHz. There are the presences of typical measurement errors of about ± 1.5 dB which refer to three standard deviations. The calculated gains are approximately 2 dB higher than the average measured gains. It should be noted that the calculation does not include any excess losses due to leakage of signal to IF, blackbody load not being perfectly black, receiver optics losses

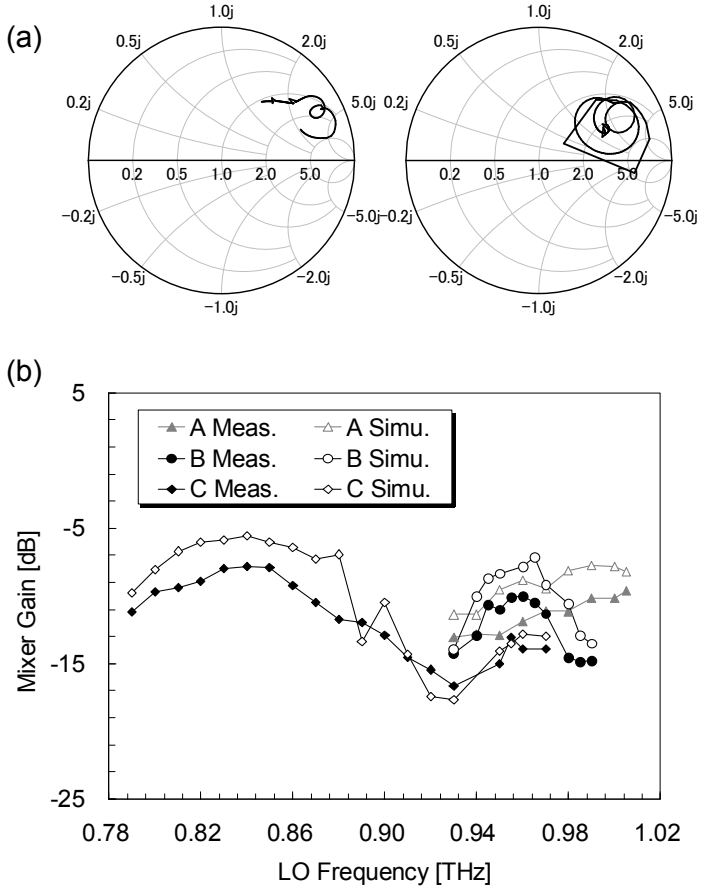

Fig. 4-5 (a) Feed impedance for the thickness of 29 μm (left) and 36 μm (right) (b) Comparison between the simulated and measured values for the mixer gain plotted as a function of the LO frequency.

in the mirrors, diagonal horn and waveguide, and dielectric losses in the beam splitter, vacuum window, MgO substrate, and SiO_2 layer.

Thus, if the lower gain in the experiment is attributed to these excess losses, the results calculated by considering the low loss of epitaxial NbN film is consistent with the measurements. Therefore, the unexpected noise performances in the experiments are attributed to the operating frequency, for the substrates being thicker than expected, and not for the Nb SIS junctions and $NbN/SiO_2/Al$ tuning circuits. To ensure continuity in the operation, our detailed analysis shows that a substrate with thickness close to 25 μm is required. Although it is still possible to fabricate such a thin MgO substrate, a narrower strip choke structure may help to use a thick substrate up to 35 μm. We believe that such improvements will reduce the noise temperatures.

4.4 Improved design

In the above design, the feed point impedance had the inductive part with frequency dependence. Although this inductive part was helpful in achieving a high mixer gain due to higher dynamic resistance, there have been suggestions that the feed impedance made the bandwidth of mixer noise temperature narrower and the noise temperature higher due to a mismatch to noise optimum impedance as described in section Chapter 5. Besides, the results in section 4.3 suggested the occurrence of the higher mode and/or the leakage of RF signal as a possible cause of the noise temperature increase more than 0.9 THz. In order to improve the noise performance, robust design would be needed for them.

4.4.1 Higher mode and choke filter design

Higher mode occurrence for the shielded microstrip line depends on a width, thickness, and dielectric constant. Even if the 25-μm-thick MgO substrate is selected as a reliable case, a narrower strip choke structure may help to suppress the higher mode because it can be avoided that RF signal couples to the side wall of the mixer chip slot. Referring to a paper of [11], a quarter-wavelength transmission line can be replaced by the stepped transmission line consisted of two connected series transmission line sections. The equivalence between the uniform quarter-wavelength long open-stub

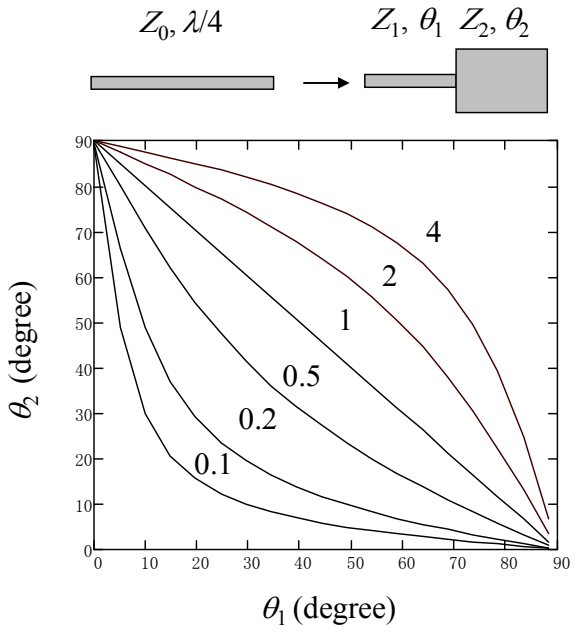

Fig. 4-6 Equivalence of stepped impedance and open circuit and quarter-wave sections (above). θ_1 versus θ_2 for different values of K (below)

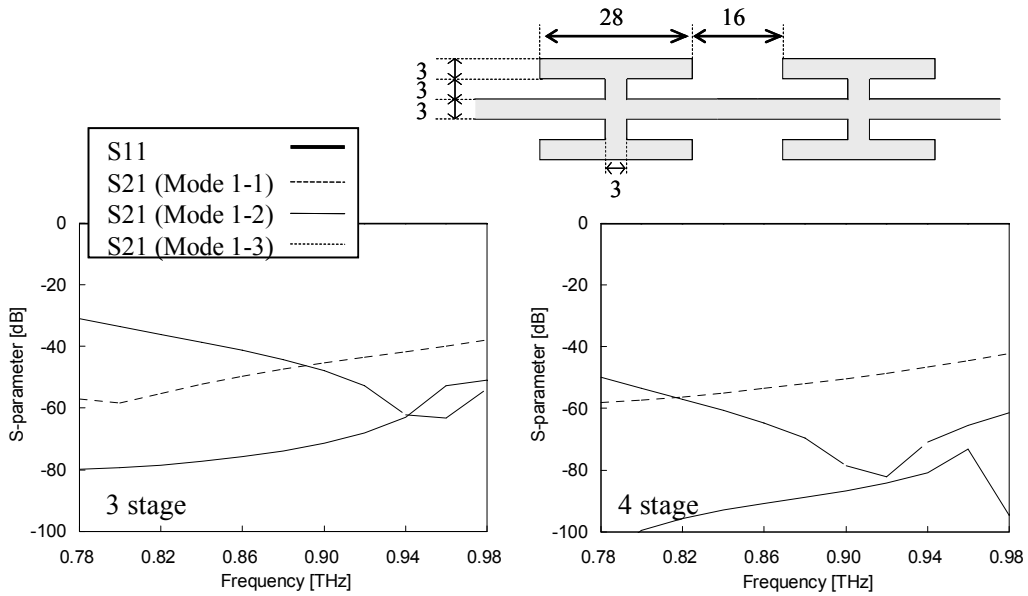

Fig. 4-7 Dimension of the optimized hammer filter and the analyzed results (left: 3 stages, right: 4 stages).

section and the stepped impedance section is investigated using transmission line theory. θ_1 and θ_2 denote the effective electrical lengths of the lines with Z_1 and Z_2 characteristic impedances, respectively. Investigating the input impedance of the stepped impedance section at resonance, the following equation can be derived:

$$K = \frac{Z_2}{Z_1} = \tan\theta_1 \tan\theta_2 , \qquad 4\text{-}1$$

where K equals to Z_2/Z_1. Design curves are drawn in Fig. 4-6 for different values of K. The total electrical length of the resonator is given by $\theta_t = \theta_1 + \theta_2$. It is noted that for $K = 1$, the total electrical length is 90◦ and the total length of the stepped resonator decreases as the impedance ratio K decreases. Therefore, in order to be shorter for the total length, K should be lower. On the other hand, for practical realization of microstrip lines, the characteristic impedances should be bounded in the region ($25\ \Omega \le Z \le 150\ \Omega$). Consequently, the corresponding practical impedance ratio must be in the range ($0.17 \le K \le 4$).

An initial value of the K is set to about 0.2 with $\theta_1 = \theta_2$ to analyze the design of the hammer chock filter. A dimension of the optimized filter and analyzed results are shown in Fig. 4-7. It is found that the both 3 and 4 stages filter can suppress the occurrence of higher modes and signal leakage below −30 dB over the 0.78–0.98 THz.

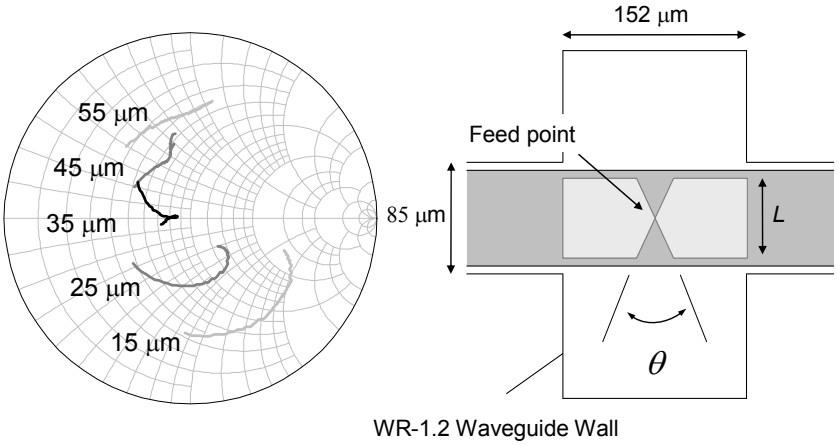

Fig. 4-8 Feed impedance of the bow-tie antenna from 0.78 to 0.95 THz when L is set to 15, 25, 35, 45, and 55 μm with the angle θ and substrate thickness t fixed to 15° and 25 μm, respectively. The smith chart is normalized to 30 Ohm

4.4.2 Probe design

According to ref. [4], L and θ (see Fig. 4-8) control the real and imaginary part of the average feed impedance. Increasing L results in an increase of $\mathrm{Re}(Z_{feed})$ and a decrease of $\mathrm{Im}(Z_{feed})$, while increasing a results in a decrease of both $\mathrm{Re}(Z_{feed})$ and $\mathrm{Im}(Z_{feed})$. On the basis of the principle, Z_{feed} was optimized with HFSS so that it remained in a small region of the Smith chart and did not have a reactive part. Fig. 4-8 shows the feed impedance of the bow-tie antenna from 0.78 to 0.95 THz when L is set to 15, 25, 35, 45, and 55 μm with the angle θ and substrate thickness t fixed to 15° and 25 μm, respectively. As illustrated in Fig. 4-8, it is found that the feed impedance has almost real impedance of 30 Ω at the center of the working frequency range when L is around 35 μm.

4.4.3 Mixer chip and tuning circuit design

Fig. 4-9 shows feed impedances of an optimized mixer chip with HFSS likewise for different thickness by combining the probe with the hammer choke filter designed in sections 4.4.1 and 4.4.2. Obviously, it can be found that the feed impedance strongly depends on the substrate thickness due to high dielectric constant of MgO. In terms of the issue for higher modes, it seems to hardly occur for thicknesses up to 30 μm from another analysis. Also shown is a photograph of a mixer chip and listed is parameters of SiO_2, NbTiN and Al films used for design of tuning circuit. The parameters are based on measurement results. As a result of the optimization for the feed impedance to have almost real one, the length L of the bow-tie antenna is determined to be 37 μm for the substrate thickness for 25 μm. To match impedances between twin-junction and feed point, a quarter-wavelength impedance transformer with the length of 28 μm and the width of 2.5 μm is inserted. The two-junction circuit uses the same one as designed in section 4.2.

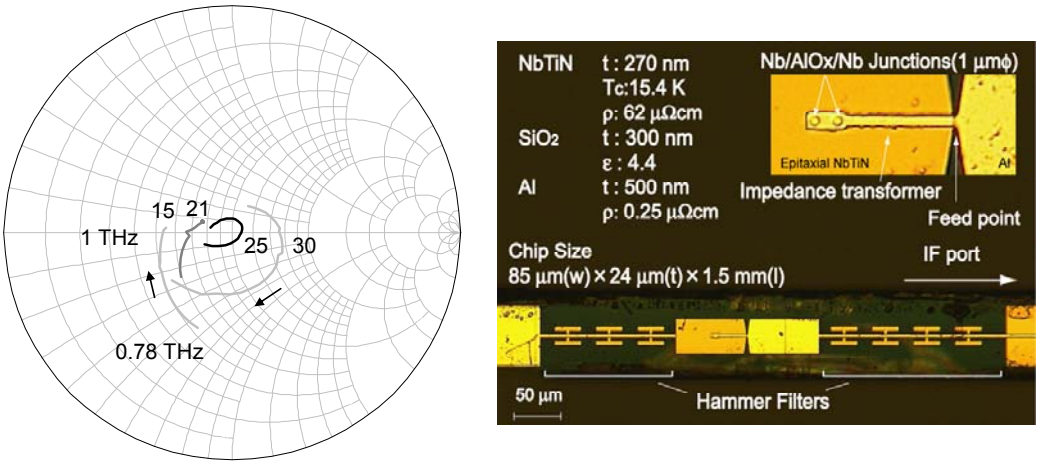

Fig. 4-9 Analyzed feed impedance including the combination of probes and hammer filter for different thickness over the 0.78 to 1 THz. The smith chart is normalized to 30 Ohm. Also shown is a photograph of a mixer chip and listed is parameters for design of tuning circuit. As a result of the optimization for the feed impedance to have almost real one, the length L of the bow-tie antenna is determined to be 37 μm for the substrate thickness of 25 μm.

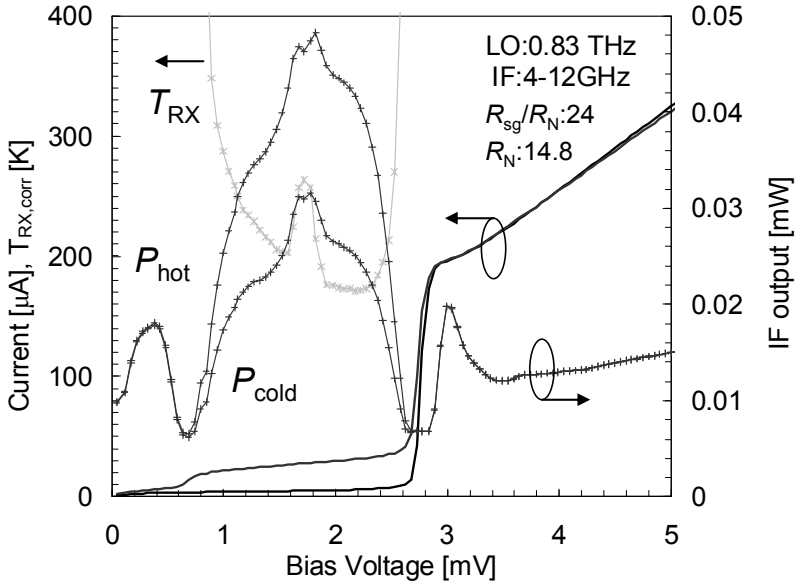

Fig. 4-10 Current, IF output power with hot and cold load and corrected noise temperature of ME-mixer at the LO frequency of 0.83 THz and over the IF of 4-12 GHz as a function of bias voltage.

4.5 Mixer performance and discussion

MD- and ME-mixers with 18- and 27-μm-thick (close to the design) MgO substrate respectively were prepared for the test of the improved design. Nb junctions with a current density of 6.5 kA/cm^2 also showed good *I-V* characteristics yielding a subgap-to-normal-state resistance ratio greater than 20. Fig. 4-10 presents the measured current-voltage characteristics of ME-mixer with and without LO at 0.83 THz. Also shown are the corrected noise temperature and the IF responses to hot and cold loads as a function of bias voltage. The maximum *Y*-factor was 2.21 dB, corresponding to an uncorrected and corrected receiver noise temperature of 248 K and of 171 K. The frequency dependence of the noise temperature for the mixers is shown in Fig. 4-11. Except for their thickness and slightly different R_N (Junction size), MD- and ME-mixers has all the same parameters (e.g. tuner length, R_{sg}/R_N). Since the slightly different R_N of 1.4 Ω between the mixers does not influence their performances relatively, the difference between their performances should depend on the feed impedance related to the substrate thickness strongly. This is interpretable that a low embedding source impedance of ME-mixer transformed by quarter-wavelength microstrip line with the characteristic impedance of 22 Ω allows broader bandwidth and lower noise because of good matching with two-junction's one. On the other hand, the higher noise temperature of MD-mixer is caused by a mismatching between the junctions and the embedding circuit, and the impedance locus having frequency dependence which inversely draws with twin-junctions impedance makes the bandwidth narrower. This result is good agreement with the theoretical expectation.

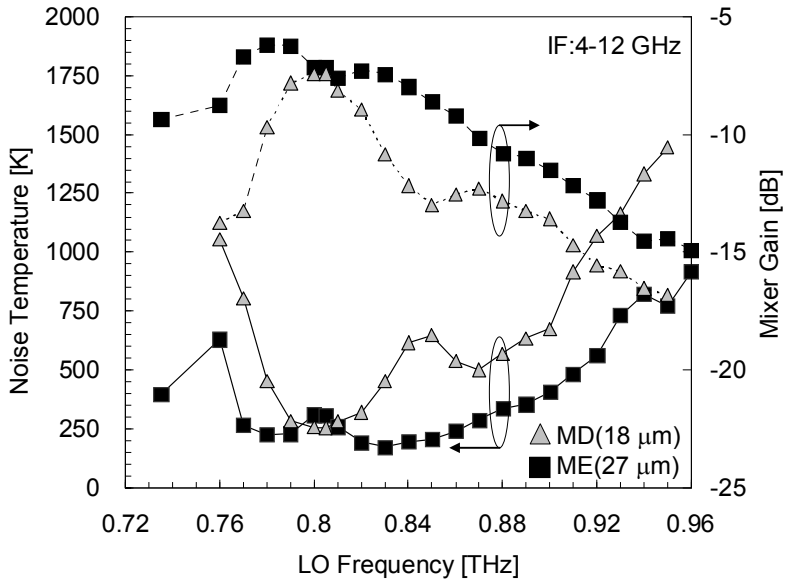

Fig. 4-11 LO frequency dependence of noise temperature for MD- and ME-mixers. Their measured substrate thicknesses were 18 and 27 μm.

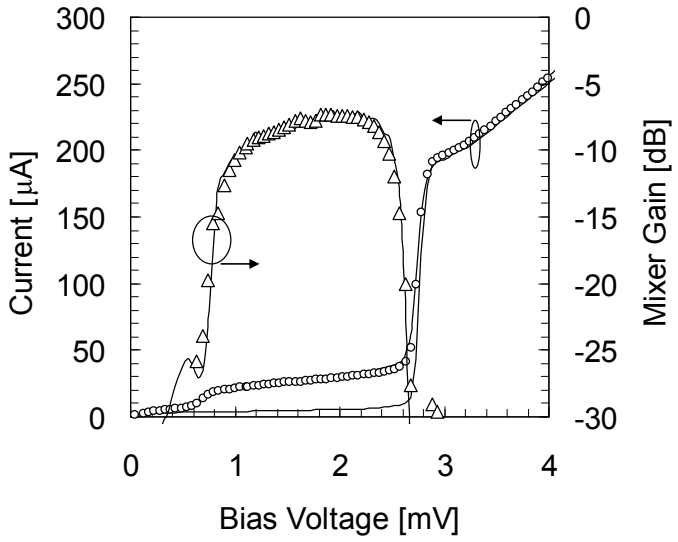

Fig. 4-12 Fitted pumped *I-V* curve to the measured one by sweeping embedding impedance on the basis of ref. [12] The mixer gain is calculated from the pumped *I-V* curve using three-port-mixing theory.

Compared to the noise performance of the mixers (e.g. MC-mixer) with the previous design described in section 4.3, the noise temperature of ME-mixer would significantly be improved. This suggests the better designs of the feed impedance having almost real part and the suitable filter to avoid the signal leakage and the occurrence of higher mode.

Table 4-I Loss break-down for two mixers with microstrip configurations using the epitaxial and a Poly-crystal NbTiN films at 4 K (see section 5.5).

	Epitaxial NbTiN		Poly-crystal NbTiN	
	Calculated	Measured	Calculated	Measured
Frequency [THz]	0.83		0.88	
Current density [kA/cm^2]	6.5		8	
Vacuum window [dB]	-0.28		-0.32	
Beam splitter [dB]	-0.55		-0.62	
Excess loss [dB]	-1.0	-7.4	-1.3	-6.5
Waveguide [dB]	0.0		-0.2	
Tuning circuit [dB]	-1.7		-1.4	
Conversion gain [dB]	-4.7		-3.6	

In addition, the loss in the superconducting microstrip line with the epitaxial NbTiN film on MgO substrate is estimated and compared to poly-crystal NbTiN film on fused quartz substrate discussed in later section 5.5. By fitting a theoretical *I-V* curve to the measured one with RF-voltage match method on the basis of ref. [12], mixer gain was estimated as a function of bias voltage (see Fig. 4-12). As listed in the Table 4-I, the higher loss of the calculated tuning circuit loss for the epitaxial NbTiN-based mixer is due to lower current density. Although there is unknown excess loss, it may be attributed to losses of the optical components. Even though the loss is included in their tuning circuit, both epitaxial and poly-crystal NbTiN-based microstrip are very low loss. If the excess loss difference of 0.3 dB is significant, it would depend only on NbTiN film characteristics, and the epitaxial NbTiN-based microstrip would have the same or lower loss compared to the poly-crystal NbTiN-based microstrip. If we can control the MgO thickness accurately or find a design solution to overcome high dielectric constant, the mixer with epitaxial NbTiN or NbN would be a promising device for frequencies up to 1.2 THz or 1.4 THz. For example, coplanar waveguide, which does not depends on the thickness, would one of the candidates as the transmission line configuration.

4.6 Conclusion

We have designed, fabricated, and tested SIS mixers with Nb/AlO_x/Nb junctions employing epitaxial NbTiN film on an MgO substrate in the frequency band approaching 1 THz. A full-height waveguide, hammer-type choke filter, and zero-depth backshort were adopted for the design. The device based on NbTiN showed a receiver noise temperature of 171 K at 0.83 THz. On the other hand, a detailed analysis of mixers on the basis of numerical simulations was consistent with the experiment results, and it revealed a possibility of further improvement in the mixer performance. This indicates that SIS mixers having such structures are promising devices for use in the terahertz band, if we can control the MgO thickness accurately or find a design solution to overcome high dielectric constant.

References

[1] W. L. Shan, M. Takeda, T. Kojima, Y. Uzawa, S.C. Shi, and Z. Wang, 19th Int. Symp. on Space THz Technology, Groningen, 28-30 April 2008.

[2] Z. Wang, A. Kawakami, Y. Uzawa, and B. Komiyama, “Superconducting properties and crystal structures of single-crystal niobium nitride thin films deposited at ambient substrate temperature,” J. Appl. Phys. 79 (10), 1996.

[3] W. Shan, S. Shi, T. Matsunaga, M. Takizawa, A. Endo, T. Noguchi, and Y. Uzawa, “Design and development of SIS mixers for ALMA band 10, ” IEEE Trans. Appl. Supercond., 17 (2), 2007.

[4] A. Navarrini and B. Lazareff, “275-370 GHz DSB and SSB waveguide mixers employing a tuned Nb/Al-AlOx/Nb SIS tunnel junction,” ALMA Memo, No. 351 [Online]. Available: http://www.alma.nrao.edu/memos/html-memos/alma351/memo351.pdf

[5] A. R. Kerr, “Surface impedance of superconductors and normal conducting EM simulators,” *MMA Memo*, No. 245 [Online]. Available: http://ww.alma.nrao.edu/memo/heml-memo/alma245/memo245.1.pdf

[6] V. Belitsky, C. Risacher, M. Pantaleev, V. Vassilev, “Superconducting microstrip line model studies at millimetre and sub-millimetre waves,” Int. J. Infrared and Millim Waves, 27 (6), 2006.

[7] T. Noguchi, S. C. Shi, and J. Inatani, “Parallel connected twin SIS junctions for millimeter and submillimeter-wave mixers—analysis and experimental-verification,” IEICE Trans. Electron., 78-C (5), 1995.

[8] D. C. Mattis and J. Bardeen “Theory of the anomalous skin effect in normal and superconducting metals,” Phys. Rev. 111, 1958.

[9] H. B. Callen and T. A. Welton, “Irreversibility and Generalized Noise,” Phys. Rev. 83 (1),1951

[10] J. R. Tucker and M. J. Feldman, “Quantum detection at millimeter wavelengths,” Rev. Mod. Phys. 57, 1985.

[11] M. A. S. Alkanhal, “Compact Bandstop Filters with Extended Upper Passbands,” Active and Passive Electronic Components 2008, Article ID 356049, 2008

[12] A. Skalare, “Determining embedding circuit parameters from DC measurements on quasiparticle mixers” Int. J. Infrared Millim Waves 10, 1989.

Chapter 5
Demonstration of a low-noise waveguide NbTiN-based SIS mixer on a quartz substrate

5.1 Motivation and Overview

In order to improve the mixer performance, it is important not only to establish the low-loss microstrip lines but also to investigate the mixer noise properties of the Nb junctions above its gap frequency where the mixer gain is significantly degraded. For the achievement of both low noise and wideband operation in this frequency range, development of mixers with a higher current density (J_c) SIS junction has been pointed out or suggested to be important in many papers [1]–[4]. In this case, J_c more than 20 kA/cm^2 might be needed to cover the RF frequency range of the ALMA Band 10. This is because the high J_c junctions have advantages of higher intrinsic mixer conversion gain, reduction of RF loss in the tuning circuits, and wider bandwidth due to the low $\omega R_N C$ Product. Where ω is angular frequency and, R_N and C are the normal resistance and capacitance of an SIS junction, respectively. Thus, if the conversion gain and the junctions coupling dominantly influence the receiver noise temperature, realization of the higher J_c junctions as possible would be the best way to improve the bandwidth.

However, such high J_c junctions might be unsuitable for the ALMA band 10 SIS mixers which requires mass production, because selecting high J_c junctions have to compromise the yield and the quality factor corresponding to R_{sg}/R_N. In general, R_{sg}/R_N of SIS junctions degrades with increasing

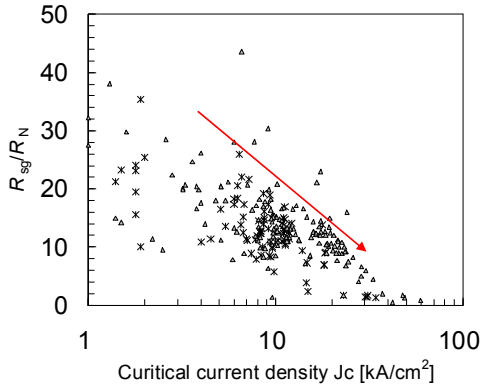

Fig. 5-1 Relation between the R_{sg}/R_N factor and the junction current density J_c. The SIS junctions are fabricated in our laboratory. Of them, the symbols are data of Nb/Al–AlOx/Nb and Nb/Al–AlNx/Nb barrier SIS junctions selected at random.

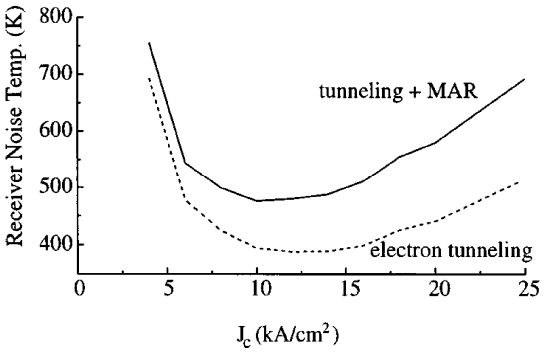

Fig. 5-2 Receiver Noise temperature calculated for a Nb junction at 1 THz with an Al tuning structure shown in ref. [5]. The dashed line is calculated ignoring Multiple Andreev Reflection

J_c (see Fig. 5-1). In addition, P. Dieleman and T. M. Klapwijk [5] say that noise temperature increases due to shot noise enhanced by Multiple Andreev Reflection (MAR) with increasing J_c shown in Fig. 5-2. Since the pinhole current is carried in Andreev clusters with charge $q\rangle\rangle e$, the associated shot noise is significantly enhanced. They report a possibility that the mixer noise can be more than twice as large as expected from the Tucker theory due to this effect and this causes a 25% increase in the receiver noise temperature at THz frequencies. These arguments have given us an impression that realization of low-noise and wideband terahertz SIS mixers might be hopeless.

In contrast, excellent noise performances have been successfully achieved with high-quality Nb junction and well-established low-loss NbTiN/SiO_2/Al tuning circuit [7]-[9], overcoming difficulties due to frequencies above Nb gap. Except input noise temperature reduction by realization of the low-loss tuning circuit, it might not have been fully understood the reason why their mixers showed both low noise and wideband performances simultaneously, because the wideband and low-noise results are obtained for moderate J_c junction around 10 kA/cm^2 without the benefits of higher J_c one. These mixers adopt very low source impedance compared to one to maximize the coupling. In this case, their results might be considered as the broad bandwidth could be obtained at the cost of peak coupling, in other words, receiver performance degradation around the center frequencies. However, this would not give us an exact aspect in terms of quantitative contributions of mixer gain and mixer noise temperature for receiver noise temperature, because an optimal impedance to minimize mixer noise temperature is different from ones to maximize mixer gain or junction coupling [10]. In order to optimize the receiver operation, the behavior of the mixer gain and mixer noise temperature for source impedance should be investigated by e.g. source-pull analysis [11]-[13] or measurement, which is often employed for microwave amplifier design.

In this section, we discuss the mixer performance employing the source impedance dependence analysis for waveguide SIS mixers with Nb/AlO_x/Nb tunnel junctions and NbTiN/SiO_2/Al tuning circuit on quartz substrate. An inverted microstrip line is adopted for the tuning circuit to reduce RF

losses. Source impedance dependence of the twin junction is theoretically and experimentally investigated to achieve both low noise and wideband performances. The heterodyne measurement result of these devices is presented in a frequency range of 0.75–1.0 THz. The receiver performance with both wideband and low noise temperatures below $3hf/k_B$ and $5hf/k_B$ will be shown at both operating temperatures of 2 K and 4 K.

5.2 Wideband and low-noise SIS mixer design

5.2.1 Mixer chip design

As well as epitaxial NbTiN-base mixers described in previous chapter, the mixer uses a WR-1.2 full-height waveguide to minimize the transmission loss in waveguide while avoiding high-order mode excitation and a bow-tie antenna probe on a fused quartz substrate with 0.085 mm wide, 0.04 mm thick and 1.5 mm long. The original design has been analyzed by W. Shan et al. in ref. [14] and the proposed antenna feed impedance of about 30 Ω should offer broadband operation over the band 10 frequency range as shown in Fig. 5-3. The leakage to the IF port is less than 20 dB over the band 10 frequencies.

The design concept is almost the same as that of MgO devices in section 4.2, which takes care about higher mode suppression and easy and accurate mounting. We optimized a bow-tie shape probe across the waveguide because of its simple configuration and convenience for DC/IF grounding. Such a probe has been widely used in reduced-height waveguide for suitably low feed impedance and wideband performance. Undoubtedly, a small quartz substrate across the waveguide will result in less perturbation of the electromagnetic field distribution in the vicinity. But for

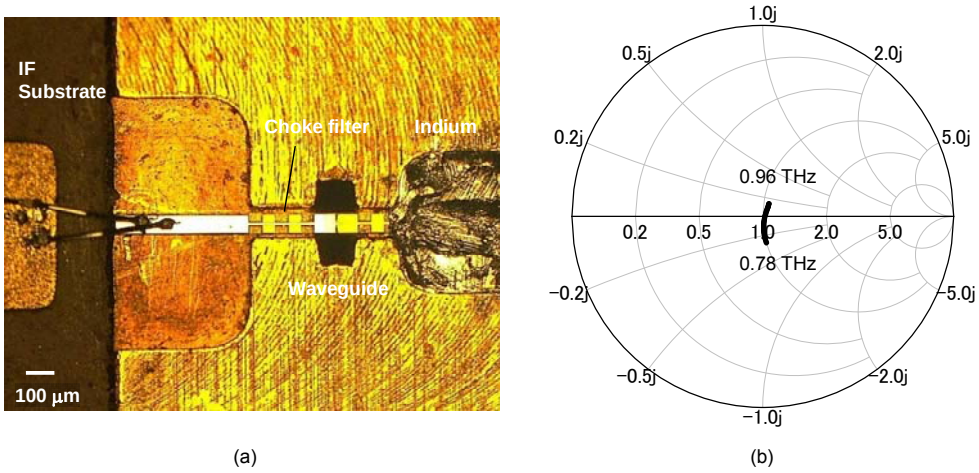

Fig. 5-3 Photograph of mixer chip mounted into chip slot (a) and the analyzed feed point impedance (b). The Smith chart is normalized to 30 Ω.

convenient device mounting, it is better to have a thick quartz substrate. The chip is set to be enough wide to allow a design of efficient choke filter, which cuts the transmission of the RF signal to the mixer's IF port. In order to minimize fabrication difficulties, we aimed to optimize the probe to allow a simple flat backshort. In addition, it is particularly beneficial to improve the mounting accuracy if the upper and lower edges of the bowtie probe can be aligned to the edges of waveguide, making the waveguide edges serving as mounting reference. With these restrains, the probe was optimized with extensive EM simulation (HFSS). The goals to be achieved are the same as ones summarized in section 4.2.

The optimizing process was very empirical. By means of adjusting the choke filter, especially the first section of high impedance lines and the open angle of the bowtie, satisfactory results were achieved. It should be noted that the open angle of the bowtie was found to be almost proportional to the real part of the feed-point impedance. A small angle leads to a low impedance favorable for SIS coupling. The open angle is 23 degree, a small value that is rarely seen in other designs.

5.2.2 Tuning circuit with the inverted NbTiN/SiO_2/Al microstrip line

We adopted a microstrip structure with the ground plane made of Al and the NbTiN strip embedded in the dielectric layer. A scanning electron microscope (SEM) image of the center of the mixer chip together with a cross sectional view is shown in Fig. 5-4. This inverted microstrip line has the potential to reduce RF losses in the tuning circuit because the currents in the lossy Al film are spread over a larger area. On the other hand, in the normal microstrip configuration where Al is used for the strip conductor [15], RF currents are concentrated in the narrow strip, which results in increasing the loss. In order to compare the two configurations, we simulated their characteristic

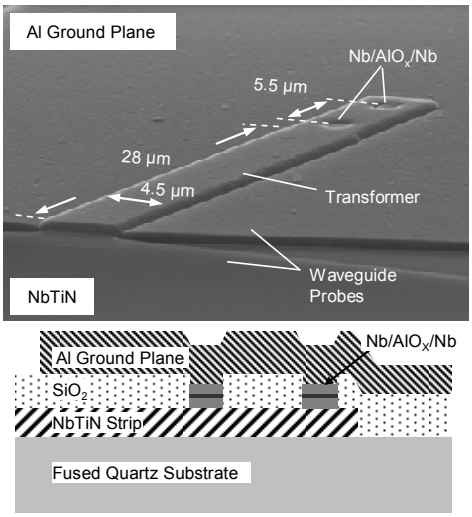

Fig. 5-4 A scanning electron microscope image and cross-sectional sketch of the twin-junction circuit.

impedance Z_0, effective dielectric constant ε_{re}, and RF losses on the basis of analysis method using the high-frequency structure simulator (HFSS). Parameters used for the simulation are listed in Table 5-I. The surface impedance of the NbTiN film is calculated on the basis of the Mattis-Bardeen theory [16]. As shown in Fig. 5-5, the result shows that the characteristic impedance of the normal and inverted microstrip configurations is almost the same while the difference in the effective dielectric constants, which are related to the wavelength-shortening ratio, is 20 %. In terms of loss, it appears that there is an improvement of 0.1 dB per wavelength for the inverted configuration which makes it a better candidate for tuning circuits at frequencies ranging from 0.7 to 1.2 THz.

Table 5-I Parameters used in the calculation for the inverted and normal microstrip characteristics. Their microstrip structures are described in Fig. 5-4 and in ref. [15]

NbTiN gap frequency:	1.2 THz
NbTiN critical transition temperature:	14.5 K
NbTiN film thickness:	270 nm
NbTiN normal state conductivity at 20 K:	$1.0 \times 10^6\ \Omega^{-1}\mathrm{m}^{-1}$
SiO_2 thickness:	300 nm
SiO_2 dielectric constant:	4.4
Al film thickness:	500 nm
Al conductivity at 4.2 K:	$4.0 \times 10^8\ \Omega^{-1}\mathrm{m}^{-1}$

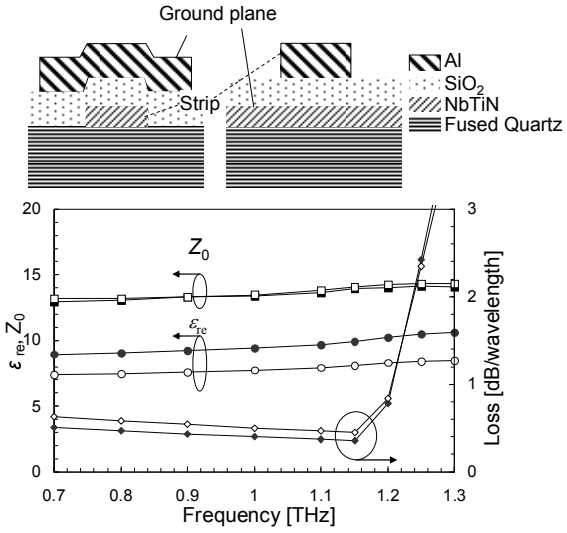

Fig. 5-5 Cross-sectional view of two microstrip configurations. Also shown is comparison of transmission characteristics between normal and inverted microstripline with a 4.5 μm width. Open and filled symbol indicate normal and inverted ones, respectively.

5.2.3 Optimum noise match design based on RF embedding analysis

In our design of the tuning circuit, we adopted Nb/AlO_x/Nb SIS junctions with the size of 1 μm in diameter and a moderate current density of 10 kA/cm^2, for which we can expect high-quality *I-V* characteristics [15]. The specific capacitance of the junctions is assumed to be 85 fF/μm^2 and the tuner length between the junctions was chosen to resonate out their capacitances at 0.87 THz. The twin-junction and the feed point of the antenna is jointed by a quarter-wave impedance transformer, which takes the role of transforming the feed impedance of 30 Ω into an appropriate source impedance seen by the twin-junction. With the aim to achieve both low noise and wideband performances, we use three-port-mixing model to analyze the twin-junction circuit. In general, minimum mixer noise temperature $T_{\min}$ and maximum mixer conversion gain $G_{\max}$ can not be realized simultaneously. This is because for either of the two cases, the optimal source impedances Z_S seen by the twin-junction, defined as $Z_{T\min}$ and $Z_{G\max}$, have different values. Noise and gain performances of the twin-junction circuit are simulated by sweeping the source impedance Z_S on a reflection coefficient plane at the LO frequencies from 0.78 to 0.96 THz. Fig. 5-6 (a) and (b) show

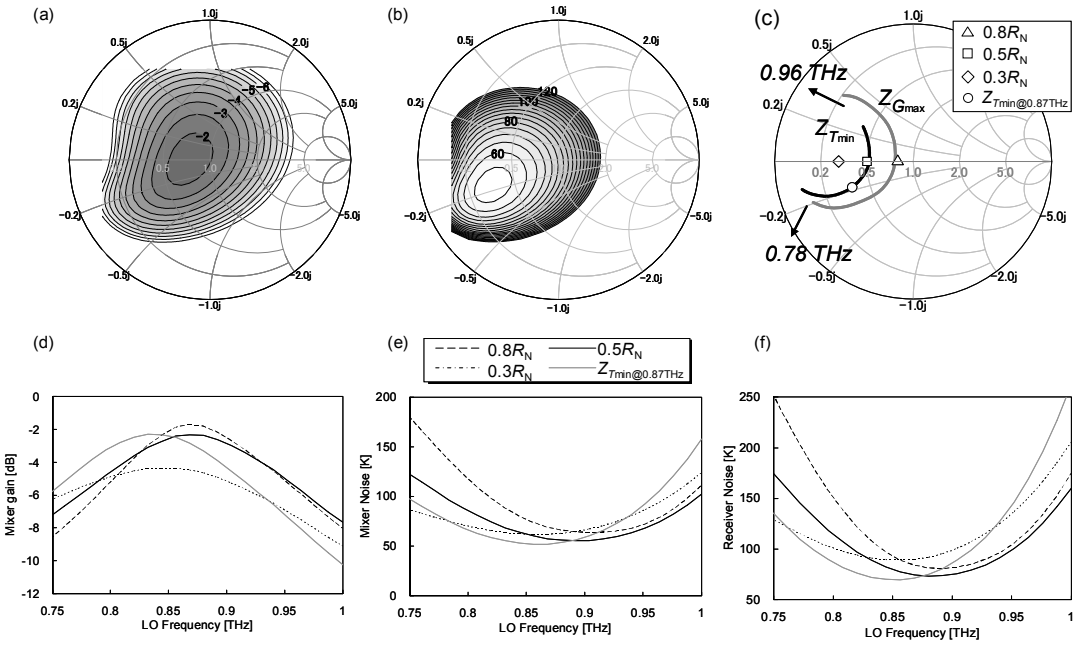

Fig. 5-6 Contours of RF source impedance dependence for (a) mixer noise temperature and (b) mixer gain of twin-junction with critical current density J_c of 10 kA/cm^2 at LO frequency of 0.87 THz. (c) LO frequency dependence of Z_{OG} and Z_{ON} over 0.78-0.96 THz. These smith charts are normalized to the normal resistance R_N of twin-junction. LO Frequency dependence of (d) mixer gain, (e) mixer noise temperature and (f) receiver noise temperature for different source impedances of $0.8R_N$, $0.5R_N$, $0.3R_N$, $Z_{T\min@0.87THz}$. Receiver noise temperature is determined from calculation results of (d) and (e) assuming IF noise temperature of 10 K.

contours of RF source impedance dependence for mixer noise temperature and mixer gain of twin-junction with critical current density J_c of 10 kA/cm^2 at LO frequency of 0.87 THz. (c) shows the LO frequency dependence of $Z_{T\min}$ and $Z_{G\max}$ over 0.78-0.96 THz. Also shown in (d), (e) and (f) are LO frequency dependence of mixer gain, mixer noise temperature and receiver noise temperature when Z_S is set to $0.8R_N$ (~$Z_{G\max@0.87THz}$), $0.5R_N$, $0.3R_N$, and $Z_{T\min@0.87THz}$. Here, $Z_{G\max@0.87THz}$ and $Z_{T\min@0.87THz}$ represent $Z_{G\max}$ and $Z_{T\min}$ at the center of the RF band. For the calculation of the receiver noise temperature the IF load impedance was set to 50 Ω and the IF noise temperature to 10 K at 8 GHz. From Fig. 5-6 (e) we conclude that the value of Z_S should be close to $0.5R_N$, because it offers the lowest receiver noise temperature and the widest RF band. While for a source impedance of $Z_S = 0.5R_N$ the conversion gain is smaller when compared to the case of perfect gain matching ($Z_S = 0.8R_N$), the receiver noise temperature is kept low.

If the feed point impedance is fixed for each mixer chip, it is possible to be transformed by changing a width of the quarter-wavelength transformer. In order to verify the source impedance dependence as above-described, we designed three mixers with transformer widths of 2.5, 3.5, and 4.5 μm to compare the performances, which are named as QB-, QC-, and QD-mixers. Real part of Z_S for QB-, QC-, and QD-mixers approximately correspond to 14.5 (>R_N), 8.9 ($0.67R_N$), and 5.9 Ω ($0.44R_N$) at a LO frequency of 0.87 THz, respectively, as shown in Fig. 5-7 (a). The parameters designed for their mixers are summarized in Table 5-II. We calculated the noise temperature for

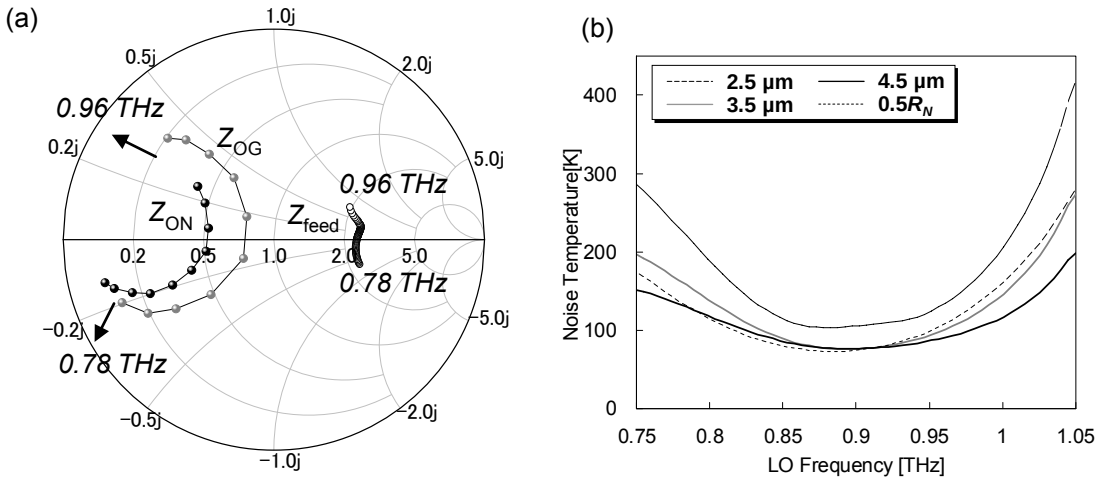

Fig. 5-7 (a) Feed impedance Z_{feed} and three source impedances Z_S transformed by quarter-wavelength microstrip line with widths of 2.5, 3.5, and 4.5 μm in a range of 0.75–1.0 THz. The arrows indicate a direction of frequency increase. (b) Receiver noise temperature for mixers with different impedance transformer width as a function of frequency. It is assumed that the IF load impedance and noise temperature at 8 GHz is 50 Ω and 10 K, respectively. Note that input losses in front of the mixer are not included.

three mixers with the different transformer widths as a function of LO frequency as shown in Fig. 5-7 (b). Not surprisingly, the D-mixer with source impedances close to $0.5R_N$ obtains the widest bandwidth and minimum noise temperature. In addition, it appears that the source impedances transformed by the quarter-wavelength transmission lines make bandwidth wider when compared to the single source impedance of $0.5R_N$, because they draw the impedance locus along the same frequency-increase direction as that of Z_{ON} on the smith chart.

Table 5-II Designed and measured parameters for three mixers. The designs of QB-, QC-, and QD-mixers have only different transformer widths of 2.5 μm, 3.5 μm, and 4.5 μm, respectively. The parameters for the mixers are measured at 4 K.

Design			
Device #	QB	QC	QD
Tuner Length (μm)		5.5	
Transformer Width (μm)	2.5	3.5	4.5
Z_S (Ω)	14.5	8.9	5.9
Junction Size (μmφ)		1.0	
Measurement			
J_C (kA/cm^2)		8	
R_N (Ω)	14.6	15.0	14.8
R_{SG} / R_N	21	17	24
Resonance step (mV)	1.80	1.78	1.80

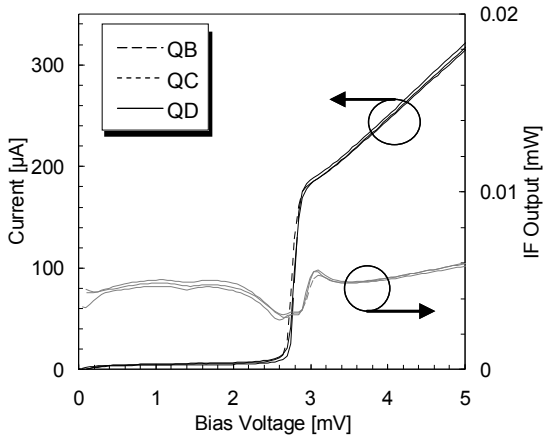

Fig. 5-8 Unpumped current- and IF output power-bias voltage curves for three mixers that have different transformer widths.

5.3 Mixer performance

5.3.1 Source impedance dependence

Fig. 5-8 shows three current-voltage and IF output power-voltage curves obtained for QB-, QC-, and QD-mixers. The parameters measured for their mixers are also summarized in Table 5-II. Their Nb junctions with a current density of 8 kA/cm^2, which is slightly lower than the designed value, showed approximately same characteristics and good *I-V* curves yielding a subgap-to-normal-state resistance ratio of around 20. We observed the resonance steps, which appear as a result of the ac-Josephson effect on the voltage axis, at the range of 1.78–1.80 mV for these mixers. This voltage corresponds to the resonance frequency of 0.87 THz. Fig. 5-9 (a) and (b) show the measured DSB receiver noise temperature and the conversion gain for three mixers, which are calculated on the basis of the Callen&Wellton formula [17] and by ref. [18]. They are corrected for losses in a 12.5-μm-thick polyimide beam splitter and vacuum window. The sharp decreases around LO frequencies of 0.76 THz and 0.98 THz are caused by water absorption. Fig. 5-9 (c) shows the contribution of mixer noise temperature subtracted that of IF noise temperature calculated from the mixer gain and an IF system noise temperature of 11.4 K. The IF system noise temperature is based on the total noise temperature of 9.4 K and the thermal noise of 2 K reflected at the mixer after being

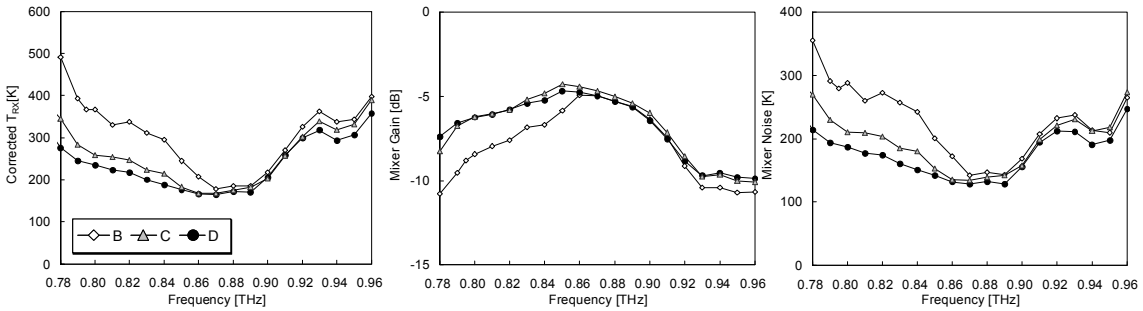

Fig. 5-9 Measured (a) DSB receiver noise temperature, (b) conversion gain, (c) and mixer noise contribution for the three mixers as a function of LO frequency. The receiver noise temperature and the conversion gain are calculated on the basis of the Callen&Wellton formula[10] and by ref. [16], and are corrected for the losses of vacuum window and beam splitter of 12.5-μm-thick polyimide film. Mixer noise contribution is calculated from the measured receiver noise, conversion gain and IF system noise temperature of 11.4 K. Note that the mixer noise contribution includes tuning circuit loss.

generated from the terminated port of isolator. The former is the noise temperature including the equivalent input noise temperature of the cryogenic isolator and the amplifier averaged over 4–12 GHz, which is measured by using cold attenuator (CAT) [18]. The latter assumes that the power reflection coefficients at the mixer and isolator termination temperature are 0.25 and 8 K, respectively. The analysis of the IF noise contribution will be presented in chapter 6.

From Fig. 5-9 (a), we observed approximately the same receiver noise temperature around LO frequency of 0.88 THz and wider bandwidth for QD-, QC-, and QB-mixers. By contrast, it is not entirely true in terms of their conversion gains; the conversion gain of QD-mixer is relatively lower than that of the QC-mixer around the center frequency, as shown in Fig. 5-9 (b). According to Fig. 5-9 (c), the QD-mixer obtains the minimum contribution of the noise temperature and the widest bandwidth. In addition, the mixer has a wider bandwidth in terms of the conversion gain when compared to the QC-mixer.

Since their mixers would have approximately the same parameters in terms of dc *I-V* characteristics (R_N, leakage current, pumped current), RF resonance circuit, and material property, the contributions of their mixer noises should depend only on the differences of source impedance. Therefore, it can be concluded that the Z_S of QD- and QC-mixers are the closest to R_{ON} and R_{OG}, respectively. On the other hand, Z_S of QB-mixer is far from both the parameters. Their experimental results are quantitatively in good agreement with theoretically calculated ones. In addition, the experimental results suggest that, in order to operate the receiver in wide bandwidth and low noise simultaneously, Z_S should be matched with R_{ON} for the resonance circuit.

We also evaluated the QD-mixer chip in more detail by optimizing the bias condition, mixer block, and IF system so as to minimize noise temperature, changing the mixer block into another one. Here the mixer is named as QD-II mixer. This is because we found that the noise temperature

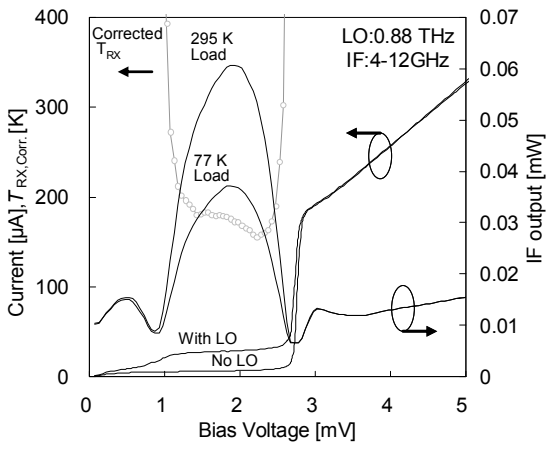

Fig. 5-10 Measured current, IF output power, and corrected noise temperature for the QD-II mixer at 4 K at LO 0.88 THz as a function of bias voltage.

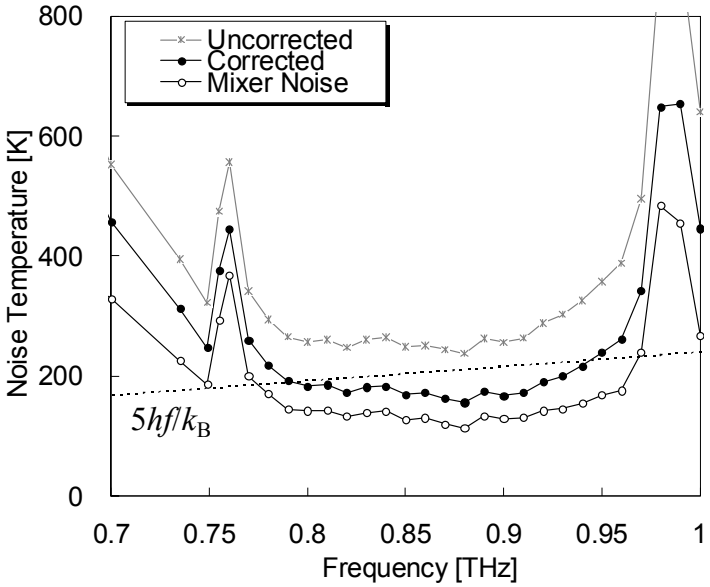

Fig. 5-11 Measured noise temperature as a function of frequency. Note that the mixer noise contribution includes tuning circuit loss.

increase at LO 0.92 THz results from mixer block. Fig. 5-10 presents the measured current, IF output power and corrected receiver noise temperature of the mixer at LO 0.88 THz as a function of bias voltage. The best noise temperature of the mixer showed 156 K. The uncorrected and corrected receiver noise temperatures are plotted in Fig. 5-11 as a function of the LO frequency. The corrected noise temperature of the mixer shows below 200 K (DSB) over the range of 0.79–0.93 THz. This would be the best result arrived so far for mixers over this frequency range at a bath temperature of 4 K. Also shown is break-down of the noise temperature as a function of frequency, which is separated into contributions of the mixer noise and IF noise. It is found that the contribution of mixer noise temperature account for 70–80 % of the receiver noise temperature and is also limiting the operational bandwidth of the receiver. Therefore, in order to obtain the wider receiver bandwidth keeping such a state-of-the-arts sensitivity, intrinsic noise property of the SIS mixer is very important as well as tuning circuit loss, rather than higher J_c junction. This could be obtained not only due to perfect matching to the optimal impedance for minimum mixer noise temperature but also due to high R_{SG}/R_N by improving the junction quality.

5.3.2 Optimal bias point for the receiver noise and the mixer gain

As above mentioned, we showed it was important to match the source impedance to noise optimum impedance. Likewise, SIS junctions should be biased at the noise optimum point. Fig. 5-12 (a) and (b) show contours of mixer gain and noise temperature for different pumped current as a function of bias voltage at LO frequency of 0.88 THz. While the optimum bias voltage for the

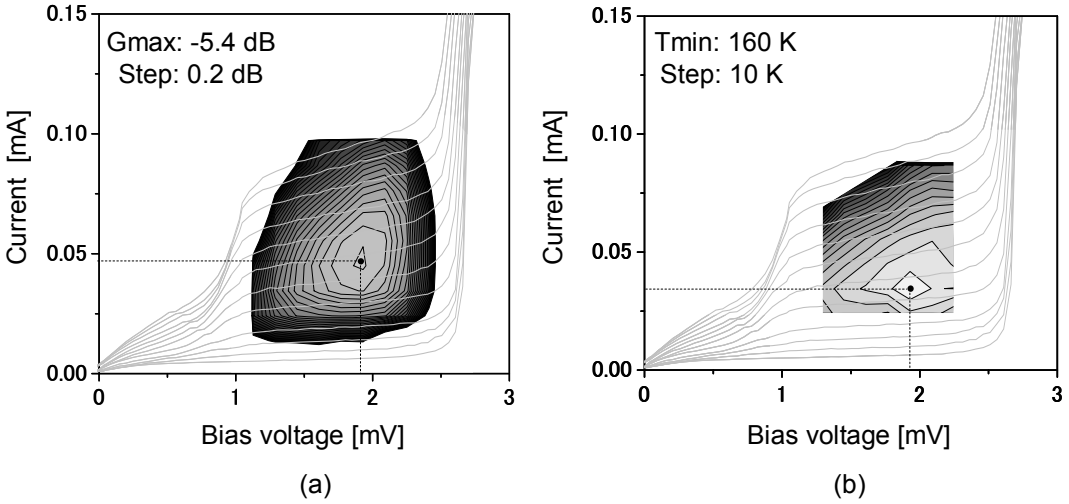

Fig. 5-12 Contours of mixer gain (a) and noise temperature (b) for different pumped current as a function of bias voltage at LO 0.88 THz.

receiver noise temperature almost coincides with the one for the mixer gain, the pumped current for the receiver noise is lower. Although a measure of the LO power has to be applied to obtain higher mixer gain, the current induced by the LO signal increase shot noise in such the situation. This effect is very similar to bias dependence of low-noise amplifiers.

5.4 Fourier transform spectrometer measurement

5.4.1 Fourier transform spectrometer

Fourier transform spectrometer (FTS) is a standard technique for broadband low-resolution spectroscopy in the near-infrared and has recently been used in the submillimeter-wave part of the spectrum [20]-[22]. A coupling measurement with the FTS permits a direct comparison with an analytical calculation of an SIS tuning circuit using *T*-matrix. Since the measurement does not include an information of IF circuits for the mixer, it would be good method to model the RF tuning circuit parameters [23]

An FTS is a Michelson interferometer in which a signal is split and then recombined after having passed trough optical paths of different lengths. The path lengths of the beams are varied and the power of recombined beam is recorded. The interferogram of a broadband source appears as a narrow spike whose peak occurs when the arm lengths are equal: when the arms have equal lengths, or are in the ”zero-phase” position, all the Fourier components add up constructively.

The important specifications of the FTS are its frequency resolution and useful bandwidth. The former is determined by the maximum path length difference x_{max} which determines the maximum

Fig. 5-13 Photograph of a Fourier Transform Spectrometer (FTS) system

time-delay $t_{max}= x_{max}/c$. In the frequency domain a longer span for the time-delay means a narrower convolving function, whose width is $\delta f = 1/t_{max}$. The useful bandwidth is determined by the sensitivity of the detector and the frequency dependence of the optical system. In other words, if the SIS receiver is operated in the direct detection mode and used as the detector, the receiver's frequency response can be characterized easily.

5.4.2 FTS measurement

We performed high frequency tests measured with a FTS system (JASCO FARIS-1) over the range of 100 to 1000 GHz (see Fig. 5-13). The best resolution is 0.25 cm^{-1}, which means a minimum data-point interval of 0.125 cm^{-1} and 3.75 GHz. Note that all results measured with the FTS are convolved with the resolution of the spectrometer. The signal from broadband Hg-arc lamp is detected as an increase in current in the SIS tunnel junction biased at 2 mV. The solid line in Fig. 5-16 has been derived from the measured data by dividing by the measured vacuum window efficiency and the calculated responsivity of the SIS junction in direct detection mode. We now calculate the responsivity of the SIS direct detector [24].

The dc tunneling current is given by Tien and Gordon [25] to be

$$I_{\mathrm{DC}}(V_0, V_{\mathrm{LO}}) = \sum_{n=-\infty}^{\infty} J_n^2(\alpha) \times I_{\mathrm{dc}}(V_0 + nhf/e), \qquad 5\text{-}1$$

where a presents the photon energy normalized pump level

$$\alpha = \frac{eV_\omega}{\hbar\omega}, \qquad 5\text{-}2$$

with $I_{\mathrm{dc}}(V)$ the current of the unpumped SIS junction at bias voltage V_0, and V_ω the applied RF voltage amplitude at frequency ω. For a direct detector the incoming signal is small ($\alpha \sim 0$) so that only single photon processes are relevant and eq. 5-1 reduces to the direct current increase as given

in [6]

$$\Delta I_{\mathrm{DC}} = \frac{V_{\mathrm{LO}}^2}{4} \frac{I_{\mathrm{dc}}(V_0 + n\hbar\omega/e) - 2I_{\mathrm{dc}}(V_0) + I_{\mathrm{dc}}(V_0 - n\hbar\omega/e)}{(n\hbar\omega/e)^2}. \qquad 5\text{-}3$$

The RF impedance Z_{RF}, of the tunnel junction can be calculated from the dissipative currents given by Tucker and Feldman [6] and the applied RF voltage V_{ω}.

$$Z_{\mathrm{RF}}(V_0, V_\omega) = V_\omega \left(\sum_{n=-\infty}^{\infty} J_n(\alpha)\left[J_{n+1}(\alpha) + J_{n-1}(\alpha)\right] I_{\mathrm{dc}}(V_0 + n\hbar\omega/e) \right)^{-1}, \qquad 5\text{-}4$$

which reduces to

$$Z_{\mathrm{RF}} = \frac{2\hbar\omega/e}{I_{\mathrm{dc}}(V_0 + \hbar\omega/e) - I_{\mathrm{dc}}(V_0 - \hbar\omega/e)}. \qquad 5\text{-}5$$

Equations 5-4 and 5-5 are valid if the SIS junction capacitance terminates all harmonic frequencies, which is not entirely satisfied in our case. However, the effects of this are small enough for the more qualitative analysis we are interested in. The responsivity $\Re$ is the ratio of the current increase to the power absorbed by the junction

$$\begin{aligned} \Re &= \frac{\Delta I_{\mathrm{DC}}}{P_{\mathrm{RF}}} \\ &= \frac{e}{\hbar\omega} \frac{I_{\mathrm{dc}}(V_0 + \hbar\omega/e) - 2I_{\mathrm{dc}}(V_0) + I_{\mathrm{dc}}(V_0 - \hbar\omega/e)}{I_{\mathrm{dc}}(V_0 + \hbar\omega/e) - I_{\mathrm{dc}}(V_0 - \hbar\omega/e)} \\ &= \frac{e}{\hbar\omega}\eta \end{aligned} \qquad 5\text{-}6$$

where η represents the quantum efficiency of the direct detector. Fig. 5-14 shows the calculated responsibility of the SIS direct detector as a function of frequency at bias voltages of 1.5, 2.0, 2.5

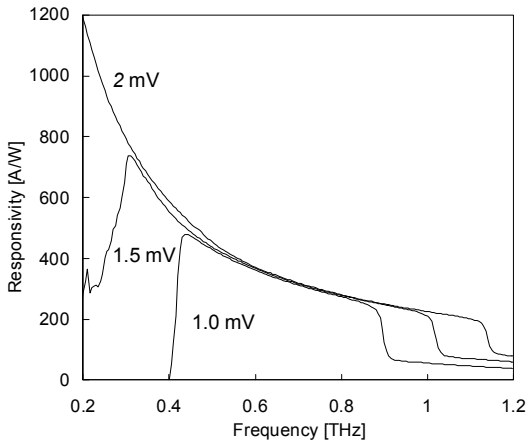

Fig. 5-14 Calculated responsivity of the QD-II SIS junction in direct detection mode. The initial drop off is due to the low dc bias voltage since the photon energy is then too small for photon assisted tunneling.

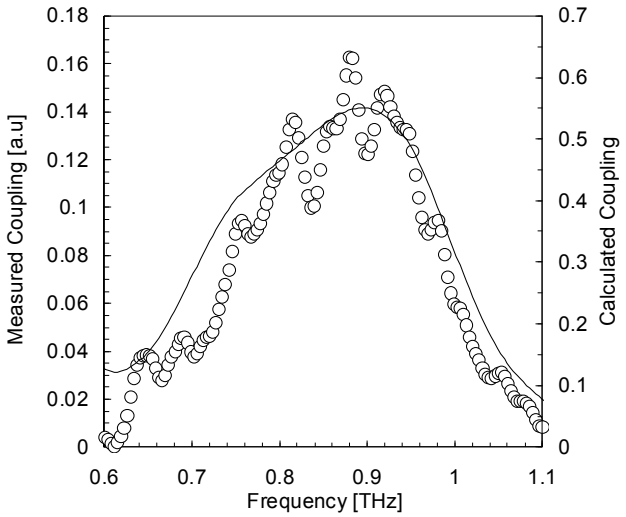

Fig. 5-15 Comparison of calculated coupling (Solid line) and measured (Open circle) by Fourier Transform Spectrometer at 4 K. Measured receiver response is corrected for frequency dependence of the Teflon vacuum window and responsivity of the SIS junctions.

mV. The frequency response of a quantum limited detector above the cut-off frequency is simply f^{-1} up to the gap frequency.

Corrected for the vacuum window efficiency and the responsivity of the SIS junction, the measured data is shown in Fig. 5-15. The direct detection response measured with the FTS is a combination of the coupling efficiency of the receiver optics to the FTS, the frequency response of the matching circuit and the detector, and the vacuum window. Remaining frequency characteristic would depend strongly on matching circuit of the mixer including twin-junction, impedance transformer and waveguide probe. Also shown is the coupling efficiency from the feed point to the junctions to be fitted with measured response. It is calculated using actual parameters, including microstrip characteristic impedance, the junction current density and parameters of Al, SiO_2 and NbTiN in 5.2.2, and specific capacitance as fitting parameter. The measured response is in good agreement with calculated coupling efficiency.

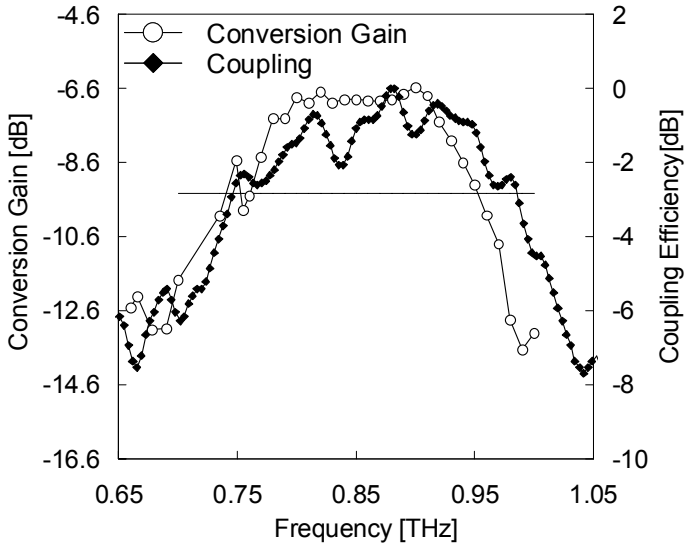

Fig. 5-16 Bandwidth comparison between the measured heterodyne conversion gain and coupling efficiency by FTS. Dashed line is traced to determine 3-dB bandwidth of them.

5.5 Mixer performance analysis

5.5.1 Bandwidth limitation

Fig. 5-16 shows a comparison of bandwidth between heterodyne DSB mixer conversion gain and Fourier Transform Spectrometer (FTS) coupling of the QD-mixer. A 3 dB bandwidth for the FTS responsivity (240 GHz) is significantly 30 GHz wider than one for the conversion gain (210 GHz). Besides, this should be attributed to uniform junction coupling efficiency to frequencies when the junctions detect directly signals. Likewise, this result might also imply that optimal impedances for the direct signal responsivity are larger than ones for mixer conversion gain, whereas they depends on the bias condition.

5.5.2 Estimation of noise parameters for the twin-junction circuit at LO 0.88 THz

In previous section, it was found that the level of the source impedance determined the mixer noise temperature. The results might give us an information of source impedance dependence of noise temperature how degree the source impedance is separated from noise optimal impedance at a LO frequency. In this section, noise parameters of the twin-junction circuit at LO 0.88 THz are estimated. While the noise parameters are usually used to design microwave amplifiers, the concept is firstly applied for SIS mixers by L. R. D'Addario [13].

In order to estimate them, a useful set of noise parameters is (T_{MIN}, R_e, Y_{opt}) such that

$$T = T_{MIN} + \frac{290 R_e}{G_S} \left| Y_S - Y_{opt} \right|^2, \qquad 5\text{-}7$$

where T is the noise temperature of the device and Y_S is input source admittance. T_{MIN} is the

minimum noise temperature, Y_{opt} is the source admittance that achieves this minimum and R_e, is noise equivalent resistance implying a measure of the noise sensitivity. Although a DSB mixer is 3-port device, here the mixer is treated as a two-port linear device.

If we can obtain the four quantities of Y_S and T, it is possible to solve the equation. The corrected noise temperature used for the calculation are those of QB, QC, QD-I and QD-II shown in section 5.3 which are measured at the same bias condition. Y_S for each mixer is deduced from pumped *I-V* curve on the basis of ref. [26] with the SIS mixer analyzer (SISMA) programmed by W. Shan. Note that the deduced source impedance includes uncertainty because a slope of first photon step weakly depends on the source impedance. For more accurate estimation, much more measurement would be needed. The twin-junction circuit parameters obtained by fitting to FTS measurement result are used for the calculation.

In Fig. 5-17, the obtained noise parameters, the deduced source impedances and pumped *I-V* curves for the four mixers are summarized, and also the constant noise circles are plotted every noise temperature of 5 K from 165 K to 190 K. According to the analysis, the obtained Y_{opt} = 1/(5.1+5.2j) involves significant inductive part. This is attributed to slightly larger junction size than the designed. Consequently, the lowest noise temperature for QD-II mixer is likely to be achieved by the low real and proper inductive parts of the source impedance. In this frequency range, since the contribution of the mixer noise temperature accounts for 70-80 % as broken down in section 5.3, the distribution of

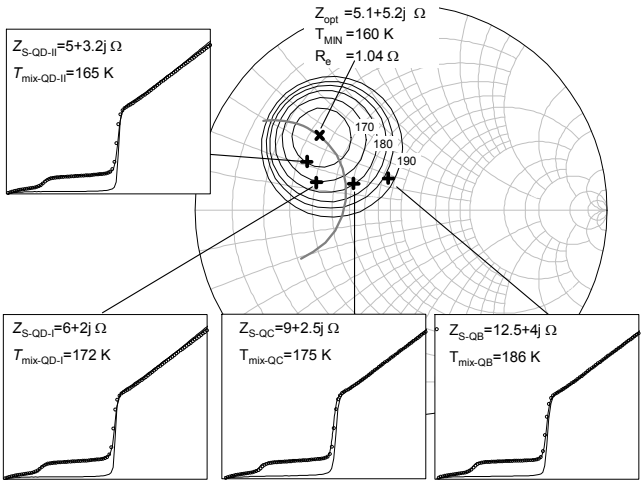

Fig. 5-17 Calculated noise parameters and noise constant circle plotted every noise temperature of 5 K from 165 K to 190 K. Also shown are a relation between source impedance and noise temperature on the Smith chart which is normalized to 14.8 Ohm. The source impedances are deduced from the pumped *I-V* curves on the basis of ref. [26] with the SIS mixer analyzer (SISMA) programmed by W. Shan.

Y_{opt} for the receiver noise temperature on the Smith chart should be almost the same as or very similar to that for the mixer noise temperature. Besides, if the frequency dependence of Y_{opt} is allowed to represent by R and C for the single junction so that the impedance locus passes through $Y_{opt@0.88THz}$ as also shown in Fig. 5-17, they can be are obtained to be 18.2 Ω ($0.6R_N$) and 0.086 pF ($1.1C_J$), respectively. R and C defined here indicate not actual junction impedance but expedient impedance to characterize the frequency dependence of noise optimal impedance. This impedance is away form junction impedance in the frequency range. Therefore, in order to achieve low receiver noise temperature, the source impedance has to be matched to noise optimal source impedance.

Another important parameter of the noise parameters is R_e which determines an interval for each constant noise circle on the smith chart. In this case, lower R_e makes it possible to spread the region of the constant noise temperature circle, and makes the bandwidth wider. This is because the spreading noise constant circle at the band edge approaches the source impedance which is usually away from Y_{OPT}. In above analysis, R_e might not be so low: when the source impedance is set to R_N, noise temperature increase about 50 K compared to the condition setting to Y_{OPT}. The best way to improve R_e is to accomplish a low-loss tuning circuit. For example, R_e would be improved by increasing J_c due to the reduction of losses in the microstrip In addition, higher J_c makes a ωRC product lower. Thus, the two effects may make the RF bandwidth of receiver noise temperature much wider. On the other hand, such a high current density junction has the potential which increases intrinsic mixer noise temperature. Therefore, benefits and disadvantages, that is, trade-off for the high current density junctions should be verified enough by experimental comparison.

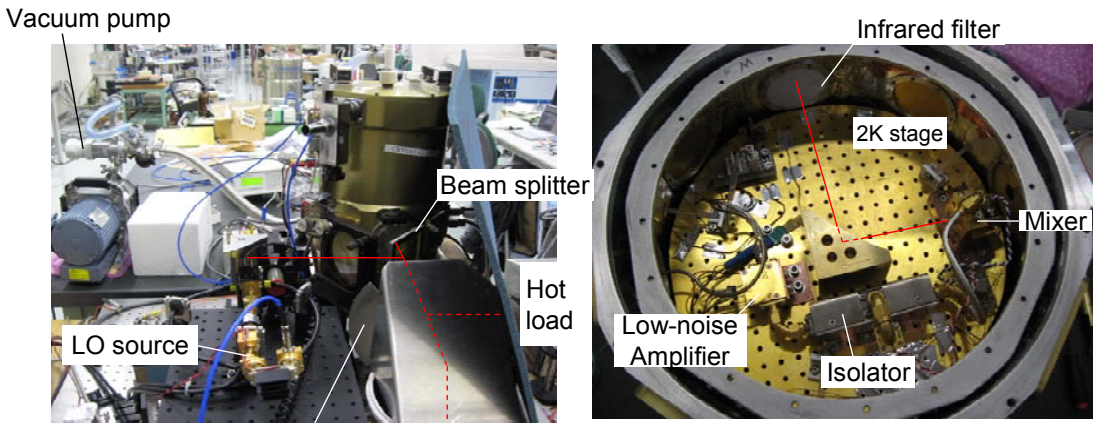

Fig. 5-18 Measurement system at an operating temperature of 2 K using a liquid helium cryostat. LO and RF signals are combined by an 8.5-μm-thick polyimide beam splitter, radiation then enters the cryostat through a 500-μm-thick Teflon vacuum window and a porous Teflon sheet as an infrared filter.

5.6 Performance at an operating temperature of 2 K

The receiver noise performance has been measured at an operating temperature of 2 K using a liquid helium cryostat where the low temperature is reached by pumping on the helium bath as shown in Fig. 5-18. LO and RF signals are combined by an 8.5-μm-thick polyimide beam splitter, radiation then enters the cryostat through a 500-μm-thick Teflon vacuum window and a porous Teflon sheet as an infrared filter. The IF signal is passed through a cryogenic isolator and amplified by the HEMT amplifier over the range of 4–12 GHz. The Nb junctions of the QD-II mixer showed good *I-V* characteristics yielding a subgap-to-normal-state resistance ratio (R_{sg}/R_N) of 37. Fig. 5-19 presents the measured current-voltage characteristics of the mixer with and without LO at 0.88 THz. Also shown is the IF responses to hot and cold loads as a function of bias voltage. The maximum *Y*-factor was 2.84 dB, corresponding to an uncorrected receiver noise temperature of 156 K. The frequency dependence of the noise temperature is shown in Fig. 5-20. Corrected for losses in the vacuum window and beam splitter, DSB noise temperatures are below 150 K over the range of 0.796–0.932 THz with the minimum being 112 K at 0.886 THz.

We estimated losses in the tuning circuit based on experimental data obtained from *Y*-factor measurements at an LO frequency of 0.88 THz. Following a method described in ref. [26], the conversion gain was determined to be -6.1 dB. This value still includes receiver input losses of 0.2 dB due to the vacuum window, 0.3 dB in the beam splitter and 0.2 dB in the 5-mm-length waveguide resulting in a corrected conversion gain of −5.4 dB. Calculations based on the three-port-mixing theory suggest a mixer conversion gain of –4.8 dB where the contribution from the tuning circuit is

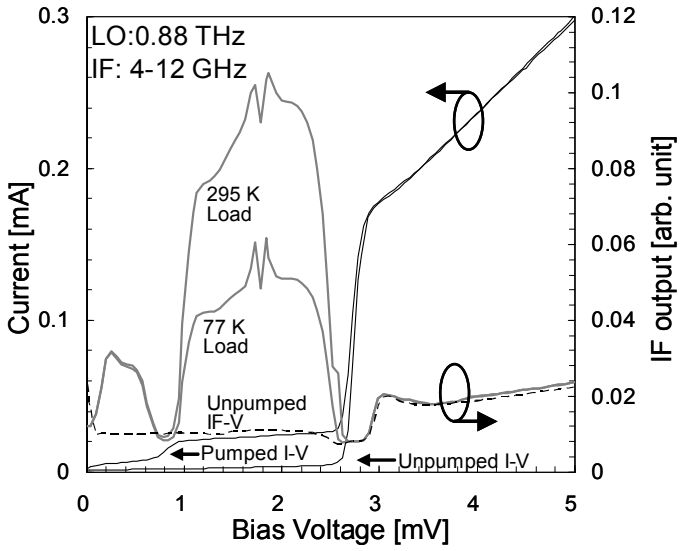

Fig. 5-19 Measured current–voltage and IF output–voltage characteristics of the unpumped mixer at 2K. Also shown are their pumped characteristics at LO 0.88 THz.

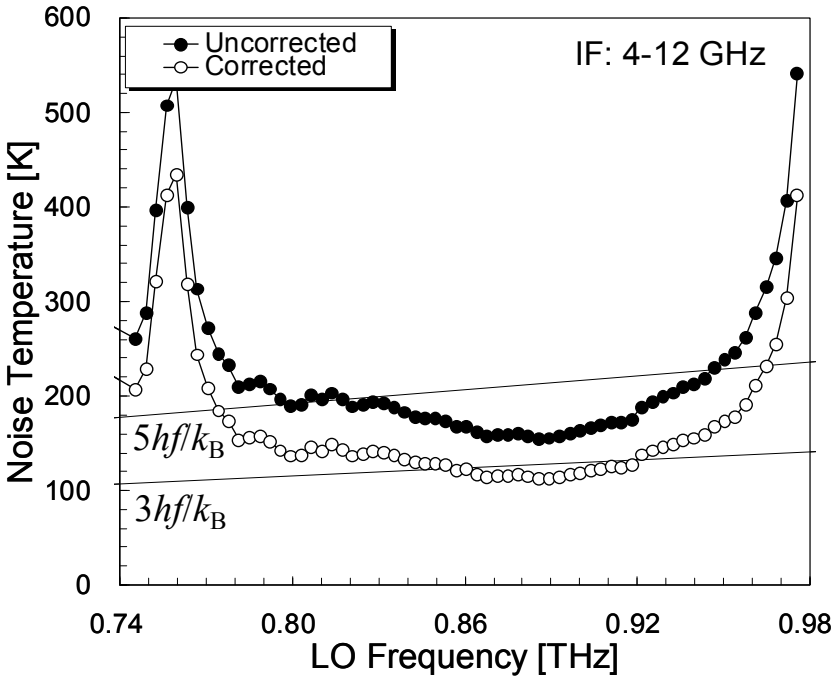

Fig. 5-20 Uncorrected and corrected DSB receiver noise temperature at 2 K. A vacuum window of 500-μm Teflon and beam splitter of 8.5-μm polyimide film were used for the measurement.

−1.4 dB. In this calculation, the source impedance Z_S was deduced by fitting the measured pumped *I-V* curve [26]. The difference of 0.6 dB between measured and calculated mixer conversion may be attributed to additional losses in the receiver optics such as the mirrors, diagonal horn, and water vapor. Therefore, the actual losses in the tuning circuit are likely close to the calculated value [16]. It must be noted that the low-noise operation of the receiver is obtained not only because of the low loss tuning circuit but other factors as well, namely the good reduction of mixer input noise due to the small leakage current.

5.7 Conclusion

We demonstrate a low noise SIS mixer with a low-loss NbTiN/SiO_2/Al microstrip line and Nb/AlO_x/Nb junctions. As a design method for low noise and wideband SIS mixers in this frequency, we suggested the one by sweeping RF source impedance. Three mixer chips with different impedance transformer widths were tested to see the source impedance dependence on the receiver performance. Their experimental results were quantitatively in excellent agreement with theoretically calculated ones. The detailed analysis revealed that the intrinsic noise properties of the SIS mixer

are very important, in order to obtain both the wider bandwidth and state-of-the-arts sensitivity. Finally, the corrected receiver noise temperatures showed below 200 K (DSB) over the range of 0.79–0.93 THz at the bath temperature of 4 K. The best noise temperature of 156 K at the LO frequency of 0.88 THz at 4 K is achieved. In addition, corrected for optical input losses in front of the mixer, DSB noise temperature is below 120 K ($< 3hf/k_B$) around LO frequency of 0.88 THz and at the operating temperature of 2 K. The results represent state-of-the-art performance for mixers in the terahertz frequency range. In addition, it would be also worth to have achieved the wide bandwidth using the moderate junction current density of 8 kA/cm^2 significantly lower than ones pointed out so far.

References

[1] A. Endo, H. Inoue, S. Asayama, T. Noguchi, M. Kroug and T. Tamura, “1Fabrication of aluminum nitride barrier SIS mixer devices using nitrogen plasma diluted by noble gases,” J. Physics: Conf. Series 97, 2008.

[2] J. Kawamura, D. Miller, J. Chen, J. Zmuidzinas, B. Bumble, H. G. LeDuc, and J. A. Stern, ”Very high-current-density Nb/AlN/Nb tunnel junctions for low-noise submillimeter mixers,” Appl. Phys. Lett. 76 (15), 2000.

[3] C. F. J. Lodewijk, O. Noroozian, D. N. Loudkov, T. Zijlstra, A. M. Baryshev, F. P. Mena, and T. M. Klapwijk, “Optimizing Superconducting Matching Circuits for Nb SIS Mixers Operating Around the Gap Frequency,” IEEE Trans. Appl. Supercond., 17 (2), 2007.

[4] A. R. Kerr, and S.-K. Pan, ”Some Recent Developments in the Design of SIS Mixers,” Int. J. lnfrared and Millimeter Waves 11 (10), 1990.

[5] P. Dieleman and T. M. Klapwijk “Shot noise beyond the Tucker theory in niobium tunnel junction mixers” Appl. Phys. Lett. 72 (13), 1998.

[6] J. R. Tucker and M. J. Feldman, “Quantum detection at millimeter wavelengths,” Rev. Mod. Phys. 57, 1985.

[7] B. D. Jackson, G. Lange, T. Zijlstra, M. Kroug, J. W. Kooi, J. A. Stern, and T. M. Klapwijk: IEEE Trans. Microwave Theory Tech.54, 2006.

[8] G. D. Lange, J. M. Krieg, N. Honingh, A. Karpov, and S. Cherednichenko, “Performance of the HIFI Flight Mixers,” Proc. 19th Int. Symp. on Space Terahertz Technology, Groningen, 28-30 April 2008.

[9] T. Kojima, M. Kroug, M. Takeda, Y. Uzawa, W. Shan, Y. Fujii, Z. Wang, and H. Ogawa, “Three Quanta Sensitivity Superconductor–Insulator–Superconductor Mixer for the 0.78–0.95 THz Band,” Appl. Phys. Express 2, 2009.

[10] Qing Ke and Marc J. Feldman, “Optimum Source Conductance for High Frequency Superconducting Quasiparticle Receivers,” IEEE Trans. on Microwave Theory and Tech., 41 (4), 1993.

[11] F. Rice, M. Sumner, J. Zmuidzinas, R. Hub, H. LeDuc, A. Harris, D. Miller, “SIS mixer design for a broadband millimeter spectrometer suitable for rapid line surveys and redshift determinations,” Proc.SPIE 4855, 2003.

[12] W. Shan, M. Takeda, T. Kojima, Y. Uzawa, S. Shi, and Z. Wang, ”Design and Performance of Waveguide Mixers with All NbN tunnel junctions on MgO substrates,” 19th International Symposium on Space Terahertz Technology, Groningen, 28-30 April 2008.

[13] L. R. D’addario, “Noise Parameters of SIS Mixers,” IEEE Trans. on Microwave Theory and Tech. 36 (1),1988.

[14] W. L. Shan, S. C. Shi, T. Matsunaga, M. Takizawa, A. Endo, T. Noguchi, and Y. Uzawa, “Design and Development of SIS Mixers for ALMA Band 10,” IEEE Trans. Appl. Supercond. 17, 2007.

[15] M. Kroug, A. Endo, T. Tamura, T. Noguchi. T. Kojima, Y. Uzawa, M. Takeda, Z. Wang, and W. Shan, “SIS Mixer Fabrication for ALMA Band10,” IEEE Trans. Appl. Supercond. 19, 2009.

[16] D. C. Mattis and J. Bardeen “Theory of the anomalous skin effect in normal and superconducting metals,” Phys. Rev. 111, 1958.

[17] H. B. Callen and T. A. Welton, “Irreversibility and Generalized Noise,” Phys. Rev. 83 (1),1951.

[18] W. Shan, T. Noguchi, S. Shi, and Y. Sekimoto, “Design and Development of SIS Mixers for ALMA Band 8” IEEE Trans. Appl. Supercond. 15, 503, 2005.

[19] J. E. Fernandez, “A Noise-Temperature Measurement System Using a Cryogenic Attenuator,” TMO Progress Report 42-135, 1998.

[20] M. Kawada, H. Takahashi, N. Murakami, Y. Okada, A. Yasuda, T. Ootsubo, H. Kaneda, T. Nakagawa, and H. Shibai, "AKARI Far-IR FTS: A Space Application of the Imaging FTS with Photoconductive Detector Arrays," in Fourier Transform Spectroscopy, OSA Technical Digest (CD) (Optical Society of America, 2009), paper FTuC1.

[21] S. Matsushita, H. Matsuo, J. R. Pardo, S. Radford, “FTS Measurements of Submillimeter-Wave Atmospheric Opacity atPampa la Bola II : Supra-Terahertz Windows and Model Fitting,” Publ. of the Astronomical Society of Japan 51, 1999.

[22] D. F. Santavicca, A. J. Annunziata, M. O. Reese, L. Frunzio and D. E. Prober, “A far-infrared Fourier transform spectrometer with an antenna-coupled niobium bolometer,” Supercond. Sci. Technol. 20, 2007.

[23] B. D. Jackson, A. M. Baryshev, G. de Lange, and J.-R. Gao, S. V. Shitov, N. N. Iosad and T. M. Klapwijk, "Low-noise 1 THz superconductor–insulator–superconductor mixer incorporating a NbTiN/SiO_2/Al tuning circuit," Appl. Phys. Lett. 79, (3), 2001.

[24] T. H. Buttgenbach, H. G. LeDuc, Paul D. Marker, and T. G. Phillips, "A Fixed Tuned Broad-band Matching Structure for Submillimeter SIS Receivers," IEEE Trans. Appl. Supercond. 2, 1992.

[25] P. K. Tien and J. P. Gordon, "Multiphoton Process Observed in the Interaction of Microwave Fields with the Tunneling between Superconductor Films," Phys. Rev. 129, 647 – 651, 1963.

[26] A. Skalare, "Determining embedding circuit parameters from DC measurements on quasiparticle mixers," Int. J. Infrared Millim Waves 10, 1989.

Chapter 6
Consideration of 4–12 GHz optimum IF circuits for the band 10 mixers

6.1 Motivation and Overview

For low noise heterodyne receivers, a first stage of an IF system is one of the important parts as well as SIS mixers. Especially, in this frequency range, the IF noise temperature contributes for about 20-30 % of the receiver noise temperature. Therefore, the first IF of the heterodyne receiver is usually cooled down to cryogenic temperature.

An interesting part of this study is consideration of impedance matching between the SIS mixer and the low noise amplifier. SIS mixers with the high dynamic resistance or negative resistance can make it possible to obtain the intrinsic high mixer gain. However, this makes impedance matching to 50 Ω network difficult and may result in occurrence of the ripple structure for IF characteristics due to standing wave or oscillation due to degradation of the stability factor. An integration of SIS mixer with the amplifier taking into account the impedance matching may be good way to improve the problem not using isolator, as suggested by S.Weinreb [1]. So far, several research institutes have tried to develop the integrated SIS mixer to improve the IF characteristics [2]–[11]. At present, SIS receiver with the extremely wider bandwidth such as 6-18 GHz is being developed [12][13]. However it does not seem to be necessarily that the achievable IF performance for the ALMA specification is obtained.

We used two cryogenic low noise amplifiers (CLNAs) and isolators, to amplify IF signal between 4-12 GHz from the two DSB mixers for the band 10 cartridge. Utilization of the isolators is to endure such multiple reflection and oscillation. In this chapter, we describes design, test and analysis of the low noise first stage of IF system using a state-of-the-art ultra low noise amplifier and low-loss isolator. In addition, improvements of frequency dependence of the receiver noise temperature and output power by detailed system consideration including the SIS mixer will be described.

6.2 Characterization of the IF components

6.2.1 4-12 GHz IF component used for the band 10 receivers

Cryogenic amplifier

To meet the ALMA specifications noise temperature below 230 K and IF flatness within 4.0 dB

per any 2 GHz, and 6.0 dB per any 8 GHz, state-of-art cryogenic amplifiers with ultra-low-noise and wideband performance are required. It is also important that their DC power consumption is enough low to meet the ICD between the cartridge and the cryostat. An MMIC-based InP HEMT amplifier developed by the group at California Institute of Technology led by S. Weinreb seems to be the best candidate for use in the band 10 cartridge [14]. Photographs of the amplifier are shown in Fig. 6-1. The characteristics are shown in later section.

Cryogenic Isolator

Commercially available 4-12-GHz cryogenic isolators by Quinstar technology Inc. will be inserted between the mixers and the CLNAs to ensure the matching between them (see Fig. 6-2). A bias-T is incorporated in the isolator (using an SMA connector on the RF load port to inject the

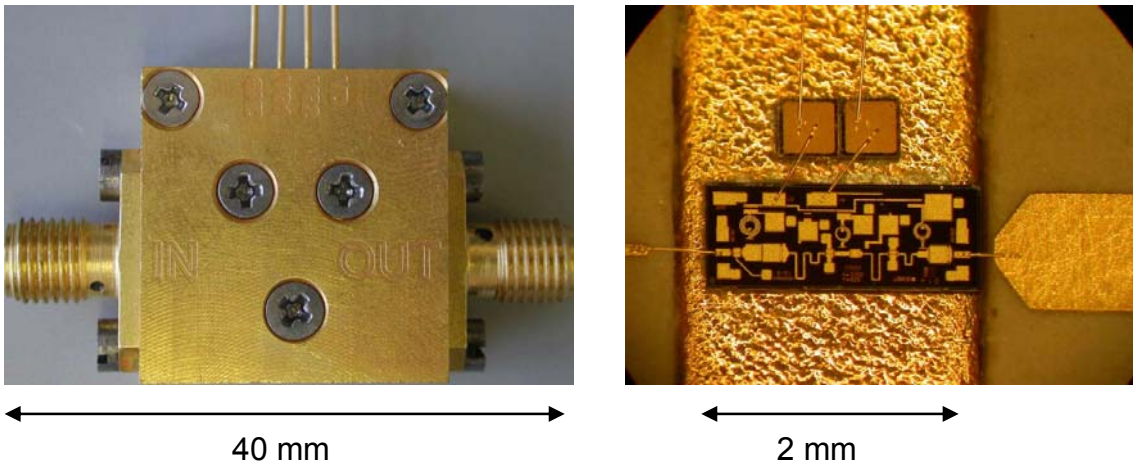

Fig. 6-1 Photographs of a cryogenic ultra-low-noise amplifier made by Caltech.

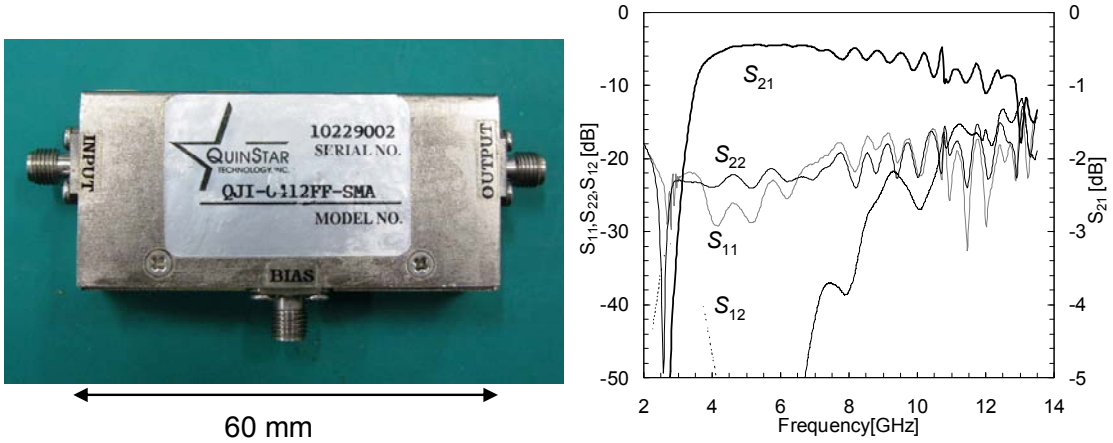

Fig. 6-2 Photograph of 4-12 GHz cryogenic isolator by Quinstar technology Inc. (left) and typical isolator characteristic at a temperature of 5 K. This result was measured by Y. Fujii.

mixer's DC bias). We have measured the performance of a sample device and Fig. 6-2 shows a typical S-parameter of the isolator measured at a temperature of 5 K.

6.2.2 Noise temperature measurement using cryogenic attenuator

To characterize the components, the cryogenic measurements were performed at an operating temperature of 4 K using a cold attenuator (CAT) system [15] in Fig. 6-3. The equivalent noise temperature of the DUT in the system can be expressed as

$$T_{\mathrm{e}} = \frac{T_{\mathrm{sys}} - (L_1 - 1)T_1 - (L_2 - 1)T_2 L_1 - \dfrac{(L_3 - 1)T_3 L_1 L_2}{G} - \dfrac{T_{rec} L_1 L_2 L_3}{G}}{L_1 L_2}, \qquad 6\text{-}1$$

where T_{sys} is the total equivalent noise temperature of the system, G is the gain of the DUT, L_1–L_3 are losses associated with input cable, attenuator, and output cable at physical temperatures of T_1–T_3, respectively, and T_{rec} is the equivalent noise temperature of the noise figure analyzer.

The noise source and instrument used for the measurement is Agilent N4002A 14-dB excess noise ratio (ENR) and Agilent N8975A NF Analyzer, respectively. The input and output cables used cupronickel coaxial cables. L_1–L_3 were measured with vector network analyzer. The measurement of T_2 used Lakeshore 218 Temperature Monitor with a calibrated DT-470 diode sensor fixed on an attenuator holder located on 4-K stage. T_1 and T_3 are estimated to be 55 K from temperature gradient between 300 K and 4 K. The amplifier was connected between the commercial 20 dB attenuator cooled at 4 K and output cable. The typical uncertainty of RSS in the measurement method is within 1.2 K [16]–[20].

The noise temperature data shown in Fig. 6-4 (a) to the amplifiers showed the outstanding performance of 3-6 Kelvin for 4-12 GHz frequency range. Fig. 6-4 (b) shows measured gain with different bias conditions. We found that the optimum operation would be achieved at the condition of

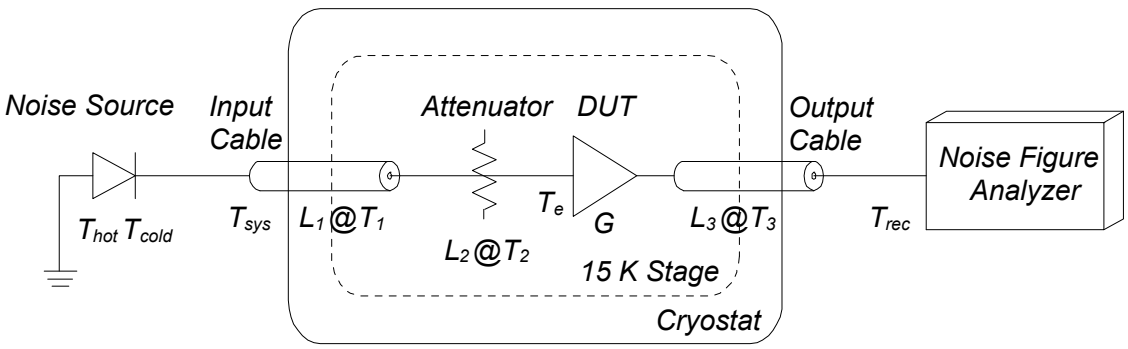

Fig. 6-3 Schematic diagram of cold attenuator (CAT) system

drain voltage (VD) of 1 V and drain current (ID) of 14 mA in the low power consumption regime. In spite of the low power consumption of 14 mW (possible to use on 4 K stage), the gain is between 35.1 and 36.9 dB throughout the measured frequency range.

In addition, we evaluated the IF system characteristic connecting the amplifier with an isolator to see more realistic IF performance. The result showed a little degradation of gain and noise temperature within 10 K at the condition of VD=1 V and ID=14 mA, but still good characteristics (see Fig. 6-5).

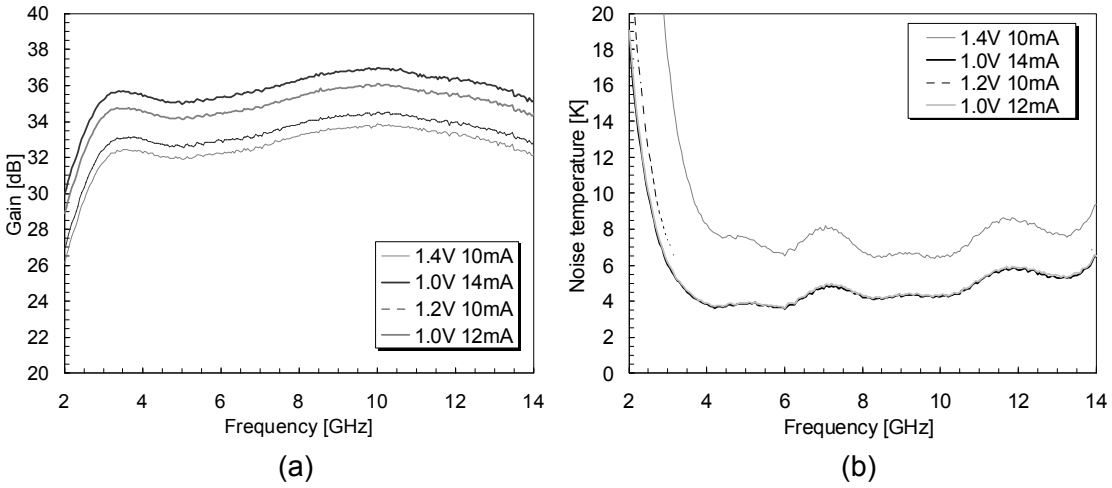

Fig. 6-4 Measured result of a typical 4-12 GHz low noise amplifier for different bias condition.

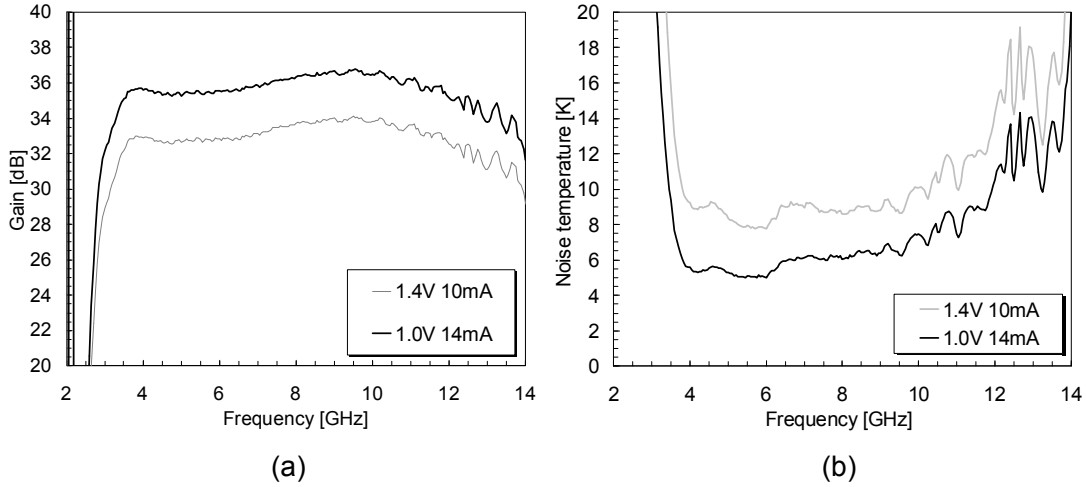

Fig. 6-5 Measured result of a typical IF characteristic for connecting the amplifier with the isolator.

6.3 IF circuits for band 10 SIS mixers

6.3.1 Design of two IF circuits

An IF circuit part of our mixer block consists of a mixer chip slot, bonding wire, IF substrate (matching circuit), and SMA connector (Fig. 6-6). The length of IF substrate can be arbitrarily changed within 9.2 mm. The IF load impedance Y_L seen by the SIS junctions, does not equal 50 Ω with higher frequency in practical case. So we designed two microstrip circuits so as to make the bandwidth wider and analyzed the S-parameter of the circuits between the junctions and output of

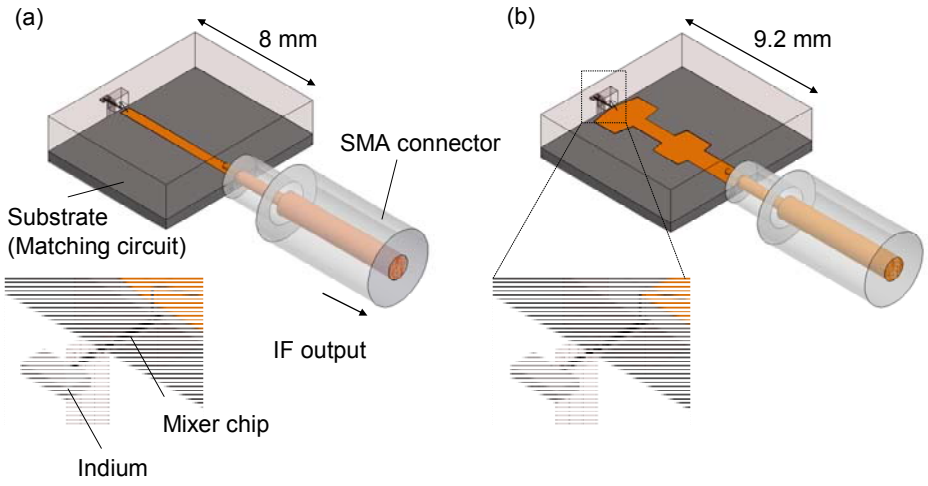

Fig. 6-6 Schematic model of two circuit designs, Design A (a) and Design (b) right

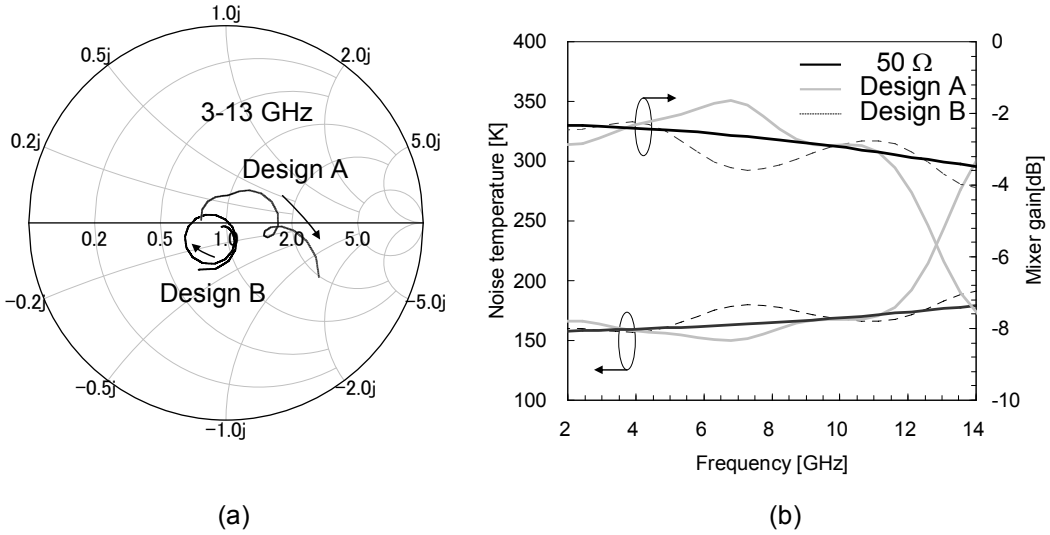

Fig. 6-7 IF load impedance analyzed with HFSS (a) and receiver noise temperature for different circuit designs of A, B, and 50 Ω as a function of IF frequency (b).

the SMA connector with HFSS. A lumped port element is placed on the RF feed point close to the junctions as a source port. Schematic model of two circuit designs and the IF load impedance analyzed are shown in Fig. 6-6 and Fig. 6-7 (a).

6.3.2 Calculation of the receiver noise temperature

In this section, calculation results for the IF dependence of the receiver performance are presented. Mixer conversion gain is computed by taking account into the frequency dependence of Y_L calculated in previous section (Fig. 6-6 (a)) into eq. 2-13. The noise T_{IF} which is generated in IF amplifier is treated as noise added at its input. However, this is not a valid model and does not include some more subtle but important phenomena. One such phenomenon is that some of the isolator's thermal noise can be radiated from its termination port [21]. If the mixer IF output reflection coefficient is imperfect, the noise is reflected back toward the isolator, where it combines with the amplifier noise (In case the mixer and amplifier are directly connected as well, the noise generated at input port of the amplifier is reflected toward the amplifier. The reflected noise is correlated with the amplifier noise). In this case, the effective IF input temperature $T_{eff,IF}$ by adding the noise component reflected from the mixer is

$$T_{eff,\mathrm{IF}} = \left|\Gamma_{\mathrm{mix}}\right|^2 T_{\mathrm{iso}} + T_{\mathrm{IF}}, \qquad 6\text{-}2$$

where T_{IF} is the equivalent noise temperature of IF chain, T_{iso} is the physical temperature of the isolator, and Γ_{mix} is a reflection coefficient depending on dynamic resistance as shown in Fig. 6-8.

$$\Gamma_{\mathrm{mix}} = S_{22,\mathrm{mb}} + \frac{S_{\mathrm{m12}} S_{\mathrm{m21}} \Gamma_{\mathrm{mix,output}}}{1 - S_{\mathrm{m11}} \Gamma_{\mathrm{mix,output}}}, \qquad 6\text{-}3$$

where S_{mij} indicates the S parameter of the mixer block and the reflection coefficient $\Gamma_{mix,output}$ at the

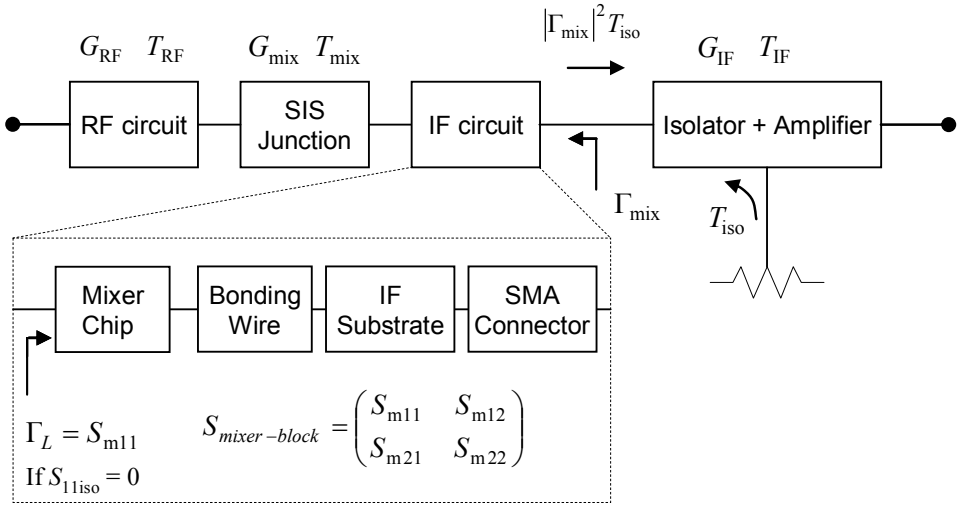

Fig. 6-8 Schematic diagram of IF circuit and the noise components

SIS junction is given by

$$\Gamma_{\mathrm{mix,output}} = \frac{Y_{\mathrm{L}}^{*} - Y_{\mathrm{mix,out}}}{Y_{\mathrm{L}}^{*} + Y_{\mathrm{mix,out}}}, \qquad 6\text{-}4$$

where $Y_{\mathrm{mix,out}}$ is obtained by subtracting the IF load admittance from the total mixer admittance at the IF frequency:

$$Y_{\mathrm{mix,out}} = \frac{1}{Z_{00}} - Y_{\mathrm{L}}. \qquad 6\text{-}5$$

This is approximately mixer dynamic conductance, which is simply the slope of the dc *I-V* curve in the presence of the LO drive.

We calculated the IF dependence of receiver noise temperature taking the Junction's parameters which were assumed to be the same as ones in section 5.2. The result calculated is shown in Fig. 6-7 (b).While the noise temperature for Design A is better over entire 4-12 GHz compared to the others instead of the narrowest bandwidth, the one for Design B is worse but the widest bandwidth.

6.4 Measurement results and the analysis

The measurement of the receiver noise temperature used two IF circuit and two sets of the IF chain using one mixer chip. Here, we named the IF sets used for the Design A and B as IF-A and IF-B.

6.4.1 Shot noise measurement

For an SIS mixer without LO pumping, the SIS junction can be treated as shot noise source. It is often used for IF chain calibration or break down of receiver noise [22][23]. Besides, an SIS junction as a noise source is being studied in detail by H. Inoue et al [24]. The merit is that the measurement can be quickly performed using the same measurement set as heterodyne one. The shot noise power density is expressed as

$$T_{\mathrm{shot}} = \frac{e}{2k_{\mathrm{B}}} R_{\mathrm{dyn}} I_{\mathrm{dc}} \coth\left(\frac{eV_{\mathrm{dc}}}{2k_{\mathrm{B}}T_{\mathrm{amb}}}\right), \qquad 6\text{-}6$$

where e is the charge of a single electron, T_{amb} is the ambient temperature and R_{dyn} is the dynamic resistance at the bias point of a voltage V_{dc} and a current I_{dc}. Then, the IF output power observed at instrument is given by

$$P_{\mathrm{IF,OUT}} = G_{\mathrm{IF}} k_{\mathrm{B}} B\left(T_{\mathrm{shot}}(1 - \left|\Gamma_{\mathrm{mix,output}}\right|^2) + T_{\mathrm{iso}}\left|\Gamma_{\mathrm{mix}}\right|^2 + T_{\mathrm{IF}}\right). \qquad 6\text{-}7$$

Adopting this method, we conducted *Y*-factor measurement for the IF noise $T_{\mathrm{IF\text{-}S}}$ with Agilent E4445A Spectrum analyzer. The observed $T_{\mathrm{IF\text{-}S}}$ includes a coupling factor of $1-|\Gamma_{\mathrm{mix,output}}|^2$:

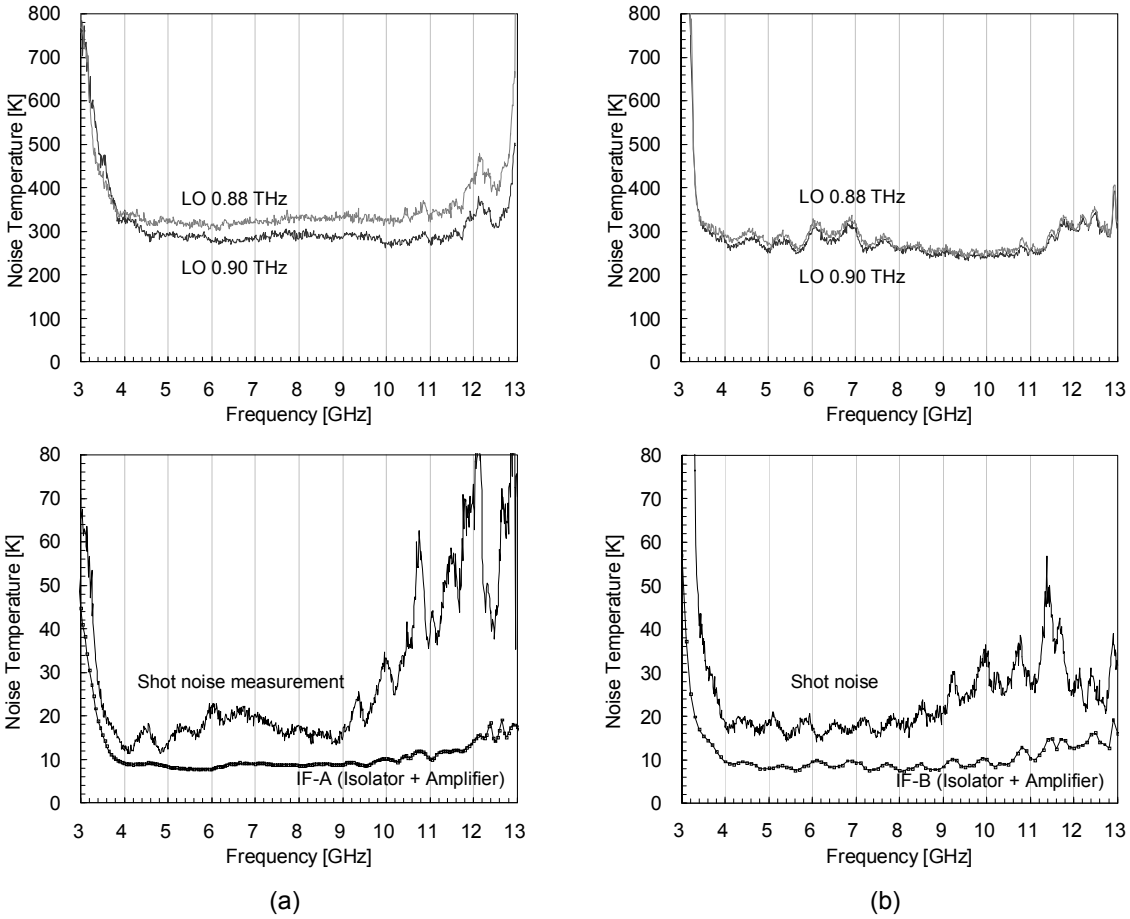

Fig. 6-9 (Uncorrected) Measured receiver noise temperature at LO 0.88 THz and 0.90 THz (above) and IF noise temperatures (below) for the Design A and IF-A (a), and Design B and IF-B (b). Their measurement was performed by using one mixer chip.

$$T_{\text{IF-S}} = \frac{T_{\text{iso}}\left|\Gamma_{\text{mix}}\right|^2 + T_{\text{IF}}}{1-\left|\Gamma_{\text{mix,output}}\right|^2}. \qquad 6\text{-}8$$

Fig. 6-9 (a) and (b) show the $T_{\text{IF-S}}$ measured for IF-A and IF-B using the IF output power at the bias voltages of 6 mV and 4 mV. Also shown is IF total noise temperature including the isolator and amplifier which is measured with CAT system for the sets of IF-A and IF-B. This result will be analyzed and discussed in later section.

6.4.2 Receiver noise temperature for two circuit designs

Receiver noise temperature measurement is performed by *Y*-factor method as the same in previous section. The measurement result is shown in Fig. 6-9 (a) and (b) for the sets of IF-A and IF-B.

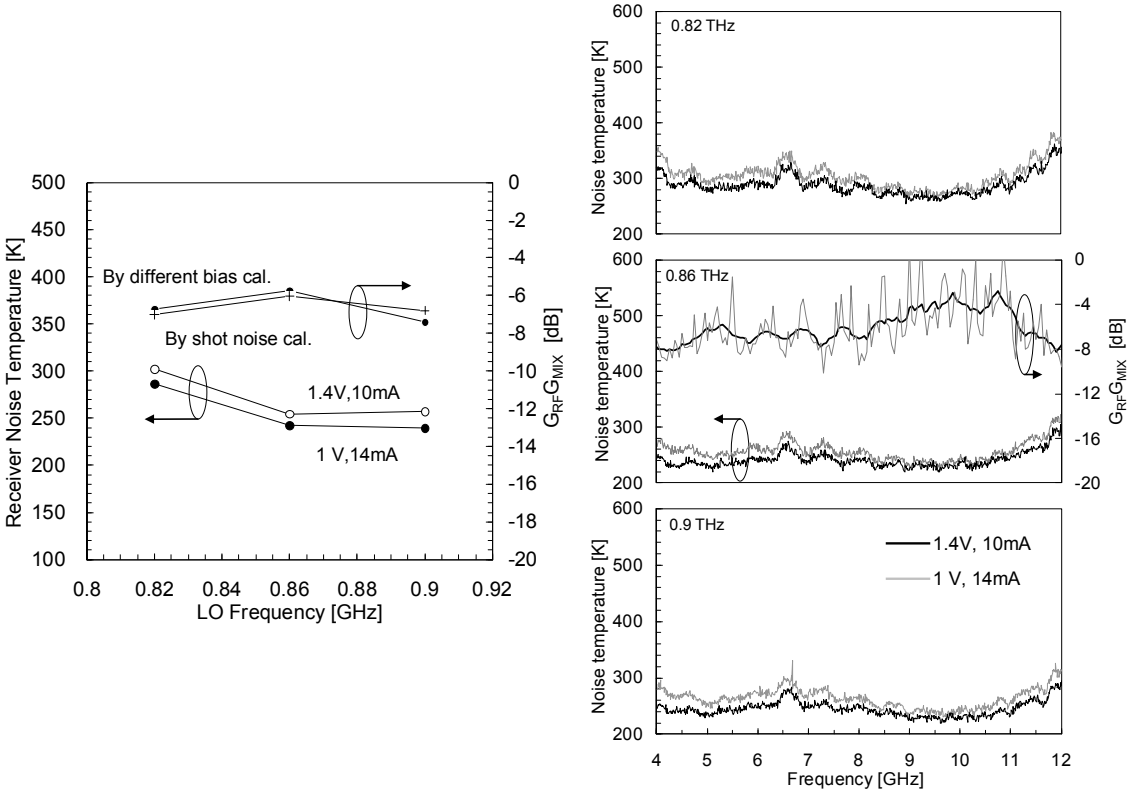

Fig. 6-10 Receiver noise temperature measured in two bias conditions of VD 1.0 V- ID 14 mA and 1.4 V-10 mA of the amplifier as a function of LO frequency (a) and for LO 0.82, 0.86, and 0.9 THz as a function of IF frequency. Also shown is G_{RF} G_{mix} estimated two method by shot noise and different bias of amplifier (a) and G_{RF} G_{mix} as a function of IF frequency (b) . The black line is averaged over ±250 MHz at a frequency.

Note that direct comparison of the noise temperature between the IF sets is difficult, because their measurement condition is not perfectly the same each other in terms of RF waveguide length, IF chain at room temperature, the operating temperature, etc.

6.4.3 Receiver noise temperature for different bias conditions of the IF amplifier

We also measured the noise temperature for the set of Design B and IF-B in different bias conditions of VD 1.0 V- ID 14 mA and 1.4 V-10 mA for the amplifier. The total IF noise temperatures T_{IF} over 4-12 GHz correspond to 6.1 K and 9.4 K which measured with CAT system. Fig. 6-10 (a) shows the receiver noise temperature measured in two bias conditions as a function of LO frequency. It is found that the difference of their receiver noise temperatures is about 15 K. Fig. 6-10 (b) shows the receiver noise temperatures for LO 0.82, 0.86, and 0.9 THz as a function of IF frequency. It was

clear that significant difference was observed involving frequency dependence. This difference should be determined by the product G_{RF} G_{mix} of the mixer gain and RF loss. Since the IF noise temperature in the different bias condition is known by CAT, it allows to be estimated for the product G_{RF} G_{mix} from eq. 1-7 and assuming the no change of effective S_{11} of the isolator:

$$G_{RF}G_{mix} = \frac{T_{IF\text{-}1} - T_{IF\text{-}2}}{T_{RX\text{-}1} - T_{RX\text{-}2}} \qquad 6\text{-}9$$

Comparison of $G_{RF}G_{mix}$ calculated from eq. 6-9 and by shot noise method suggested in section 2.4.1 are shown in Fig. 6-10 (a) as a function of LO frequency. Two $G_{RF}G_{Mix}$ are in very good agreement within the range of ±0.3 dB. In addition, the IF frequency dependence of $G_{RF}G_{mix}$ at LO 0.86 THz calculated by using T_{IF} by CAT system is shown in Fig. 6-10 (b) as well. There is a difference of mixer gain to be −4 to −8 dB within 4–12 GHz, and it is found that the noise temperature is enhanced in frequency of lower $G_{RF}G_{mix}$, as was expected. On the other hand, difference in the frequency where higher $G_{RF}G_{mix}$ of about −4 dB obtained is negligibly-small, because the IF noise is originally very small to be below 10 K.

6.4.4 Analysis

There seems to be distinctive structure among the measured receiver noise T_{RX}, IF noise $T_{IF\text{-}S}$ measured by shot noise method, and IF noise T_{IF} measured by CAT in Fig. 6-9 (a) and (b). For example, in terms of Design B (see Fig. 6-9 (b)), it is not necessarily that the peak frequencies of the ripple in IF noise T_{IF} are coincided with the ones in the receiver noise T_{RX}. Besides, even though the ripple in receiver noise T_{RX} is caused by the one in the IF noise T_{IF}, it would be difficult to interpret the peak-to-peak value of about 30 K from that of 0.5–1 K. The ratio corresponds to the mixer gain of −15 to −18 dB. Meanwhile in terms of Design A (see Fig. 6-9 (a)), the receiver noise temperature increases at around 12.5 GHz, while such increase cannot be expected from IF noise as well. Therefore, the ripple and noise increase of receiver noise would not depend on the only frequency dependence of IF noise. In Fig. 6-9 (b), the interval of the ripple is about 0.75 GHz which corresponds to the length of about 200 mm in free space wavelength. This length may approach that of Teflon coaxial cable to connecting between the mixer block and isolator.

We measured S_{11} of the isolators including the input cable at the cryogenic temperature. We used a very short input cable in the cryostat and calibrated it at room temperature, assuming little change of the propagation constant. Fig. 6-11 (a) and (b) show S_{11} in dB of the isolators used for the IF-A and IF-B. It is found that there are frequencies worse than return loss of -20 dB. In addition, we computed both IF noise temperature by shot noise $T_{IF\text{-}S}$ and receiver noise temperature T_{RX} by taking into account S_{11iso} of the isolators and IF total noise temperature T_{IF}.

$$\Gamma_{L,total} = S_{m11} + \frac{S_{m12}S_{m21}S_{11,iso}}{1 - S_{m22}S_{11,iso}} \qquad 6\text{-}10$$

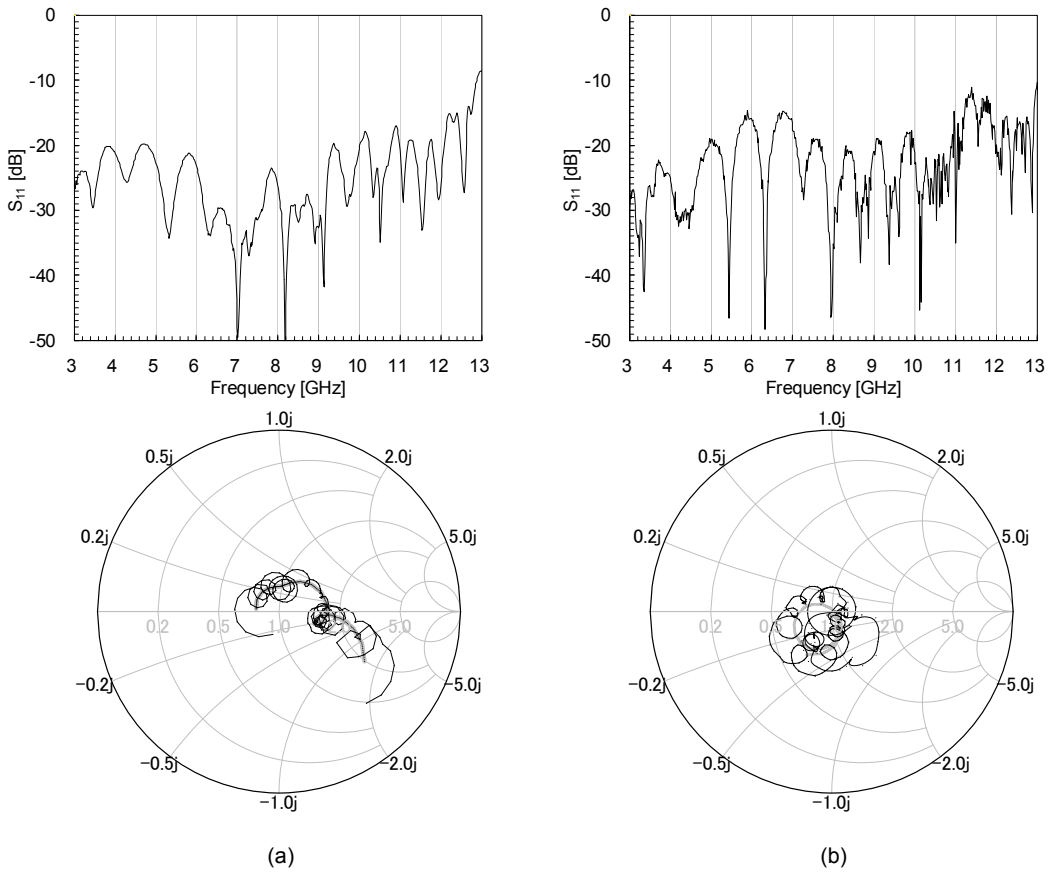

Fig. 6-11 S_{11} in dB of the isolators used for the IF-A (a) and IF-B(b) (above) and Γ_{Ltotal} taking into account $S_{11\mathrm{iso}}$ (below) over the 3-13 GHz.

$$Y_{\mathrm{L,total}} = \frac{1-\Gamma_{\mathrm{L,total}}}{1+\Gamma_{\mathrm{L,total}}}. \tag{6-11}$$

Then $T_{\mathrm{IF\text{-}S}}$ can be represented by

$$T_{\mathrm{IF\text{-}S}} = \frac{1}{1-\left|\Gamma_{\mathrm{mix,output}}\right|^2}\left(\frac{T_{\mathrm{iso}}\left|\Gamma_{\mathrm{mix}}\right|^2}{\left|1-\Gamma_{\mathrm{mix}}S_{11,\mathrm{iso}}\right|^2}+T_{\mathrm{IF}}\right). \tag{6-12}$$

In the same manner, receiver noise temperature may be given by

$$T_{\mathrm{RX}} = T_{\mathrm{RF}} + \frac{T_{\mathrm{mix}}}{G_{\mathrm{RF}}} + \frac{1}{G_{\mathrm{RF}}G'_{\mathrm{mix}}}\left(\frac{T_{\mathrm{iso}}\left|\Gamma_{\mathrm{mix}}\right|^2}{\left|1-\Gamma_{\mathrm{mix}}S_{11,\mathrm{iso}}\right|^2}+T_{\mathrm{IFtotal}}\right), \tag{6-13}$$

G'_{mix} should be taken into account frequency dependence of $Y_{\mathrm{L,total}}$. Comparison of $T_{\mathrm{IF\text{-}S}}$ and T_{RX} between the calculation and measurement is shown in Fig. 6-12. For the calculation of the receiver noise temperature it is assumed that $T_{\mathrm{RF}} + T_{\mathrm{mix}}/G_{\mathrm{RF}}$ = 200 K (for design A), 225 K (for design B),

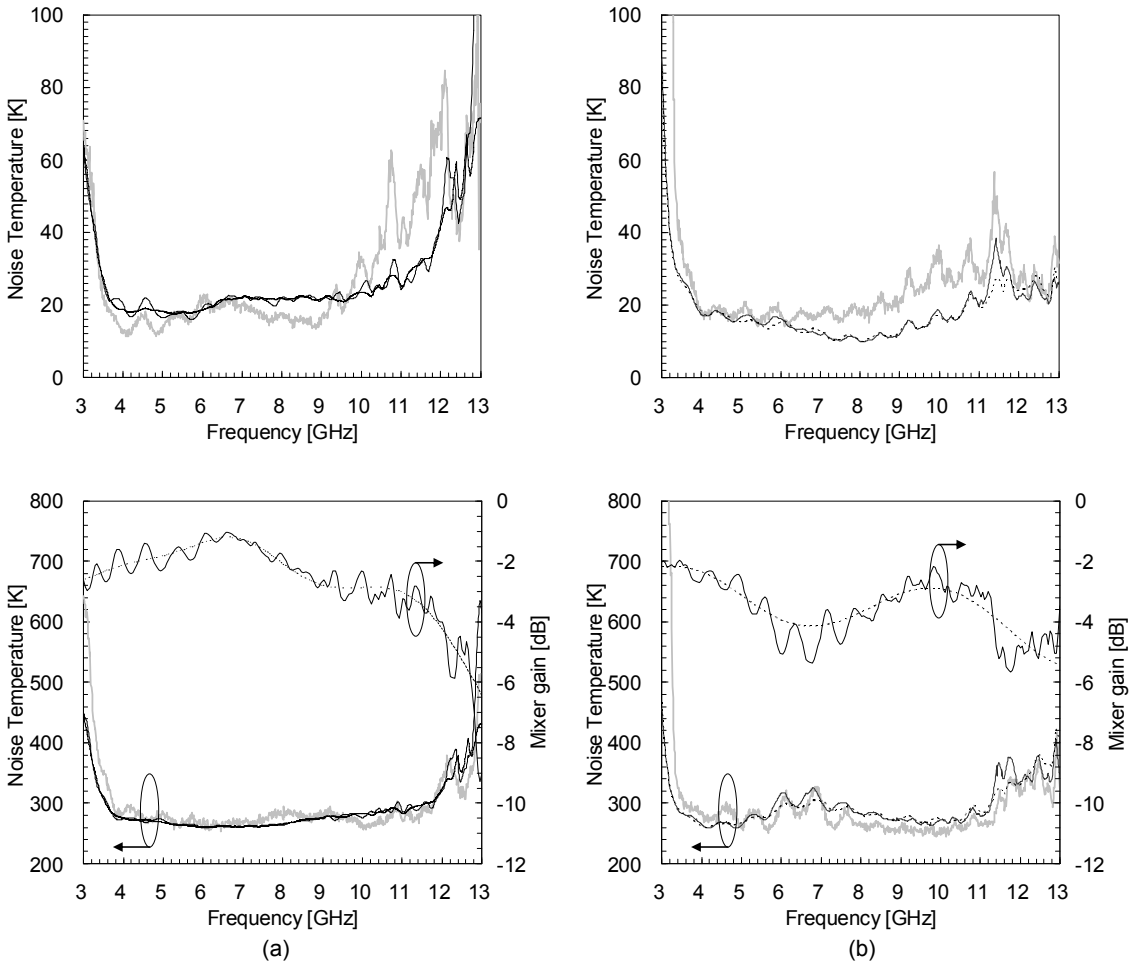

Fig. 6-12 Comparison of $T_{IF\text{-}S}$ (above) and T_{RX} (below) between the calculation (gray line) and measurement (black line) for the Design A (a) and Design B (b). Solid and dashed line indicate taking or not into account S_{11iso}. Also shown is mixer gain calculated on the basis of three-port-mixing theory.

G_{RF} = –4 dB, and T_{iso} = 8 K. The $T_{IF\text{-}S}$ calculated is not in so good agreement with the measured one, so we may need to study more detail. However, their top and bottom peak frequencies would show good agreement. Meanwhile, the mixer gain was calculated on the basis of the three-port-mixing theory. It is clearly found that the ripples appear in case the S_{11iso} is taken into account. In addition, the receiver noise temperature calculated is in excellent agreement with the measured one for the ripple structure in both amplitude and peak frequency.

As a result, we found the ripple structure and unexpected noise increase in the noise temperature depends on two causes:

1. relatively low mixer gain in IF band
2. ripple in intrinsic mixer gain derived from high dynamic resistance and worse S_{11iso}.

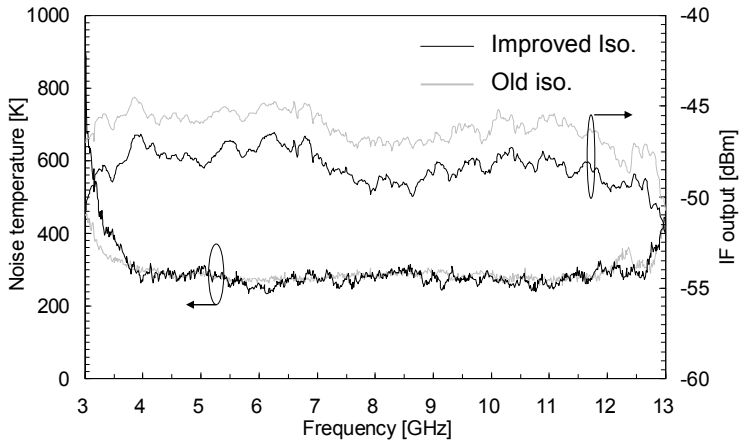

Fig. 6-13 Comparison of T_{RX} and IF output power in the case of using the improved and old (used for IF-A) isolators at LO 0.88 THz.

A good way to obtain flat IF characteristic is utilization of higher current density junctions. That would be useful to make the noise temperature flatter because of smaller dynamic resistance and higher mixer gain. Another is to develop wideband isolators keeping S_{11iso} below −20 dB.

6.5 Improvement of IF characteristics

In previous section, although having said that the receiver noise temperature for design A increase around 12 GHz, the flatness was almost perfect. However, whether the increase is improved may be one of the interests. According to our analysis, the increase was attributed to the mixer gain degradation due to worse S_{11iso} of the isolator. So we prepared an improved isolator with the good return loss below −18 dB by Quinstar technology Inc and measured the receiver noise temperature. Fig. 6-13 shows comparison of T_{RX} and IF output power in the case of using the new and old (used for IF-A) isolators at LO 0.89 THz. It can be found that the increase of T_{RX} around 12 GHz is improved, while small ripple in the new one depends on RF parts. The improvement of the ripple indicates that we should pay attention to S_{11iso} when we design the wideband IF system. In addition, the flatness of the output power within 3.5 dB was obtained in peak-to-peak over 4-12 GHz, which satisfied the ALMA specification.

6.6 Conclusion

In this chapter, design, test and analysis of the low noise first stage of IF system using a state-of-the-art ultra low noise amplifier and low-loss isolator was presented. The first IF components and IF chain was evaluated by CAT system, and we found the best condition to achieve both low noise below 10 K and low power consumption of 14 mW. The receiver noise temperature for two IF circuit designed so as to achieve wide bandwidth showed excellent flatness up to 12 GHz for the Design A, which was promising results for the ALMA specification. But it was found that there are an unexpected noise increase around 12.5 GHz for the Design A and ripple structure for the Design B from the frequency dependence of the IF noise temperature. On the other hand, receiver noise temperature calculated with the mixer gain taken into account the cryogenic $S_{11\mathrm{iso}}$ was in very good agreement with the measurement. In addition, by changing the isolator to improved one, we have demonstrated an improvement of the flatness of both the receiver noise temperature and the IF output power. Therefore, their structure should be attributed to the worse $S_{11\mathrm{iso}}$ and low mixer gain.

In conclusion, the combination of the Design A and an isolator having return loss below –20 dB is the most promising IF chain for the band 10 receivers. Besides, higher current density junctions would ensure to obtain better IF characteristics because of better matching.

References

[1] S. Weinreb, "SIS Mixer to HEMT Amplifier Optimum Coupling Network (Short Paper)," IEEE Trans. Microwave Theory and Tech. 35 (11), 1987.

[2] S. Padin, D.P. Woody, J.A. Stern, H.G. LeDuc, R. Blundell, C.-Y.E. Tong, M.W. Pospieszalski, “An integrated SIS mixer and HEMT IF amplifier,” IEEE Trans. Microwave Theory and Tech. 44 (6), 1996.

[3] J. E. Fernandez, “A Noise-Temperature Measurement System Using a Cryogenic Attenuator,” TMO Progress Report 42-135, 1998.

[4] S.-K. Pan, A. R. Kerr, M. W. Pospieszalski, E. F. Laurial, W. K. Crady, N. Homer, Jr., S. Srikanth, E. Bryerton, K. Saini, S. M. X. Claude, C. C. Chin, P. Dindo, G. Rodrigues, D. Derdall, J. Z. Zhang and A. W. Lichtenberger, “A Fixed-Tuned SIS Mixer with Ultra-Wide-Band IF and Quantum-Limited Sensitivity for ALMA Band 3 (84-116 GHz) Receivers,” proc. 15th Int. Symp.on Space Terahertz Technology, Northampton, MA, 27-29 April, 2004.

[5] A. R. Kerr , S.-K. Pan, E. F. Lauria, A. W. Lichtenberger, J. Zhang, M. W. Pospieszalski, N. Horner, G. A. Ediss, J. E. Effland, R. L. Groves, “The ALMA Band 6 (211-275 GHz) Side-

band-Separating SIS Mixer-Preamplifier," Proc. 2004 Int. Symp. on Space THz Technology, Northampton, MA, April 2004 available at http://www.alma.nrao.edu/memos/

[6] E. F. Lauria, A. R. Kerr, M. W. Pospieszalski, S. -K. Pan, J. E. Effland, and A. W. Lichtenberger, "A 200-300 GHz SIS mixer-preamplifier with 8 GHz IF bandwidth," Microwave Symposium Digest, 2001 IEEE MTT-S Int. 3, 2001.

[7] G. Engargiola, A. Navarrini, R. L. Plambeck, N. Wadefalk, "SIMPLE 1 MM RECEIVERS WITH A FIXED TUNED DOUBLE SIDEBAND SIS MIXER AND A WIDEBAND INP MMIC AMPLIFIER," Int. J. Infrared and Millimeter Waves 25 (12), 2004.

[8] J. W. Kooi, F. Rice, G. Chattopadhyay, S. Sundarum, S. Weinreb, and T. G. Phillips, "Regarding the IF output conductance of SIS tunnel junctions and the integration with cryogenic InP MMIC amplifiers," Proc. 10th Int. Symp. on Space THz Technology, Charlottesville, March 1999.

[9] A. Baryshev, E. Lauria, R. Hesper, T. Zijlstra, W. Wild, "Fixed-tuned waveguide 0.6 THz SIS Mixer with Wide band IF" ALMA MEMO 429, available at http://www.alma.nrao.edu/memos/

[10] P. Pütz, A. Hedden, P. Gensheimer, D. Golish, C. E. Groppi, C. Kulesa, G. Narayanan, A. Lichtenberger, J. W. Kooi, N. Wadefalk, S. Weinreb, and C. K. Walker, "345 GHz Prototype SIS Mixer With Integrated MMIC LNA," Int. J Infrared and Millimeter Waves 27, 2006.

[11] C. Groppi, C. Walker, C. Kulesa, D. Golish, P. Pütz, P. Gensheimer, A. Hedden, S. Bussmann, S. Weinreb, G. Jones, J. Barden, H. Mani, T. Kuiper, J. Kooi, A. Lichtenberger, T. Cecil, G. Narayanan, "SuperCam : A 64 pixel superheterodyne camera," proc. 18th International Symposium on Space THz Technology, California Institute of Technology, Pasadena, California, March, 2007.

[12] F. Rice, M. Sumner, J. Zmuidzinas, R. Hub, H. LeDuc, A. Harris, D. Miller, "SIS mixer design for a broadband millimeter spectrometer suitable for rapid line surveys and redshift determinations," Proc. SPIE 4855 2003.

[13] F. Rice, H. LeDuc, A. Harris, S. Hu, M. Sumner, J. Zmuidzinas, "Broadband heterodyne SIS spectrometer prototype: first results," NASA TECHNICAL REPORTS SEVER (NTRS) ID 20040139814 October 05, Available at http://ntrs.nasa.gov/archive/nasa/casi.ntrs.nasa.gov/20040139814_2004145197.pdf 2004

[14] S.Weinreb, "Low cost microwave ground terminals for space communications," JPL Technical Reports Server，http://trs-new.jpl.nasa.gov/dspace/bitstream/2014/11315/1/03-1587.pdf.

[15] J. E. Fernandez, "A Noise-Temperature Measurement System Using a Cryogenic Attenuator,"TMO Progress Report 42-135, Nov 1998.

[16] C. Risacher，M. Dahlgren and V. Belitsky"A Low Noise 3.4-4.6 GHz Amplifier," GigaHertz 2001 Symposium, Lund, Sweden, Nov 2001.

[17]N. Wadefalk, A. Mellberg, I. Angelov, M. E. Barsky, S. Bui, E. Choumas, R. W. Grundbacher, E. L. Kollberg, R. Lai, N. Rorsman, P. Starski, J. Stenarson, D. C. Streit, and H. Zirath, "Cryogenic Wide-Band Ultra-Low-Noise IF Amplifiers Operating at Ultra-Low DC Power," IEEE Trans. Microwave Theory and Tech.. 51 (6), 2003.

[18]T. Kojima, Y. Abe, H. Ogawa, "4-12GHz cryogenic low-noise HEMT amplifier [in Japanese]," IEICE trans. electron. C, J91-C (11), 2008.

[19]M. W. Pospieszalski and E. J. Wollack, "Ultra-lownoise InP field effect transistor amplifiers for radio astronomy receivers," Proc. GaAs 2000 Conference, Paris, France, pp.5-8, Oct. 2000.

[20]I. Lopez-Fernandez, J. D. Gallego, C. Diez, and A. Barcia, "Development of Cryogenic IF Low-Noise 4-12 GHz Amplifiers for ALMA Radio Astronomy Receivers," 2006 IEEE MTT-S Int. Microwave Symp. Dig., pp.1907-1910, June 2006.

[21]S. A. Maas, "Microwave Mixers," ARTECH HOUSE INC. 1986.

[22]W. Shan, Y. Irimajiri, S. Shi, and T. Manabe, "Characterization of the IF Noise of a Submillimeter SIS Receiver," Int. J.Infrared and Millimeter Waves 25 (2), 2004.

[23]D. P. Woody, R.E. Miller, and M. J. Wengler, "85−115-GHz Receivers for Radio Astronomy," IEEE trans. Microwave Theory and Tech. 33 (2),1985.

[24]H. Inoue, T. Noguchi and K. Kohno, "SIS junction as a microwave noise source," J. Phys. Conf. Series, in print

Chapter 7
A low-noise waveguide SIS mixer incorporating 10-dB directional coupler

7.1 Motivation and Overview

In this chapter, we report a demonstration of the low noise waveguide SIS mixer incorporating a 10-dB directional coupler and a LO receiving horn for the ALMA band 10. We are developing band 10 cartridge receivers employing waveguide technologies. As shown in previous chapter, their ultra-low noise performance of NbTiN-based SIS mixers has been demonstrated by using a conventional LO injection scheme with a dielectric thin film. To meet the specification as a receiver system, it is important to demonstrate the feasibility of waveguide technologies at terahertz frequencies by fabrication and testing of waveguide components.

So far, waveguide SIS mixers have been developed for the ALMA receivers because of the reliability and good performance. For example, waveguide corrugated horns have shown excellent beam patterns which are needed to achieve beam efficiencies specified by the ALMA. The waveguide technologies also have an advantage for the stability because of the high mechanical rigidity, especially at short wavelengths of the terahertz frequency. When a thin dielectric film is used for LO injection, it picks up acoustic noise and converts it into an amplitude modulation (AM) of the LO signal due to mechanical vibrations such as closed-cycle cryocoolers [1]. This may result in gain instability at the output of the mixers. A waveguide mixer with a LO injection employing a directional coupler is one of the candidates to solve this problem at terahertz frequencies. However, the waveguide structures become very small to fabricate, and the waveguide losses increase significantly. By detailed design, test, and characterization of the waveguide component, we found the best way to operate the receiver in low noise that a 10-dB directional coupler and a LO receiving horn were integrated for the mixer block.

7.2 Design and evaluation of the waveguide components

7.2.1 Evaluation of WR-1.2 waveguide losses at cryogenic temperature

We use a WR-1.2 rectangular waveguide with a size of 152 μm × 304 μm for transmission of RF and LO signal. In this frequency range, the absorption loss may be no longer negligible even though the waveguide length is shorter. Nevertheless, the loss at this frequencies have never evaluated at

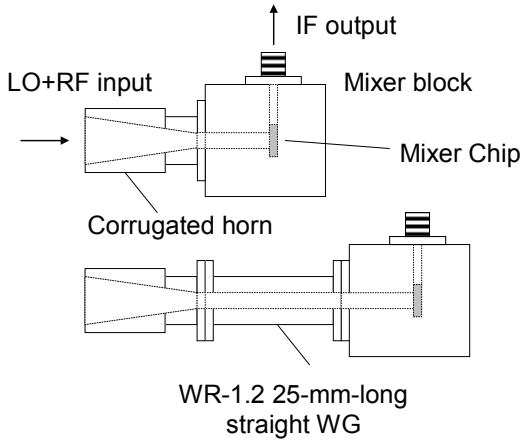

Fig. 7-1 Schematic view of waveguide loss measurement

even room temperature.

We estimated a 25-mm-long waveguide loss at cryogenic temperature. For the measurement, we used an SIS mixer consisted of a corrugated horn and a mixer block, which were connected by a waveguide flange as shown in Fig. 7-1. The transmission loss of the waveguide was simply estimated by comparing the mixer gains in the case with and without the waveguide between the mixer and the horn. Fig. 7-2 (a) shows current- and IF output power-voltage characteristics in the two measurements. It is found that the IF output power for both hot and cold load radiation in the case with the waveguide drops compared the one to without it. This should be caused by the waveguide a loss. Fig. 7-2 (b) shows the LO frequency dependence of the measured mixer gains and the estimated transmission. The loss is calculated by subtracting the mixer gain with the waveguide from the one without it. It was found that there is the waveguide loss of about 1.2 dB/25 mm. A modular type of waveguide components has signal path lengths of 20-30 mm, typically, which causes noise temperature increases of 20-30 %.

In addition, we performed theoretical calculation to confirm whether the losses at the cryogenic temperature are valid. According to ref. [2], the absorption loss of a fundamental TE_{10} mode in the waveguide can then be related to the skin depth and surface roughness by a Local limit:

$$\alpha = 8.876 \cdot \frac{\lambda}{b\lambda_g} \cdot \left(\frac{\pi}{\lambda \cdot \eta \cdot \sigma} \right)^{1/2} \cdot \left[1 + \left(\frac{\lambda_g}{\lambda_c} \right)^2 \cdot \left(1 + 2\frac{b}{a} \right)^2 \right], \text{dB/m} \qquad 7\text{-}1$$

where λ is the free space wavelength; λ_g is the waveguide wavelength in waveguide of width, a, and height, b; σ is the conductivity of the wall material and η is the impedance of free space ($120\pi\ \Omega$). The effect of the surface roughness should be included using a quasiempirical formula [3].

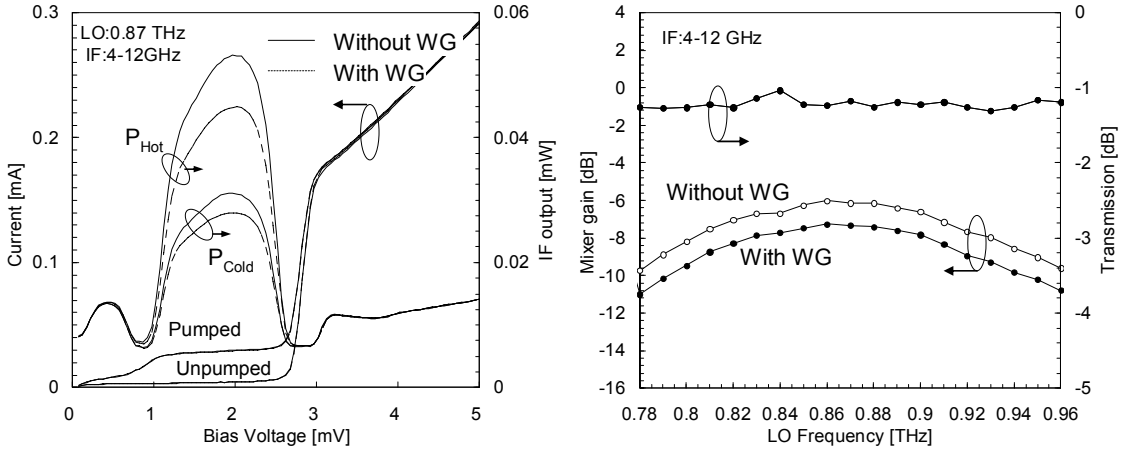

(a) (b)

Fig. 7-2 Current- and IF output-voltage characteristics in the case with and without a WR-1.2 25-mm-long waveguide at LO 0.87 THz (a). The *I-V* curves are in good agreement, and this implies that the SIS mixer is under the same condition between their measurements. Measured mixer gains with and without the waveguide and the transmissions (b).

$$\alpha' = \alpha\left[1 + \frac{2}{\pi}\arctan\left(1.4\left(\frac{\Delta}{\delta_s}\right)^2\right)\right], \qquad 7\text{-}2$$

where δ_s is the skin effect, Δ is the RMS surface roughness. Meanwhile, the conductivity improvement upon cooling depends on the purity of the metal, which relates to Residual Resistance Ratio (*RRR*). Hence, we evaluated *RRR* of a 1-μm-thick gold plate on bulk copper with the sample size of 5.5 mm × 0.6 mm between 300 K and 4 K. *RRR* of the sample was measured to be about 10 with four probe method. If the gold of the electrical conductivity σ is assumed to be 4.5×10^7 S/m [e.g. [4]] and typical surface roughness of 1 μm in the direct machining, the waveguide loss was estimated to be 1.1 dB/ 25 mm. This is consistent with the above measurement. On the other hand, the eq. 7-2 implies the surface roughness is needed to be several tens of nanometers in order to improve the loss significantly. Although micromachining technology offers surface roughness better than 100-nm RMS [5], it is unclear whether significant improvement may not be observed. Therefore, their results suggest that the waveguide coupler in the modular concept is no longer available for this frequency, in other wards; the length should be shorter as possible.

7.2.2 Mixer block design

A DSB mixer block consists of a main body, a back-piece and a superconducting magnetic coil with pole pieces. As shown in Fig. 7-3, the main body incorporates RF and LO ports, a 10 dB

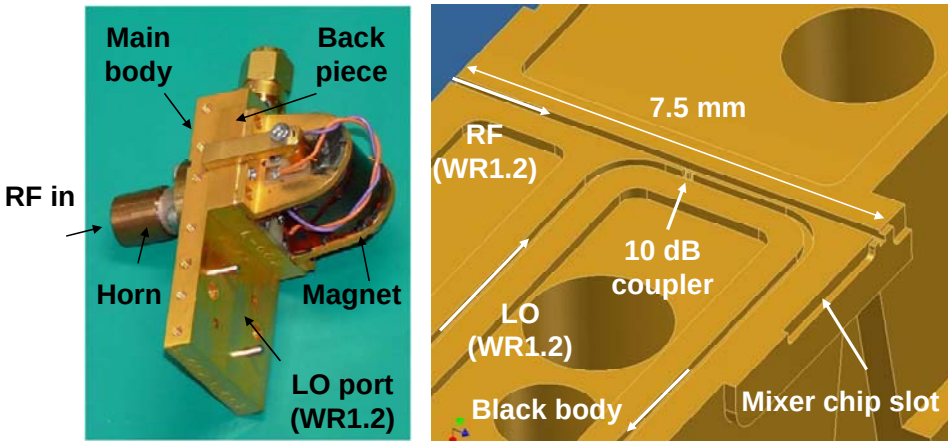

Fig. 7-3 A DSB mixer block configuration. A 10 dB two-branch coupler is integrated in the main body of the block (center-split).

two-branch line coupler and a slot for mounting a mixer chip to avoid the flange mismatch loss and to minimize the waveguide loss. The detailed design of the 10-dB coupler will be described in later section. The RF and LO signal paths of the waveguide is 7.5 mm and 31 mm long, and then the Ohmic loss is therefore estimated to be 0.4 dB and 1.5 dB at 4 K, respectively. It is expected that the noise temperature of more than 20 % is improved because of the shorter waveguide length, compared to one in the case using the modular type of the coupler. The corrugated feed horn is connected to the RF port of the mixer block with the WR-1.2 waveguide. An LO signal is injected from the LO port of the block with the WR-1.2 waveguide. This injection scheme is selected as based on later consideration. An RF signal from the feed horn and the LO signal are coupled by the 10 dB coupler in the block, and then transmitted to a mixer chip mounted in the chip slot in a microstripline configuration by using an indium contact. Remaining LO power is absorbed by a blackbody placed at the end of the waveguide.

7.2.3 10 dB coupler design

As the coupling of around 20 dB is employed in millimeter wave region, a LO signal should be weakly coupled with RF signals to avoid increases of input equivalent noise temperature due to LO amplitude modulation (AM) noise from LO port and due to the RF coupling loss in front of the mixer. In the ALMA band 10 frequency, despite a fact that the LO power to drive an SIS junction is needed to be about 0.5 μW for the low noise operation, we can obtain little LO output power of 20 μW at most as a realistic power.

Fig. 7-4 shows calculated the receiver noise temperature at LO 0.87 THz as a function of coupling in the directional coupler, using losses estimated in RF and LO signal path listed in Table I, when the obtained LO power are 5, 10 and 20 μW respectively at the mixer block. The mixer calculated is taken account into the same parameters as one designed in [6]: junction current density of 10 kA/cm^2, junction size of 1 μmϕ, IF load impedance of 50 Ω, and tuning circuit loss. In this calculation, thermal noise from LO port is neglected. The result shows that the noise temperature increases below the 10-dB coupling and above the 20-dB one due to the RF transmission loss in the coupler

Table 7-I Losses in RF and LO paths used for the calculation of noise temperature and LO power consumption in junctions

	Loss in RF path [dB]	Loss in LO path [dB]
Warm Optics (295 K)	0.1	
Infrared filter (110 K)	0.2	
Cold Optics	0.2	
Waveguide	0.3	1.5
Coupler	10log(1-x)	10log(x)
Tuning circuit	1.5	1.5
Junction coupling		0.7

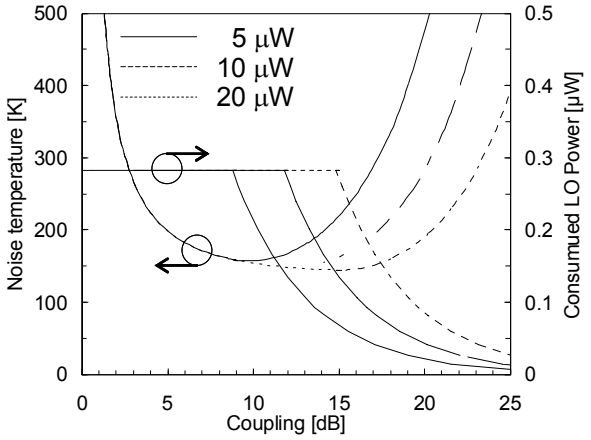

Fig. 7-4 Receiver noise temperature and consumed LO power in the SIS junctions as a function of coupling in the directional coupler, when LO power of 5, 10, 20 μW can be obtained, respectively. Parameters of the SIS mixer are summarized in ref. [6]. In terms of consumed LO power in the junction, flat area indicates that LO power is enough to pump the SIS junctions due to strong coupling.

and the lack of LO power, respectively. Even though the LO power of 10 μW can be obtained, the noise temperature seems to be degraded by 10 % even in 15-dB coupling due to the lack of LO power, compared to the best driven condition. As a result, we choose 10-dB coupling to have a margin for the lower LO power and for a higher current density junction involving low normal resistance.

We designed a 10-dB directional coupler composed of 2-branch line and WR-1.2 (304 μm×152 μm) waveguide. The base design was by S. Asayama. In order to simplify the design and fabrication of the blanch lines, they are optimized with High Frequency Structure Simulator (HFSS), and then made all the branch lines the same of equal length and spacing suggested in [7] . A tolerance analysis of the coupler has shown that the performance degrades unacceptably if all dimensions are produced exceeding a linear error of 5 μm. Although fabrication by a micromachining technology offers accuracy better than 2 μm [5], the recent machining technology makes it possible to fabricate such small waveguide components with the size of down to several tens of microns. The dimension simulation, and evaluation results will be shown in next section.

7.2.4 Evaluation of the 10 dB coupler at room temperature

A 0.9-THz vector network analyzer (VNA), which was a test equipment modifying a near-field beam pattern measurement system in ref. [8], was used for evaluations of the 10-dB coupler at room temperature as shown in Fig. 7-5. The VNA with dynamic range of around 40 dB consists of a W-band Gunn oscillator followed by a nonupler as a transmitter and subharmonic Schottky diode mixer pumped by another W-band Gunn oscillator as a receiver. Both Gunn oscillators are phase-locked to a single microwave reference, but on different sideband. The device under test (DUT) is put between the transmitter and the receiver and the insertion loss is measured.

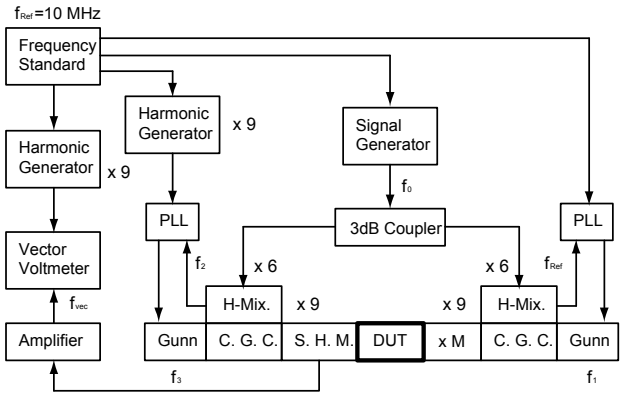

Mf1(GHz)	826.11
f1(GHz)	91.79
f3(GHz)	91.78
f0(MHz)	15.3
f2(MHz)	20
fvec(MHz)	90

Fig. 7-5 Block diagram of the 0.9-THz band vector network analyzer.

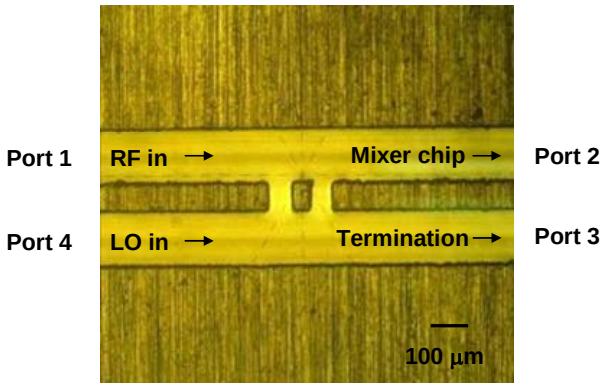

Fig. 7-6 A microscope photograph of the 10-dB directional coupler with a size of WR-1.2 waveguide fabricated by direct machining. The slit width is 60 μm.

In order to evaluate performances of a 10-dB coupler, a modular type of the one with four flanges and 30 mm long waveguide was prepared. Fig. 7-6 shows a photograph of the 10-dB directional coupler fabricated with direct machining technology. For the waveguide, a 1-μm-thick gold was plated on the copper.

Fig. 7-7 shows the measured transmission loss of the 10-dB coupler including the waveguide loss at room temperature. For the S_{21} measurement, ports 3 and 4 were terminated with waveguide loads. The typical uncertainties of the measurement, which is caused by their reflection, were about ±1 dB for S_{21} and ±0.8 dB for S_{24}, including that of calibration. Also shown is the simulated result of the 10 dB coupler which includes WR-1.2 waveguide loss estimated to be 4.0 dB/30 mm at room temperature. Their results are in reasonably agreement within the uncertainties. However, if the difference is significant, there might be slightly difference in the coupling factor due to the machining error.

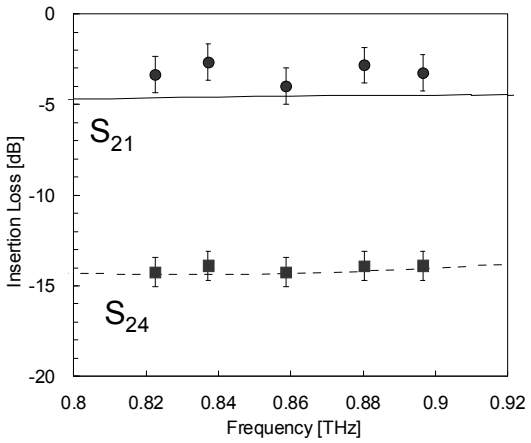

Fig. 7-7 Measured (points) and simulated (solid line) results of a transmission (S21) and coupling (S24) for the 10-dB directional coupler. Filled points indicate the result using the VNA, while open points do the result using power meter.

7.3 LO injection scheme for the band 10 cartridge

7.3.1 Consideration of waveguide and quasi-optical coupling scheme

In this frequency band close to 1 THz, it is difficult to obtain LO power satisfactorily to pump SIS mixers. The ALMA requires an LO source with no mechanical tuners. Thus, the LO system must consist of electrically-tunable component as based on solid-state devices. Although the high power output devices for terahertz region have been studied and developed in past thirty decades as review papers can be found in [9][10], the output power of the sources rapidly diminish at higher frequency (~ 20 μW at 0.9 THz, typically). For this reason we would have to come up with some kind of method to propagate the limited LO power to the SIS mixer.

A LO power injection scheme for the SIS mixer usually uses a beam splitter (quasi-optical) or a directional waveguide coupler (Wave Guide - WG). Choosing one or the other solution can be driven by different tradeoffs. Table 7-II lists the comparison between WG and QO injection schemes in relation to the ALMA band 10 cartridge designs. The choice made for the ALMA band 10 design followed a full comprehension of both the upside and downside of adopting a WG scheme or a QO scheme. On the base of the following considerations the WG scheme has been chosen for the band 10 front-end design.

One of the strongest points of the WG scheme is the high mechanical rigidity achievable for the front-end assembly. As a consequence the LO path mechanical vibrations are minimized, therefore the LO stability is increased. The leakage of the LO power is negligible as well. Another advantage

Table 7-II. Waveguide (WG) and quasi-optical (QO) injection scheme comparisons in relation to the ALMA band 10 cartridge design.

	WG	QO
Thermal isolation	Moderate	Good
Insertion loss	Moderate	Low
LO power	High	Moderate
Compactness	Good	Poor
Number of optical elements	Low	High
Effect of mechanical vibration	Little	Large
EMI	Negligible small	Potential to leak
Mounting and power flux alignment	Easy	Small error budget
Weight	Light	Heavy
Thermal load	Low	High

in using the WG scheme is the immediate reduction of the total optical components, which makes the cold optics design easy. On the other hand it seems difficult, but not impossible, to make waveguide components because the size of them is very small at the band 10 frequencies. Current machining technologies can make small waveguides features within the size of tens of microns. In terms of RF loss, waveguides have larger loss, which implies higher LO power levels tough to achieve at THz frequencies within the state-of-art technologies. Meanwhile, as a technique to study out the issue of the low LO power, a balanced waveguide mixer is a better candidate for the terahertz band [1]. The balanced mixer has the only LO power loss of 3 dB, and this comfortable reduction in LO power is reported in [11]. Besides, the LO amplitude noise can be suppressed in principle. However, the balanced mixer needs two DSB mixers having the same characteristics and RF quadrature hybrid coupler involving long waveguides to lead RF power the mixers. It might not be suitable for the ALMA receivers accompanying with the mass production and such long waveguide may cancel out the merit of the LO noise reduction.

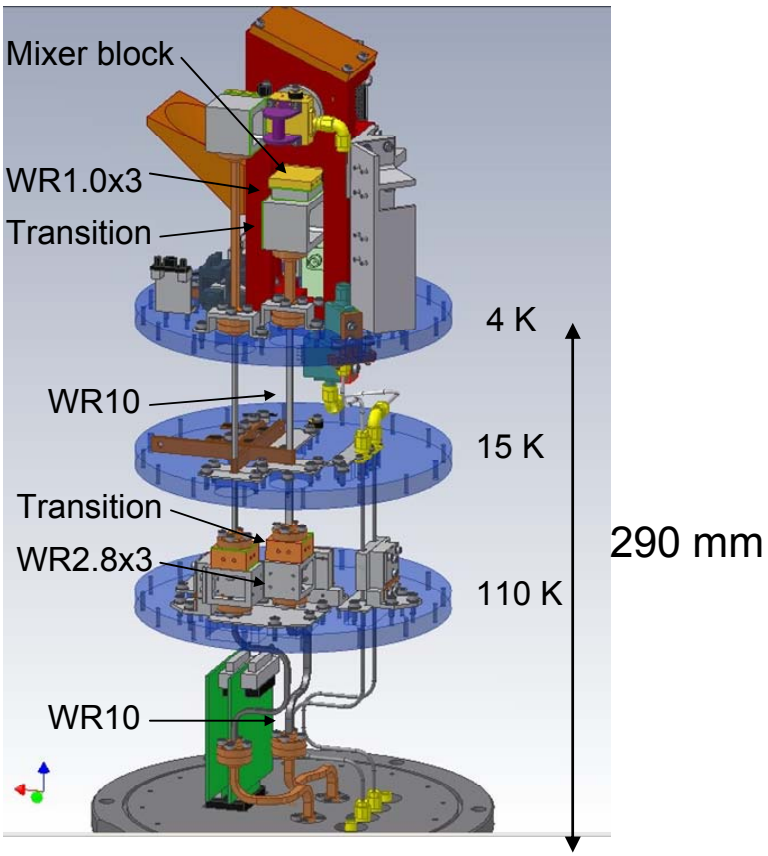

Fig. 7-8 LO signal path in the cartridge

7.3.2 LO chain for the band 10 cartridges

The WR-1.2 waveguide components have a large loss at the band 10 frequencies. To reduce the length of the waveguide for minimizing the loss, the multipliers should be placed on as close to the waveguide coupler as possible (close to 4 K stage). Since the assumed power dissipation of the tripler for 300-GHz frequency band (WR-2.8×3) is about 100 mW, it is impossible to place the two triplers (WR-2.8×3 and WR-1.0×3) on both 4 and 15 K stages to isolate thermally the cartridge and the cryostat. To solve this problem, we designed the LO path inside the cartridge, which consists of two triplers connected by an oversized waveguide as shown in Fig. 7-8. The distribution is as follows.

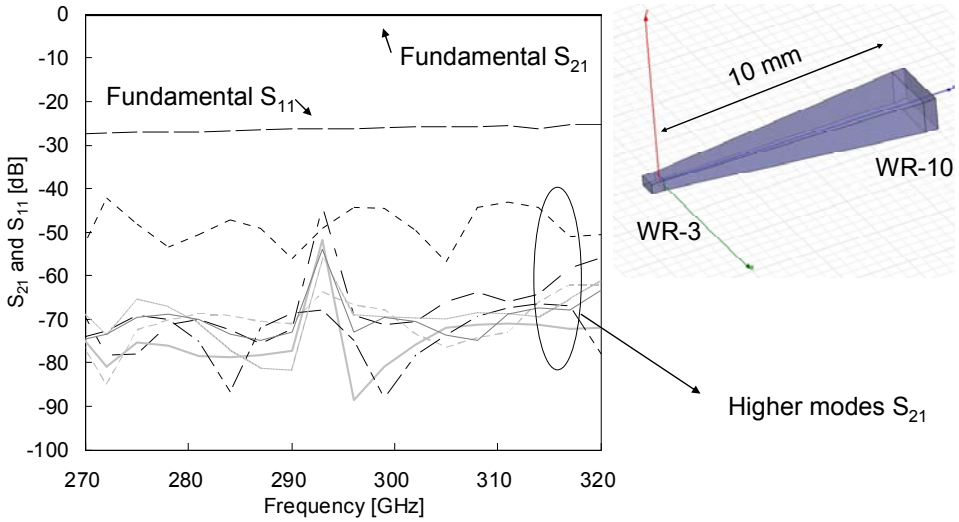

Fig. 7-9 A model of WR3-to-WR10 transition and its simulated transmissions for 8 modes.

Table 7-III LO path budget of the band inside the band 10 cartridge.

Parts	Waveguide	Input	Output	Unit	Loss	Comment
Feed through	WR10	100	89	mW	< 0.5 dB	
Waveguide	WR10	89	71	mW	1 dB	300 K to 80 K, length ~200 mm
Tripler (WR2.8x3)	WR2.8	71	1.85	mW	15.8 dB	Efficiency 2%, factor 1.3 at 80 K
Transitions + WR10 waveguide	WR3	1.85	1.47	mW	1 dB	Oversized, length ~250 mm
Tripler (WR1.0x3)	WR1.2	1.47	0.019	mW	18.9 dB	Efficiency 1%, factor 1.3 at 4 K
Waveguide	WR1.2	19	13.5	μW	1.5 dB	In mixer block
LO coupler	WR1.2	13.5	1.35	μW	10 dB	In mixer block
Mixer chip		1.35	0.8	μW	2.2 dB	NbTiN + Nb junctions

- ✓ The LO signal enters the cryostat through a hermetic feed-through in the band 88.3-104.6 GHz. Two WR-10 meandered waveguides up to the first tripler input, which are a copper waveguide and a thin-wall stainless steel waveguide with 2-μm-thick gold plate.
- ✓ At the output of the tripler (265 GHz –314 GHz), we place a WR2.8 to WR10 transition to match the output waveguide (WR2.8) with another stainless steel WR10 overmoded waveguide with 2-μm-thick gold plate to reduce the absorption loss. The overmoded waveguide is used for the only straight part to prevent mode conversion and resonant absorption in bend [12].
- ✓ Another WR10 to WR3 transition (integrated with WR3 bend) is inserted between the stainless steel WR10 waveguide and the second tripler (WR1.0 × 3).
- ✓ The tripler is attached to the coupler integrated in the mixer block directly.

According to ref. [12], insertion losses in the 200-mm-long gold-plated WR10 waveguide for the 100-GHz- and 300-GHz-bands are about 1 dB at room temperature. When the waveguide is cooled, the losses will be smaller according to the theoretical formula (related to the resistivity ratio between room and cryogenic temperatures). In the case of pure metals like gold, the ratio is roughly proportional to the temperature ratio. For example, the loss might drop to about 0.6 dB at 80 K and

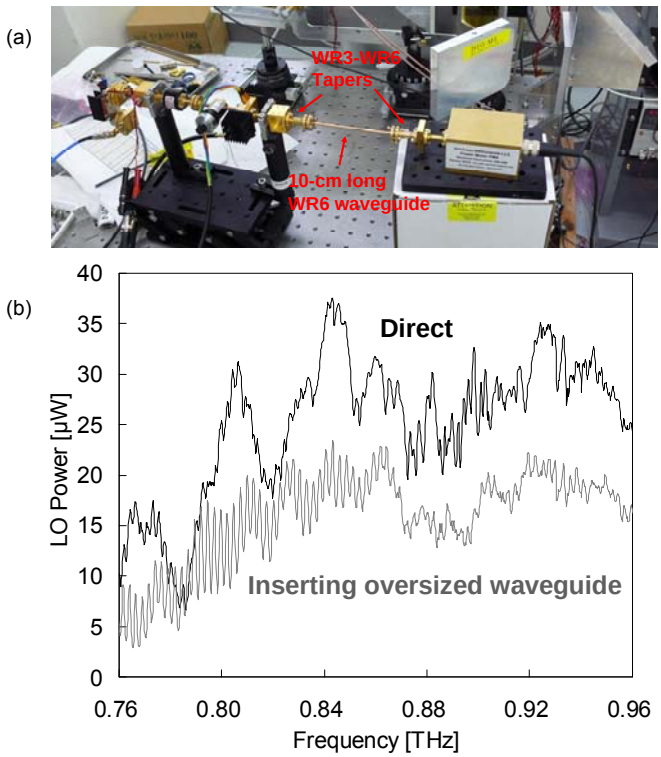

Fig. 7-10 (a) A photograph of an experimental setup for a preliminary LO power test. (b) Comparison of output power characteristics for the direct connection and inserting oversized waveguide between their tripliers.

0.3 dB at 4 K. An insertion loss of the WR3 to WR10 transition has been calculated with HFSS. Fig. 7-9 shows a model of the transition with the length of the taper of 10 mm and S_{21} (transmission) for 8 modes (TE_{10}, TE_{20}, TE_{01}, TE_{11}, TM_{11}, TE_{21}, TM_{21}, and TE_{30}). Also shown is S_{11} (return loss) for TE_{10}. It can be seen that the calculated insertion loss of the transition is negligibly small.

Table 7-III shows the LO path budget inside the band 10 cartridge. It is also assumed that sizes of Nb junctions are respectively 0.9 μm in diameter. If the LO power of 100 mW at 100 GHz is obtained, the SIS mixer can be pumped enough.

7.3.3 Preliminary test

Power measurements involving two multipliers separated by oversized waveguides have been conducted at room temperature as a preliminary test. Fig. 7-10 (a) shows a photograph of the experimental setup. Two WR3-WR6 transitions and a 10-cm-long WR6 waveguide were used. The measured WR6 waveguide loss in the 300 GHz band was about 1 dB at room temperature, which is almost same as the expected value. Fig. 7-10 (b) shows the output power after inserting the waveguide between the two multipliers. Also shown is output power when the two multipliers are directly connected. It can be seen that output power of about 15 μW is obtained at the band 10 LO frequencies. On the other hand, there are ripples due to standing-wave effect in the WR6 waveguide. If the return loss characteristics of the multipliers are improved, this effect will be reduced.

7.4 Performance of the cartridge receiver engineering model

A photograph of an assembled Band 10 receiver and schematic layout of the receiver performance measurement set-up is shown in Fig. 7-11. The vacuum window coating AR Teflon within the loss of the about 4 % was used [13]. The SIS mixer having excellent performance described in chapter 5 is used for the measurement.

7.4.1 Current response of an SIS junction for LO signals

Fig. 7-12 shows the pumped current response of the SIS junction at the bias voltage of 2.2 mV as a function of LO frequency when the LO power is maximum. The large ripple structure can be seen from the measurement. The optimum pumped current to minimize the receiver noise temperature was around 0.035 mA. Consequently, it is found that the SIS junction can not be pumped enough at several frequencies below 0.84 THz due to the ripple. The frequency interval of the ripple reflects a distance *d* between two reflection faces where standing wave arises, that is,

$$d = \frac{v}{2(f_k - f_{k-1})}, \qquad 7\text{-}3$$

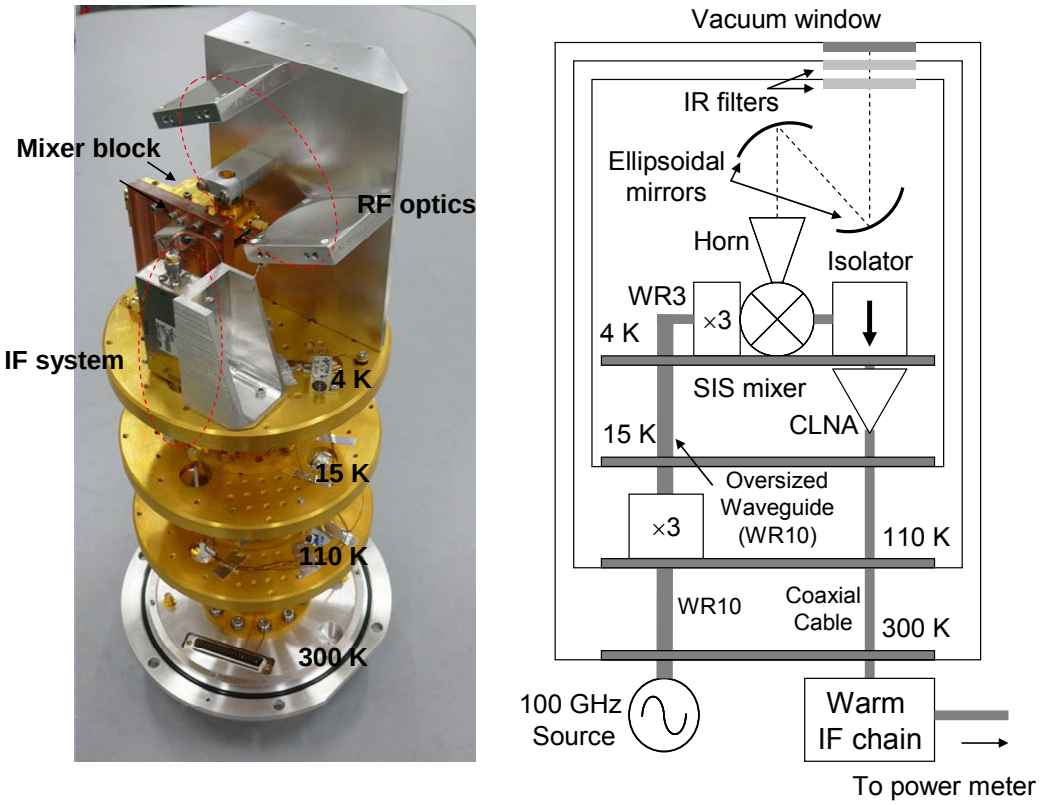

Fig. 7-11 A photograph of an assembled band 10 receiver engineering model and schematic layout of the noise temperature measurement set-up.

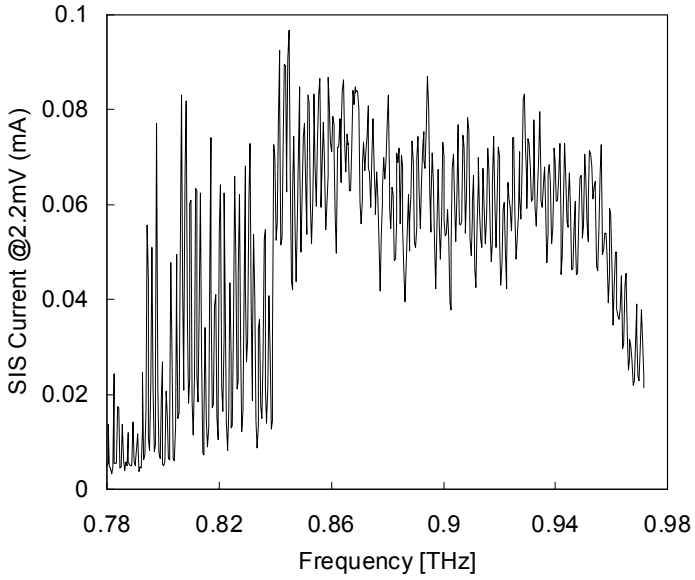

Fig. 7-12 Current response of the SIS junction at 2.2 mV as a function of LO frequency

where the f_k and v represents the frequency of kth ripple and phase velocity. The current response includes the information of device's characteristics which are placed on the LO signal path: the LO output power, transmission characteristics of the 10dB coupler, waveguide in the mixer block, and the sensitivity of the SIS mixer. From the measurement, the frequency interval observed was 1.8 GHz which corresponds to 85 mm, but there is no distance corresponding in the mixer block. Converting the ripple to 0.3 THz band, since the length equals 255 mm, it is suggested that the standing wave arises between two triplers.

7.4.2 Receiver noise temperature

The heterodyne receiver noise measurements were made by using the standard *Y*-factor method for room temperature (295 K) and liquid-nitrogen-cooled (77 K) loads as well. A measured maximum Y factor was about 1.85, which corresponded to a DSB receiver noise temperature of 179 K (about $4hf/k_B$). The frequency dependence of the receiver noise temperature was investigated at several frequencies from 0.792 to 0.945 THz. Fig. 7-13 shows the measured receiver noise temperature as a function of frequency. Noise temperature was reasonably flat over the target frequency band. This performance is the best ever reported for SIS mixers in this frequency band at a physical operating temperature of 4 K. In addition, this is first result that the uncorrected receiver noise temperature meets the ALMA band 10 specification over the entire band.

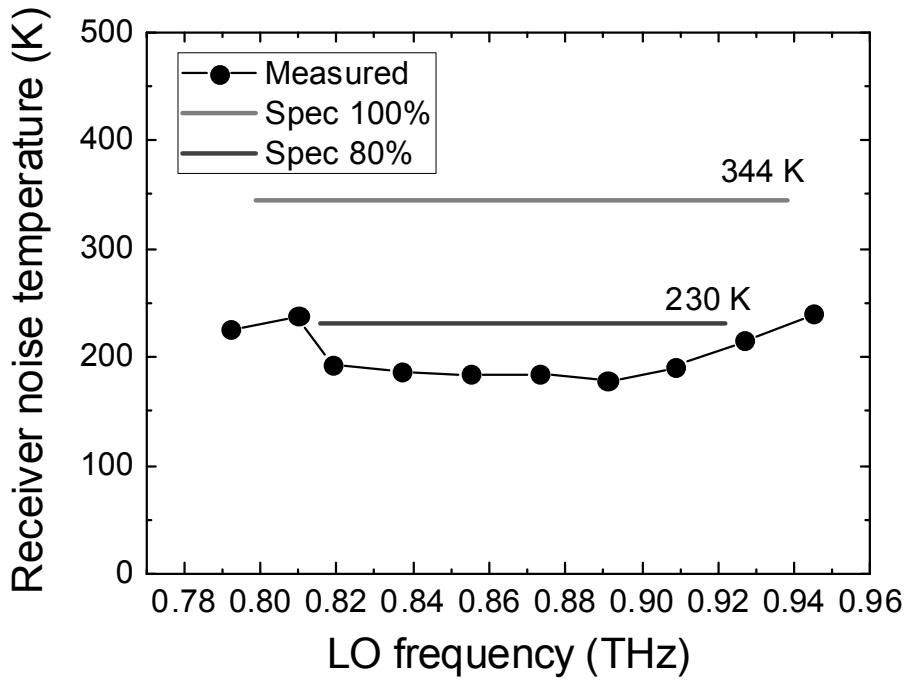

Fig. 7-13 DSB receiver noise temperatures as a function of LO frequency. The results was measured by Y. Fujii

7.5 Prototype mixer for the prototype cartridge receiver

The first solution being investigated was a full waveguide scheme which main characteristic was to have the LO source (pair of triplers devices) connected to each other by an oversized waveguide. This scheme was tested and demonstrated to suffer of large standing waves between the multipliers, which eventually made the mixing process impossible due to lack of LO pumping power at some frequencies of band 10. This implies that their multipliers have to be connected directly in order to prevent the standing wave. In terms of thermal load, the first multiplier which generates 300 GHz does not allow to be placed on the 4 K, because it generates a heat of 200 mW. Thus the LO signal for the 0.9 THz band has to be propagated from 15 K or 110 K stages. However, it is impossible to use WR-1.2 waveguide due to its loss.

In order to improve the performance, we are developing a prototype cartridge shown in Fig. 7-14. Our approach is to apply both quasi-optical and waveguide technologies eclectically: an LO signal is quasi-optically injected using two identical diagonal horns and a pair of two ellipsoidal mirrors, so called horn-to-horn scheme. Then RF and LO signals are coupled by the 10-dB waveguide coupler. The mixer block integrates the diagonal horn for receiving the LO signal and a waveguide 10-dB directional coupler as well as the engineering model to avoid losses due to misalignment at waveguide flange and due to resistance in the signal path.

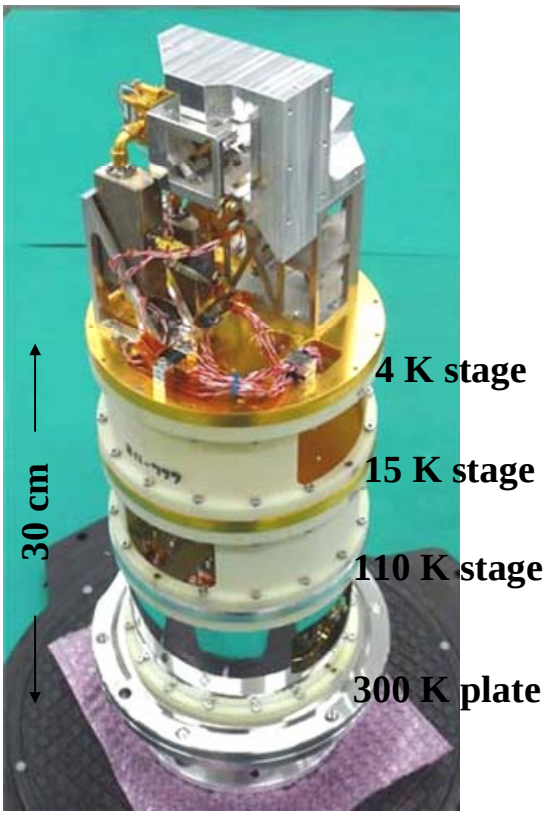

Fig. 7-14 Photograph of a prototype cartridge

7.5.1 Prototype mixer block design

Fig. 7-15 shows the designed mixer block incorporating the diagonal horn for receiving of LO signal, 10-dB directional coupler and mixer chip slot. The RF and LO signal paths of the waveguide are 6.2 mm and 12.2 mm long, and then the Ohmic loss is therefore estimated to be 0.3 dB and 0.6 dB at 4 K, respectively. Consequently, the loss in RF signal path should be negligibly small.

Two identical diagonal horns with a pair of two ellipsoidal mirrors are used for the transmission of the LO signal [14]. The diagonal horn is designed by assuming aperture electrical field as based on following the equation:

$$E_v = E_{v0} \cdot \left[\hat{x} \cos\left(\frac{\pi y}{a}\right) + \hat{y} \cos\left(\frac{\pi x}{a}\right) \right] \exp\left[-j\pi \frac{x^2 + y^2}{\lambda R_a} \right]. \qquad 7\text{-}4$$

The choice for the diagonal aperture side and axial length of respectively 1.2 and 5 mm gives a good compromise between the level of sidelobes radiation pattern broadening and gain. Furthermore, the horn of such dimensions can be easily built with standard machining technique. Simulated power coupling efficiency of the horn-to-horn is more than 60 %. Taking into account the coupling efficiency and waveguide loss, the LO power transmitted to the SIS junction is 0.8 μW, which is almost the same as power in engineering model. The diagonal horn and a measurement system of horn-to-horn coupling described in later section were designed by M. Candotti.

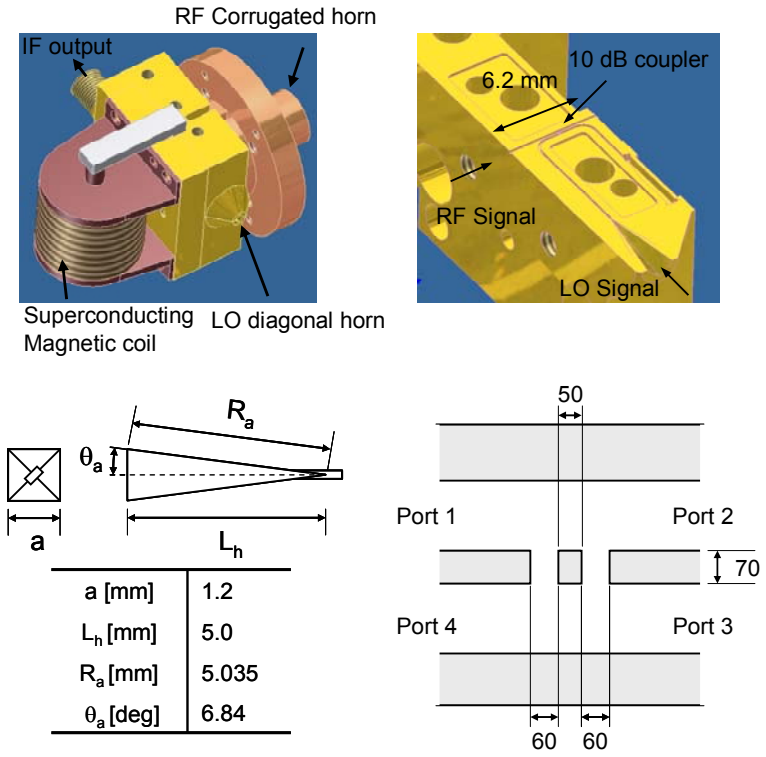

a [mm]	1.2
L_h [mm]	5.0
R_a [mm]	5.035
θ_a [deg]	6.84

Fig. 7-15 Schematics of the designed mixer block incorporating a diagonal horn and 10-dB directional coupler, and their dimension.

7.5.2 Horn-to-horn coupling measurement at room temperature

In order to verify the actual power being transmitted from the transmitter horn to receiving horn, a prototype of the LO optical system was made for room temperature evaluation. The setup for the total power measurement is shown in Fig. 7-16. One horn is attached to the sub-mm electronically tunable source and the other horn is attached to the sub-mm power meter. The power meter WR-10 waveguide interfaces with the diagonal horn WR-1 input waveguide by means of a WR-10 waveguide section. The calibration of the system is done by tightly attaching the two horn apertures, so the total power transmitted without the optical system losses and including the power meter waveguide mismatch can be taken as reference throughout band 10 frequencies. The horns are then separated and connected to their position in front of the off-axis mirrors in the LO optical system. The coupled power between the two horns is then measured again sweeping the entire band 10. In these power measurements the background contribution is removed by switching the source on and off. The measured power at each frequency is then obtained by subtracting the measured power with source off from the measured power with source on. The ratio between the power measured with optical system inserted between the two horns and the power measured from the calibration procedure gives the total power coupling of the optical system. Total power coupling for the prototype of the LO injection scheme throughout band 10 frequencies is shown in Fig. 7-16. The total power coupling efficiency is observed to be around 50 % on average. Fine structure may be due to standing wave effect between two horns, however power variation seems small.

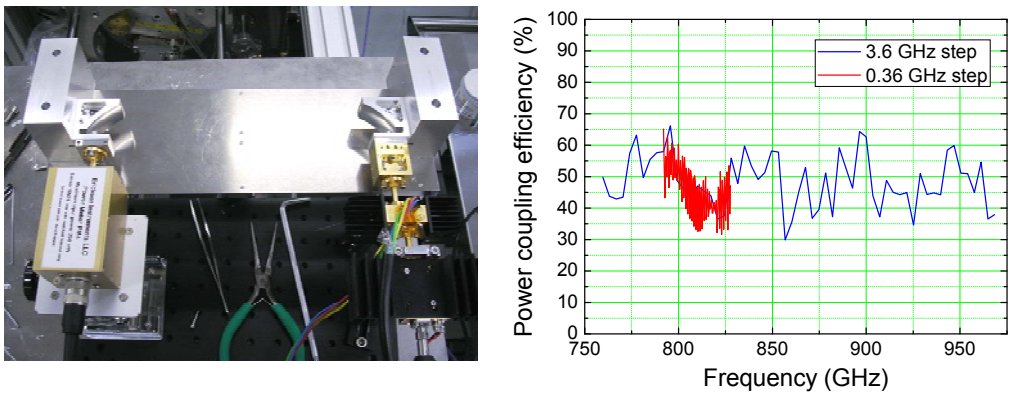

Fig. 7-16 A photograph and measured result of a total power coupling for horn-to-horn LO injection scheme throughout band 10 frequencies.

7.5.3 Heterodyne measurement sets in test cryostat

A schematic of a test receiver is shown in Fig. 7-17. The optics of the LO system is designed by Y. Fujii, and is similar to [14], but the LO source is located at room temperature for this test. The coupling system has been designed to maximize the coupling efficiency in wavelength independent manner over the entire band. LO signal radiated from a diagonal horn as a transmitter is focused on by M1 towards the other diagonal horn in mixer block via M2 and M3 reflectors. The mixer then receives the LO power from a waveguide 10 dB coupler connected to the 0.78-0.96 THz signal output. For the heterodyne measurement, RF signals from hot or cold loads are reflected by M5 toward corrugated horn [8] attached on the mixer block. The RF signal is down-converted by the low-noise SIS mixer to the IF 4-12 GHz and then is amplified by a low-noise amplifier through the isolator.

7.5.4 LO current response

Fig. 7-18 shows the typical measurement result of the current response for the LO power as well. Since the optimum pumped current of the SIS mixer is around 0.03 mA, the LO power is enough to pump it. In addition, smaller standing wave was observed. The observed frequency interval is about 0.4 GHz where a distance of reflection faces corresponds to 375 mm in free space. Although the distance is close to one between diagonal horns, it was not sure where the accurate reflection face was from this measurement. In either case, the prototype mixer showed significant improvement compared to the engineering model in terms of LO injection scheme.

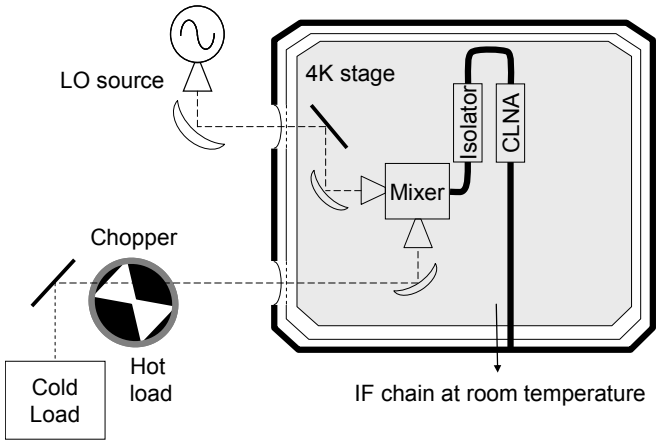

Fig. 7-17 A schematic of a test receiver with the two identical diagonal horns and the mixer block incorporating the 10-dB coupler. A polyimide film as a vacuum window and infrared filter having 5 % and 2 % reflection were used.

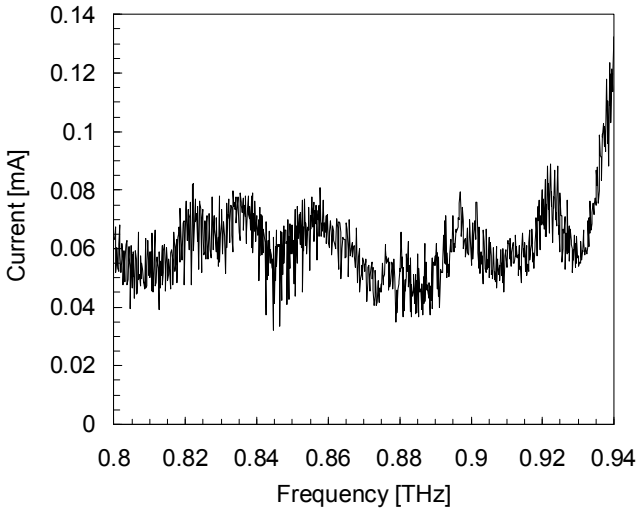

Fig. 7-18 Typical current response of SIS mixer using the prototype mixer block.

7.5.5 Heterodyne measurement

DSB receiver noise temperature averaged over IF 4-12 GHz was below 330 K ($7.5hf/k_B$) at the LO 0.801–0.945 THz as shown in Fig. 7-19 (a). The best noise temperature was 221 K at LO 0.873 THz. It should be noted that the noise temperature was including thermal noise from LO port because LO source was placed at room temperature. Besides, a polyimide film and infrared filter having losses of 5 % and 2 % reflection respectively were used. The results represent state-of-the-art performance for mixers in the terahertz frequency range. In addition, I estimated the transmission (S_{21}) and coupling (S_{24}) of the 10-dB coupler with following method. In our measurement system, it is possible to switch the LO port with the RF port, that is, possible to inject RF signals from the LO port. This allows us to measure noise temperature and mixer gain at the original LO port as shown in Fig. 7-19(b). Then, mixer gains including the optics losses measured at LO and RF port are respectively

$$G_{\mathrm{RFport}} = G_{\mathrm{RFPath}} G_{\mathrm{WG1}} \left|S_{21}\right|^2 G_{\mathrm{mix}}\,, \tag{7-5}$$

$$G_{\mathrm{LOport}} = G_{\mathrm{LOPath}} G_{\mathrm{WG2}} \left|S_{24}\right|^2 G_{\mathrm{mix}}\,, \tag{7-6}$$

where G_{RFPath}, G_{LOPath} G_{WG1}, and G_{WG2} are the gains in the LO and RF optical signal paths in front of the mixer chip and in the LO and RF waveguides, respectively. Here, since a difference of the lengths between the two waveguides for RF and LO path is 6 mm, by using the loss of 1.2 dB/25 mm and assuming that $G_{\mathrm{RFPath}} = G_{\mathrm{LOPath}}$,

$$\frac{G_{\mathrm{WG1}}}{G_{\mathrm{WG2}}} = \frac{1}{1.07}\,. \tag{7-7}$$

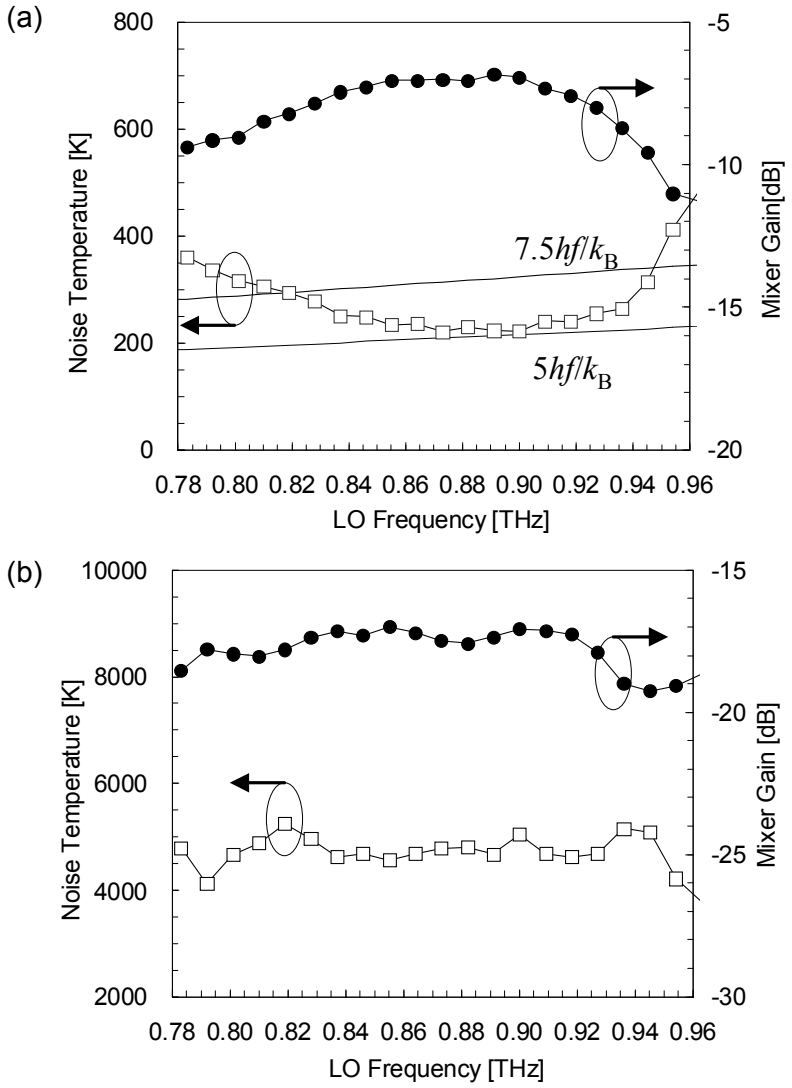

Fig. 7-19 Uncorrected receiver noise temperatures and mixer gains at RF port (a) and at LO port (b).

If $|S_{24}|^2 = 1-|S_{21}|^2$,

$$|S_{21}|^2 = \frac{1.07a}{1+1.07a}, \qquad 7\text{-}8$$

where $a = G_{\mathrm{RFport}} / G_{\mathrm{LOport}}$

Therefore the estimation of the transmission and coupling loss is allowed without a use of the modular type of 10-dB coupler at 4 K. Fig. 7-20 shows the transmission and coupling estimated on the basis of above the equation and simulated ones. The estimation would be reasonably in agreement with simulation.

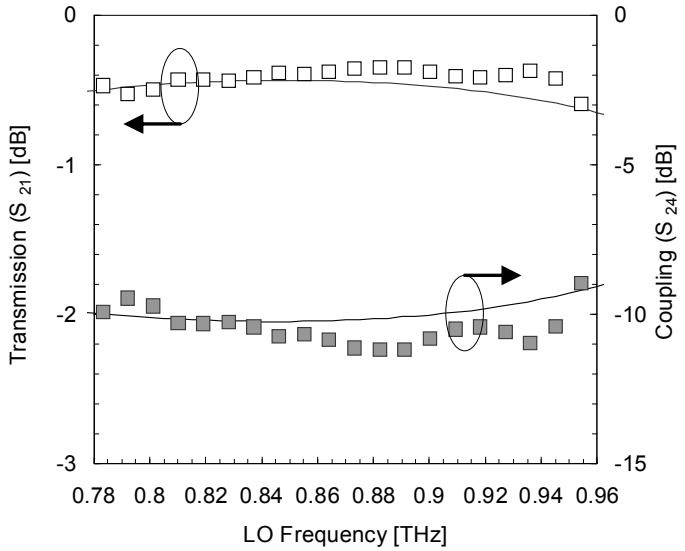

Fig. 7-20 Transmission (S_{21}) and coupling (S_{24}) of the 10-dB directional coupler estimated (points) from mixer gains measured at RF and LO ports. Also shown are simulated ones (solid line).

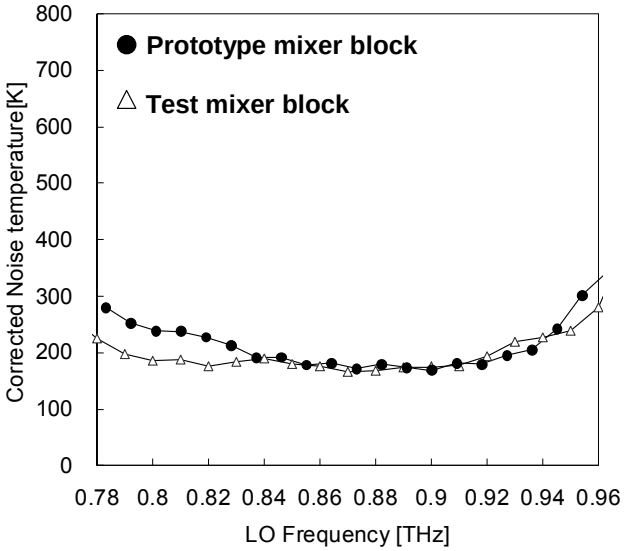

Fig. 7-21 Noise temperature of the prototype mixer block which is corrected for the vacuum window and estimated coupling of the 10-dB coupler. Also shown is one described in chapter 5, which is corrected for vacuum window and beam splitter. Note that the different mixer chips are used for their measurement, but they were fabricated at the same time and device parameters were almost same.

Fig. 7-21 shows noise temperature of the prototype mixer block which is corrected for the vacuum window and the estimated coupling of the 10-dB coupler. Also shown is one described in chapter 5, which is corrected for vacuum window and beam splitter. Note that the different mixer chips are used for their measurement, but they were fabricated at the same time and device parameters were almost same. Two corrected noise temperatures are in good agreement despite of using different measurement systems and mixer blocks. This result suggests the estimation of the coupling is reasonable method and the part of the 10-dB coupler with two slits works well as expected. The SIS mixer has a great potential for the ALMA band 10 receivers. The prototype cartridge shown in Fig. 7-14 is being tested using the prototype mixer. It is anticipated to meet the ALMA band 10 full specifications listed in chapter 1.

7.6 Conclusion

In this chapter, we presented a demonstration of the low-noise waveguide SIS mixer incorporating the waveguide 10-dB directional coupler. The mixer was used for the band-10 cartridge receiver engineering model and then the frequency dependence of the receiver noise temperature was investigated at several frequencies from 0.792 to 0.945 THz. For efficient use of the LO power, the LO chain designed inside the cartridge consisted of two triplers connected by an oversized waveguide. As shown in Fig. 7-13, the measured receiver noise temperature was reasonably flat to be about 180 K over the target frequency band. This performance is the best ever reported for SIS mixers in this frequency band at a physical operating temperature of 4 K and is the first demonstration of a low-noise SIS mixer with the waveguide directional coupler. In addition, this is first result that the uncorrected receiver noise temperature meets the ALMA band 10 specification over the entire band. However, this scheme was tested and demonstrated to suffer of large standing waves between the multipliers, which eventually made the mixing process impossible due to lack of LO pumping power at some frequencies of band 10.

In order to improve the performance, we are developing a prototype cartridge applying both quasi-optical and waveguide technologies eclectically. For the prototype cartridge, the waveguide SIS mixer incorporating the waveguide 10-dB directional coupler and diagonal horn for LO signal has been developed. DSB receiver noise temperatures are below 330 K ($7.5hf/k_B$) over the range of LO 0.801–0.945 THz with the minimum being 221 K at 0.873 THz over the range of IF 4-12 GHz, including losses of the vacuum window. This is also the state-of-the-art sensitivity at an operating physical temperature of 4 K, and the combination of quasi-optical and waveguide techniques would be a good choice to achieve an efficient LO power coupling. These results indicate that waveguide SIS mixer has a great potential for the ALMA band 10 receivers.

References

[1] D. Meledin, A. Pavolotsky, V. Desmaris, I. Lapkin, C. Risacher, V. Perez, D. Henke, O. Nystrom, E. Sundin, D. Dochev, M. Pantaleev, M. Fredrixon, M. Strandberg, B. Voronov, G. Goltsman, and V. Belitsky, ”A 1.3-THz Balanced Waveguide HEB Mixer for the APEX Telescope,” IEEE Transactions on Microwave Theory and Tech. 57 (1) 2009.

[2] G. A. Ediss, “Measurements and Simulations of Overmoded Waveguide Components at 70-118 GHz, 220-330 GHz and 610-720 GHz,” proc. 14th Int. Symp. on Space Terahertz Technology. April 22-24, 2003. ALMA Memo No. 467 Available at http://www.mma.nrao.edu

[3] D. M. Pozar, “Microwave Engineering third edition,” John Wiley & Sons, Inc. 2005.

[4] R. A. Matula, “Electrical Resistivity of Copper, Gold Palladium, and Silver,” J. Phys. and Chemical Reference Data 8 (4), 1979.

[5] A. Pavolotsky, D. Meledin, C. Risacher, M. Pantaleev, and V. Belitsky, “Micromachining approach in fabricating of THz waveguide components,” Microelectron. J. 36 (7), 2005.

[6] T. Kojima, M. Kroug, M. Takeda, Y. Uzawa, W. Shan, Y. Fujii, Z. Wang, H. Ogawa, ”Three Quanta Sensitivity SIS Mixer for the 0.78–0.95 THz Band”, Appl. Phys. Express 2, 2009.

[7] S. M. X. Claude and C. T. Cunningham, A. R. Kerr and S.-K. Pan, “Design of a Sideband-Separating Balanced SIS Mixer Based on Waveguide Hybrids,” ALMA Memo 316, Available at http://www.mma.nrao.edu

[8] Y. Uzawa, M. Sugimoto, K. Kimura, R Nohara, T. Manabe, H. Ogawa, Y. Fujii, W.-L. Shan, K. Kaneko, M. Kroug, S. Shitov, “Near-Field Beam Measurements of Corrugated Horns for ALMA band 10”, 18th Int. Symp. On Space Terahertz Technology, Caltech, CF, USA, Mar. 21-23, 2007.

[9] P. H. Siegel, “Terahertz Technology,” IEEE Transactions on Microwave Theory and Tech. 50 (3), 2002

[10] D. Dragomana, and M. Dragomanb, “Terahertz fields and applications,” Progress in Quantum Electronics 28, 2004.

[11] Y. Serizawa, Y. Sekimoto, M. Kamikura, W. Shan, T. Ito, “A 400–500 GHz Balanced SIS Mixer with a Waveguide Quadrature Hybrid Coupler,” Int. J Infrared Milli. Waves (29) 2008.

[12] A.-L. Fontana and B. Lazareff, “Mode conversion and Resonant Absorption in Bent Overmoded Waveguide,” ALMA Memo No. 550 Available at http://www.mma.nrao.edu

[13] Y Uzawa, M Kroug, T Kojima, M Takeda, M Candotti, Y Fujii, K Kaneko, W Shan, T Noguchi and Z Wang, “A sensitive ALMA Band 10 SIS receiver engineering model,” Supercond. Sci. Technol. 22. 2009.

[14]M. Candotti, Y. Uzawa, Y. Fujii, T. Kojima, ”Design study for the local oscillator injection scheme for the ALMA band 10 receiver,” presented at 19th Int. Symp. on Space THz Technology, Groningen, The Netherlands, April 28-30, 2008.

[15]Y. Uzawa, T. Kojima, M. Kroug, Y. Fujii, M. Candotti, W.-L. Shan, M. Takeda, K. Kaneko, S. Shitov, and M.-J. Wang, “Development of the 787-950 GHz ALMA Band 10 Cartridge,” 33rd International Conference on Infrared, Millimeter, and Terahertz Waves, California Institute of Technology, Pasadena, California, USA, September 15 - 19, 2008.

Chapter 8

Summary

With the aim of achieving the specification for the ALMA band 10 receivers covering the frequency range of 0.787-0.950 THz, we have developed low-noise SIS mixers. The results obtained in this work and the novelties are summarized as follows:

- ✓ **Design method and its demonstration to achieve both wide bandwidth and low noise temperature**

In chapter 5, we suggested a design method with RF source impedance sweeping analysis for obtaining both low noise and wideband performance. In order to verify the validity of the analysis, we tested three mixer chips with different impedance transformer widths to change the source impedance. The experimental result was quantitatively in excellent agreement with theoretically calculated ones. This indicates that the design method makes it possible to control SIS mixers performance more accurately.

- ✓ **Proposition of new superconducting microstrip configuration**

In chapter 5, we proposed a superconducting microstrip structure with the ground plane made of Al and the NbTiN strip embedded in the dielectric layer. This inverted microstrip line has the potential to reduce RF losses in the tuning circuit because the currents in the lossy Al film are spread over a larger area. According to our analysis with HFSS in terms of loss, it appears that there is an improvement of 0.1 dB per wavelength for the inverted superconducting configuration, compared to normal one. This result indicates that the configuration makes it a better candidate for tuning circuits at frequencies ranging from 0.7 THz to 1.2 THz.

- ✓ **Mixer performance**
  - ☺ **Nb/AlO_x/Nb junctions integrated with epitaxial NbTiN films on an MgO substrate**

In chapter 4, we proposed SIS mixers with Nb/AlO_x/Nb junctions integrated with epitaxial NbTiN films on an MgO substrate, and demonstrated the one with a low receiver noise temperature of 171 K at 0.83 THz. However, it was found that the performance was severely-dependence on the thickness of the MgO substrate with high dielectric constant. On the other hand, a detailed analysis of mixers on the basis of numerical simulations was consistent with the experiment results, and it revealed a possibility of further improvement in the mixer performance: If it make the MgO thickness accurately controllable or find a design solution to overcome high dielectric constant, the mixer with epitaxial NbTiN films would be a promising device for frequencies up to 1.2 THz. For

example, coplanar waveguide, which does not depends on the thickness, would one of the candidates as the transmission line configuration.

☺ **Nb/AlO_x/Nb junctions integrated with an inverted NbTiN/SiO_2/Al microstrip on a quartz substrate**

In chapter 5, we successfully demonstrated a low-noise waveguide mixer based on Nb/AlO_x/Nb SIS junctions integrated with an NbTiN/SiO_2/Al superconducting inverted microstrip. The mixer employs a twin-junction tuning circuit and an impedance transformer which are designed to achieve both low noise and wideband operation as above-mentioned. Corrected for optical input losses in front of the mixer, the receiver noise temperatures showed below 200 K (DSB) over the range of 0.79–0.93 THz at an operating temperature of 4 K. The best noise temperature of 156 K at the LO frequency of 0.88 THz was achieved. In addition, the corrected DSB noise temperature was below 120 K (< $3hf/k_B$) around the LO frequency of 0.88 THz and at the operating temperature of 2 K. The results represent state-of-the-art sensitivity for mixers in the terahertz frequency range. In addition, it would be also worth to have achieved the wide bandwidth using the moderate junction current density of 8 kA/cm^2 significantly lower than ones pointed out so far.

✓ **IF characteristics of receiver noise temperature and IF output power**

In chapter 6, we constructed low noise first IF chain using a state-of-the-art ultra low noise amplifier and low-loss isolator at 4−12 GHz. The first IF amplifier and IF chain were evaluated by CAT system, and we found the best condition to achieve both low noise below 10 K and low power consumption of 14 mW. On the other hand, unexpected ripple and increases in receiver noise temperature arose. By detailed analysis, we found the worse S_{11iso} than −20 dB and low mixer gain caused the ripple or the increase in noise temperature. In conclusion, the combination of the simple Design A and an isolator having return loss below −20 dB is the most promising IF chain for the band 10 receivers. By using an improved isolator, flat noise temperature and IF output fluctuation within 3.5 dB over 4-12 GHz were obtained.

✓ **Terahertz waveguide technologies and the total receiver performances**

In chapter 7, we developed the low-noise waveguide SIS mixer incorporating the waveguide 10-dB directional coupler. The mixer was used for the band-10 cartridge receiver engineering model and then the frequency dependence of the receiver noise temperature was investigated at several frequencies from 0.792 to 0.945 THz. For efficient use of the LO power, the LO chain designed inside the cartridge consisted of two triplers connected by an oversized waveguide. As shown in Fig. 7-13, the measured receiver noise temperature was reasonably flat over the target frequency band. This performance is the best ever reported for SIS mixers in this frequency band at a physical operating temperature of 4 K and is the first demonstration of a low-noise SIS mixer with the waveguide directional coupler. The noise temperature has improved by a factor of more than 6, compared to the ASTE 0.8-THz prototype cartridge receiver (sugimoto et al 2004), for

example. In addition, this is first result that the uncorrected receiver noise temperature meets the ALMA band 10 specification over the entire band.

However, this scheme was tested and demonstrated to suffer of large standing waves between the multipliers, which eventually made the mixing process impossible due to lack of LO pumping power at some frequencies of band 10. In order to improve the performance, we are developing a prototype cartridge applying both quasi-optical and waveguide technologies eclectically: The mixer block incorporates a diagonal horn for LO signal in addition to the waveguide 10-dB directional coupler. It test cryostat, DSB receiver noise temperatures are below 330 K ($7.5hf/k_B$) over the range of LO 0.801–0.945 THz with the minimum being 221 K at 0.873 THz over the range of IF 4-12 GHz, including losses of the vacuum window. Besides the state-of-the-art sensitivity, it was confirmed the standing wave was significantly improved. This indicates that the combination of quasi-optical and waveguide techniques would be a good choice to achieve an efficient LO power coupling.

- ✓ **Evaluation and measurement method**
  - ☺ **Loss measurement of terahertz waveguide at cryogenic temperature using an SIS mixer**

The insertion loss of the waveguide at cryogenic temperature was simply estimated by comparing the mixer gains in the case with and without the waveguide between the mixer and the horn. However, such measurement has never been conducted so far. It is found that there is a large waveguide loss of about 1.2 dB/25 mm. This result implies that the waveguide coupler of a modular type with long waveguide is no longer available at the frequency range. In other wards, waveguide length should be short as possible. On the basis of the measurement results, we designed a mixer block incorporating the 10-dB directional coupler to minimize the waveguide loss and flange mismatch. The results showed low noise performance as above-mentioned.

  - ☺ **Coupling factor measurement of the directional coupler at cryogenic temperature using an SIS mixer**

In chapter 7, the prototype mixer has feed horns at both LO port and RF port. In our measurement system, it is possible to switch the LO port with the RF port, that is, possible to inject RF signals from an LO port. This allows measurement of noise temperature and mixer gain at the original LO port. Then, mixer gains observed at LO and RF ports respectively should reflect the characteristics of directional coupler. Therefore, by taking a ratio of the mixer gains, we can estimate coupling factor of the directional coupler at cryogenic temperature. We confirmed the coupling of the 10-dB directional coupler by employing the estimation method and in reasonably good agreement with the simulation.

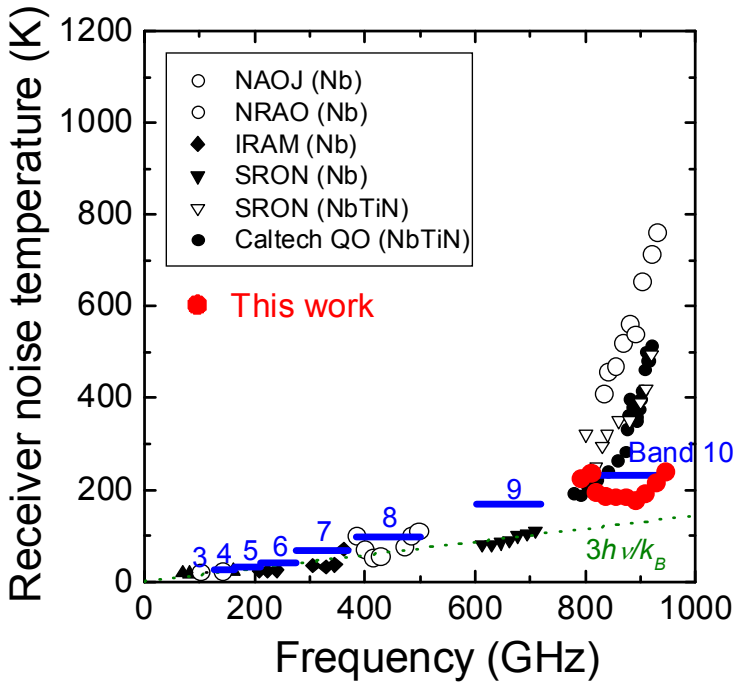

Fig. 8-1 Results of this work and a number of SIS mixers recently developed.

Finally, I present plot results of this thesis together with results of a number of SIS receivers that have been developed so far. This work successfully demonstrated the quantum limited low noise performance of waveguide SIS mixers. The SIS mixers developed in this work will be installed for the ALMA band-10 receivers, and I expect that they give us scientific knowledge we have never know by enabling extreme sensitive observation. In addition, we believe that instruments and technologies of the design, fabrication, and measurement developed in this work will be applied for a variety of high frontier terahertz field.

Appendix A
Transmission loss for polyimide films and Teflon sheets

A.1 Overview

This appendix provides measurement results of transmission loss for vacuum windows and infrared filters used for the SIS mixer test receiver. For accurate characterization of SIS mixers, we have showed receiver noise temperature corrected for transmission loss of the vacuum window and infrared filter. Their loss for the correction used the measurement results of this Appendix. The measurement was performed with the help of T. Nitta of University of Tsukuba and M. Naruse of University of Tokyo.

A.2 Measurement

Evaluated materials are summarized in Table A-I. The polyimide film A with a thickness of 12.5 μm and Zitex D were used as both beam splitter and the vacuum window, and infrared window in test receiver as described in Chapter 4, 5 and 6. The polyimide film B with a thickness of 8.5 μm and Teflon C with a thickness of 500 μm were used as the beam splitter and vacuum window. The measurement of the transmission loss was performed with a FTS measurement system. The transmission loss of the materials was simply estimated by comparing the spectrum in the case with and without the material. The calibration accuracy was within 1% at the frequencies 0.25-1 THz.

Table A-I Summary of evaluated materials. The polyimide films A and B have the same refractive index.

	Material	Thickness (μm)	Used chapter or section	Used as
A	Polyimide	12.5	Chapter 4, 5 and 6	Beam splitter and vacuum window
B	Polyimide	8.5	Section 5.6	Beam splitter
C	Teflon	500	Section 5.6	Vacuum window
D	Zitex	-	Chapter 4, 5 and 6	Infrared filter

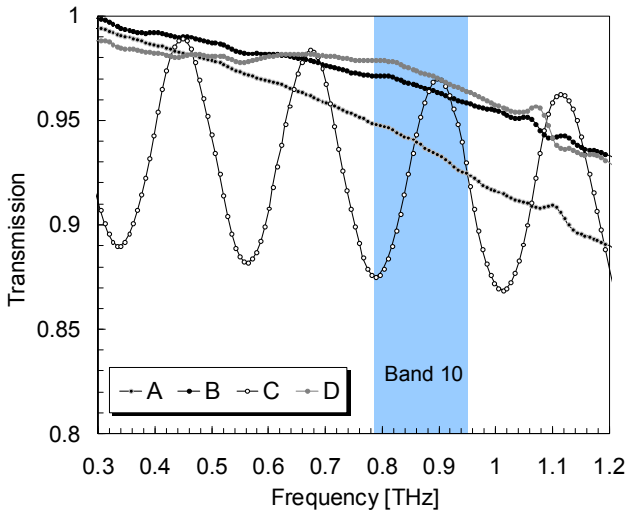

Fig. A-1 Measured results of transmission for the materials A, B, C, and D

The measurement results are shown in Fig. A-1. At the band 10 frequencies, the transmissions were measured to be within 96-97 % for B and D, and 92-95 % for A, and the ripple was observed for the transmission of A within 88-97 % due to thicker film.

A.3 Estimation of reflectivity for the beam splitter

We estimated the reflectivity of the polyimide films in the case that they are located with an angle of 45 degree, that is, the case the films are used as the beam splitter. In case of polarization with an electric field perpendicular to plane of incidence, the reflectivity R is calculated by the following formula:

$$R = \frac{4r^2 \sin^2(\Delta/2)}{(1-r^2) + 4r^2 \sin^2(\Delta/2)} \qquad \text{A-1}$$

where

$$r = \frac{\sin(i_1 - i_2)}{\sin(i_1 + i_2)} \qquad \text{A-2}$$

$$\Delta = \frac{4\pi nd \cos(i_2)}{\lambda_0} \qquad \text{A-3}$$

n and d represents the refractive index of the reflector i_1 and i_2 represent the incident and the refractive angles. Since the transmission measured with the FTS equal to $1–R$, and $i_1 = i_2 = 0$, we can estimate the refractive index n by fitting with the measured results. The calculation was performed by assuming that the absorption loss are negligible (thickness t << wavelength λ). As shown in Fig. A-2 (a), the calculation is in good agreement with the measurement if the refractive

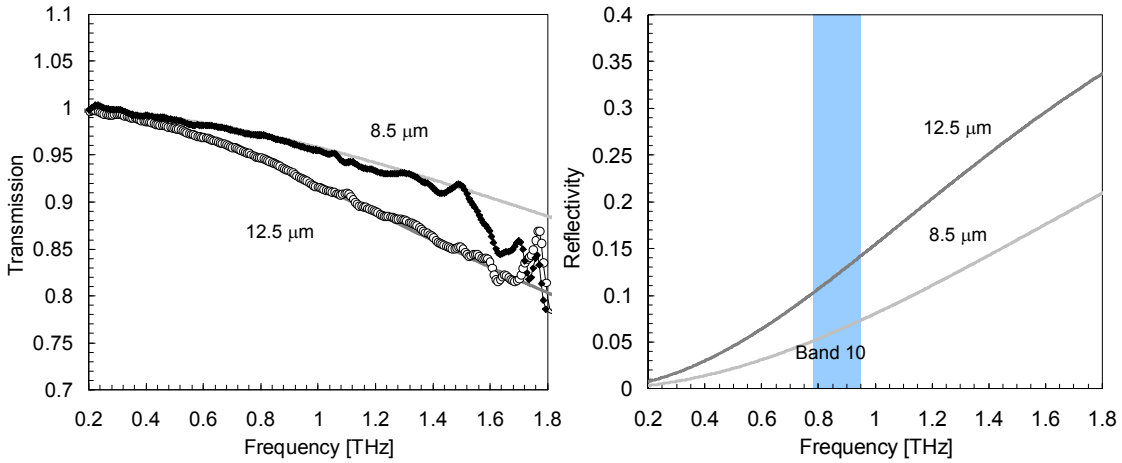

Fig. A-2 Calculated result of the transmission so as to be fitted with the measured results (a) and estimated reflectivity of the 12.5-μm- and 8.5-μm-thick polyimide films with an angle of 45 degree.. The symbols and the solid lines indicate the measurement and calculation result, respectively.

index *n* corresponds to 1.84. Therefore, the reflectivity of the 12.5-μm- and 8.5-μm-thick polyimide films as the beam splitter is calculated to be 10-14 % and 5-7 % at the band 10 frequencies as shown in Fig. A-2 (b).

Appendix B
Junction coupling measurement using an LO source

B.1 Overview

This appendix provides coupling measurement method using an LO source. The measurement allows us to estimate junction coupling efficiency with the same measurement set as a heterodyne one. A FTS measurement system is a conventional method to estimate frequency dependence of coupling efficiency for SIS mixers before the heterodyne measurement. However the FTS measurement is necessary to use a different measurement set from the heterodyne one with a transportable cryostat. Therefore, this method using the LO source might make the measurement time to be shorter. In this appendix, we confirmed the consistency between two methods by comparing the coupling measured by both ones.

B.2 Investigation using large signal source

The coupling measurement set using an LO source is shown in Fig. B-1. As well as a heterodyne measurement system shown in chapter 2, the LO source as the large signal source is an

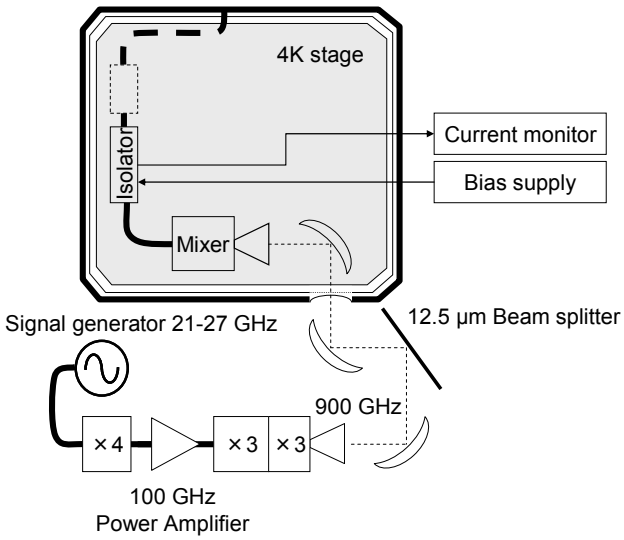

Fig. B-1 Schematic diagram of measurement system for the LO current response.

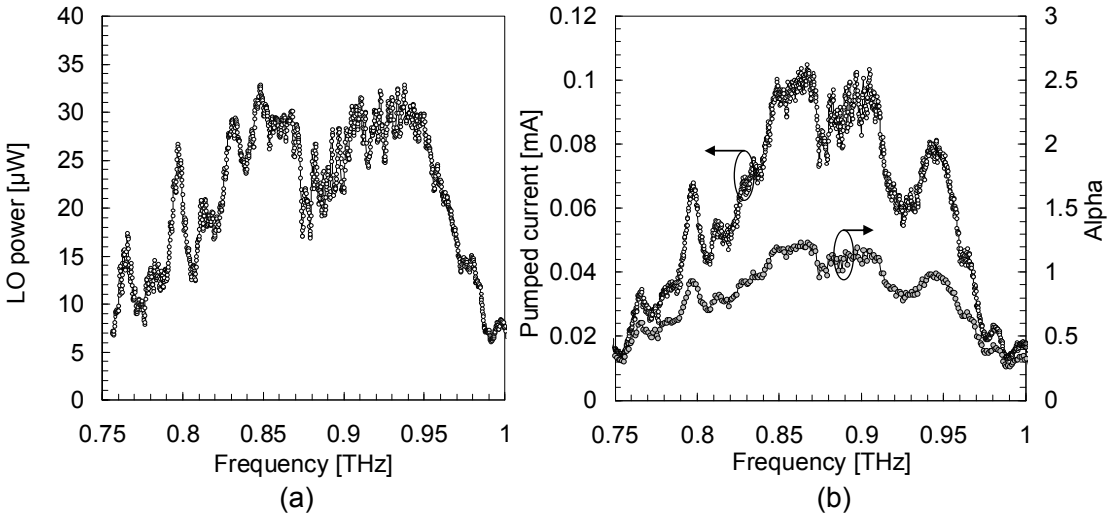

Fig. B-2 (a) LO power P_{LO} measured with an Erikson's power meter and (b) measured pumped current and pumping parameter α calculated from eq. 5-1

all-solid-state multiplier chain comprising a synthesized microwave signal generator (SG). The LO power is quasi-optically injected by a 12.5-μm-thick polyimide beam splitter with a 10-14 % reflectivity to pump the SIS junction up to α of 0-2. Frequency of the source is changed by controlling the SG with a Labview program, and the frequency range is limited by the bandwidth of the multiplier and/or the power amplifier. The pumped current of SIS junctions is read out by a digital multimeter via the circulator.

In our measurement system, it is possible to measure junction pumped-current $I_{DC}(V_0,V_\omega)$ from 0.75 to 1 THz. Then, we can deduce frequency dependence of LO voltage V_ω by calculating $\alpha = eV_\omega/\hbar\omega$ with an unpumped *I-V* characteristic and eq. 5-1. LO current $I_\omega(V_0,V_\omega)$ of the tunnel junction can be calculated from eq. 2-38. Therefore, the coupling from the LO source to the junction is giving by

$$C = \frac{V_\omega I_\omega / 2}{P_{LO}} \qquad \text{B-1}$$

The LO power P_{LO} is calibrated with a submillimeter power meter before the measurement.

As an example, let us compare measurement results on the basis of this method and a FTS. The QC-mixer in described in chapter 5 was used as a sample device. Fig. B-2 (a) shows LO power P_{LO} measured with an Erikson's power meter. The calibration is done by tightly attaching LO diagonal horn apertures and WR-10 waveguide directly. Therefore, there are slightly uncertainties due to reflection in this calibration. In these power measurements the background contribution is removed by switching the source on and off. The measured power at each frequency is then obtained by subtracting the measured power with source off from the measured power with source on.

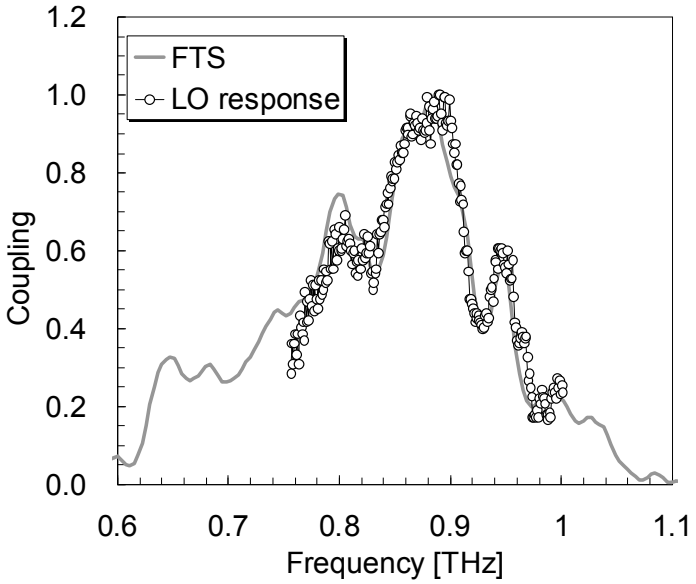

Fig. B-3 Comparison of coupling measurement results between on the basis of method using LO source and with a FTS. Their results are corrected for the optics losses in front of the mixer, such as vacuum window and beam splitter (for using LO source).

Measured pumped current and pumping parameter α calculated from eq. 5-1 are shown in Fig. B-2 (b). The pumping parameters were computed using Labview programs.

B.3 Comparison of coupling between two methods

Fig. B-2 shows comparison of coupling measurement results between two methods. Their results are corrected for the optics losses in front of the detector (mixer), such as the beam splitter (only for using LO source) and the vacuum windows. They would be in good agreement, except for around 0.75 THz. The discrepancy might be attributed to strong water absorption due to the long LO path.

Although the measurable frequency range is 0.77 to 1 THz (fractional bandwidth of ~26 %), which is narrower compared to FTS one, the bandwidth is possible to be made wider. In addition to resonance step described in Chapter 3, this measurement would be a useful way to estimate SIS mixer performances before the heterodyne measurement without the FTS measurement. Moreover, this system may also make it possible to measure transmission losses of some components, such as dielectric films.

Appendix C

Water absorption at the experimental room

C.1 Overview

This Appendix provides experimental results of atmospheric absorption under a typical condition (humidity: 25 % and temperature 22 °C) at our experimental room. Since our test cryostat is exposed to an atmospheric environment, the result measured is sensitive to water vapor along the RF path. Especially, water lines at around 0.75 THz and 0.92 THz significantly influence to noise temperature measurement of SIS mixers. In order to understand performances of SIS mixers, such as bandwidth, actual absorption of their waver lines should be corrected. Here, we estimated the transmission loss under the typical condition by compared with receiver noise temperature under a nitrogen purge.

C.2 Mixer performance measurement for two conditions

We performed mixer performance measurement in two cases that the test cryostat measurement system was under the typical environment and under the nitrogen purge (see Fig. C-1). The QC-mixer in described in chapter 5 was used for this measurement.

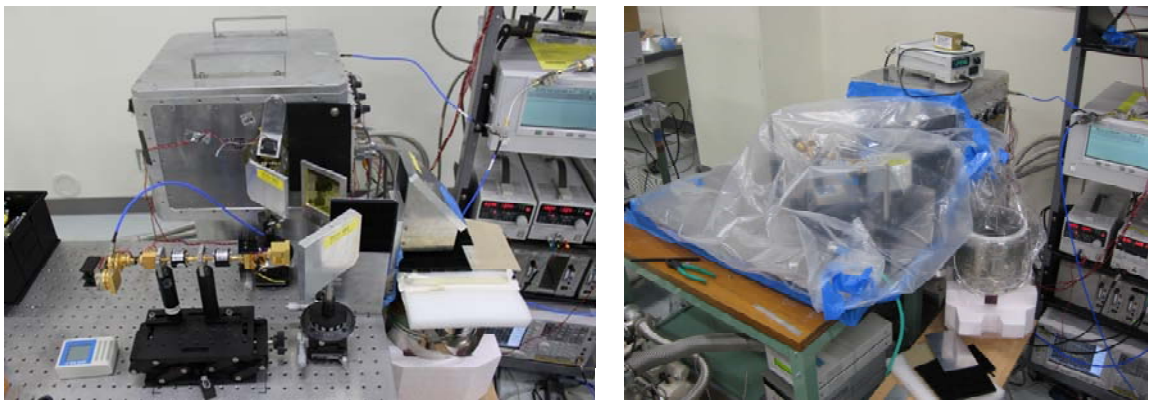

(a) (b)

Fig. C-1 Measurement system of receiver noise temperature and LO current response under the typical environment (Humidity: 24-27 %) and under the nitrogen purge (Humidity: below 10 %) at an ambient temperature of 22 °C.

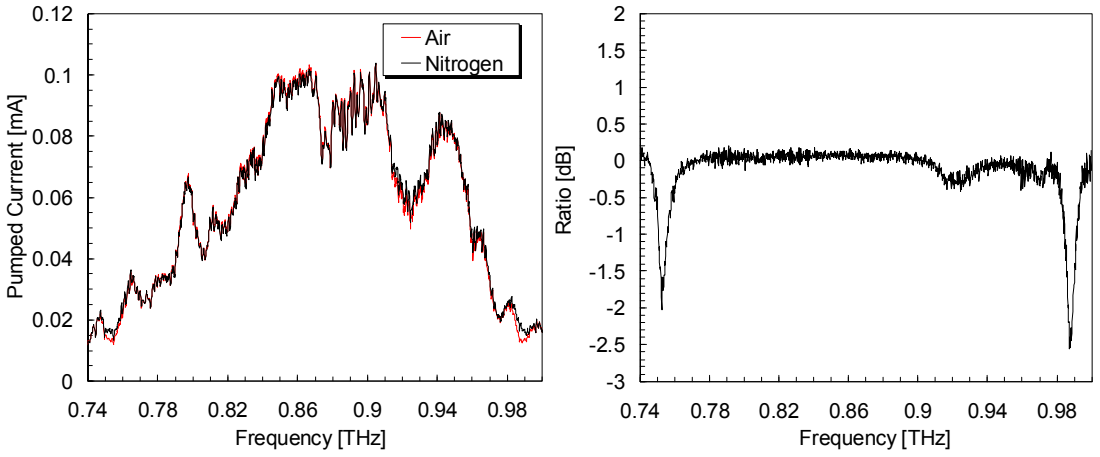

Fig. C-2 Measured results of (a) junction current response and (b) its ratio between the conditions.

C.2.1 Junction current response measurement using an LO source

To see the spectrum lines, we have to use a source with high frequency resolution enough. In this measurement, the LO source used a signal generator, an active frequency quadrapler (×4) and a nonupler (×9) which are the same as ones described in Appendix C, because it is arbitrarily controllable for a frequency interval. The results of junction current response measured are shown in Fig. C-2 (a). By taking a ratio of power coupling between the conditions, transmission losses along the signal path should be known as shown in Fig. C-2 (b). The power coupling was calculated on the basis of eq. B-1. Obviously, sharp absorption lines at around 0.752 THz and 0.988 THz, and weak and broad line at around 0.92 THz were observed. The frequencies are in good agreement with them of water spectral lines.

C.2.2 Noise temperature measurement

Heterodyne measurement is performed to see degradation of averaged noise temperature over the IF range of 4–12 GHz under the typical environment. The results measured for the two conditions are shown in Fig. C-3 (a). Unfortunately, it was impossible to measure noise temperature at LO 0.98 THz due to the weak LO power. In the same manner as the junction coupling, RF losses due to the water vapor were calculated as shown in Fig. C-3 (b), taking a ratio of noise temperature between the two conditions. Degradations of 0.15 dB in the LO range of 0.78–0.90 THz, of 1.4 dB at 0.76 THz, and of 0.25 dB at around 0.92 THz were observed.

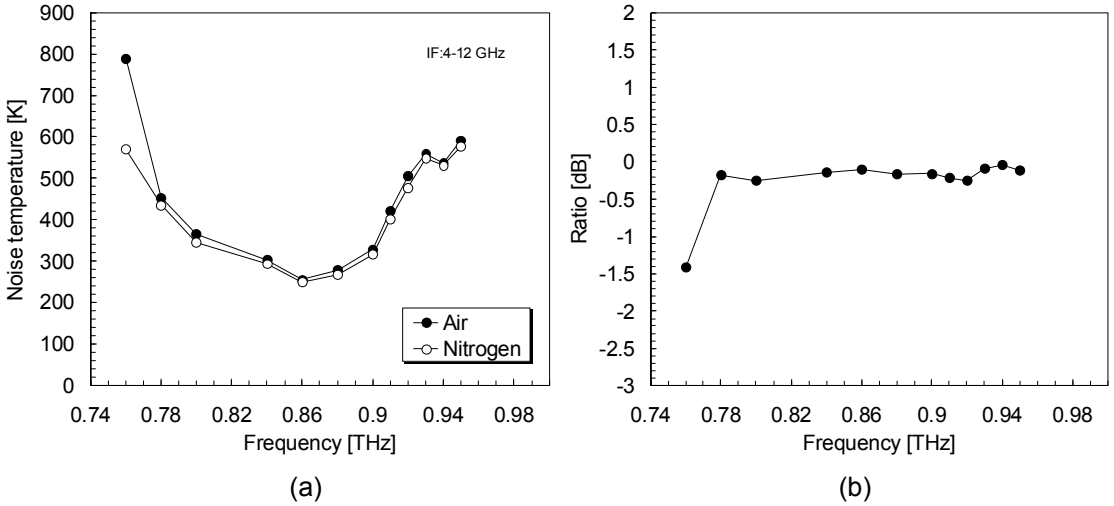

Fig. C-3 Measured results of (a) noise temperature and (b) its ratio between the conditions

C.3 Conclusion

We observed absorption lines employing two methods: junction power coupling and noise temperature. Both results gave consistent dispersion characteristics. Three atmospheric absorption spectrums at 0.752 THz, 0.988 THz, and around 0.92 THz were clearly observed by junction current response measurement. Noise temperature increase was also observed under the typical measurement environment exposed to air, compared to the environment under the nitrogen purge. Especially, the noise temperature at around 0.76 THz was degraded by about 30 %, but the value may depend on environments such as season and whether. Therefore, in order to determine performances of an SIS mixer such as accurate bandwidth, it is necessary to correct a rate of absorption, or to measure noise temperature below 0.75 THz and above 0.99 THz. On the other hand, it seems that influence due to the water vapor over the frequency range of 0.78-0.95 THz which corresponds to band 10 frequency is negligible even at 0.92 THz in the measurement system.

Appendix D
On optimization process of NbTiN films on quartz

D.1 Overview

This appendix describes an optimization process of NbTiN films on quartz. In section 3.6.1.1, fabrication of electrical properties for NbTiN films on fused quartz substrates was reported. The film properties on fused quartz substrates have significantly dependence on the deposition condition, and influence SIS mixers sensitivity near its gap frequency. In order to improve ρ_{20K} and T_c, we suggested that optimized the deposition condition yielding low ρ_{20K} and high T_c at room temperature, unlike an elevated temperature. The optimization process has been established by M. Takeda (of Sizuoka university at present) et al using facilities of NiCT located in Kobe.

D.2 Optimization process

Optimization parameters to obtain such a better film quality are total pressure, flow rate of Argon and Nitrogen, and discharge power. It is accepted that low total pressure is better to avoid deposition of impurities due to the high deposition rate. Consequently, the total pressure was fixed to be 2 mtorr.

Next step is to measure a discharge *I-V* characteristic of NbTiN as shown in Fig. D-1. The *I-V* characteristic should reflect ratio between NbTi and $NbTiN_x$ as following statement:

I. Lower current region– the entire surface of the target is nitrided by N_2 and NbTiN is formed on the surface. In such a situation, amount of N_2 ion is not so changed in the chamber because amount of NbTi atoms is low in the chamber. Therefore, the discharge impedance is increased and deposition rate is low.

II. Negative-resistance region– a part of the surface of the target is nitrided ($NbTiN_x$) and the other part is NbTi. The sputtered NbTi reacts with N_2 in the chamber and the amount of N_2 is reduced. Therefore discharge impedance becomes smaller in this region.

III. Higher current region– the NbTi is sputtered before the surface of the target is nitrided. Since the deposition rate is very high, the NbTi is not reacted with N_2 in the chamber. Therefore, the curve is closed to pure-Ar *I-V* curve without N_2 gas.

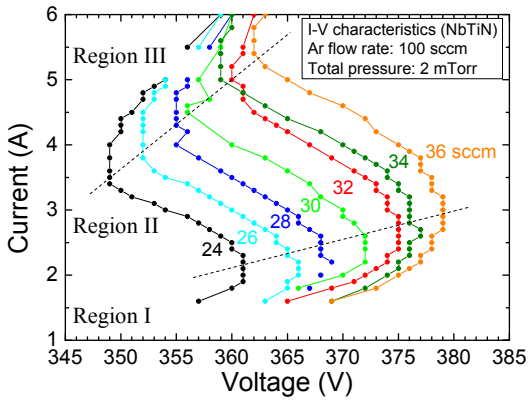

Fig. D-1 Typical discharge current-voltage characteristics for the different flow rates of N_2.

In general, since good superconducting properties (higher T_c and lower ρ_{20K}) are obtained in the negative-resistance region.

Final step is to clear up relation between flow rate of N_2 and bias current in the negative-resistance region. Fig. D-2 shows distributions of T_c and ρ_{20K} as a function of flow rate of N_2 and bias current. T_c and ρ_{20K} resistivity were measured by four probing method. It is found that a minimum resistivity of 90 μΩcm and a transition temperature of 14.5 K were obtained in the condition that the flow rate of Ar to N_2 gas was 100 to 36 sccm at a bias point of 4 A.

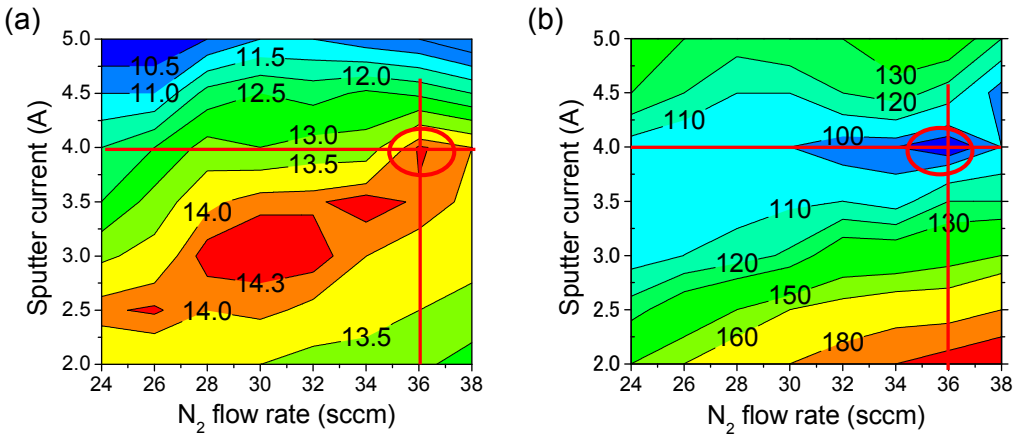

Fig. D-2 Distributions of (a) T_c and (b) ρ_{20K} as a function of flow rate of N_2 and bias current

Publications and research achievements

Refereed papers

[1] Takafumi Kojima, Matthias Kroug, Masanori Takeda, Yoshinori Uzawa, Wenlei Shan, Yasunori Fujii, Zhen Wang, and Hideo Ogawa, "Three Quanta Sensitivity Superconductor–Insulator–Superconductor Mixer for the 0.78–0.95 THz Band," Applied Physics Express, 2, 102201 2009

[2] Takafumi Kojima, Matthias Kroug, Masanori Takeda, Wenlei Shan, Yasunori Fujii, Yoshinori Uzawa, Zhen Wang and Shengcai Shi, "Performance of terahertz waveguide SIS mixers employing epitaxial NbN films and Nb junctions" IEEE Transactions on Applied Superconductivity, Vol. 19, No. 3, pp. 405 – 408, 2009,

[3] Takafumi Kojima, Yasuhiro Abe, Hideo Ogawa, "4-12GHz cryogenic low-noise HEMT amplifier [in Japanese]," The IEICE transactions on electronics. C, Vol.J91-C, No.11, pp. 658-665, 2008

[4] Wenlei Shan, Masanori Takeda, Takafumi Kojima, Yoshinori Uzawa, Shengcai Shi, Takashi Noguchi and Zhen Wang, "Low Noise Waveguide Type NbN/AlN/NbN SIS Mixers Approaching Terahertz Frequencies," IEEE Transactions on Microwave Theory and Techniques, in print.

[5] Yoshinori Uzawa, Matthias Kroug, Takafumi Kojima, Masanori Takeda, Massimo Candotti, Yasunori Fujii, Keiko Kaneko, Wenlei Shan, Takashi Noguchi and Zhen Wang, "A sensitive ALMA Band 10 SIS receiver engineering model," Superconductor Science Technology, 22, 114002, 2009

[6] Masanori Takeda, Wenlei Shan, Takafumi Kojima, Shingo Saito, Matthias Kroug, Yoshinori Uzawa and Zhen Wang, "Low-noise waveguide SIS mixer with NbN/AlN/NbN tunnel junctions tuned by an NbN/MgO/NbTiN microstrip circuit," Superconductor Science Technology, 22, 075015, 2009

[7] Matthias Kroug, Akira Endo, Tomonori Tamura, Takashi Noguchi, Takafumi Kojima, Yoshinori Uzawa, Masanori Takeda, Zhen Wang, and Wenlei Shan," SIS Mixer Fabrication for ALMA Band10," IEEE Transactions on Applied Superconductivity, Vol. 19, No. 3, pp. 171-173, 2009

[8] Masanori Takeda, Shingo Saito, Zhen Wang, Wenlei Shan, Shengcai Shi, Takafumi Kojima, Yoshinori Uzawa, Yasunori Fujii, Matthias Kroug, and Jing Li, "Mixing properties of NbN-based SIS mixers with NbTiN wirings" IEEE Transactions on Applied Superconductivity, Vol. 19, No. 3, pp. 436-439, 2009

[9] Akira Endo, Takashi Noguchi, Matthias Kroug, Sergey V. Shitov, Wenlei Shan, Tomonori Tamura, Takafumi Kojima, Yoshinori Uzawa, Takeshi Sakai, Hirofumi Inoue, and Kotaro Kohno, "A Novel THz SIS Mixer with a NbTiN-Ground Plane and SIS Microtrilayers Directly

Grown on a Quartz Substrate," IEEE Transactions on Applied Superconductivity, Vol. 19, No. 3, Page(s): 400-404, 2009

[10] Takafumi Kojima, Kouichi Kuroiwa, Yoshinori Uzawa, Matthias Kroug, Masanori Takeda, Yasunori Fujii, Kaneko Kaneko, Akihira Miyachi, Zhen Wang and Hideo Ogawa, "A low-noise terahertz SIS mixer incorporating a waveguide directional coupler for LO injection," submitted to Journal of Infrared, Millimeter, and Terahertz Waves

International Conference (First author)

[1] Takafumi Kojima, Matthias Kroug, Masanori Takeda, Wenlei Shan, Yasunori Fujii, Yoshinori Uzawa and Zhen Wang, "Terahertz waveguide SIS mixers with epitaxial NbTiN films and Nb junctions," 9th European Conference on Applied Superconductivity September 13-17, 2009, Dresden, Germany

[2] Takafumi Kojima, Matthias Kroug, Masanori Takeda, Sergey V. Shitov, Yoshinori Uzawa, Wenlei Shan, Yasunori Fujii, Zhen Wang, "A Low Noise NbTiN-based SIS Mixer for Terahertz Band," International Superconductive Electronics Conference 2009, Fukuoka, Japan, June 16-19, 2009,

[3] Takafumi Kojima, Matthias Kroug, Masanori Takeda, Wenlei Shan, Yasunori Fujii, Yoshinori Uzawa, Zhen Wang and Shengcai Shi, "Performance of terahertz waveguide SIS mixers employing epitaxial NbN films and Nb junctions", 9th Workshop on SMW Rx Technologies in Eastern Asia ASIAA, Taipei, Taiwan, November 18-20, 2008

[4] Takafumi Kojima, Matthias Kroug, Masanori Takeda, Wenlei Shan, Yasunori Fujii, Yoshinori Uzawa, Zhen Wang and Shengcai Shi, "Performance of terahertz waveguide SIS mixers employing epitaxial NbN films and Nb junctions," 2008 Applied Superconductivity Conference Chicago, Illinois U.S.A, August 17-22, 2008

[5] Takafumi Kojima, Yoshinori Uzawa, Wenlei Shan, Yasunori Fujii, Masanori Takeda, Matthias Kroug, Sergey V. Shitov, and Hideo Ogawa, "Characterization of waveguide components for the ALMA band 10," 19th International Symposium on Space THz Technology, Poster 9-3, Groningen, Netherlands, April 2008

[6] Takafumi Kojima, Matthias Kroug, Massimo Candotti, Yasunori Fujii, Keiko Kaneko, Sergey V. Shitov, Yoshinori Uzawa, Kazuya Inaoka, Hideo Ogawa, Wenlei Shan, Shengcai Shi, Masanori Takeda, Zhen Wang, Mingjye Wang, Mingtang Chen "Preliminary design of the ALMA band 10 cartridge" 8th Workshop on Submillimeter-wave Receiver Technologies in Eastern Asia, Yonsei University, Seoul, Korea January 2008

[7] Takafumi Kojima, Yasuhiro Abe, Akihiro Kurozumi, Kazuya Inaoka, Kimihiro Kimura, Taku Nakajima, Yoshinori Yonekura, Hideo Ogawa, Atsushi Hara, "The Development of Cryogenic HEMT Amplifiers for SIS mixers," 7th Workshop on Submillimeter-Wave Receiver Technol-

ogies in Eastern Asia Jointly with Workshop on the Development of Low-Noise Receiver Technology at Millimeter Waves and Terahertz Frequencies, Osaka, Japan, January 2007

Awards

[1] The 27th Japanese society of Applied Physics Awards for Research Paper Presentation, (September 8, 2009)

[2] Osaka Prefecture University President's Award (December ,2009)

Fellowship

Research Fellow of Japan Society of the Promotion of Science for young scientist (2009-2010)

Grants/Scholarships:

[1] Grant-in-Aid for JSPS Fellows (2009) 09J10535 "Study of Low Noise Terahertz SIS Mixers with All NbTiN Tuning Circuit"

[2] Scholarship from ICOM Promotion Foundation (2008, 2009:declined)

[3] Sasakawa Scientific Research Grant from The Japan Science Society (2007) "Integration of SIS Mixer and Cryogenic Low noise HEMT Amplifier for Terahertz Radio Telescopes"

Acknowledgement

I would like to acknowledge my two supervisors who have been essential to the writing of this thesis. First of all, Yoshinori Uzawa gave me interesting and important research and the great environment. I am extremely fortunate to have had the pleasure to work with such an insightful advisor, who not only served as an excellent mentor, but has never hesitated to share his wisdom. He, as the leader of the ALMA band 10 team, also showed me importance of communication and relationship of mutual trust to play a role as a part of the member. The experience would be useful in next study and job. Hideo Ogawa, with whom I have worked for the past seven years beginning as an undergraduate and continuing through my masters and doctoral work, gave me the chance to participate in such large project. Training and supervision based on his unique capacity and experiences over the past four decade always have led me in the right direction. Without them, none of this work would be possible.

I am deeply grateful to ALMA band 10 members: Matthias Kroug has discussed every experiment of SIS mixer with me and has fed back results accurately to fabrication, where I have done ones to design. The discussions made one of the biggest drivers to develop the low noise mixer. I would never forget he said, “I am so happy to see the data,” when we achieved the band 10 specification. Yasunori Fujii is a super-engineer, who has ability to perform several activities simultaneously. He always advised me to obtain better performances of mixers in terms of engineer. Kaneko Keiko is a specialist in machining processing. She taught me how to measure accurate dimension, using 3-D measurement system. Akihira Miyachi gave me helpful information on SIS junctions based on his extensive knowledge about fabrication technology. Masanori Takeda (of Shizuoka University at present) had provided us NbTiN films having excellent quality. He always has encouraged me so as to be able to enjoy my study. His joke had some relaxant effect similar to coffee break. Sergey Shitov (Institute of Radio Engineering & Electronics at present) taught me how to evaluate SIS mixers at an operating temperature of 2 K. The result obtained was partly published in Applied Physics Express. Massimo Candotti is an expert of optics development. A diagonal horn of a prototype mixer block is designed by him. Kouichi Kuroiwa, who is the same university’s student as me and new member of band 10, helped me for cryogenic waveguide loss measurement. He will take over my remaining study and upgrade our receiver to next stage.

I would like to thank Shin’ichiro Asayama of National Astronomical Observatory of Japan, for giving a motivator to join in ALMA band 10. I could obtain the chance to join the big project because of his connection between NAOJ and OPU.

I am in debt to Zhen Wang of the Communications Research Laboratory in Kobe, Hyogo, for his encouragement and support on my research. His strong backup support made me feel some relief.

I would like to acknowledge Wenlei Shan and Shengcai Shi of Purple Mountain Observatory, for helpful comments and discussions for designing ALMA band 10 SIS mixers, and using and modifying the program of the SIS mixer analyzer (SISMA). The analysis of SIS mixers in this work was performed using the SISMA.

I owe a very important debt to SIS device fabrication group: Takashi Noguchi and Youko Kiuchi (of Mitsubishi Electric TOKKI systems Corporation).

I would like to express my gratitude to Yasuhiro Abe for teaching fundamentals and practical advices of high frequency electric circuit. The knowledge provided a basis of not only the development of low noise HEMT amplifiers but also the analysis of ALMA band 10 SIS mixers.

I acknowledge Taku Nakajima (of Nobeyama Radio Observatory at present) for teaching me how to evaluate SIS receivers when I was the undergraduate. My basis to study in field of radio astronomy was established by his training.

I would like to thank student members in NAOJ; Akira Endo (of Delft University of Technology at present) provided us SIS mixers with Nb/Al-AlN/Nb junction. Mamoru Kamikura (of Mitsubishi Electric Corporation at present) has taught me a lot about waveguide components. Yasutaka Serizawa (University of Tokyo) has worked hard together as only my compeer at ATC. Hirofumi Inoue (University of Tokyo) gave me an inspiration to improve IF performance. He provided me chances playing futsal to have some fun. Masato Naruse (University of Tokyo) and Tom Nitta (University of Tsukuba) helped me for FTS measurement of dielectric films. Masayuki Kawamura (University of Tokyo at present) helped me for experiment and fabrication of cryogenic amplifiers, when he was the undergraduate of Osaka Prefecture University.

I acknowledge all ATC members for their helpful discussions and support. Special thanks to Yutao Sekimoto and Hiroshi Matsuo, who provides us opportunities to learn an extensive knowledge. I also would like to thank all ALMA members for their warm encouragement. Special thanks to Satoru Iguchi, who give me warm encourage.

The experiment reported here would not have been possible without the support and cooperation of the National Astronomical Observatory in Mitaka, Tokyo, the Communications Research Laboratory in Kobe, Hyogo. To all of these I extend my thanks and appreciation.

I am grateful to the secretaries Yoko Marumoto and Yoko Hasegawa at Osaka Prefecture University, the secretaries Taeko Yoshida, Hiromi Murakami and Ryoko Kuroda at the ATC.

I thank all the members of laboratory in Osaka Prefecture University, including Yoshinori Yonekura (Ibaraki University at present), Toshikazu Onishi, Kazuyuki Muraoka, Kimihiro Kimura, Masahiro Kaiden (of NEC TOSHIBA Space System. Ltd. at present).

I thank Gumpei Kikuchi of Kanagawa Kikou for making mixer blocks used in thesis. I also would like to acknowledge Oshima Prototype Engineering Co. for making waveguide components, such as modular 10-dB couplers.

My problem-solving skills, patience, carefulness, curiosity, cooperativeness and loyalty had been cultivated at the Osaka Prefecture University horsemanship club where I belonged during my undergraduate. Without the experiences, this doctoral work would never have been completed. Special thanks to managers, coaching staffs, team members trained through friendly rivalry, and all horses.

Finally, I would like to express my deepest gratitude to my parents, brothers, and Xi Chen, all of whom have supported me throughout this experience.

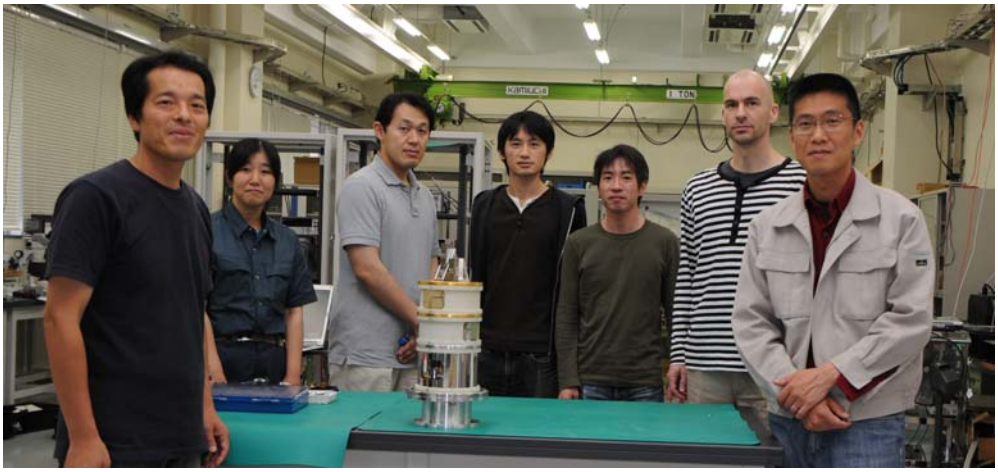

ALMA band-10 receiver development team

Laboratry members of the Osaka Prefecture University

論文要旨

Quantum Limited 0.78–0.95 Terahertz Waveguide SIS Mixers for the ALMA Band 10 Receivers (ALMA Band 10 受信機に用いる 0.78–0.95 THz 帯超低雑音 SIS ミキサ)

小嶋崇文

Superconductor-Insulator-Superconductor (SIS) ミキサは電磁波のヘテロダイン検出に最も高感度な検出器であり，電波天文学におけるミリ波サブミリ波の輝線・連続波観測に広く用いられてきた。SIS ミキサは，導波管回路，低損失伝送線路，そしてミキシングを担う SIS 接合から成る。テラヘルツ帯は電波天文学や通信分野においても長く未開拓周波数帯であったため, 現在その発展のために SIS ミキサの広帯域･高感度化が期待されている。

Atacama Large Millimeter/submillimeter Array (ALMA) 計画は，日米欧 3 者が協力し南米チリ・アンデス山脈の標高 5000 m のアタカマ高地に 66 基の電波望遠鏡を設置する巨大電波干渉計建設プロジェクトであり，2012 年から本格運用開始が予定されている。観測周波数は 30 GHz–0.950 THz であり，受信機はその大気の窓をカバーするように 10 個の周波数帯に分割して最適化され，30 年という長期運用に耐え，メンテナンスが容易なようにカートリッジ型受信機が採用されている (図 1)。Band 10 は，ALMA プロジェクトの最高周波数帯であり 0.787-0.950 THz をカバーする。Band 10 は, 0.01 秒角という高空間分解能を生かした原始惑星系円盤の内部構造と進化の解明が期待される周波数帯である。

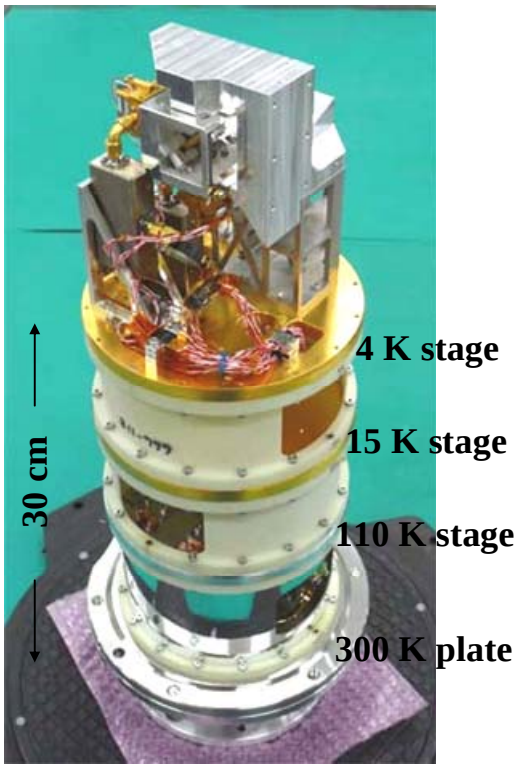

図 1 開発中のプロトタイプカートリッジの写真

このようなチャレンジングな観測を実現するために, ALMA 計画では厳しい受信機仕様の要求があり, Band 10 では量子限界雑音温度の 5 倍である 230 K という受信機雑音温度をその帯域の 80 % に渡って達成する必要がある。最も困難な開発要素は SIS ミキサ(図 2)であるが、これまで技術的困難によりこの超低雑音・広帯域特性を満たすミキサは存在し

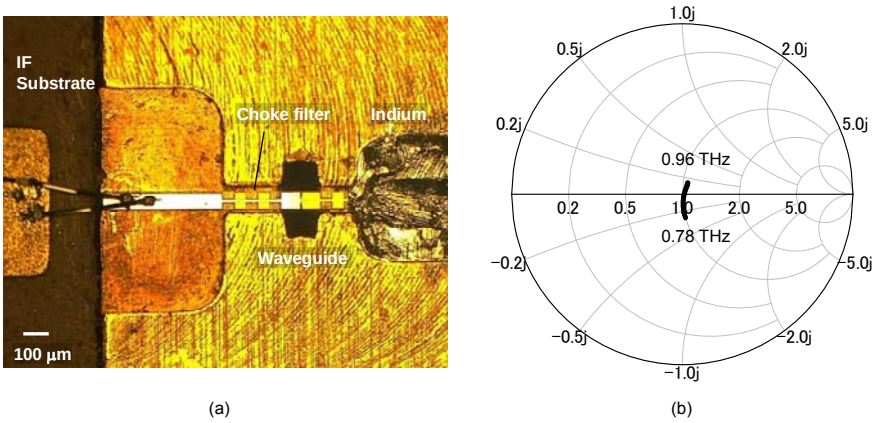

図 2　(a) SIS ミキサ内部の写真ミキサチップと (b) ミキサチップ導波管-マイクロストリップ変換の給電部分のインピーダンス。このスミスチャートは 30 Ω で規格化している。

なかった。他のバンドでは量子限界雑音の数倍という受信機が成功裏に開発されてきたこととは対照的に，当周波数帯の最大の困難は、高い信頼性のある全 Nb-SIS ミキサを用いることが出来ないことにある。これは当周波数帯が Nb のギャップ周波数（約 0.7 THz）以上であるために、Nb の電極損失が急激に増大し伝送線路の損失が増大することに因る。例えば, 伝送線路の電極材料として Nb を用いた場合, 1 波長当たり入力信号に対して 60% 以上減衰する。このように，20 年以上前から確立されてきた SIS ミキサの作製技術をそのままスケールダウンさせて当周波数帯に適用することはできない。また，SIS 接合は構造的に大きなキャパシタンスをもつため，それを打ち消すための共振構造が必要になる。この場合，その帯域はωRC で制限されるため，比帯域 19%以上が要求される Band 10 周波数帯域をカバーするためには, SIS 接合の臨界電流密度 J_c は 15 kA/cm^2 以上が必要であると指摘されてきた。これは SIS 接合に Nb/AlO$_x$/Nb を用いた場合，絶縁層 AlO$_x$ の厚さが数 nm 程度という極端に薄い SIS 接合が必要である。高い臨界電流密度は，接合品質を保ったまま実現することは現在の作製技術では困難である。したがって，当周波数帯では伝送線路の電極材料を変え，設計手法を見直すという研究開発要素が必要となる。

これらの技術的困難を解決するために，作製および設計的アプローチの両方から詳細な調査を行い，テラヘルツ帯にギャップ周波数を有する超伝導体・窒化ニオブチタン(NbTiN)を用いたミキサの開発を進めてきた。本研究は ALMA Band 10 の厳しい受信機仕様を満たすために，SIS ミキサの広帯域化および低雑音化の実証を目的としている。

第 1 章では序論として，本研究の背景，重要性とその目的について述べた。

第 2 章では，SIS ミキサの設計や解析を行うため，ミキシング原理と超伝導高周波伝送理論を解説した。SIS 接合を用いたミキシングの原理は，Tucker と Feldman によって確立されており，準粒子トンネル電流に起因する非線形電流電圧特性と，一般的なダイオードのミキシング理論を組み合わせている。また，超伝導マイクロストリップラインをモデリングするためには，超伝導の表面インピーダンスを計算する必要があり，これには

Mattis-Bardeen 理論に基づいた超伝導の複素導電率を適用した。

第 3 章では SIS 接合およびマイクロストリップラインに用いる電極材料として様々な組み合わせを検討し，選定を行った。当周波数帯では，高い変換利得の得られる SIS 接合と低い伝送損失の得られるマイクロストリップラインが必須であり，最終的に，$Nb/AlO_x/Nb$ 接合と $NbTiN/SiO_2/Al$ マイクロストリップラインの組み合わせが最も有望であることを理論的計算から確認した。また NbTiN 膜の低損失化を図るために最適な作製条件の調査を行った。さらに SIS ミキサの作製プロセスの説明をした。

第 4 章では，$Nb/AlO_x/Nb$ 接合＋$NbTiN/SiO_2/Al$ マイクロストリップラインを MgO 基板上に作製したミキサの特性を実験的に調査した。このミキサは MgO 基板上で NbTiN 膜がエピタキシャル成長し，理想的な超伝導特性が得られること利用したもので，世界的にも初めての構造である。一方，MgO は 10 程度の比較的高い比誘電率をもつために電磁波の伝搬損失の一因である基本モードの IF ポートへのリークや高次モードが発生しやすくなる。したがって，設計には 25 μm という薄い基板厚と IF ポートへのリークを強力に抑圧するためにハンマーフィルタを適用した。作製したミキサ素子は 0.83 THz において 171 K という非常に低雑音な性能を示した。これは，超伝導伝送線路が非常に低損失で働いていることを実証するものである。一方，詳細な解析により，Band 10 に用いるミキサとしては回路的にさらなる改善が必要であることを明らかにした。

第 5 章は，本博士論文の中心となる部分であり，$Nb/AlO_x/Nb$ 接合＋$NbTiN/SiO_2/Al$ マイクロストリップを溶融石英基板上に作製したミキサの特性を詳細に測定・解析した。溶融石英は従来から使用されてきた基板で扱いやすいが，NbTiN 膜は多結晶成長し，その特性がスパッタ条件に依存しやすい。このため，第 3 章で説明した最適化条件で作製した NbTiN 膜を用いた。また，伝送線路にはグラウンド電極を Al，ストリップ導体に NbTiN を用いた反転型マイクロストリップラインを適用して低損失化を図った(図 3)。SIS 接合に関しては，これまで，臨界電流密度 J_c は 15 kA/cm^2 以上が必要であると考えられてきた。そのような高い J_c の接合は一般に接合品質の劣化を招き，現状の作製技術では困難である。したがって，J_c が 10 kA/cm^2 程度の SIS 接合に対して，低雑音特性を保ったまま広帯域化が可能かどうかを設計的なアプローチから検討した。具体的には，共振回路を固定し利得と雑音が信号源アドミタンスにどのように依存するかを解析した。この結果，ミキサの雑音最小と利得最大になるインピーダ

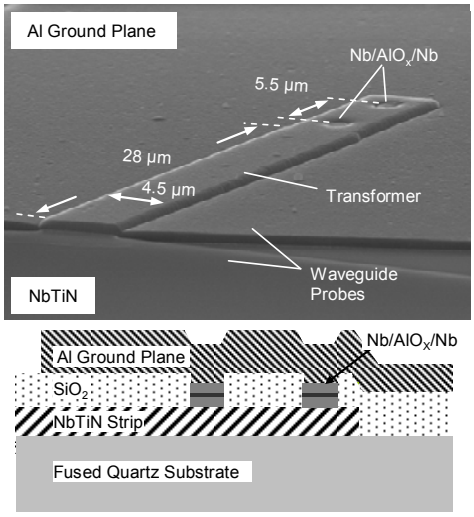

図 3　ミキサの同調回路部分の走査型電子顕微鏡写真と断面構造

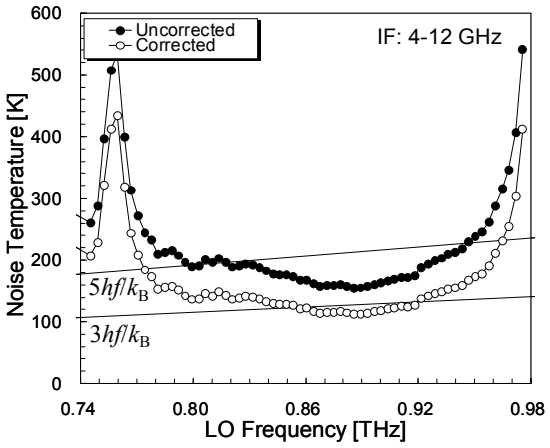

図 4　2 K における受信機雑音温度。測定には真空窓として 500 μm のテフロンとビームスプリッタとして 8.5 μm のポリイミドフィルムを用いた.

ンスが異なることが判明し，広帯域・低雑音特性を同時に満足する解が存在することがわかった。この解析に基づいて作製したミキサを測定したところ，ALMA band 10 の受信機仕様を満たしうる低雑音広帯域特性を実証することができた。また，物理温度 2 K における雑音性能を測定し, 3 倍の量子雑音に相当する 120 K という世界最高性能の超低雑音特性を示し，開発に成功した(図 4)。

第 6 章では 4-12 GHz という広帯域な IF 系回路に関して, IF 雑音および出力特性の平坦度の改善方法を検討した。当周波数帯で低雑音化の妨げとなっていた原因のひとつは IF 雑音温度とミキサの利得低下である。我々の解析では IF 雑音の寄与は全受信機雑音温度の 20-30%程度を占める。したがって，高いミキサ利得とできるだけ低い IF 系の雑音温度が求められる。しかしながら，4-12 GHz という 1 オクターブを超えるバンド幅でこれを満たすように IF 特性を保つことは非常に困難であった。高いミキサ利得はミキサの 200 Ω以上の高い出力インピーダンスによって得られるが，そのようなインピーダンスは 50 Ωの特性インピーダンスをもつ IF 系とのマッチングを難しくする。これを解決するためにミキサと IF 系とのインピーダンス特性を詳細に調査し，どのような IF 回路が適当であるかを検討した。解析の結果，アイソレータの入力リターンロスの改善が，受信機雑音温度および出力特性の改善に効果的であることを見出した。これにより IF 特性に関して，ALMA の仕様を満たす特性を得ることができた。

第 7 章では導波管型 10 dB カプラを一体化したミキサブロックの開発について説明した。導波管コンポーネントはミリ波帯では広く用いられているが，当周波数帯では大きな損失が発生することが問題となっていた。まず，長さ 25 mm の導波管を用いて冷却時の損失を評価した。その結果 1.2 dB の損失が生じることがわかった。この損失はミリ波帯で使用されているような長さ 30 mm の導波管を持つモジュラータイプの導波管カプラを使用した場合，30 %程度雑音温度が上昇してしまう。したがって，10 dB カプラをミキサブロックに一体化することでフランジでのミスマッチを避け，導波管をできるだけ短くすることにより低損失化を図った。第 5 章で開発した SIS ミキサを実装して雑音温度を測定した結果，ALMA band 10 の仕様を満たす結果を始めて実証した。

第 8 章では本研究で得られた主要な成果と今後の展開をまとめた。